EXPLORING MANY-BODY QUANTUM DYNAMICS WITH RYDBERG DRESSED FERMIONS AND TILTED HUBBARD SYSTEMS

ELMER GUARDADO-SANCHEZ

A DISSERTATION

PRESENTED TO THE FACULTY

OF PRINCETON UNIVERSITY

IN CANDIDACY FOR THE DEGREE

OF DOCTOR OF PHILOSOPHY

RECOMMENDED FOR ACCEPTANCE

BY THE DEPARTMENT OF

PHYSICS

ADVISER: PROFESSOR WASEEM BAKR

September 2021

© Copyright by Elmer Guardado-Sanchez, 2021.

All rights reserved.

Abstract

Ultracold atomic gases in optical lattices are an ideal platform for studying quantum many-body physics. The long timescales and isolated nature of these systems makes them particularly suited for exploring the dynamics of nearly closed quantum systems and their relaxation towards thermal equilibrium. In this thesis, we demonstrate the realization of two novel cold atom systems: lattice Fermi gases with non-local interactions and tilted Fermi-Hubbard systems. In both of these systems, we explore the slow relaxation of density perturbations, either due to kinetic constraints or unusual hydrodynamics.

The first system we study is a Fermi gas laser coupled to a Rydberg state. For near resonant coupling of a localized gas in a unit-filled lattice, we realize a quantum Ising model with transverse and longitudinal fields. We study the out-of-equilibrium dynamics of antiferromagnetic correlations in this spin system. For far off-resonant Rydberg coupling, we prepare itinerant Fermi gases with strong non-local interactions. In this Rydberg-dressed regime, we introduce a small Rydberg admixture to the ground state of the system which results in a laser-tunable soft-core interaction potential. We use this technique to realize a t-V model with spin-polarized fermions and study the dynamics of imprinted charge density waves. For strong off-site interactions, the number of bonds is approximately conserved, which leads to slow relaxation of these states. More generally, the Rydberg-dressing technique is promising for future studies of extended Hubbard models in multi-component systems.

The second system we study is the two-dimensional Fermi-Hubbard model in the presence of a large tilt. When the tilt is aligned with a lattice axis, the system exhibits slow thermalization and subdiffusive charge transport due to modified hydrodynamics where heat transport acts as a bottleneck for charge transport. This work sets the stage for studying the complete breakdown of thermalization expected for more generic tilt angles where Hilbert space fragmentation is expected.

Acknowledgements

There are too many people who contributed to my development over the past 6 years. I will surely miss many of you here. However, I will always be grateful to you.

First, I would like to thank my advisor, Waseem Bakr, for his constant presence and mentorship. I owe you most for the scientist I have become. Thank you for pushing me when I needed it. I will always be impressed by your ability to envision what is possible to do in an experiment and hope that some of it has stuck on me. Having said that, I would be amiss if I did not also thank my undergrad advisor Martin Zwierlein, who knew that working with Waseem was the best choice, way before I did. He too contributed in my development and I hope to continue bringing a mix of their best qualities with me wherever I go in the future.

I would like to thank the entirety of the Bakr Lab, past and present. To Peter Schauß, who joined as a postdoc along me and taught me everything about Rydberg physics. I thank him especially for agreeing to be a reader of this thesis, making sure there are no outrageously wrong statements. To Peter Brown, I will always remember working with you in our dark lab listening to an eclectic assortment of music; including, but not limited, to the whole Saturday Night Fever soundtrack. To Benjamin Spar, who taught me everything I know about Judaism and introduced me to the world of Marxist twitter. I know that I leave the lab in good hands and cannot wait to see the physics you will produce. To Stanimir Kondov, who showed me that being a fantastic physicist and athleticism were not mutually exclusive. To Debayan Mitra, from whom I learned much of my technical skills and who was also a great friend outside of lab. To the guys in the Molecule Lab, Lysander Christakis and Jason Rosenberg. I am excited to see the Molecular Microscope up and running soon. Also to our new postdoc, Zoe Yan, who joined this last crazy year. I am sure that you will guide both labs in the right direction.

I am thankful to the Princeton Physics faculty who helped me along the way. Special thanks to David Huse, whose theory support was vital for our research. His physics intuition still boggles me and makes me believe that true genius is an attainable goal. To Mike Romalis and the greater Romalis Lab, I will fondly remember all the Friday lunch "meetings". And to Lawrence Cheuk, who has been a great friend through the pandemic and source of procrastination around lab. I look forward to see your machine come online soon.

I am also very thankful for everyone else at Jadwin who has, in some way or another, helped me during my PhD. I thank Kate Brosowsky, Toni Sarchi, Darryl Johnson, Martin Kicinski, Ted Lewis, Lauren Callahan, Julio Lopez, Robert Rickett, Steve Lowe, and Geoff Gettelfinger.

I also thank everyone who made Princeton a town worth of spending my 20s in. I am very thankful to my close friends Jennie Willemsen and Arianna Sherman. I fondly remember every late night at Dbar or watching Sherlock. Thank you for making our friendship feel like family. Also to the rest of my 140 Snowden family: Tom Underwood, Matt Peterson, and Peter Humphries. Additionally, I am grateful to consider myself part of the Rockville climbing community. While not the flashiest gym, it is certainly the one with the nicest people. Lastly, I would like to thank the rest of the Drunk Mixed-Ethnicity Grad Students with whom I had a lot of fun times.

Finally, I would like to thank the entirety of my family. To my parents, Elmer and Hortensia, I owe everything I am and everything I have accomplished to your continuous love and support. To my siblings Mateo, Oscar Alfredo, Hortensia, Claudio and Paloma. I look forward to see how far you will go. Also to the Behl-Bawa family who has accepted me as a son. But above all, I thank my wife Saloni Behl, I do not know what I would do without your love and continuous email redactions. Thank you for bringing calm to my life and for pushing me to be a better person.

To my family.

Contents

	Abs	tract .		iii
	Ack	nowledg	gements	iv
	List	of Tabl	les	xii
	List	of Figu	ires	xiii
L	Inti	roducti	on	1
2	Ryc	dberg a	atoms for ultracold systems	6
	2.1	Introd	uction	6
	2.2	Scalin	gs of Rydberg atom properties	7
	2.3	Transi	tion Dipole Matrix Elements	9
		2.3.1	Radial component of the dipole matrix element	10
		2.3.2	Angular component of the dipole matrix element	13
	2.4	Lifetin	ne of Rydberg atoms	14
	2.5	Intera	ctions between electric dipoles	16
		2.5.1	Calculating C_6 coefficients with angular dependence	17
		2.5.2	C_6 values for nP pair-states of Lithium	20
	2.6	Two 2	-level Rydberg atom model	20
	2.7	Reson	ant coupling	22
		2.7.1	Rydberg Blockade Radius	23
	2.8	Off-res	sonant coupling: Rydberg dressing	23

		2.8.1	"Dressed" ground-state	23
		2.8.2	"Dressed" interaction potential	24
		2.8.3	Scaling of Rydberg dressing parameters	28
	2.9	Calcul	lating Rydberg properties using Python packages	30
		2.9.1	Multi-polar Expansion	31
3	Ryo	dberg ($ m dressing \ of \ ^6Li$	34
	3.1	Rydbe	erg dressing scheme	35
		3.1.1	Lithium states at high magnetic fields	35
		3.1.2	Dressing scheme	39
	3.2	Pair-s	tate potential calculations	41
		3.2.1	Pair-states vs. principal quantum number	42
		3.2.2	Pair-states vs. magnetic field	43
		3.2.3	Förster resonances	44
	3.3	Full R	Rydberg-dressed potential	45
		3.3.1	Overlap with nearby pair-states	45
		3.3.2	Wavefunction spread in optical lattice	48
		3.3.3	Interaction potential between atoms in different ground-states	50
	3.4	Laser	System	52
		3.4.1	Ultraviolet Laser	53
		3.4.2	Frequency stabilization	53
		3.4.3	Intensity stabilization	54
		3.4.4	Optical setup	56
		3.4.5	Rydberg dressing setup	57
	3.5	Specti	roscopy of ⁶ Li Rydberg states	58
		3.5.1	"V-scheme" spectroscopy	58
		3.5.2	MOT spectroscopy	60
	3.6	Laser	characterization with direct excitation	63

		3.6.1	Resonance vs. lattice depth	65
		3.6.2	Resonance vs. magnetic field	66
		3.6.3	Magnetic dispersion of $ nP\rangle$ Rydberg states	67
		3.6.4	Observation of anomalous "sharp" peaks near resonance	68
		3.6.5	Direct measurement of Rabi frequency	69
	3.7	Lifetin	ne characterization of Rydberg dressed atoms	71
		3.7.1	Effect of geometry	72
		3.7.2	Density-dependent lifetimes	74
		3.7.3	Effect of magnetic field	75
		3.7.4	Effect of optical potentials	77
		3.7.5	Effect of hyperfine ground-state	77
		3.7.6	Effect of principal quantum number	78
	3.8	Rydbe	erg-dressed potential characterization	79
		3.8.1	Many-body Ramsey interferometry	79
		3.8.2	Interferometry of $^6\mathrm{Li}$	81
		3.8.3	Ramsey vs. Detuning	82
		3.8.4	Indirectly measuring the Rabi frequency Ω	83
		3.8.5	Directly measuring interactions from Spin-Echo interferometry	84
4	Que	ench dy	ynamics in a 2D transverse Ising spin system	85
	4.1	Simula	ating a quantum Ising model with Rydberg atoms	86
	4.2	Exper	imental realization	89
		4.2.1	Laser System for coupling to Rydberg states	89
		4.2.2	Experimental Setup	89
		4.2.3	Single atom Rabi oscillations and coherence	90
		4.2.4	Movement of the atoms during the quenches	92
		4.2.5	Theoretical calculation of C_6	92
	4.3	Short	"sudden" quenches	93

		4.3.1	Comparison to NLCE dynamical calculations	93
	4.4	Near-	"adiabatic" quenches	97
		4.4.1	Effective temperature by comparison with classical Monte Carl	o 101
		4.4.2	Investigation of phenomenological decoherence models	102
	4.5	Concl	usion	107
		4.5.1	Current State-of-the-art	107
5	Sub	diffusi	ve charge transport in a tilted Hubbard system	109
	5.1	Introd	luction	110
	5.2	Exper	imental Setup	112
		5.2.1	Tilt Potential	113
		5.2.2	Spatial Light Modulator	116
		5.2.3	Experimental parameters	116
		5.2.4	Linear response	118
	5.3	Result	5 <mark>8</mark>	119
		5.3.1	Early-time dynamics	119
		5.3.2	Late-time dynamics	121
	5.4	Hydro	odynamic Model	122
		5.4.1	Simplified Model	123
		5.4.2	Complete hydrodynamic model	128
		5.4.3	Simultaneous fitting of the model	129
	5.5	Concl	usion	129
		5.5.1	Outlook	131
6	Que	ench D	ynamics of a Fermi Gas with Strong Long-Range Intera	c-
	tion	ıs		132
	6.1	Introd	luction	133
	6.2	Evner	imental setup	135

		6.2.1	Simulation of a $t - V$ model	135
		6.2.2	Ground and Rydberg states used in the experiments	137
	6.3	Rydbe	erg-dressed interaction potentials	138
	6.4	Lifetin	ne Characterization	139
		6.4.1	Dependence of lifetime on atom number at fixed density	143
	6.5	Quenc	h Dynamics	143
		6.5.1	Atom loss during charge density wave dynamics	145
	6.6	Nume	rical simulations	148
	6.7	Conclu	ısions	151
7	Con	clusio	n and Outlook	153
	7.1	Outloo	ok	154
\mathbf{A}	Nur	nerov'	s Algorithm	156
	A.1	Deriva	tion	156
	A.2	Imple	mentation for Rydberg atoms	157
В	Cal	culated	d C_6 values of $^6\mathrm{Li}$ pair-states.	159
\mathbf{C}	Fors	ster Re	esonances of $^6\mathrm{Li}$.	167
	C.1	C_6 coe	efficients with Pair-Interaction	168
D	Mea	asured	$ 2S\rangle ightarrow nP\rangle$ Rydberg Lines of $^6{ m Li}.$	171
Bi	bliog	rraphy		17 3

List of Tables

2.1	Scaling of Rydberg atom properties	8
2.2	Lithium model potential parameters	11
2.3	Lithium Rydberg lifetime parameters	15
2.4	Scaling of Rydberg dressing properties with n^*	28
2.5	Scaling of Rydberg dressing properties with laser power P	29
2.6	Selection rules on multi-polar expansion	32
3.1	Clebsch-Gordan coefficients between $ m_l,m_s\rangle$ and $ j,m\rangle$ basis	39
B.1	Calculated C_6 values for ⁶ Li $ nS, 1/2, \pm 1/2\rangle$ pair-states	160
B.2	Calculated C_6 values for ⁶ Li $ nP, 1/2, \pm 1/2\rangle$ pair-states	161
В.3	Calculated C_6 values for ⁶ Li $ nP, 3/2, \pm 1/2\rangle$ pair-states	162
B.4	Calculated C_6 values for ⁶ Li $ nP, 3/2, \pm 3/2\rangle$ pair-states	163
B.5	Calculated C_6 values for ⁶ Li $ nD, 5/2, \pm 1/2\rangle$ pair-states	164
B.6	Calculated C_6 values for ⁶ Li $ nD, 5/2, \pm 3/2\rangle$ pair-states	165
B.7	Calculated C_6 values for ⁶ Li $ nD, 5/2, \pm 5/2\rangle$ pair-states	166
C.1	Magnetic fields to tune Förster resonances in $ nP, nP\rangle$ states	168
D.1	Measured wavelengths of ⁶ Li $ 2S\rangle \rightarrow nP\rangle$ transitions	172

List of Figures

Rydberg atom radial wavefunctions	12
Lifetime of $^6{\rm Li}$ Rydberg atoms	14
Van der Waals interactions between Rydberg atoms	18
Calculated C_6 coefficients for the P states of $^6\mathrm{Li}$	2
Two 2-level Rydberg atom model	22
Rydberg "dressed" interaction potential	27
⁶ Li $\left 2S_{1/2}\right\rangle$ and $\left 28P\right\rangle$ states $vs.$ Magnetic Field	37
$ 28P\rangle\otimes 28P\rangle$ pair-states at a field of 600 G	4.
$ 2^*\rangle\otimes 2^*\rangle$ pair-state at 600 G $vs.$ principal quantum number	42
$ 2^*\rangle\otimes 2^*\rangle$ pair-state of $ 28P\rangle$ vs. magnetic field	4
Full Rydberg-dressed potential	46
Probability distribution of distance between two neighboring atoms .	49
Frequency stabilization of laser system and characterization of optical	
cavity	55
Laser system for $^6\mathrm{Li}$ single-photon Rydberg excitation	59
"V-scheme" spectroscopy of ⁶ Li Rydberg states	6
Precision MOT loss spectroscopy for alignment	62
Rydberg spectroscopy by blowing cold atoms at resonance	64
Effect of lattice depth on the Rydberg transition	66
Magnetic dispersion of $ 31P\rangle$ Rydberg states	68
	Lifetime of 6 Li Rydberg atoms

3.14	Observed anomalous resonance observed during spectroscopy scans $$.	69
3.15	Rabi frequency and coherence measurements for the resonant $ 2S\rangle$ \rightarrow	
	$ 23P\rangle$ transition	71
3.16	Effect of geometry on Rydberg dressed lifetimes	73
3.17	Density-dependent lifetimes of Rydberg dressed systems	75
3.18	Dressed lifetime $vs. \Delta$	76
3.19	Dressed lifetime vs. B field	77
3.20	Ramsey frequency vs. Detuning	83
4.1	Realization of a 2D quantum Ising model with Rydberg atoms in an	
	optical lattice	88
4.2	Rydberg Coupling scheme	90
4.3	Investigation of single-atom coherence	91
4.4	Sudden quench dynamics	94
4.5	NLCE convergence	97
4.6	Time evolution of spin correlations after near-adiabatic quenches and	
	comparison with phenomenological decoherence models	99
4.7	Characterizing many-body states during and after a slow quench	101
4.8	Effective temperature characteristics of an Ising system calculated with	
	the Metropolis algorithm	102
4.9	Effect of shot-to-shot Rabi Frequency fluctuations	104
5.1	Experimental setup and measurements	112
5.2	Tilt potential laser system	114
5.3	Tilt potential calibration	116
5.4	Test of linear response	118
5.5	Phase slip	120
5.6	Time decay of density waves	120

5.7	Diffusive to subdiffusive crossover	122
5.8	Thermal diffusivity	126
5.9	Local inverse temperature	127
5.10	Simultaneous fitting of hydrodynamic model	130
6.1	Realization of a $t-V$ model with Rydberg dressing	136
6.2	Rydberg dressing of ⁶ Li	137
6.3	Measuring Rydberg dressed interactions with many-body Ramsey in-	
	terferometry	140
6.4	Lifetime of itinerant Rydberg dressed fermions	142
6.5	Dependence of lifetime on atom number at fixed density	144
6.6	Interaction dependence of quench dynamics of a charge density wave .	146
6.7	Density dependence of quench dynamics	147
6.8	Atom loss during charge density wave dynamics	148
6.9	Role of interchain couplings in slowing down charge density wave re-	
	laxation	150
C.1	Förster defects of ⁶ Li $ nP\rangle \otimes nP\rangle$ Rydberg states	167
C.2	⁶ Li $C_6(\pi/2)$ coefficients vs. magnetic and electric fields	170

Chapter 1

Introduction

Technologies we depend on in a daily basis, such as high-temperature superconductors (HTSC) used in MRI machines, work through complicated quantum many-body phenomena. Even though writing down the underlying equations for such systems is relatively simple, as one increases the number of particles the problems quickly become intractable for a classical computer. In the absence of a fully programmable quantum computer, the only way to study these systems is using a quantum simulator. These machines act essentially as "analog" quantum computers where only problems of a certain kind are accessible depending on the nature of the simulator. The challenge comes in devising the right technologies to use in order to engineer the desired quantum state to study.

Over the past few decades, ultracold atoms in optical lattices have become an important approach for the study of strongly-correlated condensed matter systems [1–3]. Their high tunability and long coherence times make them an ideal platform for the quantum simulation of these kinds of problems. Particularly, the relatively recent development of quantum gas microscopy has unlocked the ability to study equilibrium and dynamical properties of lattice models with unprecedented detection and control [4]. This development has granted the capability to precisely engineer

highly-entangled quantum many-body states of matter. The experiments described in this thesis are conducted in a quantum gas microscope for fermions, one of a few of such instruments around the world coming online in 2015. In our system, we load ground-state atoms into a two-dimensional square optical lattice. These particles are able to tunnel between lattice-sites and interact via contact-like van der Waals forces with a range of only a few nanometers, much shorter than the lattice spacing. The experiment natively realizes the Fermi-Hubbard model [5] which is widely believed to exhibit the same physics as HTSC [6]. Through the author's PhD, our group has studied various aspects of both the repulsive and attractive phase-diagrams of this model [7–11].

However, in order to study systems beyond the "plain vanilla" Fermi-Hubbard model we have engineered novel platforms within our existing system [12–14]. These new experimental platforms for quantum simulation are the basis for this thesis. We achieve it in two ways.

Rydberg atoms

The first, and the main focus throughout the thesis, is the addition of a ultraviolet laser system for coupling the 6 Li ground-state atoms to a Rydberg state [15]. This allows us to add a long-range interaction to the existing degenerate Fermi gas. Through direct excitation, we have been able to realize a many-body spin system [16] and studied its quench dynamics [12]. Furthermore, through off-resonant excitation we have been able to realize the technique of Rydberg dressing [17–19]. Essentially, we create a superposition state of mostly ground state atoms $|g\rangle$ with a small admixture of the Rydberg state $|r\rangle$ which interacts with other nearby "dressed" states through a soft-core interaction potential. This allowed us to for the first time realize an itinerant lattice model with strong non-local interactions [14].

Realizing strongly interacting degenerate quantum gases with long-range interactions has been a long-sought goal in the field of quantum simulation. Many new platforms are currently in development towards this goal including magnetic atoms [20–23] and polar molecules [24, 25] in optical lattices. Unlike these, other platforms with long-range interactions like ions [26, 27], Rydberg atoms [15, 16], polar molecules in optical tweezers [28, 29] and atoms in optical cavities [30] consist of localized particles. On the other hand, itinerant quantum systems exhibit an interesting interplay between interactions, kinetic energy, and quantum statistics.

The combination of motion and Rydberg dressing can lead to novel phenomena and shed new light on the many-body physics of spinless and spinful fermionic systems with power-law interactions. In 1D, Rydberg dressing leads to quantum liquids beyond the Tomonaga-Luttinger liquid paradigm [31]. In 2D, topological Mott insulators can be emulated by placing atoms in a Lieb lattice [32]. Compared to contact or on-site interactions, the long-range interactions between Rydberg-dressed atoms makes it easier to achieve the low filling factors required for quantum Hall states [33, 34]. The interplay between hole motion and antiferromagnetism—believed to be at the heart of HTSC—can be studied in Rydberg-dressed atomic lattices emulating the $t-J_z$ model [35]. In 3D, one can achieve exotic topological density waves [36], topological superfluids [37], and metallic quantum solid phases [38].

Tilted systems

The second way is the addition of a strong external linear potential or "tilt" generated with a large off-centered optical dipole trap. This system has allowed us to explore slow thermalization and heat diffusion in a strongly interacting system near infinite temperature [13]. Here, the interactions allow for a charge density wave to quickly equilibrate about infinite temperature generating a heat modulation across

the system. The onset of the ensuing heat diffusion leads to a subdiffusive relaxation of the correlated density profile.

The physics of generic clean, strongly tilted models can be understood through a framework of Hilbert-space fragmentation (HSF) [39, 40]. For this class of systems, the strong tilts generate an effective dipole moment conservation in the system, a kinetic constraint. Like many-body localization (MBL) [41, 42] and quantum many-body scars [43, 44], HSF is a mechanism whereby isolated quantum systems can fail to reach thermal equilibrium after a quantum quench [45]. However, HSF differs from MBL in that it can exhibit nonergodic dynamics without the need for disorder. Such systems with a "clean" constraint have been theorized to be good candidates to behave as "quantum memories" where highly-entangled many-body states can be preserved [40, 46]. Our experiment explores a special case of a tilted Hubbard system where Hilbert space fragmentation is not expected, but instead we observe slow thermalization dynamics described by modified hydrodynamic equations.

The new class of models that can be experimentally realized using Rydberg dressing unlocks the potential of studying the physics of HSF in an alternative setting [47, 48]. In the limit of very strong off-site interactions, these systems develop a kinetic constraint in the form of a conservation of "bonds" or "pairs" of atoms in different sites stifling the dynamics of the system.

Outline

This thesis will mainly focus on the physics of Rydberg atoms and the considerations needed to design and build a Rydberg dressing experiment. In the first part we will present the theory and experimental background for our experiments. Ch. 2 will first introduce a general theoretical background for Rydberg atoms and their properties. Next, Ch. 3 will present both the theoretical and experimental background for the successful implementation of Rydberg dressing for ⁶Li systems. This chapter will also

show a full characterization of the Rydberg dressing lifetime and properties. In the second part we will present each of the pertinent publications related in the context of this thesis. Ch. 4 presents initial experiments where direct excitation to a Rydberg state was used to realize a 2D transverse Ising model. The following Ch. 5 shows the results studying the heat transport and charge subdiffusion of strongly interacting tilted Fermi-Hubbard models. Finally, Ch. 6 will display experiments where Rydberg dressing allowed us to for the first time study the dynamics of itinerant systems with strong non-local interactions.

Chapter 2

Rydberg atoms for ultracold systems

2.1 Introduction

Rydberg atoms are those excited in a high principal quantum number n state. This means that the valence electron is in an orbital state very far away from the core which makes the atom highly polarizable [49]. At long distances, Rydberg atoms prepared in the same state interact via long-range¹ van der Waals (VdW) potentials of the form $V_{VdW} = -\frac{C_6}{R^6}$ where C_6 is a coefficient that can be numerically calculated using second order perturbation theory.

Rydberg atoms have greatly exaggerated properties [49]. For example, they have relatively long lifetimes in the order of tens of μ s and interaction strengths in the order of hundreds of MHz for typical inter-particle spacings ($\sim 1 \,\mu$ m). Particularly these two characteristics, make resonantly coupled Rydberg atoms an ideal candidate platform to simulate frozen systems with long-range interactions such as quantum Ising

¹This qualifier will be used liberally throughout the thesis. In AMO, "long-range" interactions have come to mean any sort of interaction that is not "contact-like" in nature. We are aware that this term has a more rigorous definition in other fields and apologize for any possible confusion.

models, as the interaction timescale is much larger than their lifetime. In fact, the use of Rydberg atoms has ballooned over the past half-decade in a variety of experimental platforms including optical tweezer arrays [43, 50–53], optical cavities [54–56], optical lattices [12, 57], and many more [15, 58]. In addition, off-resonant coupling to these Rydberg states can add a small admixture of these exaggerated properties to neutral ground-state atoms and allow for the simulation of itinerant systems as described in Ch. 3 and demonstrated in Ch. 6.

This chapter starts with a summary of the theory of Rydberg physics and the sort of interaction potentials that can be tailored with resonant and off-resonant optical coupling. There will be a specific emphasis on calculations for ⁶Li atoms, but the ideas are more general and should be easily translated to any other atom or molecule. As a disclaimer, there are other good references [59–62] that describe Rydberg atoms and their interactions in the context ultracold atoms. This chapter will present the topic as the author has come to understand it over the course of his PhD.

2.2 Scalings of Rydberg atom properties

In order to design an experiment that uses Rydberg atoms, it is important to understand how their properties scale with principal quantum number which can be understood from quantum defect theory [63, 64]. In this framework, the binding energy or the outer electron can be written down similarly to Hydrogen as:

$$E_{n_*} = -\frac{R^*}{n_*^2} = -\frac{1}{1 - \frac{m_e}{m_{core}}} \frac{R_{\infty}}{n_*^2}$$
 (2.1)

Where $R_{\infty}=3289.841\,960\,250\,8(64)\,\text{THz}$ [65] is the Rydberg constant, m_e is the electron mass, m_{core} the mass of the ionic core. For ⁶Li, $R^*=3289.541\,926(2)\,\text{THz}$ [64] will end up being a small correction of $\sim 0.01\%$ on the bare Rydberg constant R_{∞} due

Property	Variable	Scaling $\propto {n_*}^{\alpha}$
Binding Energy	E_{n_*}	-2
Energy difference from nearby states	$ E_{n_*} - E_{n_* \pm 1} $	-3
Coupling to ground-state	$ \mu_{2S,nP} $	-3/2
Coupling to nearby states	$ \mu_{(n\pm 1)S,nP} , \mu_{(n\pm 1)D,nP} $	2
Orbital Radius	$\langle \hat{m{r}} angle$	2
Rabi Frequency	Ω	-3/2
Radiative Lifetime	$ au_0$	3
Blackbody Decay Lifetime	$ au_{BB}$	2
Van der Waals coefficient	C_6	11

Table 2.1: Scaling of Rydberg atom properties. Scalings of useful Rydberg atom properties with principal quantum number to take into account when designing an experiment [49].

to the large core-to-electron mass ratio². Furthermore, $n_* = n - \delta_{nlj}$ is the effective principal quantum number with some "defects" that can only be spectroscopically measured (see [64] for Lithium). In general, these defects vanish for large angular momenta which in turn start following the original Hydrogen scaling ($\propto 1/n^2$).

A summary of important scalings of Rydberg atom properties with the corrected principal quantum number is shown in Table 2.1. One can derive the more useful ones from the scaling of the dipole matrix elements (Sec. 2.3) and the binding energy (Eqn. 2.1). For experiments with neutral atoms coupled through an optical transition, the Rabi frequency Ω at a fixed optical power goes as the coupling of the ground-state atoms with the Rydberg state which vanishes at a rate of $\propto n_*^{-3/2}$. Another very important property is the lifetime of the atoms which has two main components as explained in (Sec. 2.4). The radiative lifetime is dominated by the spontaneous decay to the ground-state (Fig. 2.2b-c) and as such goes as the inverse square of such coupling ($\propto n_*^3$) while the black-body lifetime has a more complicated relation as

²Since it is a small correction, for some of the coming explanations it will be assumed to be a negligible difference.

it is dominated by stimulated absorption/emission of a black-body photon and can be shown to increase quadratically ($\propto n_*^2$) [66]. Therefore the scaling of the full effective lifetime will depend on which component it is being dominated by as shown in Fig. 2.2a. Finally, the C_6 coefficient goes as the coupling to nearby states to the fourth power divided by the energy separation to those states resulting in a very strong scaling of $\propto n_*^{-11}$ (Eqn. 2.18). Careful consideration of the scalings of all these parameters and how they modify the tailored interaction potentials is necessary to design a successful experiment.

2.3 Transition Dipole Matrix Elements

Since the scalings of Rydberg properties depend mainly in the coupling of different states through a photon, it is useful to describe the matrix elements of the dipole operator $\hat{\boldsymbol{\mu}} = e\hat{\boldsymbol{r}}$ which are also referred to as the dipole matrix elements (DME). We can write the full dipole matrix element between two states in the $|n, l, j, m\rangle$ basis³ as:

$$\mu_{a,b} = \langle b | \, \hat{\boldsymbol{\mu}} \, | a \rangle = \langle n_b, l_b, j_b, m_b | \, \hat{\boldsymbol{\mu}} \, | n_a, l_a, j_a, m_a \rangle = \mathcal{R}_{n_b, l_b, j_b}^{n_a, l_a, j_a} \mathcal{A}_{l_b, j_b, m_b}^{l_a, j_a, m_a}$$
(2.2)

In this formula, $\mathcal{R}_{n_b,l_b,j_b}^{n_a,l_a,j_b}$ represents the radial component of the DME (Eq. 2.9) and $\mathcal{A}_{l_b,j_b,m_b}^{l_a,j_a,m_a}$ represents the angular component of the DME (Eq. 2.11). We are able to do this, because the full wavefunction is separable in two terms:

$$|n, l, j, m\rangle = |\Psi_{nljm}(\mathbf{r})\rangle = |\psi_{nlj}(r)\rangle \otimes |\chi_{ljm}(\theta, \phi)\rangle$$
 (2.3)

³Here we have chosen to work in the $|n, l, j, m\rangle$ fine structure basis which is most useful at zero field. However, the equations shown can be used for other basis as well, one would just need to keep track of the important angular momenta or use the Clebsch-Gordan coefficients (Table. 3.1).

Where all radial dependence goes in the first term and the second term only has angular components to it. In the following, we will explain how to numerically calculate each of the DME components and their implications.

2.3.1 Radial component of the dipole matrix element

In order to calculate the radial component of the DME, we need two main ingredients. First, we need to be able to write down the potential for said electron in a highly-excited Rydberg state, which we will be able to do using a model potential [67]. Second, we will need to write down Schödinger's equation in a way that can be numerically solved using Numerov's algorithm [68].

Alkali-metal Rydberg atom model potential

For Alkali-metal Rydberg atoms, it is possible to think of the valence electron potential as a perturbation of the typical Hydrogen -1/r potential. Essentially, the nucleus and inner bound electrons will constitute a polarizable core with total charge +e and the valence electron will orbit at some far away distance. This model potential has the form [67]:

$$V(r) = -\frac{Z_l}{r} - \frac{\alpha_c}{2r^4} \left(1 - e^{-(r/r_c)^6} \right)$$
where $Z_l = 1 + (Z - 1) e^{-a_1 r} - r e^{-a_2 r} (a_3 + a_4 r)$ (2.4)

Here, $\alpha_c = 0.1923$ is Lithium's core polarizability, Z is the atomic mass, and the parameters a_i, r_c are the ones described in Table. 2.2.

Numerically solving the Schrödinger equation

Using the model potential (Eq. 2.4), the binding energy (Eq. 2.1), and substituting in the separable wavefunction (Eq. 2.3) we can write down the Schödinger equation

Parameter	l = 0	l = 1	$l \ge 2$
a_1	2.47718079	3.45414648	2.51909839
a_2	1.84150932	2.55151080	2.43712450
a_3	-0.02169712	-0.21646561	0.32505524
a_4	-0.11988361	-0.06990078	0.10602430
r_c	0.61340824	0.61566441	2.34126273

Table 2.2: Lithium model potential parameters. Parameters for the model potential shown in Eq. 2.4. The parameters are taken from [67].

in atomic units⁴ as:

$$\left(-\frac{1}{2}\nabla^2 + V(r)\right)\Psi_{nljm}(\mathbf{r}) = E_{n_*}\Psi_{nljm}(\mathbf{r})$$
 (2.5)

$$\left(-\frac{1}{2}\left(\frac{\partial^2}{\partial r^2} + \frac{2}{r}\frac{\partial}{\partial r}\right) + \frac{l(l+1)}{2r^2} + V(r)\right)\psi_{nlj}(r) = -\frac{1}{2n_*^2}\psi_{nlj}(r) \tag{2.6}$$

Here, we have used the fact that $\chi_{lmj}(\theta,\phi)$ is a spherical harmonic providing an extra energy term proportional to the angular momentum l. The final step in this derivation is to substitute the radial wavefunction with a modified function $U_{nlj}(r) = r\psi_{nlj}(r)$. This transformation is useful for two reasons. For one, in spherical coordinates it is straightforward to normalize as $\int_0^\infty |\psi_{nlj}(r)|^2 r^2 dr = \int_0^\infty |U_{nlj}(r)|^2 dr = 1$. But also, it is easy to show that $\frac{\partial^2}{\partial r^2} U_{nlj}(r) = r \left(\frac{\partial^2}{\partial r^2} + \frac{2}{r} \frac{\partial}{\partial r} \right) \psi_{nlj}(r)$ which allows us to reduce the Schrödinger equation to:

$$\left(-\frac{1}{2}\frac{\partial^2}{\partial r^2} + \frac{l(l+1)}{2r^2} + V(r)\right)U_{nlj}(r) = -\frac{1}{2n_*^2}U_{nlj}(r)$$
 (2.7)

$$\left(\frac{\partial^2}{\partial r^2} - \frac{l(l+1)}{r^2} - 2\left(V(r) + \frac{1}{2n_*^2}\right)\right) U_{nlj}(r) = 0$$
(2.8)

⁴The model potential from [67] is written down in these units so it was used for convenience. It is important to note that in these units, the energy scale is the Hartree $E_H = 2R_{\infty}$ which has an important extra factor of 2 on the usual Rydberg constant.

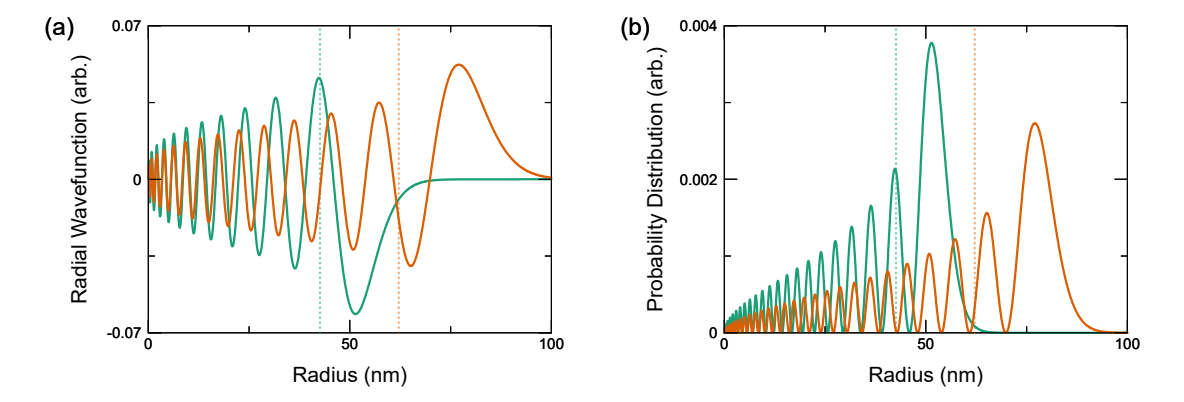


Figure 2.1: **Rydberg atom radial wavefunctions.** Radial Wavefunctions (a) and probability distributions (b) for the ⁶Li $23P_{1/2}$ (green) and $28P_{1/2}$ (orange) which are the states used for pertinent simulations in this thesis. These were calculated using a model potential [67] and Numerov's algorithm [68]. Dotted lines correspond to the average orbital radius of the distribution $\langle \hat{\boldsymbol{r}} \rangle = \langle \Psi_{n,l,j,m}(r) | \hat{\boldsymbol{r}} | \Psi_{n,l,j,m}(r) \rangle = \langle \psi_{n,l,j}(r) | \hat{r} | \psi_{n,l,j}(r) \rangle$.

Which is a second order differential equation that can be numerically solved using Numerov's algorithm [68] as explained in App. A. Fig. 2.1 shows the numerically solved modified radial wavefunctions $U_{nlj}(r)$ for ⁶Li Rydberg states $23P_{1/2}$ and $28P_{1/2}$ ⁵ which are important for experiments pertinent to this thesis.

Radial DME

Finally the radial component of the dipole matrix element can be calculated by numerically integrating the coupling between two wavefunctions by the orbital radius operator:

$$\mathcal{R}_{n_b,l_b,j_b}^{n_a,l_a,j_a} = \langle \psi_{n_b l_b j_b}(r) | \hat{r} | \psi_{n_a l_a j_a}(r) \rangle = \int_0^\infty \psi_{n_b l_b j_b}^*(r) r \psi_{n_a l_a j_a}(r) r^2 dr$$
$$= \int_0^\infty U_{n_b l_b j_b}^*(r) r U_{n_a l_a j_a}(r) dr \qquad (2.9)$$

In the case of a = b this is exactly the expectation of the orbital radius $\langle \hat{r} \rangle$.

⁵The effect of j on these is very small as it only slightly modifies the quantum defect δ_{nlj} [64].

2.3.2 Angular component of the dipole matrix element

In order to calculate $\mathcal{A}_{l_b,j_b,m_b}^{l_a,j_a,m_a}$, it will be useful to rewrite the dipole moment operator in terms of the possible polarization vectors of the coupling photon:

$$\hat{\boldsymbol{\mu}} = e\hat{\boldsymbol{r}} = e\hat{\boldsymbol{r}} \left(Y_1^{-1}(\hat{\theta}, \hat{\phi}) e^{-1} + Y_1^0(\hat{\theta}, \hat{\phi}) e^{0} + Y_1^{+1}(\hat{\theta}, \hat{\phi}) e^{+1} \right)$$
(2.10)

Where Y_l^{-m} are the spherical harmonics and $\{e^{-1}, e^0, e^{+1}\}$ correspond to $\{\sigma^-, \pi, \sigma^+\}$ transitions respectively. This essentially shows the effect that a photon can have on the momentum of a quantum state dependent on its polarization. Here, the component of \hat{r} will only affect the radial component $\psi_{nlj}(r)$ of the wavefunction as explained in the previous subsection. Calculating the full angular component of the DME will follow from the recursive application of the Wigner-Eckhart theorem [69] and using the identity $\int Y_{l_1}^{m_1} Y_{l_2}^{m_2} Y_{l_3}^{m_3} d\Omega = \sqrt{\frac{(2l_1+1)(2l_2+1)(2l_3+1)}{4\pi}} \begin{pmatrix} l_1 & l_2 & l_3 \\ 0 & 0 & 0 \end{pmatrix} \begin{pmatrix} l_1 & l_2 & l_3 \\ m_1 & m_2 & m_3 \end{pmatrix}$. A full derivation of this can be found in [70]. The final form of this angular component can be shown to reduce to:

$$\mathcal{A}_{l_{b},j_{b},m_{b}}^{l_{a},j_{a},m_{a}} = (-1)^{j_{b}+j_{a}+s+1-m_{b}} \sqrt{(2l_{a}+1)(2l_{b}+1)(2j_{a}+1)(2j_{a}+1)} \times \begin{cases} l_{b} & 1 & l_{a} \\ j_{a} & s & j_{b} \end{cases} \sum_{q} \begin{pmatrix} j_{b} & 1 & j_{a} \\ -m_{b} & q & m_{a} \end{pmatrix}$$
(2.11)

Here, the matrix between parenthesis () is a Wigner-3j symbol and the matrix between $\{\}$ is the Wigner-6j symbol. The number $q = \{-1, 0, 1\}$ corresponds to the type of transition $\{\sigma^-, \pi, \sigma^+\}$ respectively. Only one of the terms in the Wigner 3j symbol sum will be nonzero corresponding to the correct change of m in the transition allowed by the selection rules as shown in Table. 2.6.

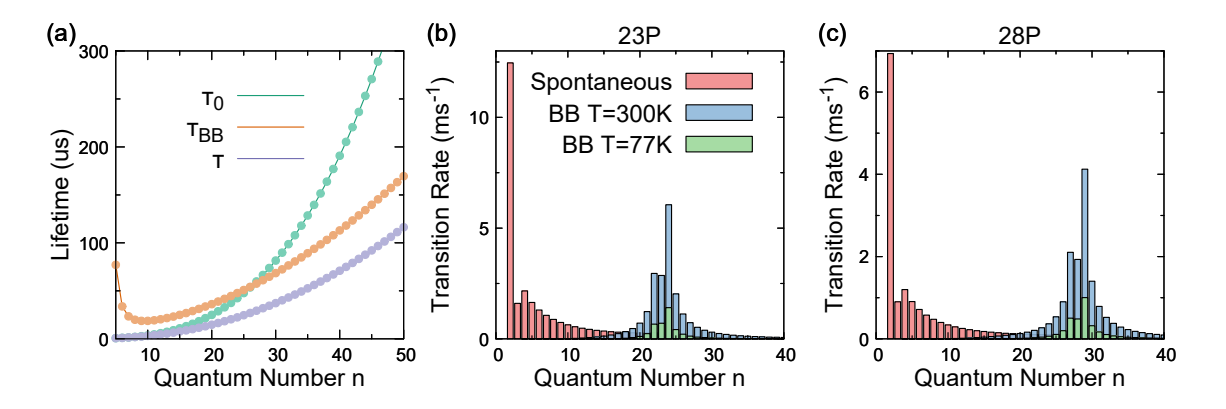


Figure 2.2: **Lifetime of** ⁶**Li Rydberg atoms.** (a) Spontaneous (τ_0 green) and black-body (τ_{BB} orange) components of the full Rydberg atom lifetime (τ purple) as a function of principal quantum number n. (b-c) Transition rate of decay channels binned by principal quantum number n and divided in spontaneous decay (red) and black-body stimulated transitions (blue for $T=300\,\mathrm{K}$ and green for $T=77\,\mathrm{K}$. (b) Rydberg state used in Ch. 4. (c) Rydberg state used in Ch. 6. Data was calculated using the ARC python package [76].

2.4 Lifetime of Rydberg atoms

Probably only second to the long-range interaction, the lifetime of Rydberg atoms is their most important property. Certainly it is the one that caused most headaches for our experiments and which we spent most of our time characterizing and understanding (Sec. 3.7). The lifetime of Rydberg atoms has two main components: spontaneous emission down to the ground-state and black-body stimulated decay to nearby Rydberg states. The second one of these is most problematic and has limited many experimental realizations of Rydberg platforms [71–75] through non-trivial decay mechanisms. Fig. 2.2 shows the couplings of pertinent Rydberg states for this thesis divided by both components of the lifetime. It also shows the potentially strong effect that temperature can have on the problematic decay channels.

It is possible to calculate independently both components of the lifetime making use of dipole matrix elements. In the case of spontaneous emission it is well

Parameter	l = 0	l=1	$l \ge 2$
$ au_s$	0.8431	2.8807	0.4781
δ	2.9936	2.9861	2.9963
A	0.051	0.040	0.058
В	0.097	0.078	0.148
C	1.991	1.712	1.934
D	3.852	3.610	3.783

Table 2.3: Lithium Rydberg lifetime parameters. Parameters for the Rydberg lifetime shown in Eq. 2.13. The parameters and equation are taken from [66].

approximated by Fermi's golden rule:

$$\frac{1}{\tau_0} \approx \Gamma_{nP \to 2S} = \frac{8\pi^2 e^2}{3\epsilon_0 \hbar \lambda_0^3} |\mu_{nP,2S}|^2$$
 (2.12)

From this expression, it should be obvious that the scaling of the radiative lifetime will be cubic ($\tau_0 \propto n_*^3$) since we know that the dipole matrix element to the ground-state scales as $\mu_{nP,2S} \propto n_*^{-3/2}$ (Table. 2.1).

For the case of the black-body induced decay, it is also possible to write down a similar equation were we take into account the distribution of radiation $B(\lambda, T)$ according to Planck's law. However, there exist parametric approximations for the full lifetime of Alkali-metal Rydberg atoms [66]. The form of this equation is:

$$\tau = \left(\frac{1}{\tau_s n_*^{\delta}} + \frac{A}{n_*^{D}} \frac{21.4}{\exp\left(315780 \frac{B}{n_*^{CT}}\right) - 1}\right)^{-1}$$
(2.13)

Here $\{\tau_s, \delta, A, B, C, D\}$ are the parameters described in Table. 2.3, T is in units of [K] and τ in units of [ns]. The first term corresponds to the spontaneous emission and has roughly the expected scaling. The second term is more complicated but in the large n limit can be shown to roughly have a $\propto n^{*2}$ scaling.

The full scaling of τ with principal quantum number is a bit complicated as for low n it is dominated by spontaneous emission τ_0 but at higher n (and room temperature) it is dominated by the black-body enabled decay channels (τ_{BB}). We chose to work with relatively low n in order to not be dominated by τ_{BB} and avoid non-trivial many-body decay mechanisms. In fact, the states we ended up working with (23P and 28P) are right around where both components of the lifetime are roughly equal at room temperature (Fig. 2.2a).

In our experiment, directly measuring τ is not quite feasible because the Rydberg states have opposite polarizabilities to the ground-state. This means that the position where the ground-state atoms are trapped in our optical lattice, the Rydberg atoms are anti-trapped leading to strong heating. This was not a big issue for the experiments explored in Ch. 4 as the timescales of the interaction timescales were much faster. We can however indirectly measure τ using the Rydberg dressing scheme which will be explored in Sec. 3.7. In general, we assumed the values from Eq. 2.13 for which we later found relatively good agreement experimentally.

2.5 Interactions between electric dipoles

As stated in the introduction, the large electron orbit radius of Rydberg atoms generates an effective dipole moment (μ) . When you get two Rydberg atoms close to each other, they can interact via the exchange of virtual photons. If the quantum states of the two neighboring atoms (e.g. $|a\rangle$ and $|b\rangle$) have different quantum numbers such that they can exchange a single-photon $(\langle a|\hat{\mu}|b\rangle \neq 0)$, then they can interact via what are called dipole-dipole interactions $(V_{d-d} = C_3/R^3)$ [77]. However, if the states cannot exchange a single photon $(\langle a|\hat{\mu}|b\rangle = 0)$, such as states with the same angular momentum l, then they can only interact via a second-order process in what

are called van der Waals forces $(V_{VdW} = C_6/R^6)$ [53]. Fig. 2.3a shows a Feynman diagram of this two-photon interaction.

We will focus on the van der Waals interaction as it is most pertinent to the experiments performed as part of this thesis. However it is also possible to take advantage of the dipole-dipole interactions by using microwaves to excite multiple Rydberg states at a time [78–81].

2.5.1 Calculating C_6 coefficients with angular dependence

A numerical calculation of the interaction potential is possible using second order perturbation theory. Multiple theses already contain rigorous calculations [59, 60, 62]. In this subsection, we will present a method to easily calculate C_6 coefficients with full angular dependence.

The van der Waals interaction potential between two atoms $|a\rangle$ and $|b\rangle$ can be calculated through the formula:

$$\frac{C_6}{R^6} = \sum_{\alpha, \beta \neq a, b} \frac{\left| \langle \alpha \beta | \hat{V}(\mathbf{R}) | ab \rangle \right|^2}{\delta_{\alpha \beta}}$$
 (2.14)

Here, $\hat{V}(\mathbf{R})$ represents the two-particle Hamiltonian coupling from pair-state $|a\rangle \otimes |b\rangle$ to $|\alpha\rangle \otimes |\beta\rangle$ (Fig. 2.3a). $\delta_{\alpha\beta} = E_{\alpha} + E_{\beta} - E_{a} - E_{b}$ is the energy difference between the intermediate pair-states and the interacting pair-state⁶.

Classically, if we have two atoms with parallel dipole moments (aligned to a magnetic field for example) μ_a and μ_b a distance R apart at an angle θ (Fig. 2.3b), The potential $V(\mathbf{R})$ can be written as:

$$V(\mathbf{R}) = \frac{\mu_a \cdot \mu_b}{R^3} - \frac{3(\mu_a \cdot \mathbf{R})(\mu_b \cdot \mathbf{R})}{R^5}$$
(2.15)

 $^{^6}$ This is also sometimes referred to as the Förster defect as explained in App. $^{\rm C}$.

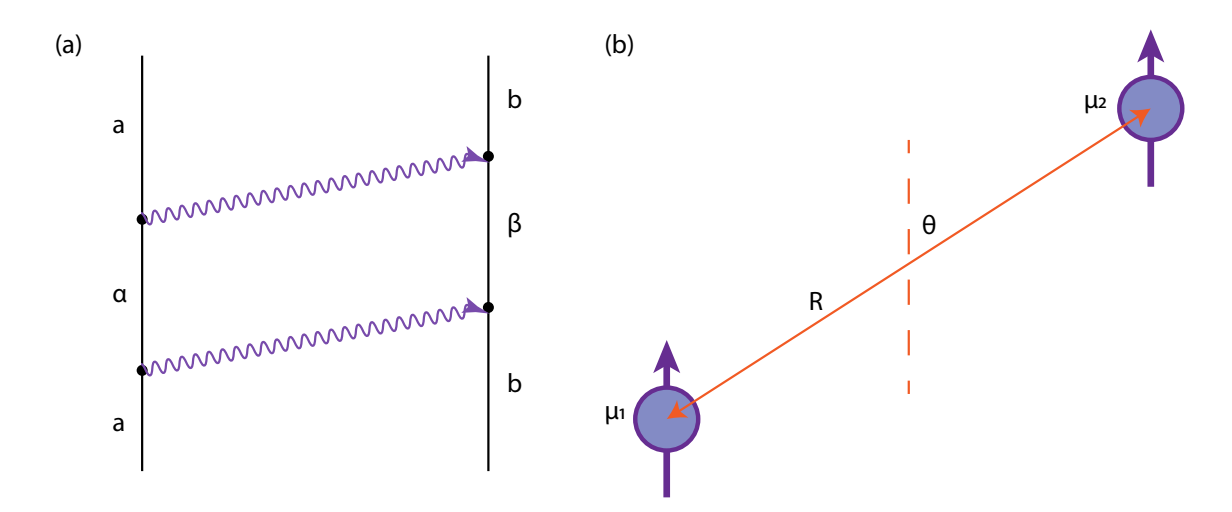


Figure 2.3: Van der Waals interactions between Rydberg atoms (a) Feynman diagram of the VdW second order process. (b) Schematic of two Rydberg atoms with parallel dipole moments.

We can further reduce this expression using the full angular form of the dipole moment (Eq. 2.10) and removing the spherical coordinate ϕ due to the symmetry of having the dipoles be parallel⁷ (Fig. 2.3b). Here we will use the notation $\{\hat{\mu}_{i+}, \hat{\mu}_{i0}, \hat{\mu}_{i-}\}$ for $\{\sigma^-, \pi, \sigma^+\}$ transitions of the atom i which define the change Δm by the photon polarization. The following expressions represents the full dipole matrix element with angular dependence between a pair parallel dipoles:

$$\hat{V}(R,\theta) = \frac{1}{R^3} [(\hat{\mu}_{a-}\hat{\mu}_{b+} + \hat{\mu}_{a+}\hat{\mu}_{b-} + (1 - 3\cos^2\theta)\hat{\mu}_{a0}\hat{\mu}_{b0})
- \frac{3}{\sqrt{2}}\sin\theta\cos\theta(\hat{\mu}_{a0}\hat{\mu}_{b+} + \hat{\mu}_{a0}\hat{\mu}_{b-} + \hat{\mu}_{a+}\hat{\mu}_{b0} + \hat{\mu}_{a-}\hat{\mu}_{b0})
- \frac{3}{2}\sin^2\theta(\hat{\mu}_{a+}\hat{\mu}_{b+} + \hat{\mu}_{a+}\hat{\mu}_{b-} + \hat{\mu}_{a-}\hat{\mu}_{b+} + \hat{\mu}_{a-}\hat{\mu}_{b-})]$$

$$\hat{V}(R,\theta) = \frac{1}{R^3} [-(1 - 3\cos^2\theta)(\frac{1}{2}\hat{\mu}_{a-}\hat{\mu}_{b+} + \frac{1}{2}\hat{\mu}_{a+}\hat{\mu}_{b-} - \hat{\mu}_{a0}\hat{\mu}_{b0})
- \frac{3}{\sqrt{2}}\sin\theta\cos\theta(\hat{\mu}_{a0}\hat{\mu}_{b+} + \hat{\mu}_{a0}\hat{\mu}_{b-} + \hat{\mu}_{a+}\hat{\mu}_{b0} + \hat{\mu}_{a-}\hat{\mu}_{b0})
- \frac{3}{2}\sin^2\theta(\hat{\mu}_{a+}\hat{\mu}_{b+} + \hat{\mu}_{a-}\hat{\mu}_{b-})]$$
(2.17)

⁷By an external magnetic field for example.

Since the Van der Waals interaction is a virtual two-photon process where the atoms return to their initial states, the possible full transitions defining the C_6 coefficient have only three kinds of terms with explicit angular dependence:

- 1. c_1 with dependence $(1 3\cos^2\theta)^2$ for $|\Delta m_a + \Delta m_b| = 0$ transitions⁸. This term corresponds to transitions where the net angular momentum is conserved. This means that only for transitions where one atom increases while the other decreases in its m value or when both maintain the same m. Note that for the transitions with a change in m there is an extra factor of $\frac{1}{4}$.
- 2. c_2 with dependence $-\frac{9}{2}\sin^2\theta\cos^2\theta$ for $|\Delta m_a + \Delta m_b| = 1$ transitions. This term corresponds to only one atom changing m value while the other one remains invariant. The minus sign comes from the asymmetry of this transition due to the opposite polarizations needed to return only one atom back to its original state.
- 3. c_3 with dependence $\frac{9}{4}\sin^4\theta$ for $|\Delta m_a + \Delta m_b| = 2$ transitions. This term corresponds to both atoms increasing or decreasing its m value by 1.

With all these formulas, we can now calculate the C_6 coefficient between two states $|a\rangle$ and $|b\rangle$ by adding all the terms corresponding to all possible intermediate states $|\alpha\rangle$ and $|\beta\rangle$ to c_1 , c_2 , or c_3 depending on which category they fit in. The terms are calculated in terms of the dipole matrix elements and the state energies through the formula:

$$c = \sum_{\alpha,\beta \neq a,b} \frac{\left| \left\langle \alpha \right| \hat{\mu} \left| a \right\rangle \right|^2 \left| \left\langle \beta \right| \hat{\mu} \left| b \right\rangle \right|^2}{E_{\alpha} + E_{\beta} - E_a - E_b}$$
(2.18)

Even though forbidden transitions will already have an angular component of the DME equal to 0 due to the Wigner 3j and 6j functions (Sec. 2.3.2), it is very

 $^{^8\}Delta m_a = m_a - m_\alpha$ and $\Delta m_b = m_b - m_\beta$

important to take into account the selection rules (Table. 2.6) when summing over all possible intermediate states α and β . This will greatly reduce calculation time. It is also important to mention that it only makes sense to calculate C_6 coefficientes between two atoms with states that cannot be directly coupled ($\langle b | \hat{\mu} | a \rangle = 0$) in order to satisfy the perturbation theory expansion. Otherwise, there would be a resonant channel where the atoms exchange quantum states (dipole-dipole interactions).

2.5.2 C_6 values for nP pair-states of Lithium

A calculation for the C_6 coefficients of all possible nP pair-states was carried for values of $n = \{20, 100\}$. Only the values for positive m values was calculated as it was found that it was invariant under a sign change of m but not in its absolute value. We calculated all the c_1 , c_2 , c_3 values (App. B) so we can extract the C_6 coefficient with angular dependence as:

$$C_6(\theta) = c_1 \cdot (1 - 3\cos^2\theta)^2 + c_2 \cdot \frac{9}{2}\sin^2\theta\cos^2\theta + c_3 \cdot \frac{9}{4}\sin^4\theta$$
 (2.19)

Fig. 2.4 shows the calculated value of C_6/n_*^{11} at zero magnetic field. As expected, the values are mostly constant when taking into account the $C_6 \propto n_*^{11}$ scaling. We can also note the Förster resonance around n = 32, 33 which will be further explored in Sec. 3.2.2. All interactions for P states of ⁶Li are attractive.

2.6 Two 2-level Rydberg atom model

The interaction potentials of Rydberg atoms coupled in a light-field are usually simplified to be only two-particle in nature. Higher order corrections of the potentials are possible to calculate as shown in Ref. [60]. As long as these higher order processes are not resonant, they are mostly negligible, allowing us to treat the interaction potential as purely two-particle in nature.

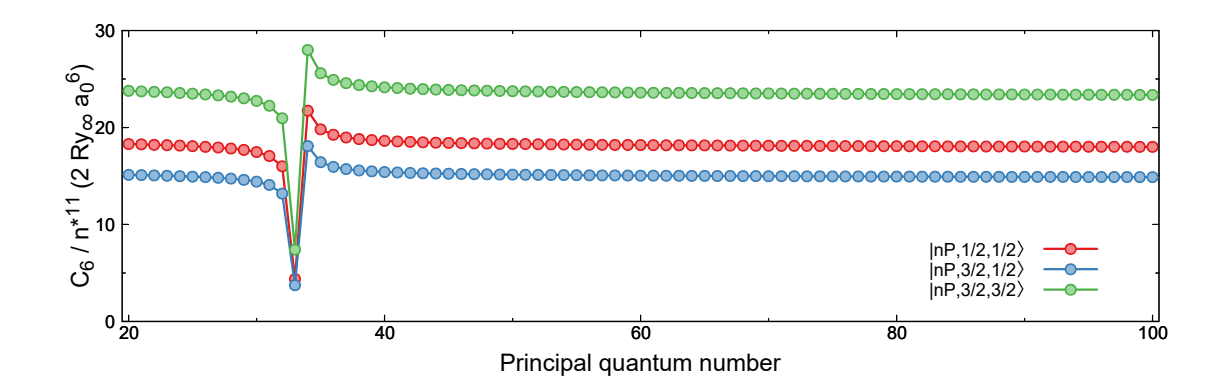


Figure 2.4: Calculated C_6 coefficients for the P states of ${}^6\text{Li}$ Van der Waals interaction coefficients between $|nP, 1/2, 1/2\rangle$ (red), $|nP, 3/2, 1/2\rangle$ (blue), and $|nP, 3/2, 3/2\rangle$ (green) Rydberg states. A Förster resonance can be appreciated around n = 32, 33. The C_6 coefficient is in atomic units $[2R_{\infty}a_0^6]$.

In this limit, we can first write down a toy model of two 2-level atoms a distance R apart as shown in Fig. 2.5a. In the Born-Oppenheimer approximation we can write down the individual Hamiltonians for each particle in the $\{|g\rangle \text{ (ground)}, |r\rangle \text{ (Rydberg)}\}$ basis as:

$$\hat{H}_{1} = \hat{H}_{2} = \hat{H}_{single} = \frac{\Omega}{2} (|r\rangle \langle g| + |g\rangle \langle r|) - \Delta |r\rangle \langle r| = \begin{pmatrix} 0 & \Omega/2 \\ \Omega/2 & -\Delta \end{pmatrix}$$
(2.20)

Where Ω is the Rabi coupling of the light field and Δ is its detuning from resonance.

With this single-particle Hamiltonian in mind, we can write down the full two-particle Hamiltonian (Fig. 2.5b) as:

$$\hat{H}(R) = \hat{H}_{single} \otimes \hat{\mathbb{I}} + \hat{\mathbb{I}} \otimes \hat{H}_{single} + V(R)(|r\rangle \langle r| \otimes |r\rangle \langle r|)$$
(2.21)

$$\hat{H}(R) = \begin{pmatrix} 0 & \Omega/2 & \Omega/2 & 0 \\ \Omega/2 & -\Delta & 0 & \Omega/2 \\ \Omega/2 & 0 & -\Delta & \Omega/2 \\ 0 & \Omega/2 & \Omega/2 & -2\Delta + V(R) \end{pmatrix}$$
(2.22)

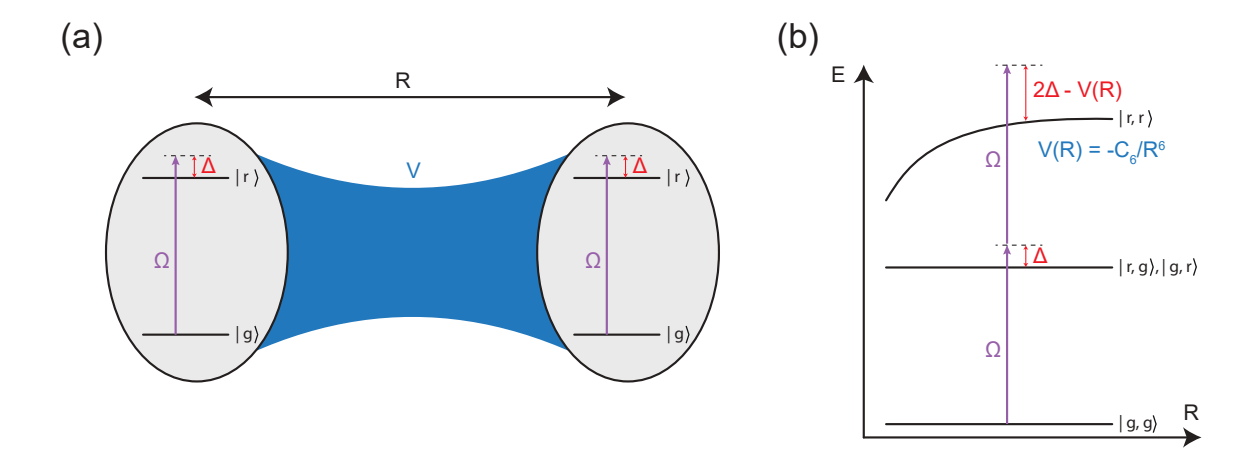


Figure 2.5: **Two 2-level Rydberg atom model.** (a) Two 2-level Rydberg atoms coupled in the same light-field with strength Ω and detuning Δ interact with each other at a distance. (b) Two-particle energy level scheme for the diagram in (a) showing the full Hamiltonian within the Born-Oppenheimer approximation.

Where $V(R) = -\frac{C_6}{R^6}$ is the van der Waals potential between two nearby Rydberg atoms.

2.7 Resonant coupling

In the case of resonant coupling, experimentally we can realize a transverse Ising model (Ch. 4). In order to obtain Eq. 4.1 one simply needs to take into account Eqs. 2.20 and 2.21 with the identities for the Pauli matrices:

$$\hat{\sigma}_x = |r\rangle \langle g| + |g\rangle \langle r|$$
 and $\hat{\sigma}_z = \hat{\mathbb{I}} - |r\rangle \langle r|$ (2.23)

This will realize a transverse Ising Hamiltonian where the Rabi coupling Ω is a transverse field $\hat{\sigma}_x$, the detuning Δ will be a parallel field $\hat{\sigma}_z$ field, and the interaction potential will be a $\hat{\sigma}_z\hat{\sigma}_z$ term coupling the spins. In Ch. 4 we describe an experiment where we study the quench dynamics of this Hamiltonian and attempt to prepare an antiferromagnetic phase quenching through a quantum phase transition at different rates.

2.7.1 Rydberg Blockade Radius

The only final consideration for resonant coupling is the effect of the so-called Rydberg Blockade [82–86]. Essentially, the van der Waals interactions between Rydberg atoms can be quite strong compared to the Rabi coupling of the ground-state to the Rydberg state. If one atom is in a Rydberg state, the excitation of neighboring atom to a Rydberg state is strongly suppressed within a blockade radius $R_b = \left| \frac{C_6}{\Omega} \right|^{1/6}$. Thus, it is important to choose the right R_b Rydberg state such that the relationship between the inter-particle spacing (lattice spacing R_b in our case) and R_b is suitable for the intended quantum simulation.

2.8 Off-resonant coupling: Rydberg dressing

The idea of off-resonantly coupling neutral ground-state atoms to a Rydberg state was first proposed a decade ago [17, 18]. This technique is referred to as Rydberg dressing. The general idea is that by off-resonantly coupling the ground-state atoms via a laser with Rabi frequency Ω and detuning Δ from resonance you can add a small admixture $\beta = \frac{\Omega}{2\Delta} \ll 1$ of the Rydberg state. This has the effect of adding the interesting properties of Rydberg atoms to ground-state atoms. In this section we will explain the basics of this technique and how to derive it.

2.8.1 "Dressed" ground-state

In order to understand the idea of a "dressed" ground-state and its properties we need only take into account first order perturbation theory of the single-particle Hamiltonian \hat{H}_{single}^{10} shown in Eq. 2.20 for the limit $\Omega \ll \Delta$. In this formalism we can write

⁹This comes from equating the van der Waals potential to the Rabi coupling in the $\Omega \gg \Delta$ limit. For atoms a distance less than R_b away, the $|rr\rangle$ state is so far detuned due to interactions that a second atom cannot be also excited to the Rydberg state.

¹⁰We can divide this Hamiltonian in perturbed and unperturbed components due to the Rabi coupling: $\hat{H}_{single} = \hat{H}_{\Delta} + \hat{H}_{\Omega}$.

down the dressed ground-states as:

$$|\tilde{g}\rangle \approx |g\rangle + \frac{\langle r|\hat{H}_{\Omega}|g\rangle}{E_g - E_r}|r\rangle = |g\rangle + \frac{\Omega/2}{\Delta}|r\rangle = |g\rangle + \beta|r\rangle$$
 (2.24)

Here, \hat{H}_{Ω} accounts for the perturbation component of the full Hamiltonian and E_i are the energies of the unperturbed component corresponding to the diagonal terms. This dressed ground-state will inherit the properties of the Rydberg atoms.

In particular the lifetime of the dressed atoms will now be $\tau_{dr} = \beta^{-2}\tau$ due to the probability of the dressed atom to be in the Rydberg state $|r\rangle$. This enhancement over the bare Rydberg lifetime can be quite sizable depending on the chosen dressing parameters Ω and Δ extending the lifetime from the order of tens of μ s to the order of ms which is of the order of typical kinetic timescales in ultracold atom experiments.

2.8.2 "Dressed" interaction potential

The dressed atoms will also inherit a long-range interaction potential in the form of a distance-dependent light shift due to the light-field. This is somewhat similar to the Rydberg-Blockade effect discussed in Sec. 2.7.1. In order to understand its properties, we will need to apply again perturbation theory but to the two-particle Hamiltonian of Eq. 2.22. First, it is easy to show that up to second-order perturbation in the $R \to \infty$ limit, the two-particle ground-state is the same as expected from the single-particle dressed ground-state:

$$|\tilde{g}\tilde{g}\rangle = |\tilde{g}\rangle \otimes |\tilde{g}\rangle = \frac{1}{1+\beta^2}(|g\rangle + \beta |r\rangle) \otimes (|g\rangle + \beta |r\rangle)$$
 (2.25)

$$|\tilde{g}\tilde{g}\rangle = (1 - \beta^2)|gg\rangle + \beta(|rg\rangle + |gr\rangle) + \beta^2|rr\rangle + O[\beta^3]$$
(2.26)

Where the term $(1+\beta^2)^{-1}$ comes from normalizing Eq. 2.24. The interaction potential will arrive from finding the distance dependent eigenenergy of the two-particle dressed

ground-states $E_{\tilde{g}\tilde{g}}(R)$. To find this we need to add corrections up to fourth order in perturbation of the \hat{H}_{Ω} component. It is easy to show from geometric reasons that the first and third order corrections will vanish as there is no path connecting back to the ground-state (Fig. 2.6a). Therefore, to figure out the second-order correction we have to realize that there are only two possible paths back to $|gg\rangle$ going back-and-forth to $|gr\rangle$ or $|rg\rangle$:

$$E_{gg}^{(2)} = \frac{\left| \langle gg | \hat{H}_{\Omega} | gr \rangle \right|^{2}}{E_{qg}^{(0)} - E_{qr}^{(0)}} + \frac{\left| \langle gg | \hat{H}_{\Omega} | rg \rangle \right|^{2}}{E_{qg}^{(0)} - E_{rg}^{(0)}} = 2 \frac{(\Omega/2)^{2}}{\Delta} = \frac{\Omega^{2}}{2\Delta}$$
 (2.27)

Here $E_i^{(0)}$ correspond to the diagonal terms of Eq. 2.22. In the case of the fourth-order correction to the energy, we will need to take into account 8 distinct paths as shown in Fig. 2.6a:

$$\begin{split} E_{gg}^{(4)} &= -\frac{\left| \langle gg | \, \hat{H}_{\Omega} \, | gr \rangle \right|^{4}}{\left(E_{gg}^{(0)} - E_{gr}^{(0)} \right)^{3}} - \frac{\left| \langle gg | \, \hat{H}_{\Omega} \, | rg \rangle \right|^{4}}{\left(E_{gg}^{(0)} - E_{rg}^{(0)} \right)^{3}} \\ &- \frac{\left| \langle gg | \, \hat{H}_{\Omega} \, | gr \rangle \right|^{2} \left| \langle gg | \, \hat{H}_{\Omega} \, | rg \rangle \right|^{2}}{\left(E_{gg}^{(0)} - E_{gr}^{(0)} \right)^{2} \left(E_{gg}^{(0)} - E_{rg}^{(0)} \right)} - \frac{\left| \langle gg | \, \hat{H}_{\Omega} \, | rg \rangle \right|^{2} \left| \langle gg | \, \hat{H}_{\Omega} \, | gr \rangle \right|^{2}}{\left(E_{gg}^{(0)} - E_{gr}^{(0)} \right)^{2} \left(E_{gg}^{(0)} - E_{rg}^{(0)} \right)} + \frac{\left| \langle gg | \, \hat{H}_{\Omega} \, | rg \rangle \, \langle rg | \, \hat{H}_{\Omega} \, | rr \rangle \right|^{2}}{\left(E_{gg}^{(0)} - E_{gr}^{(0)} \right)^{2} \left(E_{gg}^{(0)} - E_{rr}^{(0)} \right)} + \frac{\left| \langle gg | \, \hat{H}_{\Omega} \, | rg \rangle \, \langle rg | \, \hat{H}_{\Omega} \, | rr \rangle \right|^{2}}{\left(E_{gg}^{(0)} - E_{rg}^{(0)} \right)^{2} \left(E_{gg}^{(0)} - E_{rr}^{(0)} \right)} \\ &+ \frac{\langle gg | \, \hat{H}_{\Omega} \, | gr \rangle \, \langle gr | \, \hat{H}_{\Omega} \, | rr \rangle \, \langle rr | \, \hat{H}_{\Omega} \, | rg \rangle \, \langle rg | \, \hat{H}_{\Omega} \, | gg \rangle}{\left(E_{gg}^{(0)} - E_{gr}^{(0)} \right) \left(E_{gg}^{(0)} - E_{rg}^{(0)} \right)} \\ &+ \frac{\langle gg | \, \hat{H}_{\Omega} \, | rg \rangle \, \langle rg | \, \hat{H}_{\Omega} \, | rr \rangle \, \langle rr | \, \hat{H}_{\Omega} \, | gr \rangle \, \langle gr | \, \hat{H}_{\Omega} \, | gg \rangle}{\left(E_{gg}^{(0)} - E_{rg}^{(0)} \right) \left(E_{gg}^{(0)} - E_{rr}^{(0)} \right) \left(E_{gg}^{(0)} - E_{gr}^{(0)} \right)} \end{aligned} \tag{2.28}$$

Adding Eqs. 2.27 and 2.29 we can get the full eigenenergy of the dressed ground-state as:

$$E_{\tilde{g}\tilde{g}}(R) = E_{gg}^{(2)} + E_{gg}^{(4)} + O[\Omega^{6}] = \frac{\Omega^{2}}{2\Delta} \left(1 + \frac{\Omega^{2}}{2\Delta} \left(\frac{1}{2\Delta - V(R)} - \frac{1}{\Delta} \right) \right)$$
(2.30)

From this equation, it is easy to show that in the $R \to \infty$ $(V(\infty) \to 0)$ limit we get $E_{\tilde{g}\tilde{g}}(\infty) = 2\delta_{AC}(\Delta, \Omega)$. Where δ_{AC} is the single-particle light-shift:

$$\delta_{AC}(\Delta, \Omega) = -\frac{\Delta}{2} + \frac{1}{2}\sqrt{\Omega^2 + \Delta^2} = \frac{\Omega^2}{4\Delta} \left(1 - \frac{\Omega^2}{4\Delta}\right) + O[\Omega^6]$$
 (2.31)

Finally, with all of these calculations in mind we can solve for the Rydberg dressed interaction potential:

$$U_{dr}(R) = E_{\tilde{g}\tilde{g}}(R) - 2\delta_{AC} = \frac{\Omega^4}{8\Delta^3} \left(\frac{1}{\frac{2\Delta}{V(R)} - 1} \right) = \frac{\Omega^4}{8\Delta^3} \left(\frac{1}{-\frac{2\Delta R^6}{C_6} - 1} \right)$$

$$U_{dr}(R) = -\frac{U_0}{1 + (R/R_c)^6}$$
(2.32)

Here we have made some assumptions that are particular to Lithium. As explained in Sec. 2.5.2, for Lithium-6 P states all van der Waals potentials are attractive which is why we define $V(R) = -\frac{C_6}{R^6}$ to keep $C_6 > 0$. In general, this derivation would not work if the detuning Δ is such that the $|rr\rangle$ potential becomes resonant at any distance as the Born-Oppenheimer approximation would break down (Fig. 2.5b). For the simple Rydberg dressing scheme described here, one can only produce an interaction potential of the same sign as the van der Waals potential. So if the chosen Rydberg state is attractively interacting so will be the dressed ground-state atoms and vice-versa.

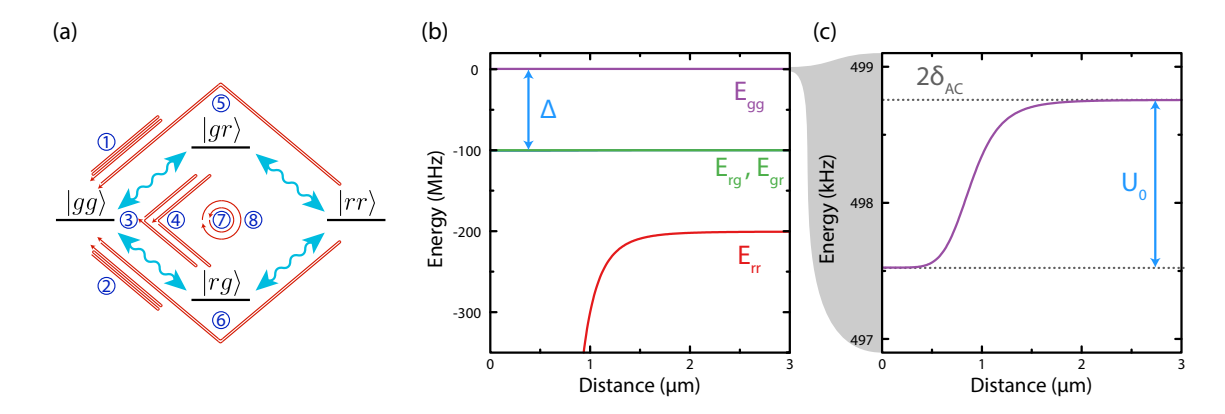


Figure 2.6: Rydberg "dressed" interaction potential. (a) Diagram of the twoparticle states, blue lines denote the connections between them through the exchange of a photon (\hat{H}_{Ω}) , red lines denote the 8 possible paths for fourth-order perturbation theory. (b) Eigenenergies of the Hamiltonian in Eq. 2.22 for parameters $C_6 = 100\,\mathrm{MHz}\mu\mathrm{m}^6$, $\Delta = 100\,\mathrm{MHz}$, and $\Omega = 10\,\mathrm{MHz}$; each color corresponds to a different eigenvalue. (c) Same as (a) but zoomed-in on the dressed ground-state eigenenergy $E_{\tilde{g}\tilde{g}}(R)$ (Eq. 2.30). Here we can appreciate the soft-core dressed interaction potential from Eq. 2.32. The top dotted gray line notes the light shift of the atoms δ_{AC} (Eq. 2.31) and the bottom one guides the eye for the potential depth U_0 .

The potential described by Eq. 2.32 and shown in Fig. 2.6c is a soft-core long-range interaction potential with two main parameters:

$$U_0 = \frac{\Omega^4}{8\Delta^3}$$
 and $R_c = \left(\frac{C_6}{2\Delta}\right)^{\frac{1}{6}}$ (2.33)

It is interesting to note that the potential depth U_0 depends solely on the dressing parameters Δ and Ω . This comes about as an extra correction of the light-shift that the atoms feel when the strong van der Waals forces effectively decouple the $|rr\rangle$ state. The effect of the C_6 coefficient rather than defining the potential strength will set the range of the interactions R_c . The interaction strength will be reduced from van der Waals interactions of the order of hundreds of MHz at typical inter-particle spacings to the order of kHz allowing one to reach non-trivial regimes where the long-range interaction and kinetic energy scales compete with each other.

This interaction potential is of course an approximation of the true potential that atoms would "feel". Numerically diagonalizing the matrix of Eq. 2.22 is quite simple

Property	Variable	Scaling $\propto {n_*}^{\alpha}$		
Troperty	Variable	fixed Δ	fixed β	
Rabi Frequency	Ω	-3/2	-3/2	
Laser Detuning	Δ	0	-3/2	
Rydberg Admixture	β	-3/2	0	
Dressed Radiative Lifetime	$\beta^{-2}\tau_0$	6	3	
Dressed Blackbody Decay Lifetime	$\beta^{-2} \tau_{BB}$	5	2	
Dressed Potential Depth	U_0	-6	-3/2	
Dressed Potential Range	R_c	11/6	25/12	

Table 2.4: Scaling of Rydberg dressing properties with n^* . Scalings of useful Rydberg dressing properties with principal quantum number.

and in order to find the interaction potential one needs to calculate the eigenenergy of the eigenvector which has most overlap with the ground-state $|gg\rangle$. In Ch. 3 we will explore all the considerations that went into calculating and measuring the true dressed potential on the atoms. However, this perturbative approximation provides a very useful tool to design a Rydberg dressing experiment and understanding the principles behind the technique.

2.8.3 Scaling of Rydberg dressing parameters

Since the Rydberg dressing parameters depend so strongly on the laser parameters Ω and Δ , it will be useful to rewrite the scalings of these parameters as a function of principal quantum number n^* (Table. 2.4) and as a factor of laser power P at a fixed n (Table. 2.5).

In terms of experimental realization, Rydberg dressing can be done using a single UV laser as described in Sec. 3.4. This means that for a given experiment, the overall power P of the laser will be relatively constant irrespective of the principal quantum number one is coupling to. The Rabi frequency of a laser light-field goes as the square

Property	Variable	Scaling $\propto P^{\alpha}$		
Troperty	Variable	fixed Δ	fixed β	
Rabi Frequency	Ω	1/2	1/2	
Laser Detuning	Δ	0	1/2	
Rydberg Admixture	β	1/2	0	
Dressed Lifetime	$\beta^{-2}\tau$	-1	0	
Dressed Potential Depth	U_0	2	1/2	
Dressed Potential Range	R_c	0	-1/12	
Interaction-to-Lifetime ratio	$U_0 au_{dr}$	1	1/2	

Table 2.5: Scaling of Rydberg dressing properties with laser power P. Scalings of useful Rydberg dressing properties with laser power showing the importance of having a strong dressing light field. Particularly, the interaction-to-lifetime increases irrespective of which parameters Δ or β are fixed.

root of the laser power given by the relation:

$$\Omega = \sqrt{\frac{4e^2P}{\epsilon_0\pi\hbar^2cw_0^2}}\mu_{2S,nP} \tag{2.34}$$

Where w_0 is the waist of the laser. With this relation and the Rydberg property scalings from Table. 2.1 in mind, we can write down corrected scaling laws for the the Rydberg dressing properties in two limits: one keeping the detuning Δ from resonance constant and one keeping the Rydberg admixture β constant. These limits are useful to think about the interaction potentials one can engineer using the available parameters. The scalings are summarized in Tables. 2.4 and 2.5.

The first takeaway from these tables is that the interaction range R_c is most susceptible to principal quantum number and increases roughly quadratically while it is essentially independent of power. This should not be a surprise as the C_6 coefficient depends very strongly on n^* as well. This means that for a known achieved laser power P one would only have a range of nP states to chose from in order to get

a desired interaction potential for a fixed inter-particle spacing (such as an optical lattice spacing).

The second takeaway is that power matters. Essentially all parameters scale favorably with power P. Particularly the figure of merit of the interaction-to-lifetime ratio $U_0\tau_{dr}$ which benchmarks the coherence of the system. For any experimental realization it is very important to maximize the power of the available laser. Much work of this thesis went into maintaining the correct working of our ultraviolet laser (Sec. 3.4) to maximize its power throughput but also to stabilize it and avoid extra decoherence mechanisms due to intensity noise. It is also noteworthy that the Rabi frequency also depends strongly on its focus waist w_0 , carefully designing the optical setup will be important and careful considerations should be made to understand how it affects the achievable simulation models as explained in Ch. 6.

2.9 Calculating Rydberg properties using Python packages

While the perturbative limit is sufficient to understand a great deal of the properties of Rydberg atoms for the purpose of planning an experiment, more complicated calculations are required to fully understand the interaction potentials. Nowadays there are two Python packages that simplify this task and which were used for this thesis: the Alkali-Rydberg Calculator (ARC) [76] and Pair Interaction (PI) [87]. There are advantages to each package and we used them where their strengths were most useful.

Alkali-Rydberg Calculator

The ARC package [76] provides a very convenient and well documented package with great functionalities. However, it lacks the ability to solve for the Hamiltonian with strong magnetic fields which is necessary for our experiment. Nevertheless, it

is incredibly useful for properties that are invariant under magnetic field such as lifetimes and decay channels. It was however an invaluable resource to plan for our experiment as shown in Fig. 2.2 and to compare for early perturbative calculations for pedagogical purposes.

Pair Interaction

The PI package [87] does provide the capability of high magnetic fields with the caveat of a more wanting documentation. A great deal of work was done to decipher the various and very useful functions in order to build scripts used for analysis and exploration. In the end, this package was what allowed us to best understand the interaction potentials of our system and the one we relied on the most. All of the calculations pertaining the pair potential calculations presented in Ch. 3 and Ch. 6 were performed using this package. A very useful capability of this package is that it can save the overlap of a particular pair potential with the Rydberg states in $|n,l,j,m\rangle$ basis providing a very useful tool to calculate dressing potentials as shown in Sec. 3.3. The only caveat is that one needs to take into account the Clebsch-Gordan coefficients (Table. 3.1) to transform into the high magnetic field $|nl, m_l, m_s, m_I\rangle$ basis (Sec. 3.1.1).

2.9.1 Multi-polar Expansion

Solving for the full Hamiltonian between two Rydberg states involves taking into account many nearby pair states and how their couplings modify each other. In the previous sections, a lot of work went into describing the perturbative calculation with only dipole-dipole couplings. This is sufficient for large distances. However for close distances, which are most important for experiments, taking into account higher order processes is needed. We will refer to this multi-polar expansion in terms of two variables: $\kappa = 1, 2, \ldots$ for dipole, quadrupole, etc. and $\rho = \kappa_1 + \kappa_2 + 1$

Low Field	High Field		
$\Delta l = \begin{cases} \pm 0, 2, \dots \kappa & \text{for } \kappa \text{ even} \\ \pm 1, 3, \dots \kappa & \text{for } \kappa \text{ odd} \end{cases}$	$\Delta l = \begin{cases} \pm 0, 2, \dots \kappa & \text{for } \kappa \text{ even} \\ \pm 1, 3, \dots \kappa & \text{for } \kappa \text{ odd} \end{cases}$		
$\Delta s = 0 \text{ (same)}$	$\Delta s = 0 \text{ and } \Delta m_s = 0$		
$\Delta j = \pm 0, 1, \dots \kappa \text{ and } j + j' \le \kappa$	$\Delta I = 0 \text{ and } \Delta m_I = 0$		
$\Delta m_j = \pm 0, 1, \dots \kappa$	$\Delta m_l = \pm 0, 1, \dots \kappa$		

Table 2.6: Selection rules on multi-polar expansion. Selection rules for matrix elements of spherical harmonics with multi-polar expansions in the low and high magnetic field limits. The parameter $\kappa = 1, 2, \ldots$ refers to dipole, quadrupole, etc. expansions [87]. The difference arises from the change of useful quantum numbers according to the Paschen-Back effect discussed in Sec. 3.1.1.

where the index refers to each atom considered in the pair calculation. For example, $\rho = 3$ (minimum) implies a calculation with only dipole-dipole interactions. This also presents an expansion of the usual selection rules:

Particularly the PI package also allows for the addition of a diamagnetic term to the full Hamiltonian. No appreciable difference in the pair-potentials, memory usage, or speed of the calculations was found in our studies so we always had this term on.

Implementation on Pair Interaction

To solve the pair-potential Hamiltonian, you first define a specific pair-state you are interested in the $|n,l,j,m\rangle\otimes|n',l',j',m'\rangle$ basis. Constraints on the amount of states that will be taken into account for the calculation need to be defined in order to improve speed and memory usage. These constraints are the range of energies for the single Rydberg state ΔE_{single} , the range of principal quantum number Δn , the range of angular momenta Δl , and the range of energies of pair states to consider ΔE_{pair} . The values selected for these should be sufficient such that we are taking into account all the relevant states for the selected multi-polar expansion ρ as expected from the selection rules in Table. 2.6. For our calculations, we fixed $\Delta n = 3$ and $\Delta l = 3$;

this gave us a sufficient breadth of states to get correct results. The ranges in the energies were a bit more important to set correctly as they are the most important constraint on the size of the eigenbasis. In principle ΔE_{single} is always larger than ΔE_{pair} because some pairs of states of very different energies will form a pair state that is very close to our target states. For calculations on $|28P\rangle$ pair-states we found that $\Delta E_{single} = 500\,\text{GHz}$ and $\Delta E_{pair} = 200\,\text{GHz}$ was sufficient. However, for larger principal quantum numbers we reduced this as the density of states increases according to the binding energy Eq. 2.1.

We can also define the limit of the multi-polar expansion ρ , the angle of interaction θ , as well as electric E and magnetic B fields as vectors. Finally, we have chosen a reasonably spaced grid of distances that enable us to see the features of the potentials at the distances important for our lattice.

Chapter 3

Rydberg dressing of ⁶Li

The previous chapter introduced the physics of Rydberg atoms and their properties. The technique of Rydberg dressing is also discussed and its potential impact as a quantum simulation tool is evident. Our group is not the first to develop this technique. Other groups have successfully implemented it in heavy atoms such as Rb and Cs with impressive results realizing many-body dynamics and electrometry measurements in frozen systems [55, 71–75, 88–91]. However, Rydberg dressing of itinerant systems has been an elusive goal. This limitation has been mostly due to non-trivial decay mechanisms limiting the achievable lifetime of the atomic sample as will be discussed in Sec. 3.7.

In our experiment, we set out to develop the technique of Rydberg dressing for the fermionic species of 6 Li. The main driver for this endeavor was the opportunity to take advantage of lithium's light mass in order to engineer itinerant systems with long-range interactions. We have successfully implemented such a system in the form of a t-V model as detailed in Ch. 6. In this chapter, we will cover both the theoretical and experimental considerations that were taken for the successful implementation of this technique in 6 Li.

3.1 Rydberg dressing scheme

Our experiment was designed to be a very flexible quantum simulator of the Fermi-Hubbard model with single-site resolution [92, 93]. However, Rydberg dressing was not considered in its original design. This presented some constraints both in technical difficulties (e.g. window coatings) and in terms of the actual Rydberg dressing scheme (e.g. polarization, state, etc.). 6 Li has a broad Feshbach resonance in the $\sim 700-850$ G range [94]. As such, our experiment includes a set of coils that can provide very stable fields up to these large magnetic fields in order to tune the interactions of the system [92]. The existing protocols to generate low-entropy many-body states of ground state atoms operated at relatively large magnetic fields of ~ 600 G. Given this, we considered the idea of performing Rydberg dressing at such fields, finding that the strong magnetic dispersion of Rydberg atoms (Fig. 3.1b) provides a "cleaner" realization of the basic Rydberg dressing ideas explained in Sec. 2.8. This is in contrast with previous realizations of Rydberg dressing in other species which focused on very low magnetic fields in the mG range [55, 75, 90].

3.1.1 Lithium states at high magnetic fields

Before going into the behavior of specific states with high magnetic fields, it will be useful to have in mind the selection rules $\Delta l = 0$ and $\Delta m_l = 0, \pm 1$ (for π, σ^{\pm} photons respectively) at high fields (Table. 2.6). This means that $|2S_{1/2}\rangle$ ground-state atoms can only be connected to a $|nP\rangle$ Rydberg state under a single-photon dressing scheme. Moreover, a single-photon cannot change the nuclear moment m_I or spin m_s of an atom either. Therefore, the specific final $|m_l, m_s, m_I\rangle$ state will be defined only by the chosen initial hyperfine ground-state and the polarization of the photon.

Paschen-Back regime

At low magnetic fields, the hyperfine coupling dominates over the Zeeman coupling and the "good" quantum numbers are $\hat{F} = \hat{J} + \hat{I}$ and its projection along the magnetic field. At very large fields, also known as the Paschen-Back regime, the field overpowers all angular momenta $(\hat{L}, \hat{S}, \text{ and } \hat{I})$ cross-couplings aligning them. This presents a change in the "good" quantum numbers to the $|m_l, m_s, m_I\rangle$ basis for the particular projection of each momenta to the magnetic field. In this limit, the eigenenergies are defined by the initial fine- and hyperfine-structure splittings (ΔE_{FS}) and ΔE_{HFS} plus a magnetic dispersion term we can write down as:

$$\Delta E_{PB} \approx B\mu_B \left(g_l m_l + g_s m_s + g_I m_I \right) \tag{3.1}$$

Here, B is the magnetic field; $\mu_B \sim 1.4 \,\mathrm{MHz/G}$ is the Bohr magneton; and $g_l \sim 1$, $g_s \sim 2$, and $g_I \sim -0.0005$ are the g-factors of their respective angular momenta [95]. Note how the nuclear spin \hat{I} g-factor is much smaller than the others. Therefore, for Rydberg atoms were the initial hyperfine-structure splitting is very small, states with different m_I are essentially degenerate.

Ground-states

Fig. 3.1a shows the full energy dispersion of the $|2S_{1/2}\rangle$ ground-states of ⁶Li up to a field of 500 G. In our experiment we worked mostly at a field of ~ 595 G. At this strong field, the ground-states are not quite yet in the Paschen-Back regime. Finding an analytical solution of the full state for ⁶Li ground-states is possible [96]. The existing protocols of our machine made it simpler to work with states $|1\rangle - |3\rangle$. At

¹Throughout the thesis we also refer to this basis as $|nl, m_l, m_s, m_I\rangle$ to describe the full state.

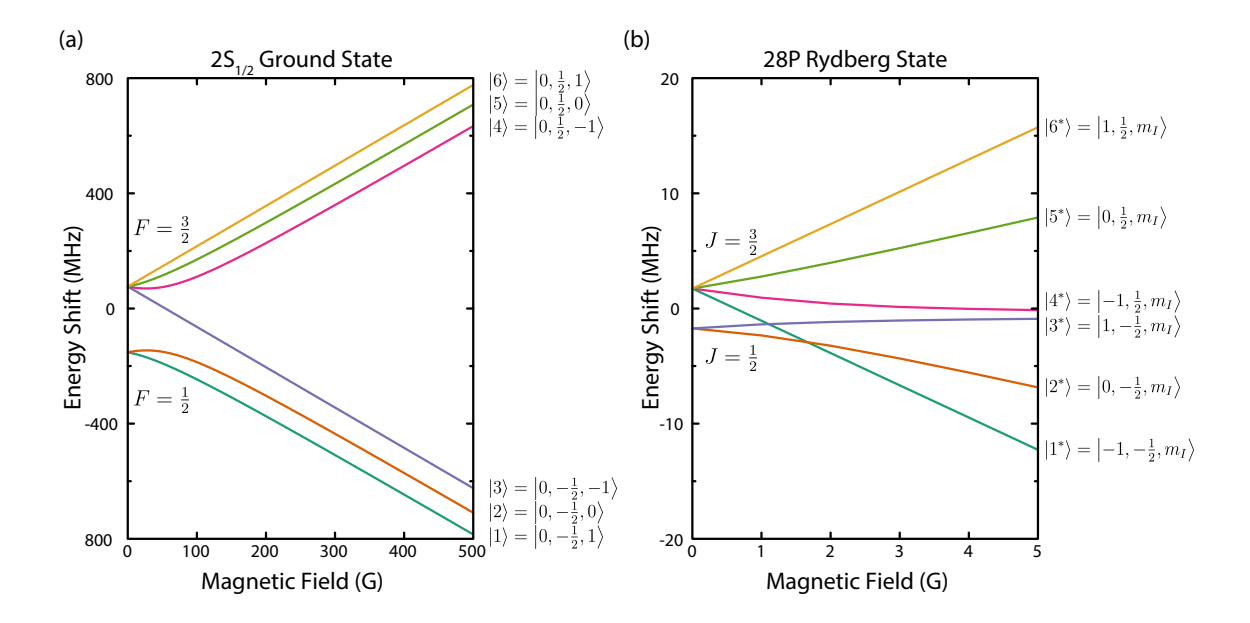


Figure 3.1: ${}^{6}\text{Li} |2S_{1/2}\rangle$ and $|28P\rangle$ states vs. Magnetic Field. ${}^{6}\text{Li}$ atomic states dispersion with magnetic field for (a) $|2S_{1/2}\rangle$ ground-states and (b) $|28P\rangle$ Rydberg states. Each color corresponds to a different state. $|k\rangle$ and $|k^*\rangle$ states are labeled by increasing energy at high magnetic fields and shown in the $|m_l, m_s, m_I\rangle$ basis. The Rydberg states do not specify a m_I value as its energy separation is negligible compared to ground-states. Note how the Rydberg states reach the Paschen-Back regime much quicker than the ground-state atoms.

these fields, states $|1\rangle$ and $|2\rangle$ are $\geq 98\%$ pure while state $|3\rangle$ remains completely pure at all fields² in their respective $|m_l, m_s, m_I\rangle$ basis.

With this in mind, we prefer Rydberg dressing protocols where the initial state is $|3\rangle$ to avoid complicated effects of dressing mixed states. However, experimentally we did not find any difference in the lifetime with initial hyperfine ground-state. In fact, most of our characterization of lifetimes and interaction was done starting in the $|1\rangle$ (and $|2\rangle$ in the case of Ramsey interferometry) state.

Rydberg nP states

Fig. 3.1b shows the full energy dispersion of the $|28P\rangle$ Rydberg state of ⁶Li up to a field of 5 G.The dispersion of different $|nP\rangle$ Rydberg states is expected to be very

²State $|6\rangle$ is also pure at all fields, but pumping atoms to this highest energy ground-state is a bit complicated. Future possible protocols though might benefit from using this initial state.

similar. The energy levels were calculated using Pair Interaction [87]. As expected from Eq. 3.1, the Rydberg states disperse according to their total angular momentum projection onto the magnetic field direction. The main difference with ground-state atoms is that the hyperfine-splitting is much smaller leading to states with different m_I to be closely degenerate and unresolved. This leads to the simplification that Rydberg states with the same m_l and m_s quantum numbers but different m_I values will still interact via a van der Waals interaction potential as described in Sec. 2.5.1. We can make this assumption because the states being closely degenerate leads to very long timescales for the exchange of a photon due to the Heisenberg uncertainty principle³. For the following discussions, we will number the Rydberg states with increasing energy and differentiate them from ground-states by adding an asterisk $|k^*\rangle$ to them.

With the selection rules in mind (Table. 2.6) we will note that ground-states $|1\rangle - |3\rangle$ can only connect to Rydberg states $|1^*\rangle - |3^*\rangle$ via a single-photon transition dependent on its polarization. The m_I value of the Rydberg state will be defined by the specific ground-state used. The strong dispersion of the states with magnetic fields does provide an advantage over the Rydberg dressing schemes of other groups since at our typical fields the closest Rydberg states in a different hyperfine state are $2 \times \mu_B \times 600 \,\mathrm{G} \sim 1.7 \,\mathrm{GHz}$ away. This allows us to think of any dressing scheme as connecting mainly to a single pair-potential with "mostly" van der Waals character (Sec. 3.3) up to small corrections and avoided crossings.

Basis transformation

As explained in Sec. 2.9, the Pair Interaction package used to calculate the pairpotentials works in the $|j,m\rangle$ basis which is only really useful at or near zero magnetic field. For this reason, it is useful to calculate and write down the Clebsch-Gordan

³Also, a single photon cannot change the m_I value of the atom as seen in Table. 2.6 and higher multi-polar couplings are exponentially smaller in amplitude.

		j,m angle					
		$\left \frac{1}{2}, -\frac{1}{2}\right\rangle$	$\left \frac{1}{2}, +\frac{1}{2}\right\rangle$	$\left \frac{3}{2}, -\frac{3}{2}\right\rangle$	$\left \frac{3}{2}, -\frac{1}{2}\right\rangle$	$\left \frac{3}{2}, +\frac{1}{2}\right\rangle$	$\left \frac{3}{2}, +\frac{3}{2}\right\rangle$
$ m_l,m_s angle$	$ 1^*\rangle = \left -1, -\frac{1}{2}\right\rangle$	0	0	1	0	0	0
	$ 2^*\rangle = \left 0, -\frac{1}{2} \right\rangle$	$\frac{1}{\sqrt{3}}$	0	0	$\sqrt{\frac{2}{3}}$	0	0
	$ 3^*\rangle = \left +1, -\frac{1}{2}\right\rangle$	0	$\sqrt{\frac{2}{3}}$	0	0	$\frac{1}{\sqrt{3}}$	0
	$ 4^*\rangle = \left -1, +\frac{1}{2}\right\rangle$	$-\sqrt{\frac{2}{3}}$	0	0	$\frac{1}{\sqrt{3}}$	0	0
	$ 5^*\rangle = \left 0, +\frac{1}{2} \right\rangle$	0	$\frac{1}{\sqrt{3}}$	0	0	$-\sqrt{\frac{2}{3}}$	0
	$\left 6^*\right\rangle = \left +1, +\frac{1}{2}\right\rangle$	0	0	0	0	0	1

Table 3.1: Clebsch-Gordan coefficients between $|m_l, m_s\rangle$ and $|j, m\rangle$ basis. Note that the rows correspond to the Rydberg states $|k^*\rangle$ in descending order.

coefficients between the basis. Table. 3.1 shows these coefficients. One interesting property to point out from the table is that states $|1^*\rangle$ and $|6^*\rangle$ are pure at all magnetic fields. This makes them possible ideal candidates for future dressing schemes to avoid overlaps with other states at short distances. It is important to note that Pair Interaction can take into account extra terms in the Hamiltonian such as multi-polar expansions and diamagnetism. As such, when comparing the calculated pair-states in the $|j,m\rangle$ basis, we find numerical deviations from the values of Table. 3.1 on the order or $\sim 1\%$. This is not true for the pure states.

3.1.2 Dressing scheme

The configuration of the Rydberg excitation light used in our experiment only allows us to excite the Rydberg transition with linear polarization. This is due to the strong magnetic field pointing in the vertical direction z while the laser is pointing in direction y as shown in Fig. 3.8. This configuration makes it such that the polarization of the laser light is only well-defined when we have vertical linear polarization (z). Anything else will be some superposition of the possible polarizations. For example,

if we sent horizontal polarization, the light "seen" by the atoms will be equally in σ^+ and σ^- . For any arbitrary polarization and laser pointing, one only has to care that for the quantization axis along z, the polarizations are defined as $\pi^0 = \hat{z}$ and $\sigma^{\pm} = \frac{1}{\sqrt{2}} (\hat{x} \pm \hat{y})$. Thus all you need to do is decompose the incoming polarization into this basis.

With this simplest configuration, the most natural dressing scheme is to connect ground-states $|1\rangle - |3\rangle$ with Rydberg state $|2^*\rangle$ using a vertically polarized π photon. It would be ideal to use state $|3\rangle$ due to it being pure under magnetic field fluctuations. However, for a few measurements such as Ramsey spectroscopy (Sec. 3.8) it is necessary to use states $|1\rangle$ and $|2\rangle$ to avoid resonant excitations.

Possible improved schemes

As previously mentioned, there are two Rydberg states that remain pure for all fields and as such have less overlap with neighboring states. Ideally, we could think of two "perfect" dressing schemes: $|3\rangle \rightarrow |1^*\rangle$ and $|6\rangle \rightarrow |6^*\rangle$. However, in order to do this we would need to either send the UV laser from the bottom (technically challenging in our setup) or generate a magnetic field along the lattice direction y so that circular polarization can be well-defined. The second option presents its own issues, such as realistically only being able to produce $\leq 10G$ with our current setup. In addition, with the quantization axis pointing along the lattice plane the interactions will be asymmetric (Sec. 2.5.1).

Another option, is to use the horizontal polarization and take a hit of $\frac{1}{\sqrt{2}}$ in the Rabi frequency. Though one would also need to take into account what the effect of the opposite circular polarization will be. In this particular case, a potentially very viable scheme is $|6\rangle \rightarrow |6^*\rangle$, as the extra σ^- light will have minimal effects since the dressing detunings need to be positive farther away from state $|4^*\rangle$.

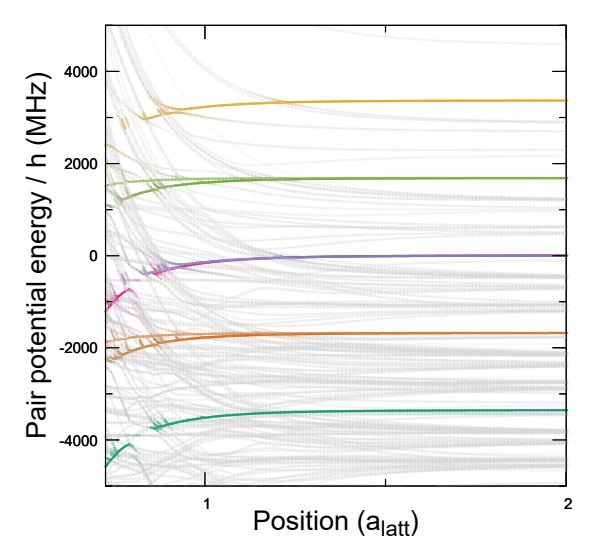


Figure 3.2: $|28P\rangle \otimes |28P\rangle$ pair-states at a field of 600 G. Pair-states between ⁶Li $|28P\rangle$ Rydberg states separated according to Eq. 3.1 for a field B=600 G. The colors represent overlap with the $|k^*\rangle \otimes |k^*\rangle$ pair states as numbered in Fig. 3.1b. The "jungle" of gray lines correspond to other nearby pair states with different quantum numbers and mostly no overlap to the target states. These states however cause avoided crossings.

3.2 Pair-state potential calculations

In Sec. 2.9.1 we described the methods for calculations made using Pair-Interaction [87]. Now, with a better understanding of the dressing scheme and the high field physics of Rydberg atoms, we performed a lot of exploratory calculations to better understand the dressed potentials and lifetime limitations.

The types of potentials that we are most interested in are the ones made by pairs of the same Rydberg state $|nP\rangle \otimes |nP\rangle$. Using the Pair-Interaction package we built scripts that, for a desired principal quantum number, calculated all nearby pair-states and kept track of their overlap with all $|k^*\rangle \otimes |m^*\rangle$ pair-states⁴ as a function of distance.

Fig. 3.2 shows one of these calculations for the $|28P\rangle \otimes |28P\rangle$ states at a magnetic field of 600 G. Here, we can appreciate the huge "jungle" of nearby states with different quantum numbers. While most of them have no overlap with the target states, they do cause avoided crossings that need to be taken into account when calculating dressed potentials as detailed in Sec. 3.3. It is also important to note that

⁴We are most interested in pair-states with the same components (e.g. $|k^*\rangle \otimes |k^*\rangle$). However, keeping track of mixed states is useful for molecular potentials.

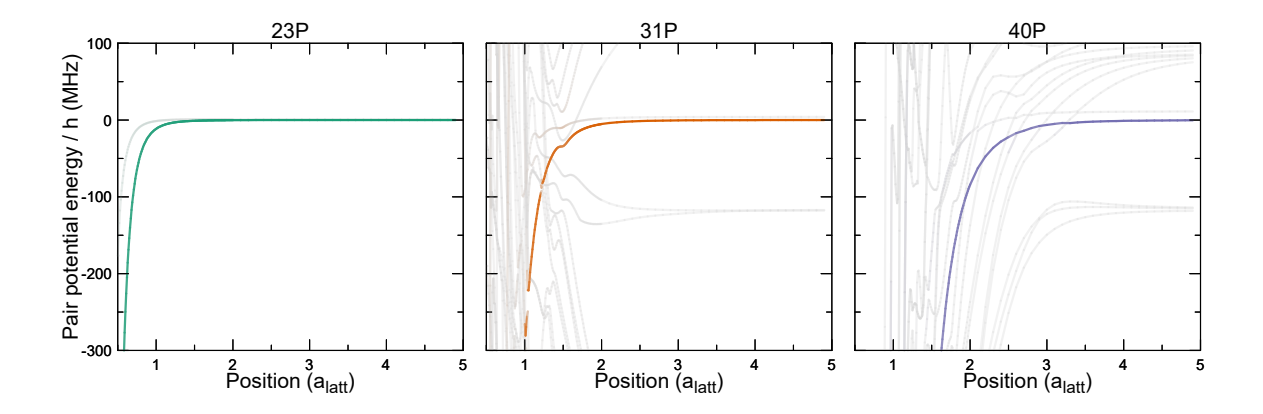


Figure 3.3: $|2^*\rangle \otimes |2^*\rangle$ pair-state at 600 G vs. principal quantum number. The $|2^*\rangle \otimes |2^*\rangle$ pair-state at a 600 G field is shown for $|23P\rangle$, $|31P\rangle$, and $|40P\rangle$ Rydberg states. The strength of the color denotes the overlap with the $|2^*\rangle \otimes |2^*\rangle$ pair-state. Note how the "jungle" of gray lines gets farther out, possibly leading to non-trivial loss mechanisms due to resonant couplings.

we observe the expected dispersion from Eq. 3.1 as $E_{|k^*\rangle\otimes|m^*\rangle}(\infty) = E_{|k^*\rangle} + E_{|m^*\rangle}$. At 600 G this separation is ~ 1.7 GHz which is quite large compared to typical dressing detunings $\Delta \lesssim 100$ MHz allowing us to connect individual hyperfine ground-states with a single state of the Rydberg fine-structure.

As we decided to use a dressing scheme with vertical linear polarization, the rest of the discussion in this section will focus only on $|2^*\rangle \otimes |2^*\rangle$ states.

3.2.1 Pair-states vs. principal quantum number

A first important consideration is what specific $|nP\rangle$ Rydberg state to connect to. This is by far the biggest knob in our experiment. Originally, from the scalings shown in Table 2.4 we estimated that the $|31P\rangle$ state would be an ideal candidate for our intended scheme. This would be a sufficiently strong interaction strength to lifetime ratio and a suitable range. However, we quickly found that the lifetime of the atoms was not close to the expected Rydberg dressed lifetime. We explored the dependence

with other principal quantum number states and found that the lower we got, the closer the measured lifetime was to the expected Rydberg dressed lifetime⁵.

Fig. 3.3 shows the calculated $|2^*\rangle \otimes |2^*\rangle$ pair potentials for different principal quantum numbers. The "clean" van der Waals picture of the Rydberg potentials is only true at low principal quantum numbers. As one increases this knob, the "jungle" of lines with all of their overlaps and avoided crossings gets farther and farther away. It is our understanding that one component of the non-trivial loss mechanisms we encountered in our system is related to resonant coupling with nearby pair-states rather than black-body decay. This was evidenced by our finding that lower principal quantum numbers such as $|28P\rangle$ had increased relative lifetime to the theoretically expected one. Particularly damaging should be cases such as the ones shown in the second and third panels of Fig. 3.3 for $|31P\rangle$ and $|40P\rangle$ where these nearby pair states are at typical inter-particle spacings in our lattice.

3.2.2 Pair-states vs. magnetic field

Another big knob in our experiment was the magnetic field. As explained before, we did most of our characterization and all of our experiments at a $\sim 592\,\mathrm{G}$ purely due to convenience on the existing protocols. After some characterization, we found that the range of $300-600\mathrm{G}$ was good for two reasons. First, these fields are large enough that we can simplify our understanding as only coupling to the desired fine-structure Rydberg state. Second, at larger fields we measured reduced lifetimes (Fig. 3.19) which we attribute to having the strong magnetic dispersion bringing resonant pair-states near the target state leading to similar decay mechanisms such as the ones limiting large principal quantum numbers as explained in the previous subsection. Fig. 3.4 shows the calculated $|2^*\rangle \otimes |2^*\rangle$ pair potentials of $|28P\rangle$ for different magnetic

⁵This was before our better understanding came from the Pair Interaction simulations.

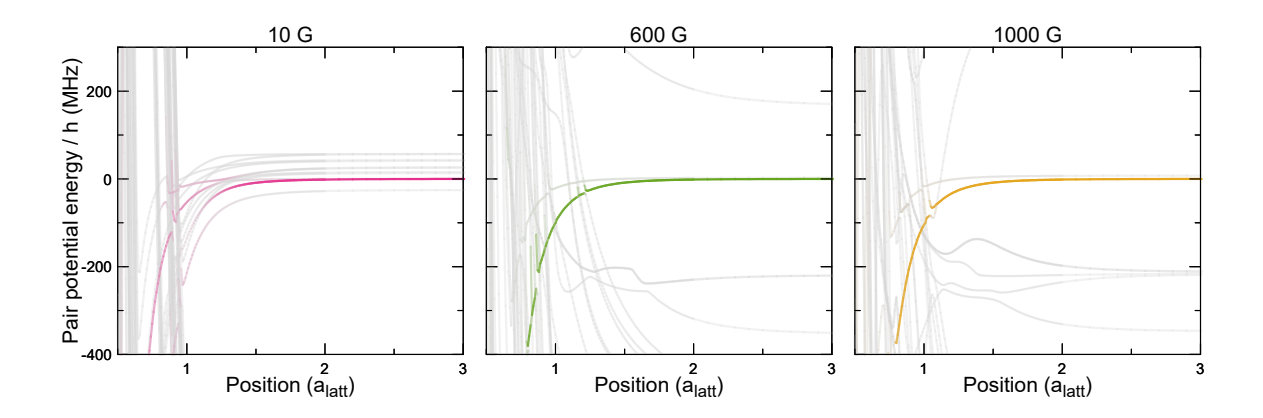


Figure 3.4: $|2^*\rangle \otimes |2^*\rangle$ pair-state of $|28P\rangle$ vs. magnetic field. The $|28P\rangle$ Rydberg state $|2^*\rangle \otimes |2^*\rangle$ pair-state is shown for $B=10\,\mathrm{G}$, $600\,\mathrm{G}$, and $1000\,\mathrm{G}$. The strength of the color denotes the overlap with the $|2^*\rangle \otimes |2^*\rangle$ pair-state. At low fields, $|k^*\rangle$ states are not yet well separated leading to many close lines with non-vanishing overlaps. At very high fields, the magnetic dispersion is so large that many more lines are around the desired target state.

fields. We eventually used the pair-state shown in the second panel of this figure for our experiments described in Ch. 6.

3.2.3 Förster resonances

While not used in our system, as part of this thesis we studied the possibility of dressing ⁶Li near a Förster resonance [97–103]. In Sec. 2.5.1 we described the van der Waals character of Rydberg pair-potentials (e.g. labeled $|a,b\rangle$) as a second order perturbation theory effect due to a virtual two-photon exchange to a different pair-state ($|\alpha,\beta\rangle$). From Eq. 2.14 we understand that the strength of these couplings comes not only from the dipole matrix elements between the states, but also from the energy difference $\delta_{\alpha\beta} = E_{|\alpha\beta\rangle} - E_{|ab\rangle}$ between the states. We call this energy difference a Förster defect.

A Förster resonance appears when, for some parameter values, a particular defect $\delta_{\alpha\beta}$ vanishes leading to heavily modified pair-state potentials. This can happen at zero field for particular principal quantum numbers n. Fig. 2.4 shows how the numerically

calculated C_6 coefficients diverge around $|33P\rangle$. However, the previous sections show how magnetic fields also have a strong effect on the nearby pair-states. In App. C we show calculations of the Förster defects and resonances of ⁶Li and their behavior at different magnetic fields. In principle, one could use this knowledge to engineer a dressing scheme to a "molecular" potential with a valley right at the lattice spacing allowing for much more favorable dressing potential scalings as proposed in Ref. [102].

3.3 Full Rydberg-dressed potential

In Sec. 2.8 we worked through the derivation of the Rydberg-dressed potential between two ground-state atoms off-resonantly coupled to Rydberg states which interact via van der Waals forces. Through this derivation we arrived at a soft-core interaction potential of the form shown in Eq. 2.32. We do mention that this potential is an approximation valid only in the $\beta \to 0$ limit. This is not a problem because numerical diagonalization of the 4 × 4 matrix of Eq. 2.22 is simple enough to extract more realistic potentials in terms of specific parameters. However, in order to find the "true" interaction potential between two ⁶Li atoms in our optical lattice we need to take into account a few extra considerations. In this section we will describe each of these considerations and how to arrive at the full Rydberg-dressed potential shown in Fig. 3.5.

3.3.1 Overlap with nearby pair-states

The simple van der Waals picture is not exactly correct as evidenced in the figures of Sec. 3.2. For the true Rydberg pair-state landscape there is non-zero overlap with other nearby pair-states which depend on the separation between the atoms. Particularly at close distances, there are overlaps of the target state $(|r\rangle \otimes |r\rangle = |r, r\rangle)$ with multiple other nearby pair-states $|p(\mathbf{R})\rangle$. In order to extract a more realistic

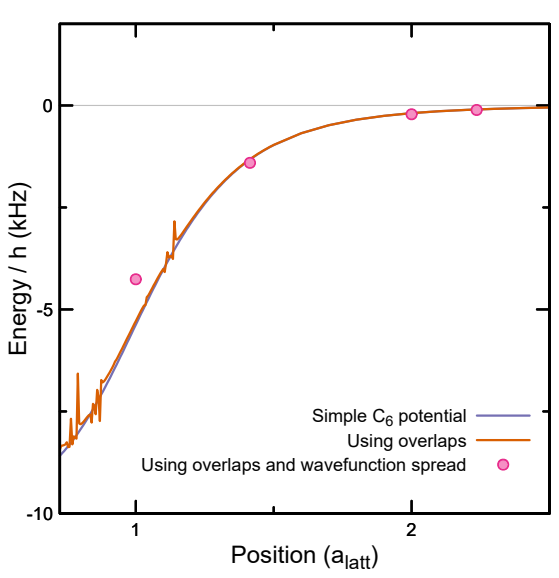


Figure 3.5: Full Rydberg-dressed potential. Different degrees of approximation for the calculation of Rydberg dressed potentials between |1| ground-state atoms connected to the $|28P\rangle$ Rydberg state at $592\,\mathrm{G}$ and parameters $\Omega = 2\pi \times 766\,\mathrm{MHz}$ and $\Delta = 2\pi \times 35 \, \text{MHz}$. First we have the "simple" dressed potential from Eq. 2.32 for a van der Waals potential with C_6 = $2\pi \times 90.19 \,\mathrm{MHz} \, a_{latt}{}^6$. Second, the potential taking into account overlaps with nearby pair-states (Eq. 3.3). Finally, we also take into account the wavefunction spread of Fig. 3.6. This figure corresponds to Fig. 6.1b(inset).

dressed potential, we need to take into account the dressing of our ground-state atoms with all of these other states taking into account the individual overlaps with the target state. In the following, we will denote the overlap as $\alpha^p(\mathbf{R}) = \langle r, r | p(\mathbf{R}) \rangle$.

In order to do this, we are going to numerically solve the dressing Hamiltonian from Eq. 2.21 for each individual pair-state potential $V^p(\mathbf{R})$:

$$\hat{H}^{p} = \hat{H}_{single} \otimes \hat{\mathbb{I}} + \hat{\mathbb{I}} \otimes \hat{H}_{single} + V^{p}(\mathbf{R}) |r\rangle \langle r| \otimes |r\rangle \langle r|$$
(3.2)

Here, the pair potentials $V^p(\mathbf{R})$ correspond to the calculated eigenenergies $E_{|p\rangle}(\mathbf{R})$ subtracting the offset corresponding to the bare energy of the target state $E_{|r,r\rangle}(\infty)$. The parameter Δ is the same as the intermediate states $|g,r\rangle$ and $|r,g\rangle$ are not affected by the overlaps. The superscript p denotes each pair potential.

We can numerically solve for all dressed potentials $U_{dr}^k(\mathbf{R})$ by diagonalizing the individual Hamiltonians \hat{H}^p and subtracting the expected light-shift offsets. Finally, we can add all of these up taking into account the distance-dependent overlaps in

order to extract:

$$U_{dr}(\mathbf{R}) = \sum_{p} |\alpha^{p}(\mathbf{R})|^{2} U_{dr}^{p}(\mathbf{R})$$
(3.3)

As we can observe in Fig. 3.4b, if we follow the overlap, we get essentially a simple van der Waals potential up to some avoided crossings. Therefore, we expect that the dressed potential taking into account overlaps from Eq. 3.3 will be very similar to that of Eq. 2.32. In Fig. 3.5 we observe exactly this where the "full" dressed potential has only small differences with the one calculated using the extracted C_6 coefficient. However, now we can appreciate the effect of crossing "resonances" at close distances where avoided crossings with the main pair-state happen. These resonances are mostly sharp enough to not affect the overall potential.

Engineering repulsive interactions by dressing on a large avoided crossing

In general, the calculations made using the python packages seem to capture quite well the true nature of Rydberg pair potentials. Recently, Ref. [103] performed spectroscopic measurements of molecular bound states created by an avoided crossing of two coupled Rydberg pair-states of ⁸⁷Rb. What they found is that they could predict with very high precision the energies of the molecular bound states even taking into account the small modification due to an avoided crossing with a non-coupled pair-state. These results mean that we can trust and use the calculations from the python packages to "explore" the Rydberg parameter space. Potentially opening the door to exploit "exotic" Rydberg dressing schemes which can provide more favorable scalings or tunability.

In Ref. [102] one of such schemes is described where one would dress close to a valley (or hill for attractive potentials) of a molecular potential like the one explored

in Ref. [103] positioned approximately at $1 a_{latt}$. Depending on the height of the valley, one can expect much more favorable interaction-to-lifetime ratios.

However, we do not need to limit ourselves to molecular potentials between coupled pair-states. As shown in Fig. 3.2 the size of the avoided crossings with non-coupled states can be quite sizable. One could imagine a way to engineer a dressed potential with opposite sign to the natural van der Waals interaction by choosing the detuning such that it falls right in the middle of one of such avoided crossings. As long as resonances to pair-states with non-zero overlap are avoided, the Born-Oppenheimer approximation is still valid. Depending on the position R of the crossing, one could tune repulsive interactions for 6 Li atoms or even more exotic potentials where the nearest neighbor and next-nearest neighbor interactions are of opposite sign.

3.3.2 Wavefunction spread in optical lattice

The second consideration that we need to make is that since $^6\mathrm{Li}$ is so light, the atoms in our optical lattice have a significant wavefunction spread and we cannot think of them merely as point particles. To first order, we can write down the Wannier functions of the atoms in our 2D lattice as a separable wavefunction $\Psi(x,y,z) = \psi(x)\psi(y)\psi(z)$ where $\psi(r) = \frac{1}{(2\pi\sigma_r^2)^{1/4}}\exp\left(-\frac{r^2}{4\sigma_r^2}\right)$ are the ground-states of a quantum harmonic oscillator. For these wavefunctions, the spread $\sigma_r = \sqrt{\frac{\hbar}{2m\omega_r}}$ depends on the mass and the trapping frequency in the particular dimension.

In our experiment, our atoms are trapped in a mixture of a 2D optical lattice in the x-y plane with $a_{latt}\approx 752\,\mathrm{nm}$ and a tightly confined vertical lattice to keep the atoms in the 2D regime. In the particular case of the experiments described in Ch. 6, the lattice trapping frequencies were $\omega_{x,y}\approx 2\pi\times 54\,\mathrm{kHz}$ leading to spreads in the x-y plane of $\sigma_{x,y}\approx 124\,\mathrm{nm}\approx 0.17\,a_{latt}$. The vertical lattice trapping frequency is $\sigma_z\approx 2\pi\times 17\,\mathrm{kHz}$ leading to $\sigma_z\approx 222\,\mathrm{nm}\approx 0.3\,a_{latt}$. These wavefunction spreads cor-

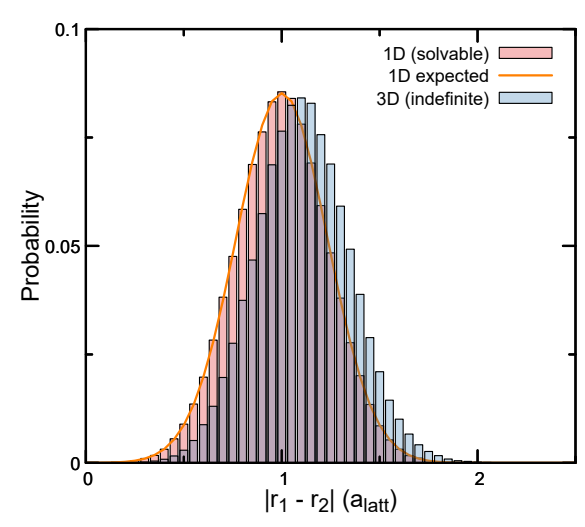


Figure 3.6: Probability distribution of distance between two neighboring atoms. The spreads used are $\sigma_{x,y} = 0.17 \, a_{latt}$ and $\sigma z = 0.3 \, a_{latt}$ corresponding to the lattice depth at which we performed the quench dynamics measurements from Ch. 6. Note how the full 3D distribution has an average separation of slightly larger than a lattice site. This is an effect of the extra spread in the other two dimensions.

respond to the standard deviation of the approximately Gaussian probability densities for the positions of each atom at a lattice site.

We are interested in finding the probability distribution $P(|\mathbf{r_1} - \mathbf{r_2}|)$ of the distance between two atoms at particular lattice sites. While the problem is easy to state, for 3D probability distributions (even Gaussian ones) it is not analytically solvable. The 1D case is analytically solvable though. To overcome this issue, we employ a Monte-Carlo method where we randomly generate positions $\mathbf{r_1}$ and $\mathbf{r_2}$ and calculate the resulting distance $|\mathbf{r_1} - \mathbf{r_2}|$. We average and bin about 10^5 samples and extract a discrete probability distribution for the distance between atoms. Fig. 3.6 shows this probability distribution for the 3D and 1D case 1 a_{latt} apart along with the known 1D expected distribution $P_{1D}(|\mathbf{r_1} - \mathbf{r_2}|) = \frac{\delta r}{2\sigma\sqrt{\pi}} \exp\left(-\frac{(\mathbf{r_1} - \mathbf{r_2} - a_{latt}\hat{x})^2}{4\sigma^4}\right)$ to benchmark the method.

We find that the average distance between nearest neighboring atoms is actually a bit larger than 1 a_{latt} which is expected due to the probability spread in the directions perpendicular to the separation. This will have the effect of reducing the "effective" interaction that nearest neighboring atoms feel⁶. We can repeat this method for all other possible distances of the atoms in the lattice and multiply their probability

⁶Depending on the "steepness" of the potential, it can also have the effect of increasing the interaction strength as is the case of the next-nearest neighbor interaction of Fig. 3.5.

distributions with the "full" dressed potential of Eq. 3.3 and find the actual interaction energy between dressed atoms in our lattice. The pink points of Fig. 3.5 show these interactions which were also used to benchmark the Ramsey spectroscopy (Sec. 3.8 and Fig. 6.3c-d).

It is important to mention that this method assumes an isotropic potential. As described in Sec. 2.5.1 the van der Waals potential depends on the angle θ between the aligned dipoles and the separation vector \mathbf{R} . This affects the particular pair-state potentials and overlaps as well and it is possible to take the angle θ into account for the calculations. In principle, it is possible to carry out an exact calculation taking this effect into account. However, for the parameters of Fig. 3.6 we only expect the standard deviation of the angle to be $\sigma(\theta) = \sqrt{\langle \theta^2 \rangle} \approx 5.7^{\circ}$ since $\langle \theta \rangle = 0$. This should be a small enough angle that averaging using the pair potentials for $\theta = 0$ is a reasonable approximation.

3.3.3 Interaction potential between atoms in different ground-states

The considerations previously mentioned are useful in general when dressing a system consisting of atoms only in one ground-state. However, certain protocols such as Ramsey interferometry discussed in Sec. 3.8 require us to start in a superposition state of two different hyperfine states. Particularly in the case of Lithium, this presents an issue in the form of the hyperfine splitting $\Delta_0 \sim 2\pi \times 76 \,\mathrm{MHz}$ (Fig. 3.1a) being of the same order as the dressing detuning Δ . Therefore, unlike the previous Rydberg dressing experiments with ⁸⁷Rb of Ref. [75], we will need to take into account the interaction potential between atoms in two different hyperfine ground-states.

To obtain the dressed potential between two atoms in different ground-states we will follow a similar process to the one described in Sec. 2.8. First, we start by writing down the single-particle Hamiltonians for each atom in the $\{|i\rangle, |r\rangle\}$ basis similar to

Eq. 2.20 where $i \in \{1, 2\}$ labels each ground-state:

$$\hat{H}_1 = \begin{pmatrix} 0 & \Omega/2 \\ \Omega/2 & -\Delta \end{pmatrix} \quad \text{and} \quad \hat{H}_2 = \begin{pmatrix} 0 & \Omega/2 \\ \Omega/2 & -(\Delta + \Delta_0) \end{pmatrix}$$
(3.4)

Using these and the van der Waals potential $V(R) = -C_6/R^6$, we write down the two-particle dressing Hamiltonian as

$$\hat{H}_{dr}(R) = \hat{H}_1 \otimes \hat{\mathbb{I}} + \hat{\mathbb{I}} \otimes \hat{H}_2 + V(R)(|r\rangle \langle r| \otimes |r\rangle \langle r|). \tag{3.5}$$

Here we are assuming that even though each hyperfine ground-state will connect to a Rydberg state with different m_I , these Rydberg states are not resolved and thus interact as if they were the same $|r\rangle$.

We calculate the dressed potential by solving for the eigenenergy of the eigenstate with maximum overlap with the bare ground-state $|1\rangle \otimes |2\rangle$. This can be done numerically, or using perturbation theory up to 4th order in Ω assuming $\Omega \ll \Delta$. In this limit, we find that the relevant eigenenergy has the form

$$E_{\left|\tilde{1},\tilde{2}\right\rangle}(R) = -\frac{\Omega^4(2\Delta + \Delta_0)}{16\Delta^2(\Delta + \Delta_0)^2} \left(\frac{1}{1 + \frac{(2\Delta + \Delta_0)R^6}{|C_6|}}\right) + \delta_{AC}(\Omega, \Delta) + \delta_{AC}(\Omega, \Delta + \Delta_0), \tag{3.6}$$

where δ_{AC} are the expected single-particle light-shifts (Eq. 2.31) and the first term is the desired interaction potential which has some corrections that depend on Δ_0 compared to Eq. 2.32.

Variation of Rabi couplings

Similarly, we can consider the case of the Rydberg dressed potential between two atoms which experience the same detuning Δ but different Rabi couplings Ω_1 and

 Ω_2 . This is realistic in our experiment since the laser used is tightly focused at the atoms as shown in Fig. 6.3b leading to a varying Rabi coupling over the atomic cloud. However, the effect is not drastic. Taking for example an average Rabi coupling Ω and individual $\Omega_i = \alpha_i \Omega$, where $\alpha_1 + \alpha_2 = 2$, we will find that the Rydberg dressed potential will be affected only in its depth by a factor of $U_0^* = \alpha_1^2 \alpha_2^2 U_0$. The change in Ω does not affect the range of interactions which remains sensitive only to Δ and the C_6 coefficient. This is one of the reasons we have limited our experiments to small systems where the variation of Ω is minimal; therefore allowing us to simplify our thinking of the interaction term and only care about the average Ω within the small system.

3.4 Laser System

For single-photon excitation to the Rydberg state, we use a deep ultraviolet (UV) laser system at 230 nm based on frequency-quadrupling light from a diode laser source which we bought from Laser & Electro-Optic Solutions. A significant amount of time was spent mantaining the laser at high intensity output. Working with UV light is quite complicated and requires special considerations in the design of its optical paths. Unfortunately, nearly every material absorbs light at our wavelength. Typical N-BK7 optics very low transmission and even for uncoated UV-grade fused silica we lose about ~ 10 % per optical element⁷. While it is possible to get better transmittance with specialized AR-coatings, this can get expensive and inflexible quite fast. In our experiment we only used standard uncoated Thorlabs UV-grade fused silica singlet lenses, specially AR-coated 45° Laser-Optik mirrors with > 98.5% reflection, and 0th order half- and quarter-waveplates from Altos Photonics. These considerations were needed in order to maximize the final UV power at the atoms which is very important for Rydberg dressing as shown in Table. 2.5. In this section, we will describe the

⁷About 4% per uncoated surface and some small absorption.

technical aspects of our laser system to do single-photon excitation to $|nP\rangle$ Rydberg states of our atoms.

3.4.1 Ultraviolet Laser

As previously mentioned, we bought a laser system from Laser & Electro-Optic Solutions. The system consists of 3 main components. First, there is a 920 nm MOPA laser consisting of a diode and Tapered Amplifier which outputs $\sim 1.5 \, \mathrm{W}$. This laser has an extra output of $\sim 10 \, \mathrm{mW}$ which is used for frequency stabilization. Second, there is a frequency doubling bow-tie cavity using a KNbO₃ non-linear crystal which when properly tuned outputs $\sim 750 \, \mathrm{mW}$ at $460 \, \mathrm{nm}$. Finally, there is a second frequency doubling bow-tie cavity using an α -BBO crystal which requires a constant flux of oxygen in order to avoid degradation. This second cavity was not as efficient, and when properly aligned we could expect $\gtrapprox 40 \, \mathrm{mW}$ of $230 \, \mathrm{nm}$ UV light⁸.

The UV output of this system is a beam with horizontal linear polarization focused $1.5\,\mathrm{m}$ away to a waist of $\sim 0.6\,\mathrm{mm}$. The beam-shape is not exactly Gaussian, there are ripples in the horizontal direction which are attributed to the walk-ff in the crystal. However, when focused down to the order of tens of μ m it does have an almost perfectly Gaussian profile up to some small side-lobes.

3.4.2 Frequency stabilization

The frequency of the 920 nm laser is stabilized to a Stable Laser Systems ultralow expansion glass (ULE) cavity using a Pound-Drever-Hall scheme. In order to lock the laser at arbitrary frequencies, we use a fiberized Electro-Optic Modulator (EOSpace PM-0S5-10-PFA-900/930) to lock the laser to a tunable sideband dependent on

 $^{^8}$ When the laser was new we could easily achieve up to 75 mW. However, the dressing experiments happened almost 3 years later by which time the crystal had degraded. A lot of careful alignment on the specific point the light passed through the crystal was needed just to get $> 40 \,\mathrm{mW}$

the frequency driving the EOM [104]. A schematic of the experimental setup is shown in Fig. 3.7a.

The ULE cavity is surrounded by a homebuilt temperature controlled heat shield inside of a vacuum chamber to ensure its stability and reliability as a reference. The temperature is stabilized to $\sim 30\,^{\circ}\text{C}$ with a very slow PI servo with time constant of about 3 hr. Fig. 3.7b shows oscilloscope data of the transmission lines of the ULE cavity. The measured free spectral range (FSR) is 1497.15(1) MHz. We also looked at the transmission profile of a single line and measured a linewidth of 372(1) kHz (Fig. 3.7c). Assuming that the measured linewidth is not limited by the laser itself, we conclude that the finesse of our ULE cavity is ~ 4000 . This is important, because the final linewidth of the 230 nm light will be four times that of the stabilized 920 nm laser due to the frequency-quadrupling.

3.4.3 Intensity stabilization

Particularly for Rydberg dressing, it is important to have a very stable intensity. The fractional power stability of the UV light after the second cavity is about 10% which was sufficient for experiments realizing an Ising model through resonant coupling to a Rydberg state (Ch. 4). However, in the case of dressing, power stability is more critical due to the interaction strength having a quartic dependence on the Rabi frequency ($U_0 \propto \Omega^4$). Furthermore, the stability of the power during spin-echo Ramsey interferometry protocols (Sec. 3.8) is important to cancel the phases accumulated due to the single-particle light shift. We manage to improve the fractional power stability to much better than 1% by adding a noise-eater.

The noise-eater consists of an electro-optic polarization modulator or Pockels cell (QuBig PCx2B-UV), an α -BBO Glan-Taylor polarizer (EKSMA 441-2108), and two custom UV waveplates. We drive the Pockels cell using a $\pm 200\,\mathrm{V}$ high-voltage amplifier (Thorlabs HVA200) and a NewFocus PI servo controller. The Pockels cell

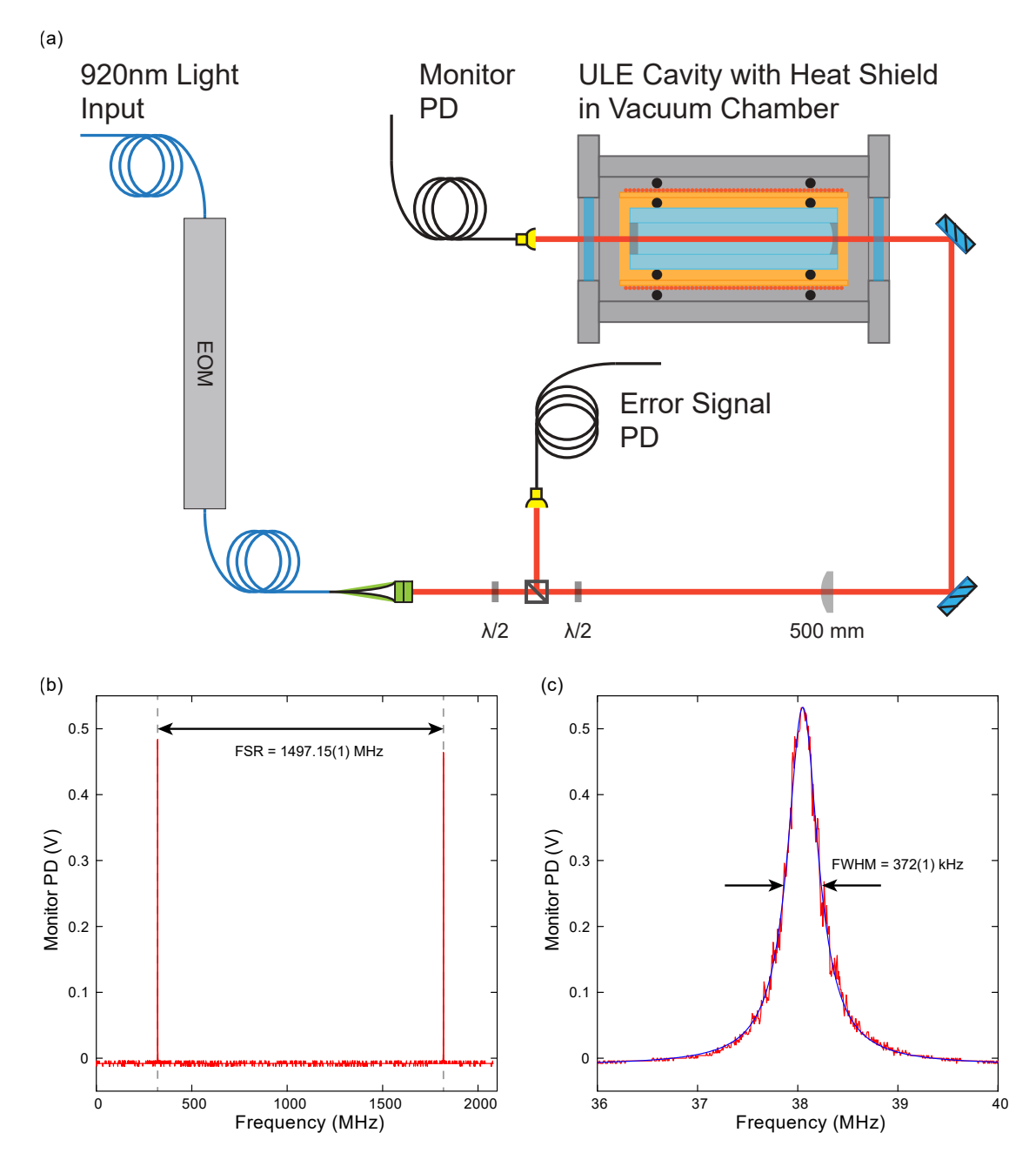


Figure 3.7: Frequency stabilization of Laser system and characterization of optical cavity. (a) Experimental setup schematic of the Pound-Drever-Hall setup for locking of laser to ULE cavity. (b) Transmission peaks of ULE cavity under a sweep. The measured free spectral range (FSR) is of 1497.15(1) MHz. (c) Zoom into one of the transmission peaks of the ULE cavity. The measured linewidth is 372(1) kHz.

essentially acts as a voltage-tuned variable waveplate. Together with the waveplates and the polarizer, we can tune the system to get stable laser light with an efficiency of $\sim 60\%$. The polarization output of the polarizer was aligned to be vertical. By measuring the laser power using a pick-off and feeding back on the noise-eater, we suppressed intensity noise for frequencies up to 1 MHz and eliminated shot-to-shot drifts in the UV light intensity. The electronics had to be kept as close as possible to the setup due to concerns about the high-voltages and to obtain fast servo response. This upgrade to the system was required to be able to get the results described in Ch. 6. Fig. 3.8b shows this noise-eater as part of the general laser system for Rydberg dressing.

3.4.4 Optical setup

There have been two general iterations of the optical setup one for each of the experiments described in Ch. 4 and Ch. 6. Common to both of them is the use of a specially AR coated UV-grade fused silica acousto-optic modulator (IntraAction ASM-1501LA61). This AOM works using an acoustic "shear" mode and provides an efficiency of $\sim 85\%$ on the first order. It has a center frequency of 150 MHz and a ± 25 MHz tuning range. We drive it using a fast voltage-controlled oscillator (MiniCircuits ZX95-200A+). The main laser system and the AOM sit in the main experiment laser table and using a periscope we bring it up to the vacuum chamber level. We use a final lens with 500 mm focal length to focus the beam at the atoms in the center of the table. One important limitation of our current setup is that the machine was not designed with single-photon Rydberg excitations in mind. Therefore, it was unknown to us whether the UV would make it through the UV-grade fused silica coated windows or if it would make a hole in the coating. We observe a total reflection of $\sim 30\%$ from the first window and a transmission of $\sim 50\%$ from the second window leading us to estimate an efficiency of $\sim 70\%$ of the incoming UV light at the atoms.

The reflections are quite strong and careful consideration of the input angles had to be taken into account to avoid spurious reflections at the atoms⁹. The UV beam is aligned close to the light-sheet potential optics and is aligned parallel to the y axis of our optical lattice.

2D Ising setup

To obtain fast amplitude and frequency control of the UV light, we placed the AOM at the focus of a telescope and imaged it onto the atoms. This way, we were able to freely tune the frequency driving the AOM with the 1st order while keeping it aligned to the atoms. With this setup, we are able to modulate both the Rabi coupling and detuning of the laser by adjusting the amplitude and frequency at which we drive the AOM. Fig. 3.8a shows a schematic of this setup. Tightly focusing the light to a waist $\sim 40\,\mu m$ at the AOM also has the effect of reducing the efficiency of the AOM to $\sim 55\%$.

The 150 MHz frequency of the AOM has to be taken into account as an offset to the cavity sideband values measured with spectroscopy. A mirror after the last focusing lens was used to fine align the UV beam at the position of the atoms inside of the vacuum chamber. The expected beam waist of the UV beam at the atoms due to the telescope setup is $\approx 31 \,\mu m$.

3.4.5 Rydberg dressing setup

For dressing, we did not need the fast modulation of the frequency. We cared mostly about a stable and powerful source. We achieved this by adding the noise-eater to the setup and modifying the telescope so that the beam was focused to a waist of $\sim 16\,\mu\mathrm{m}$ at the atoms. We attempted even more aggressive telescopes but the extra difficulty in alignment outweighed the gain in Ω . The AOM here was used mostly

⁹At some point we lost a week because we aligned a reflection rather than the main beam.

as a very fast switch to generate pulses of a precise width necessary for the correct characterization of the dressed potential. Fig. 3.8b shows a schematic of this setup.

3.5 Spectroscopy of ⁶Li Rydberg states

Once the laser is set up and the optics are roughly aligned, the next important step is to align the laser to the particular wavelength necessary to couple to specific $|nP\rangle$ Rydberg states. This was not a necessarily simple question as the NIST Atomic Spectra Database [105] only lists the transition wavelengths up to $|32P\rangle$. It is possible however to calculate the expected transition wavelength using the binding energy (Eq. 2.1) and the ionization energy as explained in App. D.

In Table. D.1 we summarize the transitions that were found as part of this thesis. We find that the calculated expected values can be trusted up to the resolution that the ULE cavity resonances provides. In this section, we will explain the spectroscopy setup and procedures used to identify these transition wavelengths.

3.5.1 "V-scheme" spectroscopy

For initial identification of the Rydberg lines, we performed a "V-scheme" spectroscopy [106] with the 230 nm beam and a diode laser driving the D_2 transition of lithium at 671 nm on an external spectroscopy cell with a hot ⁶Li vapor¹⁰. The basic principle of this scheme is to "shelve" some of the ⁶Li atoms in the Rydberg state using the 230 nm laser beam and thus affect the absorption spectra of a counterpropagating 671 nm laser. The effect is very small, therefore, needed to use a balanced photo-diode and compare the difference of the signals of two beams: one with counterpropagating UV light and one without it. To find a reference of the transition there

¹⁰We needed to use a large current DC power supply to heat up the spectroscopy cell. We found that usual AC power supplies lead to strong magnetic field effects were the line "shakes" decreasing the signal-to-noise of the measurement.

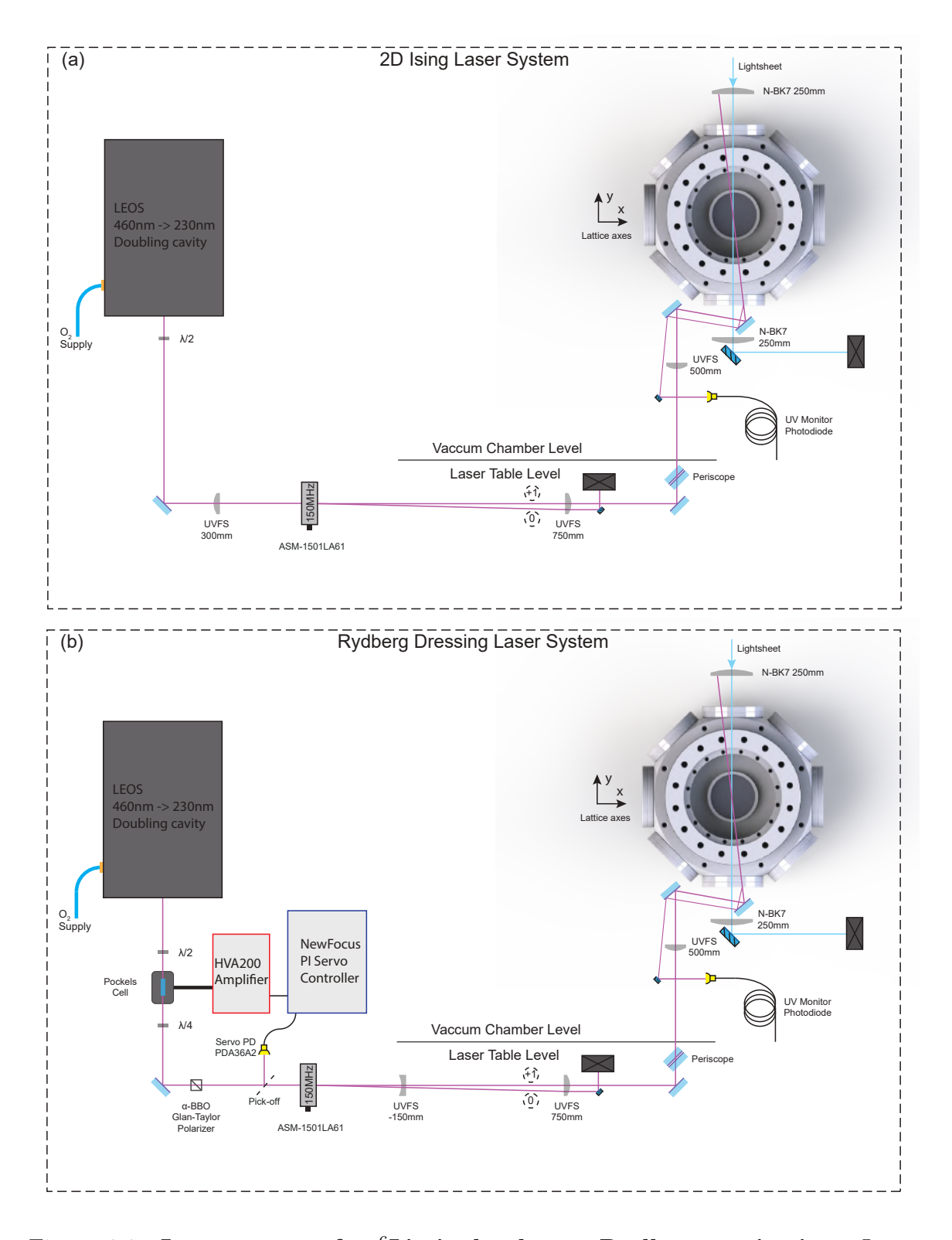


Figure 3.8: Laser system for 6 Li single-photon Rydberg excitation. Laser system for experiments where 6 Li ground-state atoms are directly coupled to a $|nP\rangle$ Rydberg state. (a) Version for experiments realizing a 2D transverse Ising spin model (Ch. 4). (b) Version for experiments with long-range interacting itinerant systems via Rydberg dressing (Ch. 6).

was the possibility of measuring a simple Doppler-Free Spectroscopy (DFS) spectra by unblocking or unblocking a beam. Fig. 3.9a shows a schematic of the experimental setup for this mixed "V-scheme" and DFS setup. The UV light is sent directly from the experiment table to the laser table using a flip mirror before the optics of Fig. 3.8.

For Doppler-Free Spectroscopy of the ⁶Li D_2 line, we expect to see two depletions due to the hyperfine ground-states and a crossover peak. The distance between the depletions should be equal to 228 MHz (Fig. 3.9b). When performing the "V-scheme" spectroscopy we only expect to see two depletions corresponding to the hyperfine ground-state transitions. However, the distance between these is $(228\,\mathrm{MHz})\left(1+\frac{230\,\mathrm{nm}}{671\,\mathrm{nm}}\right)\approx307\,\mathrm{MHz}$; this is due to the relative difference in Doppler shift for each wavelength. Fig. 3.9c shows the spectra for both DFS and "V-scheme" spectroscopy for $|23P\rangle$, identifying the important transitions.

This method allowed us to find the transition wavelengths up to $|40P\rangle^{11}$ and is good up to the order of MHz for the sideband frequency referenced to the ULE cavity. More precise schemes are needed to find the line using cold atoms.

3.5.2 MOT spectroscopy

After finding the position of the line, we perform what we call "MOT spectroscopy". The first step towards a degenerate quantum gas in our experiment is loading atoms from a Zeeman slower into a Magneto-Optical Trap (MOT) [92]. For experiments with UV light, we found that we could use resonant light to deplete our MOT by blowing away atoms resonantly excited to a $|nP\rangle$ Rydberg state. With this method, we are able to find the correct transition to a precision of approximately 400 kHz. This was used to find the $|44P\rangle$ Rydberg state which we could not find using the "V-scheme" spectroscopy. Both MOT and V-scheme spectroscopy find the Rydberg lines at zero field. In general, we observed that when coupling with atoms at a high

 $^{^{11}}$ Since the dipole matrix element scales inversely with principal quantum number (Table. 2.1), higher n values have signals which are below the noise level of the spectroscopy scheme.

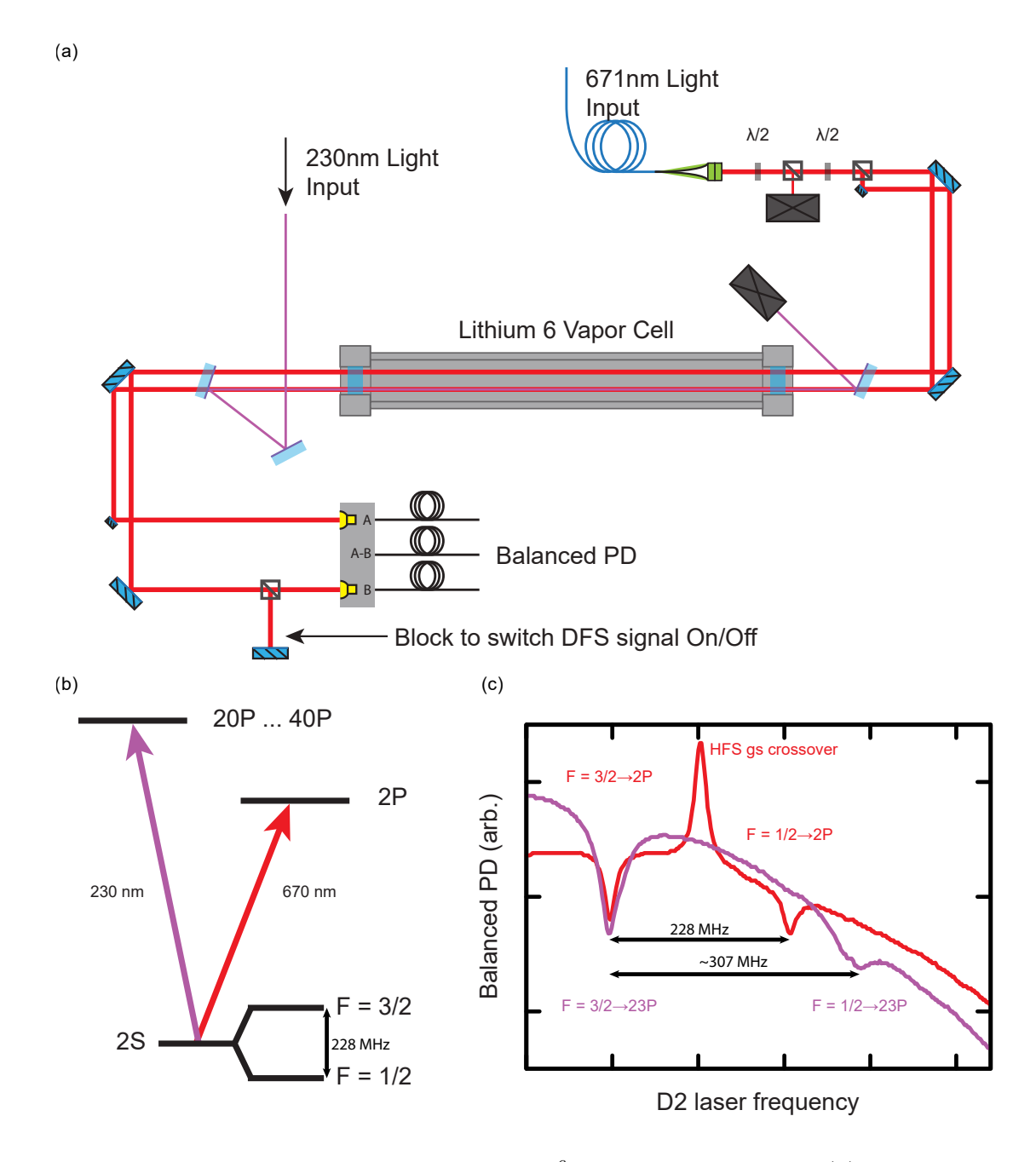


Figure 3.9: "V-scheme" spectroscopy of ⁶Li Rydberg states. (a) Experimental setup schematic of the spectroscopy. (b) Energy Level diagram with the pertinent states and lasers for the "V-scheme" spectroscopy. (c) Measured profiles of Doppler-Free Spectroscopy signal (red) and "V-scheme" spectroscopy signal (violet) for $|23P\rangle$.

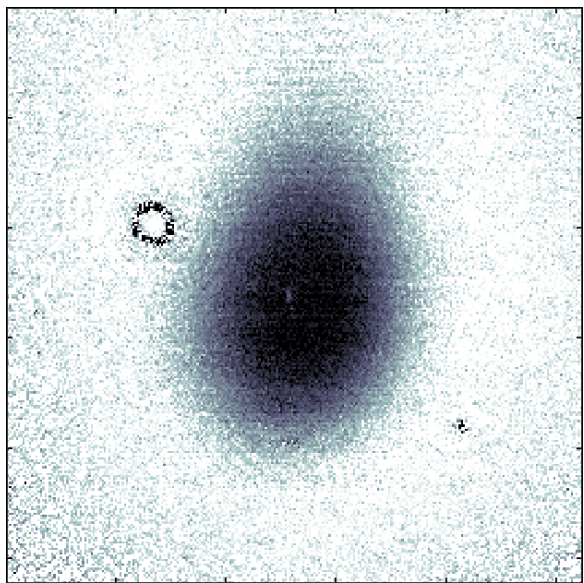


Figure 3.10: Precision MOT loss spectroscopy for alignment. We blow atoms out of a MOT right before imaging over a short pulse after loading. This allows us to precisely align the UV beam very close to the position of the atoms. The MOT is much larger ($\sim 1\,\mathrm{cm}$) than the optical potentials ($\sim 100\,\mathrm{\mu m}$) providing a much larger target for pre-alignment. In this figure, the UV beam position corresponds to the small depletion close to the center of the MOT. The axes are rotated by -90° with respect to the experimental x-z plane.

magnetic field in the optical potentials we had to tune the sideband frequencies up by approximately $12\,\mathrm{MHz}$ corresponding to approximately $48\,\mathrm{MHz}$ for the $230\,\mathrm{nm}$ quadrupled photons.

Additionally, by changing the length of the pulse and taking advantage of an imaging system parallel to the UV laser beam we are able to very precisely prealign the beam to the position of the atoms in the final trap. A sample image of an aligned UV beam is shown in Fig. 3.10. Since the MOT is much larger than the optical potentials it provides a perfect target for precise pre-alignment of tight UV beam which can have a waist as small as 16 µm. We can also coarsely tune the focus position of the last lens in Fig. 3.8 by paying attention at the size of the hole made by the UV beam on the MOT.

Precise alignment procedure

After pre-aligning the beam using the MOT loss spectroscopy (Fig. 3.10) we fine align the beam in two different ways. The first method is to keep doing resonant blowing of increasingly smaller pulses and intensities using ND filters. We could repeat this at the different stages of the experimental sequence [92]. Finally aligning to the atoms in a 2D optical lattice potential. This procedure worked well enough for the 2D Ising experiments (Ch. 4) which had a large waist of approximately 32 μm.

However, since the Rayleigh range depends quadratically on the waist, once we shrunk our beam for the Rydberg dressing experiments aligning using loss became much more difficult ($w = 16 \,\mu\text{m}$ and $z_R = 3.5 \,\text{mm}$). We figured out that by doing Ramsey interferometry (Sec. 3.8) we could very clearly observe spatial differences on the single-particle light-shift. Fig. 6.3b(ii) shows for example how the cloud forms "ripples" corresponding to the tight waist of the UV beam along the perpendicular direction. We used this clear visual pattern to align the beam exactly to the center of our cloud with very high precision. This method is so effective that it also allowed us to precisely tune the direction of incidence of the UV beam with a lattice direction to within 1° precision. We could also fine tune the focus of the beam to the cloud by seeing the Rayleigh range effect on the direction parallel to the beam until it was as flat as shown in Fig. 6.3b.

3.6 Laser characterization with direct excitation

While the measurements of the "V-scheme" and "MOT" spectroscopy let us find the Rydberg transitions to a precision of a $< 1\,\mathrm{MHz}$, for the experiment we need much more precise calibration of the resonances. This will help us know the detuning Δ of the laser from the transition. Unlike in the spectroscopy cell, in our experiment, the ⁶Li atoms are cold, trapped in an optical potential, and at a magnetic field of 595 G perpendicular to our 2D lattice. These will lead to Zeeman (Eq. 3.1 and single-particle light-shifts (δ_{AC}) of the transition which would move the resonance by a few MHz. Furthermore, the experimental protocols require the precise knowledge to of the Rabi coupling Ω of the laser from the ground-state atoms to the Rydberg state.

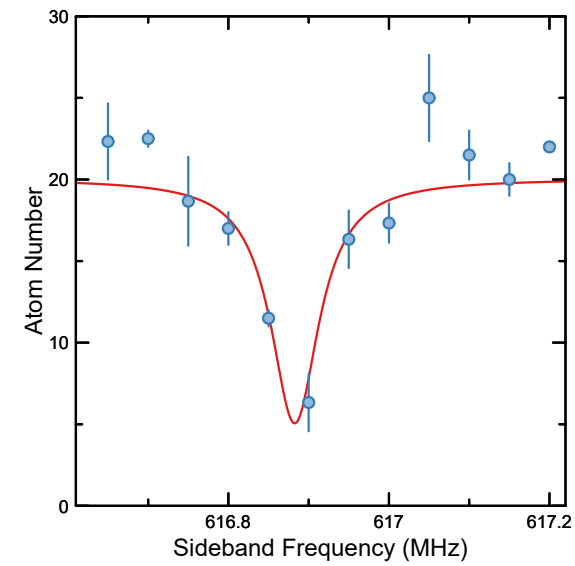


Figure 3.11: Rydberg spectroscopy by blowing cold atoms at resonance. We perform spectroscopy of the $|2S\rangle \rightarrow |nP\rangle$ Rydberg state transitions of ⁶Li by resonantly blowing cold atoms in the optical lattice. Choosing the length and strength of the UV pulse we can minimize Fourier and Power broadening effects. Also by blowing on a "sparse" system we achieve roughly "single-atom" measurements. This particular scan was of the $|1\rangle \rightarrow |31P\rangle$ transition in a shallow lattice of \sim 6.2 E_R depth corresponding to the first point of Fig. 3.12.

First, we found the resonance by blowing away atoms with UV pulses that were much longer than the lifetime of the Rydberg state which is on the order of tens of µs. Here we look at the loss of atoms when the laser is tuned resonantly to the transition between the ground-state and the Rydberg state. By decreasing the UV power with ND filters and using long blowing pulses (ms) we were able to decrease the power and Fourier broadening of the peak. By varying the density of the cloud on which we perform this blowing spectroscopy, we can observe broadening due to interactions between neighboring Rydberg atoms or direct excitation of pair-states. To avoid such broadening, we mostly characterized our laser in the very sparse regime where atoms were on average many lattice sites apart from each other. This allows us to treat the measurements as averaging multiple "single-atoms" at a time. Fig. 3.11 shows a sample scan for the $|31P\rangle$ transition at \sim 592 G and low lattice depth and sparse loading. We are able to experimentally measure a combined laser/Rydberg linewidth of \sim 100 kHz.

Using this very simple technique we performed a lot of characterization about the behavior of the resonance of $^6\text{Li} |nP\rangle$ Rydberg states with various parameters of our experiment. By tuning the cavity sideband frequency using a GPIB controlled function generator (HP 8648A) we were able to take many different scans of resonant blowing ground state atoms while maintaining the laser locked. It is important to repeat that due to the quadrupling nature of our laser, all differential frequencies on the sidebands correspond to a quarter of the real energy differences on the UV photons ($\hbar\Delta\nu = \Delta E/4$).

3.6.1 Resonance vs. lattice depth

A very strong concern we had before starting this experiment was what effect would an optical lattice generated using 1064 nm light would have on the Rydberg lines. To first order, we knew that the polarizabilities of the ground-state and $|nP\rangle$ Rydberg states had opposite sign. This means that the Rydberg atoms would be anti-trapped by the optical lattice in the position where the ground states are trapped. Furthermore, in Fig. 2.1 we show that the Rydberg atom electronic wavefunction has a radius $\langle \hat{r} \rangle \sim 50 \, \mathrm{nm}$ from the core. For these distances, the optical lattice already has $\sim 5 \, \%$ variation in its power and can couple directly to the valence electron leading to higher order corrections to the model potential of Eq. 2.4. Additionally, the ground-state atoms have a wavefunction spread of $\sim 100 \, \mathrm{nm}$ (Sec. 3.3.2). All of these considerations would make for an increasingly difficult calculation with possibly non-trivial behaviors. Instead, we opted to experimentally study the effects of the lattice depth (power) on the resonance. Fig. 3.12 shows a summary of this study done for the $|1\rangle \rightarrow |31P\rangle$ transition in sparse systems.

What we find is that the dependence of the Rydberg state transition is roughly linear with lattice depth. The slope of this linear dependence (Fig. 3.12a) is $\Delta \nu / \Delta V_{latt} = 10.0(7) \, \text{kHz}/E_R$. If we take into account the quadrupling of the light and the known $E_R = h14.66 \, \text{kHz}$ we get a dependence $\Delta E_{|31P\rangle}/\Delta V_{latt} = 2.7(2)$. Furthermore, we observe a clear effect on the measured HWHM of the lorentzian fits (Fig. 3.12b). The effect seems to be that lattice depth broadens the transition meaning that low lattice

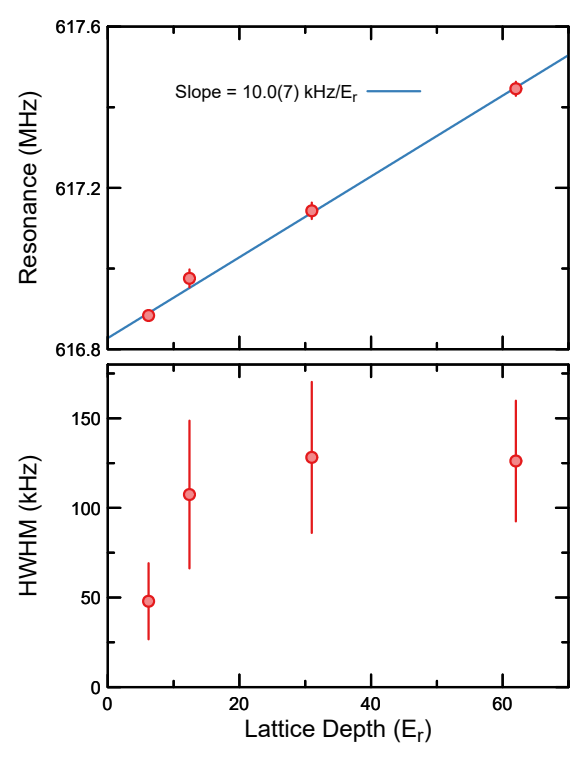


Figure 3.12: Effect of lattice depth on the Rydberg transition. We study the dependence of the $|1\rangle \rightarrow |31P\rangle$ transition with lattice depth for sparse systems. We find a linear behavior with slope $\Delta \nu / \Delta V_{latt} = 10.0(7) \, \text{kHz}/E_R$. This corresponds to a $\Delta E_{|32P\rangle}/\Delta V_{latt} = 2.7(2)$ dependence of the transition resonance with lattice depth. The fitted HWHM of the lorentzian also shows a behavior with lattice depth where the depth effectively broadens the line. The first point in both plots corresponds to the fit shown in Fig. 3.11.

depths are possibly best. This is good for Rydberg dressing experiments with itinerant systems which require low lattice depths with strong tunneling. We repeated less careful studies for other $|nP\rangle$ states finding the same slope within errorbars and the same qualitative behavior of the HWHM.

3.6.2 Resonance vs. magnetic field

A second important consideration is the effect of strong magnetic fields on the transition. From Sec. 3.1.1 we know that most states disperse linearly according to Eq. 3.1. Furthermore, in our particular scheme using linear polarization, we know that the $|1-3\rangle$ ground states move with the same slope as the $|2^*\rangle$ Rydberg state (Fig. 3.1). However, just like with lattice depth there are higher order corrections to this simple picture. $|1\rangle$ is not a pure state and from the Breit-Rabi formula we expect ~ 5 MHz non-linearity between 300 – 600G. Furthermore, the magnetic field can have a non-trivial effect on the polarizabilities as $\alpha^0 \propto (E_{n'S,n'D} - E_{nP})^{-1}$. From various mea-

surements, we observe that the magnetic field has a roughly linear effect on the $|2S\rangle \rightarrow |nP\rangle$ transition with slope $\Delta\nu/\Delta B \sim 0.03\,\mathrm{MHz/G}$ with no strong difference on the particular hyperfine ground-state used.

Given how important it was to know Δ in our experiments, we would perform a resonance scan every morning or whenever we changed any parameters in order to be able to keep Δ constant throughout. We found that all lines were stable during any given day and in general we observed no day-to-day drifts unless the experiment temperature changed drastically. Even then, the line would not move by more than 1 MHz. Even with all the complicated effects that these parameters can have on the Rydberg landscape, we always observed roughly the expected behavior from calculations that only take into account a magnetic field for purposes of Rydberg dressing.

3.6.3 Magnetic dispersion of $|nP\rangle$ Rydberg states

As a sanity check, we decided to directly measure the magnetic dispersion of Eq. 3.1. To do this, we used a waveplate to change the polarization of the UV light such that it had a strong σ^- component at the atoms. This allowed us to measure the cavity sideband frequencies ν for both the $|1\rangle \rightarrow |2^*\rangle$ and $|1\rangle \rightarrow |1^*\rangle$ transitions of the $|31P\rangle$ Rydberg state at three different magnetic fields. Fig. 3.13 shows the extracted energy differences between the measured resonances with a linear fit. We extract a slope $\Delta E/h\Delta B = 1.30(3)$ MHz/G which is very close to the expected Bohr magneton $\mu_B/h = 1.4$ MHz/G. It is unclear why the slope is not exactly what we expect. However as explained in the previous subsections, it is possible that the magnetic field affects the single-particle light-shift felt by the Rydberg states in the optical potential. Anyways, the measured slope is close enough to conclude that we roughly have a good understanding of the Rydberg landscape in our experiment. This particular measurement was not repeated at different principal quantum numbers but

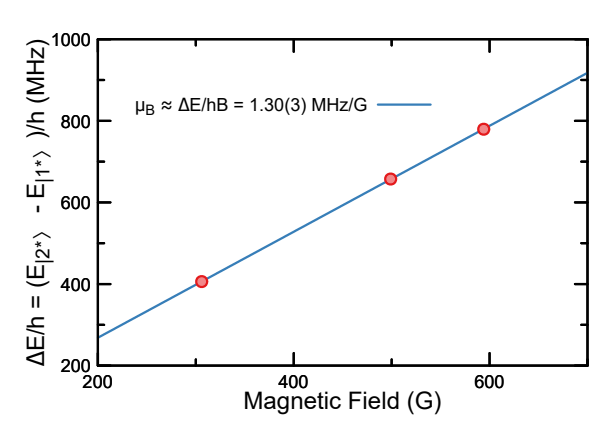


Figure 3.13: Magnetic dispersion of $|31P\rangle$ Rydberg states. Energy difference measured between the $|1\rangle \rightarrow |2^*\rangle$ and $|1\rangle \rightarrow |1^*\rangle$ transitions of the $|31P\rangle$ Rydberg state. We fit a line with slope $\Delta E/h\Delta B = 1.30(3)\,\mathrm{MHz/G}$ close to the expected Bohr magneton μ_B .

we did not have any indication that it should have a strong effect given that we observe the same effect of the field on the $|2S\rangle \to |2^*\rangle$ transitions for different n.

3.6.4 Observation of anomalous "sharp" peaks near resonance

For particular transitions and fields, we observed anomalous resonances that we were not able to match to any particular transition. These resonances where often very strong and "sharp" leading to full loss of the system and often accompanied of side-bands which we attribute to recoil from the lattice. Two-photon transitions do not make sense unless we are fully ionizing the ⁶Li atoms. Other options for explanations of these are that they are "forbidden" transitions. In any case, we avoided using schemes where a resonance was observed in order to avoid non-trivial behaviors. For example, Fig. 3.14 shows one of these resonances for the $|3\rangle \rightarrow |23P\rangle$ transition at ~595 G. In this particular instance, we decided to change to using the $|1\rangle$ hyperfine ground-state which did not show any anomalous behavior and used that scheme to realize a 2D transverse Ising system (Ch. 6). In that first experiment, we did not explore the effect of low lattice depths (Sec. 3.6.1), as such all observed lines were broadened (Fig. 3.12). Therefore, initially we extracted the $\Gamma \leq 100\,\mathrm{kHz}$ laser linewidth from these anomalous resonances (Fig. 3.14). We allowed ourselves to do this since any optical transition has to be limited by the laser linewidth.

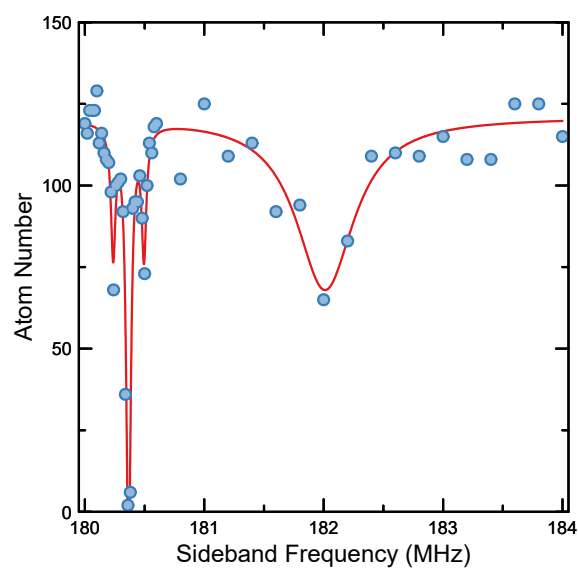


Figure 3.14: Observed anomalous resonance observed during spectroscopy scans. We observe anomalous resonances in the $|3\rangle \rightarrow |23P\rangle$ transition at $\sim 595\,\mathrm{G}$. The resonance has clear symmetric sidebands which are roughly in the order of the expected lattice recoil. The linewidth of this line gives us a $\Gamma \leq 100\,\mathrm{kHz}$ upper bound on the laser linewidth.

3.6.5 Direct measurement of Rabi frequency

Once the Rydberg resonance position was identified by blowing away the atoms, we now performed very short UV pulses with variable length to directly measure the Rabi frequency Ω of the transition. Unlike the blowing experiment were atoms are simply "pushed" out of the trap in a very long pulse, here we are coherently exciting the atoms to the Rydberg state. At the end of the pulse, the atoms have certain probabilities of being in the excited (Rydberg) state or the ground-state. We image only the ground-state distribution after removing the Rydberg atoms by rapidly increasing the lattice depth to a value suited for fluorescence imaging, leading to rapid photo-ionization or expulsion of the anti-trapped Rydberg atoms. We measure the efficiency to remove Rydberg atoms to be 90(3)%. Fig. 3.15a shows experimental results of a Rabi oscillation for $|23P\rangle$; we attribute the decay of oscillations to the intensity stability ($\approx 10\%$) of the laser rather than to short T_1 decoherence time which should be comparable to the Rydberg state lifetime of $\approx 20\,\mu s$. The maximum Rabi frequency of the $|23P\rangle$ transition we could get with the original laser setup (Fig. 3.8a) was $\Omega_{max} = h \times 5.4(1)$ MHz.

As we know that the UV beam is not homogeneous at the atoms but rather it has a Gaussian profile, it is important to measure how much of a variation it has over the region of interest of our experiments. Taking advantage of the single-site resolution of our Fermion microscope, we can measure the small variations of the Rabi frequency at different points of the cloud over one of the lattice axes. In this way, we were able to experimentally measure the beam waist at the atoms and the spatial variation of Ω over the region of interest to be 35 µm (Fig. 3.15b).

This method of calculating Ω was useful for the initial Ising experiments (Ch. 4). However, for Rydberg dressing we wanted to be much more precise and developed an indirect way of measuring Ω using Ramsey interferometry which is explained in detail in Sec. 3.8.

Probing coherence

Since we can directly observe the Rabi oscillations of the resonant $|g\rangle \rightarrow |r\rangle$ system, we can probe the coherence of the system by doing a spin-echo Ramsey sequence of UV pulses. The pulse sequence is $\pi/2 - \tau - \pi - \tau - \pi/2$ pulse where τ is a delay time in between UV light pulses which put the initially ground-state atoms into a superposition with the Rydberg state. The ground-state fraction is measured at the end of the sequence (Fig. 3.15c). In the case of a perfectly coherent system, the pulse sequence always reduces to a 2π pulse and all atoms should return to their ground-state. However, even for $\tau=0$, the measured ground-state fraction is reduced to ~ 0.8 which we attribute to shot-to-shot laser intensity fluctuations. This reduced fraction is maintained for delay times of up to $2\tau=1\,\mu s$ with no obvious decay trend indicating that there is no loss of the quantum state coherence over the pulse lengths studied in the experiments of Ch. 4.

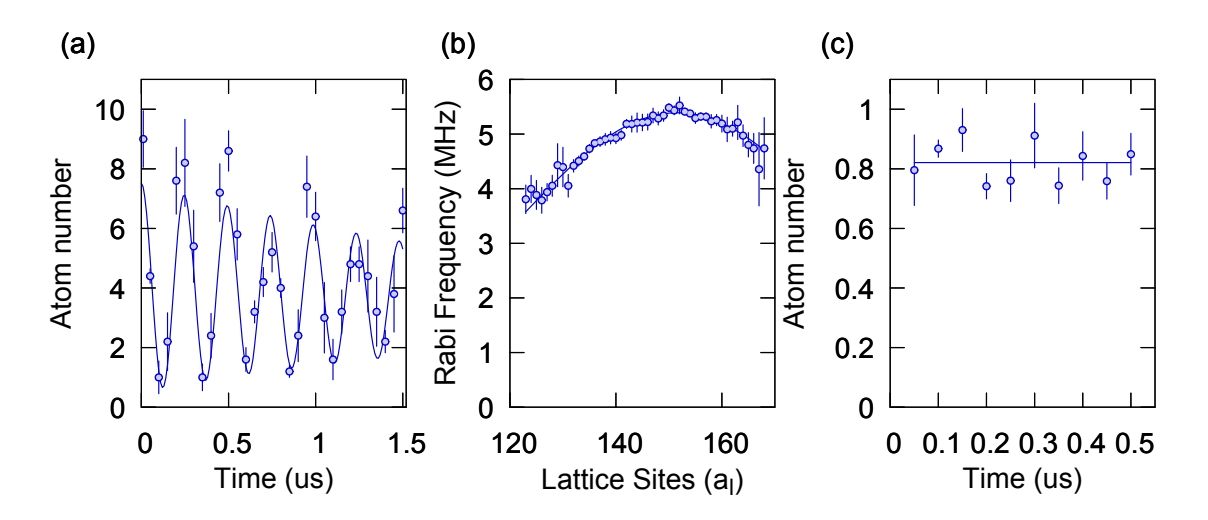


Figure 3.15: Rabi frequency and coherence measurements for the resonant $|2S\rangle \rightarrow |23P\rangle$ transition. (a) "Single atom" Rabi Oscillation of a sparse cloud. (b) Rabi Frequency Gaussian profile over the atoms. (c) Measurement of the ground-state fraction after a spin-echo pulse sequence, indicating no loss of coherence over $\leq 1 \,\mu s$.

3.7 Lifetime characterization of Rydberg dressed atoms

In Sec. 2.8 we explained how by off-resonantly coupling ground-state atoms with a Rydberg state we can put them in a superposition state where they have a very small admixture $\beta = \frac{\Omega}{2\Delta}$ of the Rydberg state. This technique applied to ⁶Li leads to the possibility of engineering long-range itinerant systems such as the one studied in Ch. 6. In our experiment, we are able to study condensed matter systems where the motional timescales are $\tau_{tunn} < 1 \text{ ms } (t \geq 2\pi \times 1 \text{ kHz})$ thanks to the light mass of ⁶Li. For the accessible Rydberg states using our UV laser, the bare Rydberg lifetimes are of the order of tens of µs (Fig. 2.2a). Given the power of our laser and choosing an appropriate detuning Δ from resonance we would theoretically expect Rydberg dressed lifetimes $\tau_{dr} = \beta^{-2}\tau$ much larger than the tunneling time τ_{tunn} .

However, in practice this is not the case. Previous realizations of Rydberg dressing using Rb and Cs atoms described in Refs. [71–75] have reported much shorter

lifetimes than expected from the simple picture of Sec. 2.8. The main understanding of what is limiting these experiments is the so-called "black-body avalanche" effect. This is a global loss mechanism where a single dressed atom decays into a nearby Rydberg state via the exchange of a photon with the black-body radiation surrounding the system. The formed impurity is fully collapsed into a Rydberg state leading to resonant pair-state excitations at a facilitation radius $|C_3/\Delta|^{1/3}$ under the UV laser light-field broadening the line and destroying the system. Recently, experiments using Rb in optical tweezers have been able to directly study this loss mechanism finding good agreement with this resonant facilitation radius picture [107].

In our experiment using 6 Li we have not observed exactly the same effect. The observed lifetimes are lower than expected from the simple dressing picture. But the scaling of the avalanche loss mechanism has a characteristic scaling with atom number ($\tau_{eff} \propto N^{-1}$ [62]) which we do not observe (Figs. 3.16 and 6.5). One possible explanation for this difference is that given the light mass of 6 Li, the energy gained by the impurity due to a photon recoil or the strong dipole-dipole forces is enough to "kick" it out of the system before the "avalanche" fully onsets. We do not have a clean theoretical framework for the non-trivial decay mechanisms that limit our system. However, in this section we will detail all of the characterization we did to understand the achieved Rydberg dressed lifetimes and to choose suitable parameters were we can realize a strongly-interacting itinerant system (Ch. 6).

3.7.1 Effect of geometry

Early in our characterization, we decided to work with the $|31P\rangle$ Rydberg state. From the expected scalings of Table. 2.4 we expected optimal control of long lived Rydberg dressed atoms with strong nearest-neighbor interactions. Very quickly we realized that similar to previous experiments with Rb and Cs the achieved lifetimes were much shorter than expected and dependent on atom number. Following the

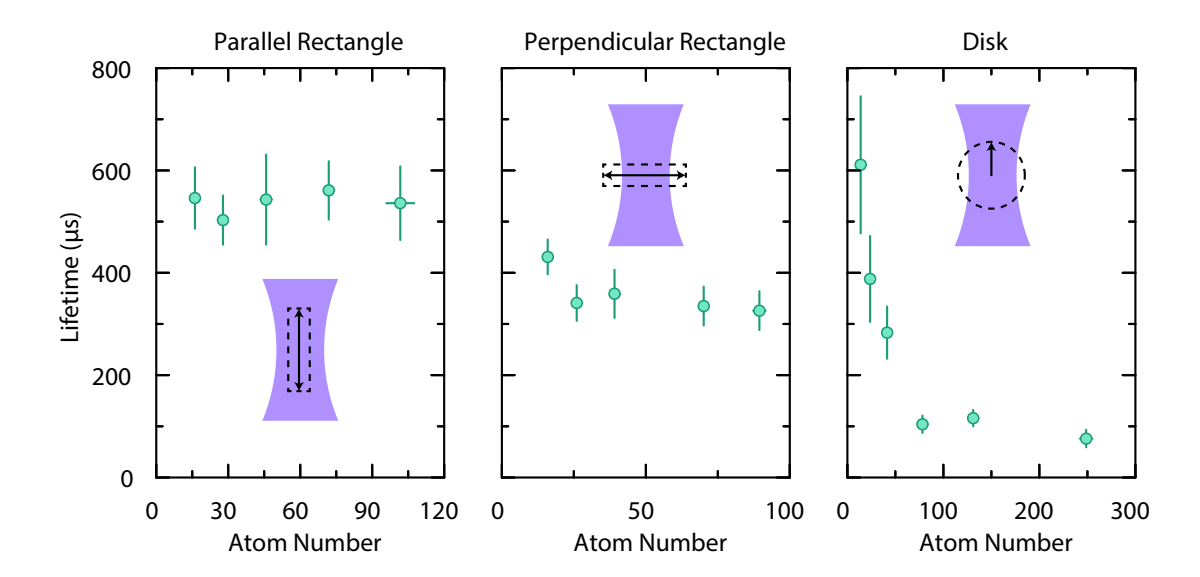


Figure 3.16: Effect of geometry on Rydberg dressed lifetimes. Initial atom number decay of systems coupled to the $|40P\rangle$ Rydberg state. We observe that the geometry of the system has a very strong effect on the achieved lifetimes. Particularly, we observe that increasing the atom number of thin rectangles aligned with the UV dressing beam does not have any effect on the lifetime. Parameters: $\Omega = 2\pi \times 5.6(1) \,\text{MHz}$, $\Delta = 2\pi \times 40 \,\text{MHz}$, and $B = 592(1) \,\text{G}$.

expected scalings, we decided to study couplings to $|40P\rangle$ hoping we would achieve better coherence times. Here we realized something interesting. We could prepare thin rectangular 2D systems along the UV dressing beam and observe no change in the lifetime with varying atom number. The effect was different for other geometries and the measurements are summarized in Fig. 3.16.

A possible explanation is that in ^6Li we are avoiding the facilitation radii even in 2D systems similar to what was achieved on small 1D systems of Rb [90]. The UV dressing laser has a very tight waist and it is conceivable that the differential light-shifts in the perpendicular direction lead to resonances. In the case of the different configuration of Fig. 3.16, light-shift assisted perpendicular resonances appear for the "perpendicular rectangle" geometry and more damaging diagonal resonances can further plague the "disk" geometries. This measurement was repeated for $|31P\rangle$ (Fig. 6.5a) and less thoroughly for $|28P\rangle$ finding that the width of the system could

increase for lower principal quantum numbers without change in the atom number independence effect.

For all following characterization we limit our studies to systems whose width in the direction perpendicular to the UV dressing beam is short enough to keep us in this limit where atom number has no measurable effect on the decay.

3.7.2 Density-dependent lifetimes

When we started studying the lifetime of Rydberg dressed many body systems, we noticed that the observed atom number decay could not be understood by a single exponential model $N(t) = N_0 e^{-t/\tau}$. What we observed was a time-dependent lifetime $\tau(t)$ where the decay rate would "slow-down" as we lost more and more atoms in the system. We came to the understanding that the system had a density-dependent lifetime and studied the decay by fitting single exponential models to "bins" of atoms in a rolling manner. This method allowed us to extract the measured lifetimes as a factor of the density for varying dressing parameters Δ , Ω , and B. Fig. 3.17 shows a sample of this analysis method for a thin rectangular system coupled to the $|31P\rangle$ Rydberg state. Same as the data of Fig. 6.4, we observe that as the system loses more atoms and becomes sparser we recover the expected τ_{dr} of the simple dressing model.

It is important to note that in order to arrive at the conclusion of a density-dependent lifetime we performed many experiments where the size of the system and initial atom number was varied for the same dressing parameters. We observe matching results for all this variations leading to the conclusion that density (not atom number) is the most important factor for our observed decay. This is in sharp contrast with the black-body avalanche picture previously discussed in literature [62, 107].

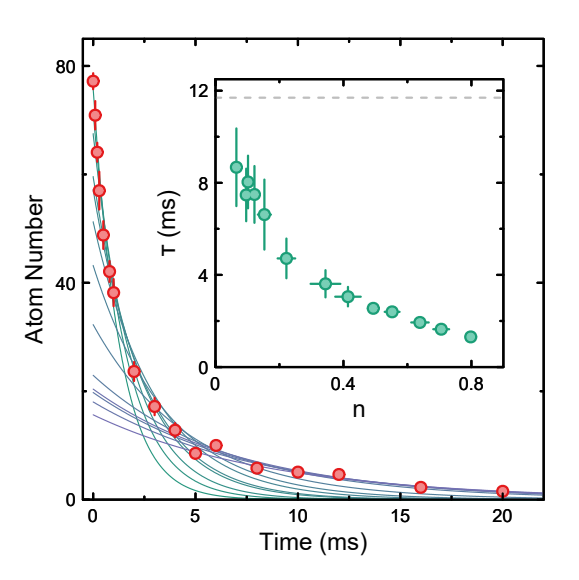


Figure 3.17: **Density-dependent life**times of Rydberg dressed systems. Observed atom decay of ^6Li ground-state atoms dressed with the $|31P\rangle$ Rydberg state. We initialize the system in a long and thin rectangular configuration along the UV laser beam direction. The observed decay cannot be explained by a single exponential so we resort to fitting exponentials to bins of 6 data points. (inset) Extracted lifetimes τ as a function of density n. Grey dotted-line is expected lifetime τ_{dr} . Parameters: $\Omega = 2\pi \times 6.9(1) \,\text{MHz}$, $\Delta = 2\pi \times 60 \,\text{MHz}$, and $B = 592(1) \,\text{G}$.

Lifetime $vs. \Delta$

The simple Rydberg dressed lifetime has a characteristic scaling with detuning Δ of $\tau_{dr} = \beta^{-2}\tau \propto \Delta^2$. We are able to observe this expected scaling for single-exponential model fits to systems initialized in the very sparse limit. However, for dense systems we observe a clearly different scaling. In Fig. 3.18 we show the measured lifetime scalings for sparse and dense systems along with fits to power laws. The expected scaling is observed for the sparse system which should correspond to the single-particle limit. Moreover, we are able to extract a bare Rydberg lifetime of $\tau = 33(5)$ µs which roughly agrees with the expected $\tau_{Ryd} = 38.7$ µs from Eq. 2.13. For the case of the rapid initial decay of dense systems we observe a steeper scaling fitting a power law of $\alpha = 3.5(2)$. If we limit the fit to the larger detunings where the simple Rydberg-dressing picture ($\beta^2 \ll 1$) can be assumed, we are able to fit a $\tau_{dr} \propto \Delta^3$ model within errorbars.

3.7.3 Effect of magnetic field

Being one of the biggest "knobs" in our experiment and a key difference from previous experimental realizations, we performed a lot of experiments studying the effect of

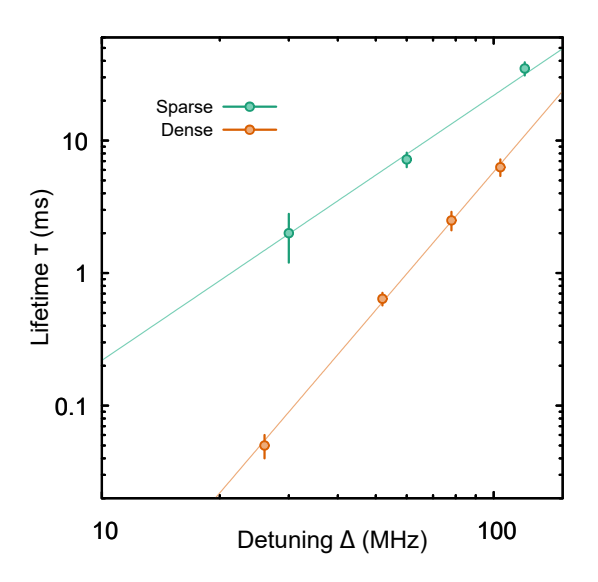


Figure 3.18: **Dressed lifetime** vs. Δ . Measured lifetimes of a long strip system of ground-state atoms coupled to the $|31P\rangle$ Rydberg state. (green) If the system is initialized with a sparse density (single-particle limit) we observe the expected $\tau_{dr} \propto \Delta^2$ scaling. From the fit we extract $\tau = 33(5)$ µs as the bare Rydberg lifetime. (orange) If the system is initialized close to full density and we extract just the initial decay rate we observe a steeper scaling than expected. By fitting to a power law $(\tau_{dr} \propto \Delta^{\alpha})$ we extract $\alpha = 3.5(2)$. Parameters: $\Omega = 2\pi \times 7.7(1)$ MHz and B = 592(1) G.

the magnetic field on the atom number decay. In general, we did not observe any clear effect as long as we took the care to keep Δ the same given the observed shifts in the resonance detailed in Sec. 3.6.2. There was however a study where we saw a clear difference between the atom number decay at very high fields for atoms coupled to $|28P\rangle$. Fig. 3.19 shows the atom number decay for 4 very different large magnetic fields. What we observe is not a gradual effect, but rather a sharp change of the profile at some critical field between 660 G and 720 G. At $|28P\rangle$ for typical fields ~ 592 G we observe longer lifetimes at high densities (Fig. 6.4). But at higher fields, we observe that the decay profile drastically changes and more closely resembles the data measured for $|31P\rangle$ (Fig. 3.17) and other higher principal quantum numbers.

As discussed in Sec. 3.2.2 and shown in Fig. 3.4, the magnetic field has a strong effect on the "jungle" of extra pair-state lines close to our target state. It is possible, that above a certain field one of these lines with non-zero overlap with the target state appears. This could imply that direct resonant excitation to nearby pair states, and not black-body induced decay, is what is limiting the lifetimes in our experiment.

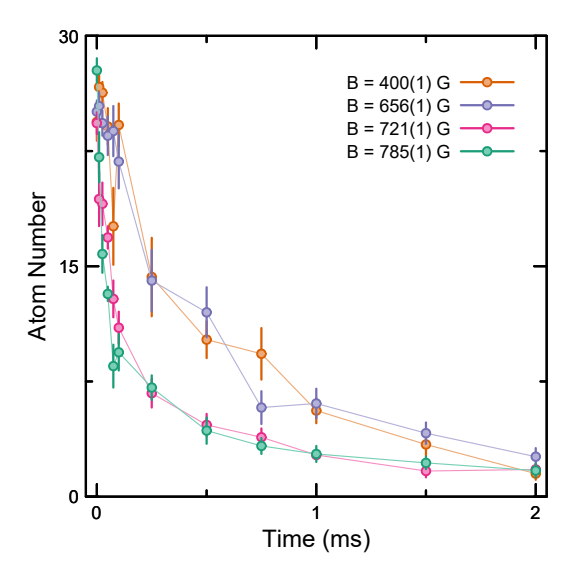


Figure 3.19: **Dressed lifetime** vs. B field. Observed atom number decay of square ground-state systems coupled to the $|28P\rangle$ Rydberg state. Each color corresponds to a different magnetic field B. We do not observe a clear dependence of the decay with magnetic field. However, for very high fields we do observe that the decay profile drastically changes and decays much faster similar to what is observed in higher $|nP\rangle$ Rydberg dressed systems (Fig. 3.17). Parameters: $\Omega = 2\pi \times 9.5(1)$ MHz and $\Delta = 2\pi \times 40$ MHz.

3.7.4 Effect of optical potentials

Our 2D optical trap is comprised of two different lattice potentials: a red-detuned lattice in the x-y plane made using 1064 nm light and a blue-detuned vertical lattice in the z direction made using 532 nm light to provide tight confinement and achieve the 2D regime [92, 93]. We studied the effect of both of these potentials on the lifetime of the Rydberg dressed atoms and found no effects when keeping Δ constant by accounting for the light-shift due to the potentials (Sec. 3.6.1).

This result is particularly interesting for the case of the the optical lattice because it means that the presence of tunneling does not facilitate extra loss mechanisms. This was a topic of theoretical debate in Refs. [108, 109] before our recent results summarized in Ch. 6 and particularly in Fig. 6.4c showed that tunneling does not affect the lifetime in our system.

3.7.5 Effect of hyperfine ground-state

In Sec. 3.1.1 we described the properties of the hyperfine ground-states at high fields. The usual ground-states we use in our experiment are $|1\rangle$ and $|3\rangle$ of which only the former is pure at all magnetic fields [96]. In our experiment we can initialize the

system in either of them by first resonantly blowing away the other state. When comparing schemes that use each of these two initial states, and taking into account the different position of the resonance, we did not find any difference in their measured lifetimes. This points towards our conjecture that Rydberg states that differ only in they m_I quantum number can be treated the same. However, as already explained in Sec. 3.1.1, out of an abundance of caution we decided to start using state $|3\rangle$, which is pure at all fields, for the itinerant experiments shown in Ch. 6.

3.7.6 Effect of principal quantum number

Theoretically, the Rydberg-dressed lifetimes have a characteristic scaling with principal quantum number as shown in Table. 2.4. This scaling depends on whether we are limited by spontaneous emission or black-body induced decay. It also depends on which dressing parameters we decide to keep constant. Even so, this scaling is always positive meaning that we would expect the dressing lifetimes to improve with increasing principal quantum number of the coupled $|nP\rangle$ Rydberg state.

Experimentally, we found the opposite behavior. Initially we started using the $|31P\rangle$ Rydberg state finding too low lifetimes compared to the expected dressed lifetimes τ_{dr} . We then used larger $|nP\rangle$ states finding an even worse fraction of the expected lifetimes. It was not until we tried $|28P\rangle$ that we achieve a reasonable fraction of $\sim 1/3\tau_{dr}$ for half-filled 2D systems of ≤ 50 atoms. This allowed us to study a parameter space with sufficient coherence to observe a clear effect of interactions on the relaxation dynamics of charge-density-waves [14].

While this experimental characterization was under way, we still lacked the full understanding of our high field dressing scheme (Sec. 3.1) and the possible effects that nearby pair-potentials could have (Sec. 3.2). In Figs. 3.3 and 3.4 we can observe how many more nearby pair potentials approach distances $\sim 1 a_{latt}$ as a function of increasing principal quantum number and magnetic field respectively. This fact and

the observation of an "onset" of a more rapid decay with high magnetic fields in $|28P\rangle$ makes us believe that the decay mechanism limiting our system is resonant excitation to nearby pair-states which have non-zero overlap with the target state.

3.8 Rydberg-dressed potential characterization

In order to characterize the full Rydberg-dressed potentials described in Sec. 3.3 we use many-body Ramsey interferometry between the two lowest hyperfine ground-states of 6 Li. The use of this technique to characterize Rydberg-dressed potentials was originally proposed in Ref. [110] and subsequently implemented for Rb in Ref. [75].

3.8.1 Many-body Ramsey interferometry

Experimentally, we can realize this technique by initializing the system in a spin-polarized gas of $|1\rangle$ atoms on a deep lattice with suppressed tunneling. Next, we perform Ramsey $(\pi/2 - \tau - \pi/2)$ and spin-echo $(\pi/2 - \tau - \pi - \tau - \pi/2)$ sequences of RF and UV pulses in order to indirectly measure the Rabi frequency and directly probe the Rydberg dressing long-range interactions respectively. We can achieve this by looking at density profiles and correlations after blowing away one of the two spin states.

In the frozen gas regime, we can write down the many-body Hamiltonian over which the Rydberg-dressed atoms evolve during an UV pulse as a classical Ising model where the lowest hyperfine states correspond to different spins:

$$\hat{H}_{dr} = H_0 + \frac{1}{2} \sum_{i} \delta_i \hat{\sigma}_z^{(i)} + \frac{1}{8} \sum_{i \neq j} V_{ij} \hat{\sigma}_z^{(i)} \hat{\sigma}_z^{(j)}$$
(3.7)

Here, H_0 is an energy offset, the second term is a longitudinal field of strength δ_i dominated by the single-particle light-shift, and the third term is an effective interaction term with strength V_{ij} . Specific choices of pre-factors will become obvious later on.

A procedure to exactly calculate the experimental observables of different pulse sequences is described in the supplement of Ref. [75] and in Ref. [62]. This calculation relies on correctly writing down the unitary operators corresponding to the evolution of the spin system under the dressing Hamiltonian of Eq. 3.7 ($\hat{U}_{dr} = e^{-i\int_0^{\tau} \hat{H}_{dr} dt}$). Using this unitary time evolution and the operators corresponding to the RF pulses we can exactly calculate the final expectation values of arbitrary operators of different pulse sequences in terms of the accumulated phases $\phi_i = \int_0^{\tau} \delta_i(t) dt$ and $\Phi_{ij} = \int_0^{\tau} V_{ij}(t) dt$ over the length τ of the dressing pulse.

Ramsey pulse sequence

For a $\pi/2 - \tau - \pi/2$ pulse sequence, the observable is the expected single-component density $\hat{\sigma}^i_{\uparrow\uparrow} = |\uparrow\rangle \langle\uparrow|$ which can be calculated to be:

$$\langle \hat{\sigma}_{\uparrow\uparrow}^i \rangle = \frac{1}{2} - \frac{1}{2} \cos(\phi_i) \prod_{j \neq i} \cos\left(\frac{\Phi_{ij}}{2}\right)$$
 (3.8)

This observable depends on both the phases accumulated due to single-particle light-shifts and interactions. However, by choosing large enough detunings Δ we can make it such that the effect of interactions is negligible compared to the light-shift (Fig. 3.20).

Spin-echo pulse sequence

For a spin echo $\pi/2 - \tau - \pi - \tau - \pi/2$ pulse sequence, the observable is the single-component density correlation which can be calculated to be:

$$\left\langle \hat{\sigma}_{\uparrow\uparrow}^{i} \hat{\sigma}_{\uparrow\uparrow}^{j} \right\rangle_{C} = \frac{1}{8} \left(\prod_{k \neq i,j} \cos \Phi_{k,ij}^{(+)} + \prod_{k \neq i,j} \cos \Phi_{k,ij}^{(-)} \right) - \frac{1}{4} \cos \Phi_{ij}^{2} \prod_{k \neq i,j} \cos \Phi_{ik} \cos \Phi_{jk}$$

$$(3.9)$$

where $\Phi_{k,ij}^{(\pm)} = \Phi_{ik} \pm \Phi_{jk}$ and $\Phi_{ii} = 0$. This observable depends purely on the phases accumulated due to interactions and it is our main way to directly probe the long-range interactions of the system (Fig. 6.3c-d).

3.8.2 Interferometry of ⁶Li

Having explained the observables of the two pulse sequences, all that is left is to write down the many-body dressing Hamiltonian of $^6\mathrm{Li}$ atoms in the form of Eq. 3.7. As explained in Sec. 3.3.3, we need to take into account the dressing of both states because the hyperfine splitting between the two lowest ground-states is only 75.806(3) MHz and the detunings we use are between 30 MHz and 100 MHz. For our interferometer, we use hyperfine ground states $|1\rangle \equiv |\uparrow\rangle$ and $|2\rangle \equiv |\downarrow\rangle$. The many-body dressing Hamiltonian is

$$\hat{H}_{dr} = \sum_{i} \left(\delta_{i}^{\uparrow} \hat{\sigma}_{\uparrow\uparrow}^{(i)} + \delta_{i}^{\downarrow} \hat{\sigma}_{\downarrow\downarrow}^{(i)} \right)$$

$$+ \frac{1}{2} \sum_{i \neq j} \left(V_{ij}^{\uparrow\uparrow} \hat{\sigma}_{\uparrow\uparrow}^{(i)} \hat{\sigma}_{\uparrow\uparrow}^{(j)} + V_{ij}^{\downarrow\downarrow} \hat{\sigma}_{\downarrow\downarrow}^{(i)} \hat{\sigma}_{\downarrow\downarrow}^{(j)} \right)$$

$$+ V_{ij}^{\uparrow\downarrow} \hat{\sigma}_{\uparrow\uparrow}^{(i)} \hat{\sigma}_{\downarrow\downarrow}^{(j)} + V_{ij}^{\downarrow\uparrow} \hat{\sigma}_{\downarrow\downarrow}^{(i)} \hat{\sigma}_{\uparrow\uparrow}^{(j)} \right),$$

$$(3.10)$$

where δ_i^{α} is the single-particle light shift for spin α at site i, $V_{ij}^{\alpha\beta}$ is the Rydberg dressed potential between spins α and β at sites i and j, and $V_{ij}^{\uparrow\downarrow} = V_{ij}^{\downarrow\uparrow}$. Using the relations $\hat{\sigma}_{\uparrow\uparrow}^{(i)} = \frac{1}{2} \left(\hat{\mathbb{I}} + \hat{\sigma}_z^{(i)} \right)$ and $\hat{\sigma}_{\downarrow\downarrow}^{(i)} = \frac{1}{2} \left(\hat{\mathbb{I}} - \hat{\sigma}_z^{(i)} \right)$, we can rewrite the Hamiltonian as an Ising model of the form:

$$\hat{H}_{dr} = H_{0}$$

$$+ \frac{1}{2} \sum_{i} \left(\delta_{i}^{\uparrow} - \delta_{i}^{\downarrow} + \frac{1}{2} \sum_{j \neq i} \left(V_{ij}^{\uparrow \uparrow} - V_{ij}^{\downarrow \downarrow} \right) \right) \hat{\sigma}_{z}^{(i)}$$

$$+ \frac{1}{8} \sum_{i \neq j} \left(V_{ij}^{\uparrow \uparrow} + V_{ij}^{\downarrow \downarrow} - 2V_{ij}^{\uparrow \downarrow} \right) \hat{\sigma}_{z}^{(i)} \hat{\sigma}_{z}^{(j)}$$

$$\hat{H}_{dr} = H_{0} + \frac{1}{2} \sum_{i} \delta_{i}^{*} \hat{\sigma}_{z}^{(i)} + \frac{1}{8} \sum_{i \neq i} V_{ij}^{*} \hat{\sigma}_{z}^{(i)} \hat{\sigma}_{z}^{(j)}$$

$$(3.11)$$

Where $\delta_i^* = \delta_i^{\uparrow} - \delta_i^{\downarrow} + \frac{1}{2} \sum_{j \neq i} \left(V_{ij}^{\uparrow \uparrow} - V_{ij}^{\downarrow \downarrow} \right)$ and $V_{ij}^* = V_{ij}^{\uparrow \uparrow} + V_{ij}^{\downarrow \downarrow} - 2V_{ij}^{\uparrow \downarrow}$ are the corrected longitudinal field and interaction terms. We can use these corrected terms to calculate the accumulated phases and use them on Eqs. 3.8 and 3.9. We can exactly recover the equations of Ref. [75] if we set every term except δ_i^{\uparrow} and $V_{ij}^{\uparrow \uparrow}$ to 0. This is because for Rb the hyperfine splitting is much larger ($\sim 5\,\mathrm{GHz}$) and one can safely assume that only state $|1\rangle$ is being dressed.

3.8.3 Ramsey vs. Detuning

One of the initial measurements we did with the interferometry was to study the scaling of the Ramsey fringe frequency ϕ with detuning Δ . In figuring out how to properly model the data we first realized that the dressing of state $|2\rangle$ could not be ignored. Furthermore, there is an extra collective field term in the longitudinal field of Eq. 3.12. This interaction effect effectively reduces the measured Ramsey frequencies ϕ as shown in Fig. 3.20. In the beginning we had the idea of fitting a C_6 coefficient based on this scaling. However, we found that the spin-echo pulse sequence

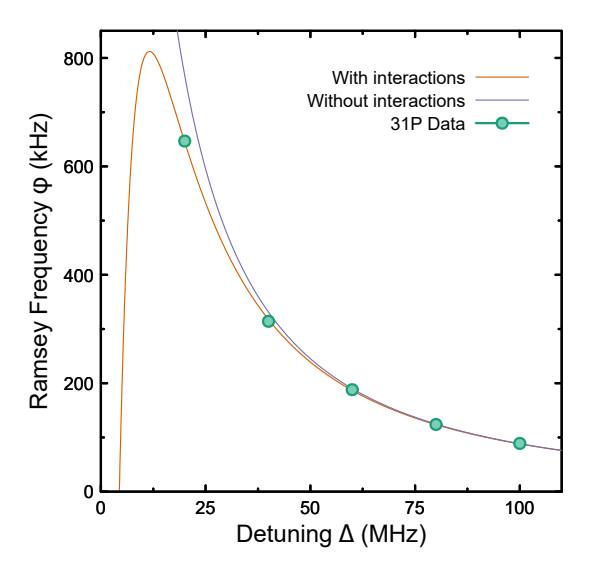


Figure 3.20: Ramsey frequency vs. Detuning. Measured Ramsey frequencies ϕ of a $\pi/2 - \tau - \pi/2$ pulse for various different detunings Δ in a gas dressed with $|31P\rangle$ Rydberg state. We fit a model that takes into account the collective field due to the long-range interaction potential. It is important to take into account these interactions otherwise we do not find good agreement with theory. The effect is minimal for largest detunings.

was a much better probe of the interactions since it removes all effects due to the single-particle light-shifts.

3.8.4 Indirectly measuring the Rabi frequency Ω

At large detunings, the collective field term due to the Rydberg-dressed interactions is negligible. On an almost daily basis, we performed a Ramsey pulse sequence for $\Delta \approx 2\pi \times 100 \,\mathrm{MHz}$ to indirectly measure the Rabi frequency Ω and align the laser beam if needed. At this large detuning, the ramsey fringe frequency ϕ depends only on the single-particle light-shifts of states $|1\rangle$ and $|2\rangle$ as $\phi = \delta_{AC}(\Omega, \Delta) - \delta_{AC}(\Omega, \Delta + \Delta_0)$. Here, Δ_0 is the hyperfine splitting and δ_{AC} is the single-particle light-shift from Eq. 2.31. Doing a Taylor expansion for $\Omega^2/\Delta^2 \ll 1$ we can solve for the Rabi frequency and find the following relation:

$$\Omega = \sqrt{\frac{4\phi}{\left(\frac{1}{\Delta} - \frac{1}{\Delta + \Delta_0}\right)}} \tag{3.13}$$

Using this equation we are able to not only extract the Rabi coupling Ω , but also we can measure the waist of the Gaussian UV dressing beam by looking at its profile

over a large could (Fig. 6.3b). This technique is so precise that we used it to fine align the dressing beam at the atoms to very good precision.

3.8.5 Directly measuring interactions from Spin-Echo interferometry

In principle, one could also measure density oscillations after a spin-echo pulse sequence and directly extract an oscillation frequency equal to the interference of interactions for the lattice distances. However, this would require perfect filling, as difference in holes from shot-to-shot will inevitably lead to decoherence. Furthermore, as discussed in Sec. 3.7, the lifetime depends heavily on the density and is minimal at unit filling.

Instead, we have opted to look at the density-density correlations from Eq. 3.9 after very short pulses, similar to what was done in Ref. [75]. This observable is much less susceptible to imperfect filling, and can be shown to scale quadratically with the interaction for $V(r)\tau \ll 1$. In Fig. 6.3c-d we show a comparison between the measured correlations and theory. We find very good agreement when taking into account the full Rydberg-dressed potential (Sec. 3.3) and an offset attributed to atom loss.

In our experiment, we have opted to trust the C_6 coefficients extracted from numerical calculations using the Pair-Interaction package [87]. We did not find any clear deviations from what we physically observed when taking into account all of the modeling described throughout this chapter. If in the future we are able to increase the coherence, further characterization techniques will need to be developed in order to measure this interaction potential rather than using a priori calculations.

Chapter 4

Quench dynamics in a 2D transverse Ising spin system

This chapter presents the work published as

- E. Guardado-Sanchez, P. T. Brown, D. Mitra, T. Devakul, D. A. Huse,
- P. Schauß, and W. S. Bakr. Probing the quench dynamics of antiferromagnetic correlations in a 2D quantum Ising spin system. *Phys. Rev. X* 8 (2018) [12]

As we were performing the characterization of the UV laser system described in the previous chapter we realized that it would be possible for our system to simulate a two-dimensional transverse Ising spin Hamiltonian with broken Z_2 symmetry, through direct excitation to a Rydberg state whose blockade radius R_b (Sec. 2.7.1) is on the order of the lattice spacing. Previous work in both optical lattices [111, 112] and tweezer arrays [88, 113, 114] had focused on larger blockade radii and its effects. However, this regime makes it hard to study many-body states with a large Rydberg fraction. In contrast, the regime studied in our work is particularly interesting because it features a direct quantum phase transition between a paramagnet and an

antiferromagnet with broken Z_2 symmetry. Our work is closely related to studies in one-dimensional [43, 114] and two-dimensional [50, 115] tweezer arrays.

Using our platform, we explored the dynamics of a two-dimensional quantum Ising model by coupling a nearly defect-free array of neutral atoms in an optical lattice to a low-lying Rydberg state [49]. The spin coupling in the model arises due to a van der Waals interaction between atoms in the Rydberg state. If one atom is in a Rydberg state, the excitation of another atom to a Rydberg state is strongly suppressed within a blockade radius R_b [82–86]. This is because the interaction between the Rydberg atoms within this radius is much larger than the laser coupling strength. While there exists a variety of well-developed theoretical techniques to study the equilibrium properties of quantum spin systems [116–122], the toolkit for simulating real-time dynamics of these systems is rather limited and can only capture the evolution accurately for short times, especially for systems in more than one dimension [116, 123–125]. In this work, we benchmark state-of-the-art numerical techniques to the results of our quantum simulator and find reasonably good agreement.

4.1 Simulating a quantum Ising model with Rydberg atoms

We realize a quantum Ising spin system with an array of ⁶Li atoms in an optical lattice with near unit-occupancy. The lattice is deep enough to suppress tunneling over the timescale of the experiments. We prepare all the atoms in the same hyperfine ground state $|\downarrow\rangle$. Interactions are introduced by globally coupling the atoms with a single laser field to a Rydberg state $|\uparrow\rangle$. The van der Waals interaction between atoms in the Rydberg state is isotropic and takes the form $V_{ij} = C_6/|r_i - r_j|^6$. The Hamiltonian

of the system is given by:

$$\hat{H} = \Omega \sum_{i} \hat{S}_{i}^{x} + \sum_{i} (\mathcal{I}_{i} - \Delta) \hat{S}_{i}^{z} + \sum_{i \neq j} \frac{V_{ij}}{2} \hat{S}_{i}^{z} \hat{S}_{j}^{z}$$

$$(4.1)$$

Here \hat{S}_i^{α} are the spin 1/2 operators for the *i*th lattice site and $\alpha=x,y,z$. The first two terms of this Hamiltonian describe transverse and longitudinal magnetic fields that couple to the pseudospin. The Rabi frequency Ω that drives a transition between the ground and the Rydberg state for an isolated atom determines the transverse field, while the detuning Δ of the laser frequency from atomic resonance determines the longitudinal field (Sec. 2.7). $\mathcal{I}_i = \sum_{j,(i \neq j)} \frac{V_{ij}}{2}$ can be taken as a site independent detuning in a large system as ours. We work with an attractively interacting $(V_{ij} < 0)$ Rydberg state ($|23P\rangle$). In the absence of the fields, the Hamiltonian's most excited state is a classical antiferromagnet, which is the ground state of the Hamiltonian $\hat{\tilde{H}} = -\hat{H}$. For $R_b = (C_6/\Omega)^{1/6} \gg a_{latt}$, the ground state phase diagram of $\hat{\tilde{H}}$ in Ω/Δ parameter space contains multiple Rydberg crystalline phases with different Rydberg atom fractions [43, 126–129]. However for $R_b \sim a_{latt}$, the regime we study in this experiment, \hat{H} can be approximated by a nearest-neighbor Ising Hamiltonian with coupling $J=C_6/a_{latt}^6$. A phase diagram for this model is shown in Fig. 4.1a and has only one ordered phase, the antiferromagnet [130, 131]. The initial state in the experiment is the paramagnetic ground state of \hat{H} for positive detuning $\Delta \gg J \gg \Omega$. In this work, we quench the system from this initial state to the antiferromagnet with varying degrees of adiabaticity and study the ensuing dynamics of the spin correlations.

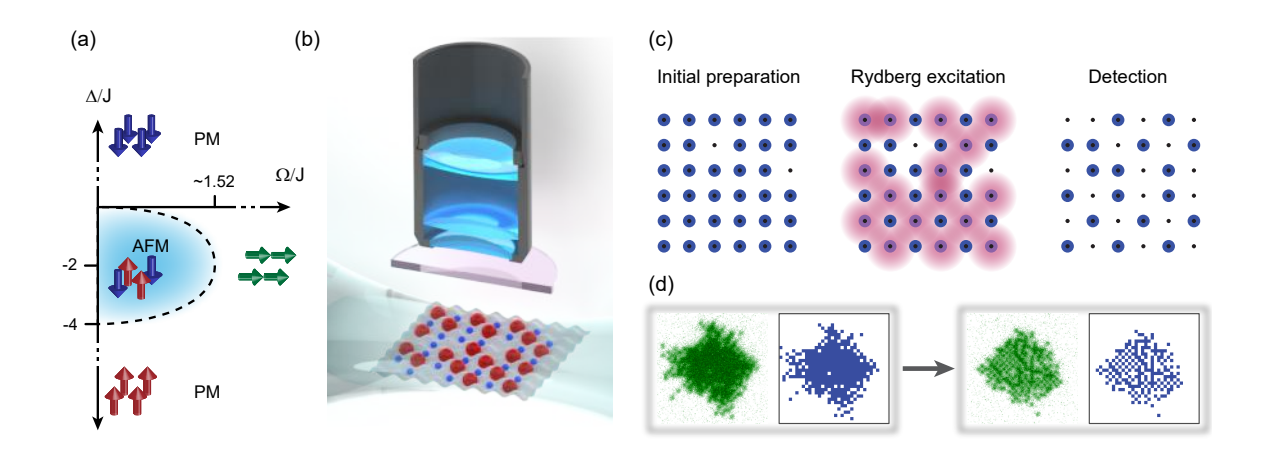


Figure 4.1: Realization of a 2D quantum Ising model with Rydberg atoms in an optical lattice. (a) Ground-state phase diagram of the 2D quantum Ising model H with nearest neighbor coupling J. This is an approximate phase diagram of our Rydberg system when the blockade radius is comparable to the lattice spacing. Transverse and longitudinal fields are controlled by the Rabi frequency Ω and laser detuning Δ , respectively. There is only one ordered phase, the antiferromagnet (AFM). Outside of this region there is a paramagnetic (PM) phase where the spins align with the field. (b) Experimental setup consisting of a 2D array of atoms at the focus of a high-resolution objective, capable of resolving individual sites of the lattice. Atoms in the ground state (small blue spheres) are directly coupled to the 23P Rydberg state (large red spheres) with 230 nm laser light. (c) Typical atom configurations at different stages of the experiment. The initial state consists of an array of atoms in the electronic ground state (blue, left). This state is guenched into a state with antiferromagnetic correlations (Rydberg atoms in red, center). By increasing the lattice depth, Rydberg atoms are lost and only the ground state atoms are imaged (right). (d) Raw fluorescence images of an initial (left) and a post-quench (right) configuration with strong antiferromagnetic correlations, together with reconstructed images (each blue pixels depicts a detected atom in the ground state).

4.2 Experimental realization

We prepare nearly defect-free 2D arrays of atoms by taking advantage of Pauli blocking in a highly spin-imbalanced degenerate Fermi gas loaded into a square optical lattice at a magnetic field of 595 G (for details see [92, 93]). At this strong fields, the spin mixture consists of the first $|1\rangle = |2S, 0, -1/2, 1\rangle$ (in $|nl, m_l, m_s, m_I\rangle$ basis) and third $|3\rangle = |2S, 0, -1/2, -1\rangle$ lowest hyperfine ground states of ⁶Li, with $|1\rangle$ as the majority. The minority atoms, needed to thermalize the gas while loading into the lattice, are subsequently removed with a pulse of resonant light. We focus our analysis on an annular region with outer (inner) radius of 9 (4) sites where the average occupancy of the remaining state $|1\rangle$ atoms, measured from repeated preparations of the system, is maximal and corresponds to 95.7(4) %.

4.2.1 Laser System for coupling to Rydberg states

We couple the state $|1\rangle$ atoms to the $|23P, 0, -1/2, 1\rangle$ Rydberg state using single-photon excitation with a linearly-polarized ultraviolet (UV) laser at 230 nm (Fig. 4.2). The experiments are performed at a bias magnetic field of 595 G pointing orthogonal to the 2D layer, allowing us to address a single Rydberg state. Up to 60 mW of UV light is available from a frequency-quadrupled diode-laser system (Sec. 3.4). The light is π -polarized and focused to a waist of 35 μ m. The intensity and the frequency of the light can be changed rapidly to control the time dependence of the transverse and longitudinal fields in the Hamiltonian. The UV laser had an intensity stability better than 10%. The linewidth at 230 nm was measured to be $\approx 100 \, \text{kHz}$ (Fig. 3.6).

4.2.2 Experimental Setup

The atoms are located at the focus of a high resolution objective that can resolve individual sites of the optical lattice (Fig. 4.1b). The Rydberg dynamics take place

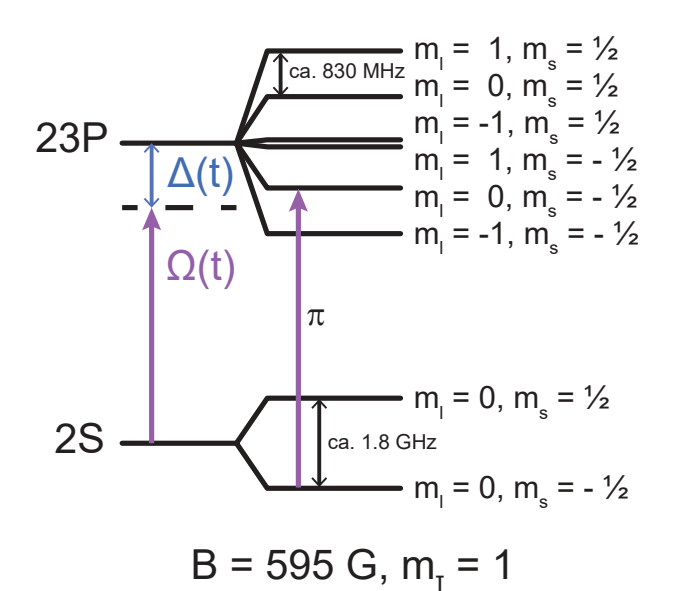


Figure 4.2: Rydberg Coupling scheme. Level diagram showing laser coupling with linear (π) polarization from the ground state to the $|23P\rangle$ Rydberg state at a magnetic field of 595 G.

in a lattice of depth 55 E_R , where $E_R = (\pi \hbar)^2/2ma_{latt}^2$ is the recoil energy and $a_{latt} = 1064 \text{ nm}/\sqrt{2}$. We image the distribution of ground state atoms after removing Rydberg atoms with an efficiency of 90(3) % by increasing the lattice depth to $2500E_R$, leading to rapid photo-ionization or expulsion of the anti-trapped Rydberg atoms (Fig. 4.1c). We obtain site-resolved fluorescence images of the ground state atoms by collecting ~ 1000 photons per atom scattered from laser beams in a Raman cooling configuration [7].

4.2.3 Single atom Rabi oscillations and coherence

We calibrate the transverse and longitudinal fields of the Hamiltonian using sparse clouds where the average spacing between atoms is much larger than R_b . The location of the Rydberg resonance ($\Delta = 0$) is determined by finding the laser frequency which maximizes atom loss during a long exposure to the UV light, since atoms in the Rydberg state experience an anti-trapping optical potential (Sec. 3.6). The Rabi frequency Ω is determined by measuring single atom Rabi oscillations (Sec. 3.6.5), and we attain a maximum Rabi frequency $\Omega_{max} = 2\pi \times 5.4(1)$ MHz (The errorbar

takes into account shot-to-shot intensity fluctuations). Ω varies 4.9(3) % over the region of interest due to the Gaussian intensity profile of the UV beam.

To measure the strength of the laser coupling to the Rydberg state, we measure Rabi oscillations in a sparse cloud where the interactions between the Rydberg atoms are negligible. A typical single atom Rabi oscillation is shown in Fig. 4.3a. The decay of the Rabi oscillation is mainly due to shot-to-shot fluctuations of the laser intensity. In addition we measure the coherence of the atoms in a sparse cloud using a Ramsey echo sequence: $\pi/2 - \tau - \pi - \tau - \pi/2$ pulse, where τ is a delay time. The ground state fraction is measured at the end of the sequence (Fig. 4.3b). Even for $\tau = 0$, corresponding to a 2π pulse, the measured ground state fraction is reduced to ~ 0.8 , because of laser intensity fluctuations. However, for a total delay $2\tau = 1 \mu s$, corresponding to 6h/J, we do not observe any decay of the ground state fraction, indicating that there is no loss of coherence.

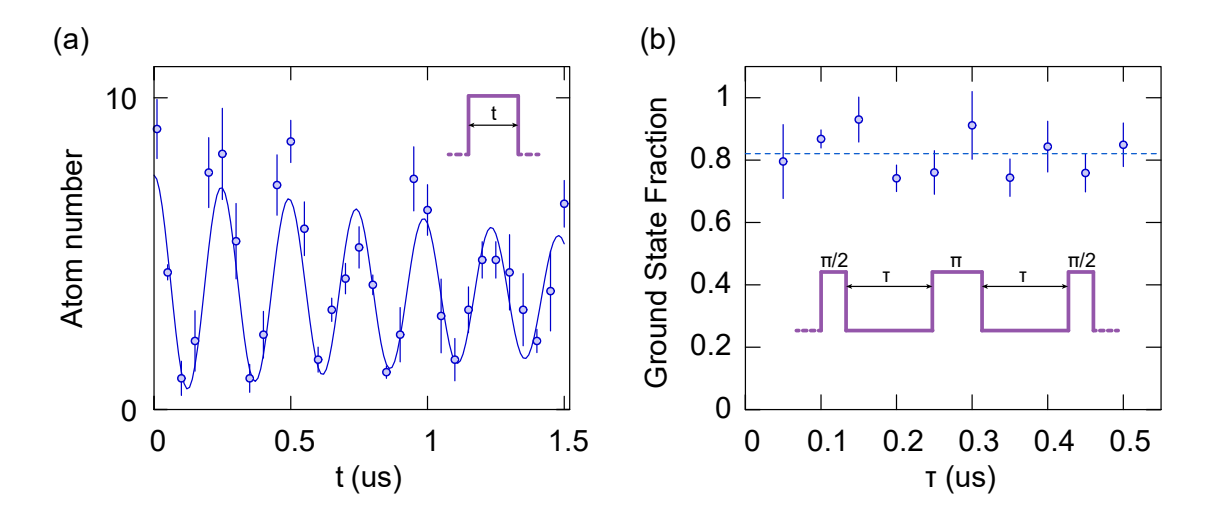


Figure 4.3: Investigation of single-atom coherence. (a) Single atom Rabi oscillation. Fitted 1/e decay of the amplitude is $\sim 1.5 \,\mu s = 9h/J$. (b) Measurement of the ground state fraction after a Ramsey echo sequence, indicating no loss of coherence over times longer than the quench times used in this work ($\sim 1 \,\mu s = 6h/J$).

4.2.4 Movement of the atoms during the quenches

The ground-state atoms in our experiment are trapped in an optical lattice. However, the Rydberg state is anti-trapped by the lattice. There are also other even stronger forces that can lead to movement of the atoms, mainly van der Waals forces between atoms in Rydberg states and photon recoil kicks. From the experimentally fitted value for C_6 , we estimate Rydberg atoms accelerate toward each other with $a(r) = \frac{6C_6}{r^7m}$ where $a \approx 3.2 \times 10^6 \,\mathrm{m/s^2}$ for neighboring Rydberg atoms and $a(\sqrt{2}a_{\mathrm{lat}}) \approx 2.8 \times 10^5 \,\mathrm{m/s^2}$ for next-neighbor Rydberg atoms. This leads to a displacement of $0.09a_{\mathrm{latt}}$ ($0.01a_{\mathrm{latt}}$) for a typical quench time of 200 ns for nearest neighbor (next-nearest neighbor) Rydberg atoms. We note that the excitation of two Rydberg atoms on neighboring sites is largely suppressed due to the blockade. Recoil and anti-trapping forces lead to much smaller displacements of the atoms. In our calculations, we cannot include the movement of atoms during the quenches due to the tremendous increase in Hilbert space size. One approach to account for some aspect of the movement is to model its effect as two-particle decoherence, as discussed in Sec. 4.4.2.

4.2.5 Theoretical calculation of C_6

The C_6 coefficient, which determines the strength of the van der Waals interaction, depends strongly on the principal quantum number. We obtain a theoretical $C_6/h = -1.92(6) \text{ MHz } \mu\text{m}^6 = -10.6(3) \text{ MHz } a_{latt}^6$ for the $|23P, 0, -1/2, 1\rangle$ state at an offset field of 595 G. The angular dependence of the interaction potential in the P-state is unimportant in our experiments since the magnetic quantization axis is orthogonal to the plane of the lattice, leading to an isotropic interaction for atoms in the 2D plane. For these parameters, $\hbar\Omega_{max}$, $J\gg h/\tau$, where $\tau\sim 20~\mu\text{s}$ is the lifetime of the Rydberg state [66], leading to negligible decay over the relevant timescales.

We calculate the value of C_6 for the state $|23P, 0, -1/2, 1\rangle$ at 595 G with two different techniques. First we use a perturbation theory calculation in the m_l basis which yields $C_6/h = -1.915 \,\mathrm{MHz} \,\mu\mathrm{m}^6$ (Sec. 2.5.1). As a second approach we use a pair state ED in the m_j basis at 595 G using [87] and perform a basis transformation to the m_l -basis (Table. 3.1). A fit to the potential curve then yields C_6 . Depending on the inner cutoff r_0 for the fit we obtain values between $C_6/h = -1.974 \,\mathrm{MHz} \,\mu\mathrm{m}^6$ for $r_0 = 0.7 \,\mu\mathrm{m}$ and $C_6/h = -1.864 \,\mathrm{MHz} \,\mu\mathrm{m}^6$ at $r_0 = 1 \,\mu\mathrm{m}$ which leads us to the error estimate previously mentioned.

4.3 Short "sudden" quenches

As an initial experiment we study dynamics in the Ising system after a sudden quench, where the transverse field is switched on quickly compared to h/Ω . The system is initially in a product state, with all spins in $|\downarrow\rangle$ ($|1\rangle$), and we image the atoms after an evolution time T. From the images, we extract the spin correlators $C(\mathbf{r}) = 4 \langle S_{\mathbf{i}}^z S_{\mathbf{i}+\mathbf{r}}^z \rangle_c = 4(\langle S_{\mathbf{i}}^z S_{\mathbf{i}+\mathbf{r}}^z \rangle - \langle S_{\mathbf{i}}^z \rangle \langle S_{\mathbf{i}+\mathbf{r}}^z \rangle)$. The correlators C(0,0), C(1,0), C(0,1) and C(1,1) are shown in Fig. 4.4a-d for $\Omega T/h = \pi/2$ ($\Omega = h \times 4.05(2)$ MHz) and varying detuning Δ . The correlator C(0,0) is linked to the magnetization as $C(0,0) = 1 - 4 \langle S_{\mathbf{i}}^z \rangle^2$. We observe a change in the sign of the nearest neighbor correlations as the detuning Δ is varied.

4.3.1 Comparison to NLCE dynamical calculations

For such short times, the correlations remain short-range and therefore we can compare our results to calculations obtained using a dynamical version [132] of the numerical linked cluster expansion (NLCE) [121, 133]. The dynamics is computed on clusters of increasing size (the "order" of the expansion) and the results are expected to converge if the correlation length is smaller than the cluster size. We

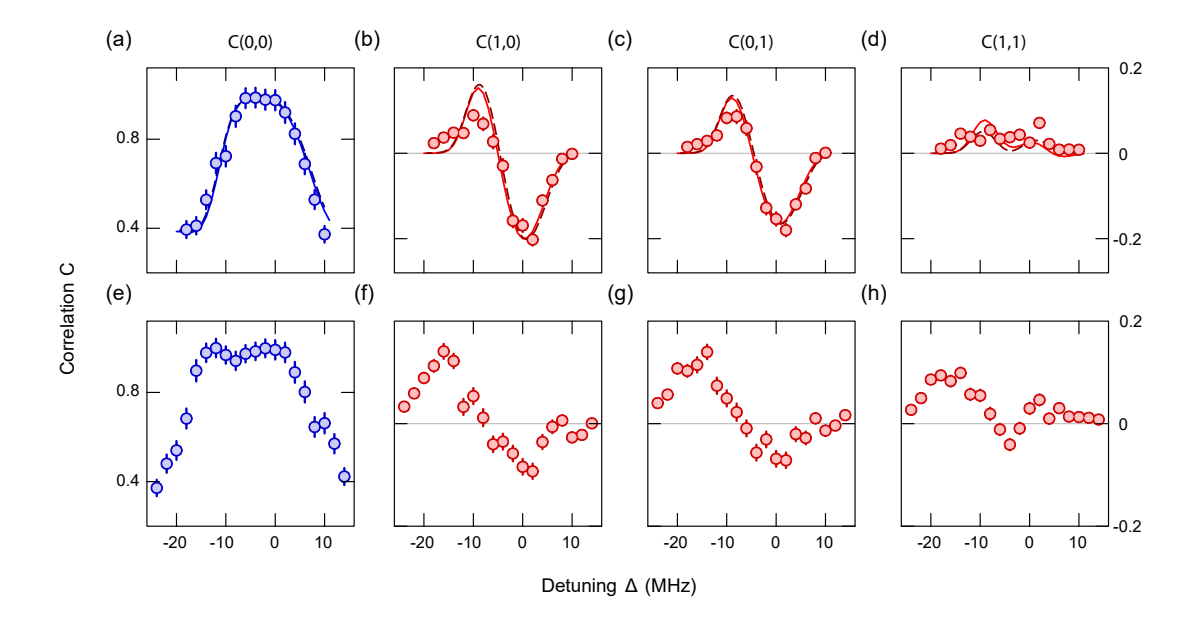


Figure 4.4: **Sudden quench dynamics.** (a-d) Spin correlations after a sudden quench with $\Omega T/h = \pi/2$ ($\Omega = h \times 4.05(2)$ MHz) at various detunings Δ . The correlators shown are C(0,0) (a), C(1,0) (b), C(0,1) (c), and C(1,1) (d). For comparison we show the fits to dynamics computed with NLCE (solid line) and exact diagonalization on a 4×4 lattice with open boundary conditions (dashed line). (e-h) Spin correlations after a longer quench of $\Omega T/h = 3\pi/2$ ($\Omega = h \times 5.3(1)$ MHz) at various detunings.

find good convergence for times $\Omega T \lesssim \pi$. The 11th order NLCE results for the on-site and nearest-neighbor correlations are fit to the measured correlations after the quench with two free parameters: the van der Waals interaction coefficient C_6 and a scaling factor α corresponding to the Rydberg imaging efficiency. The NLCE dynamics calculations take into account interactions up to next-nearest neighbors and experimental imperfections including the finite rise and fall time of Ω and 2.8% anisotropy of the lattice spacing [7], which translates to an 18% anisotropy of the interactions on the nearest neighbor sites. We also compare the data to exact diagonalization results on a 4 × 4 lattice. From these fits, we obtain an experimental $C_6/h = -1.1(1) \,\mathrm{MHz} \,\mu\mathrm{m}^6 = -6.0(3) \,\mathrm{MHz} \,a_{latt}^6$ and a scaling factor $\alpha = 0.89(1)$, which agrees with the expected detection efficiency. The fitted value of C_6 is about 40% lower than the theoretically calculated C_6 , which has possible systematic errors

due to uncertainties in the matrix elements in lithium, in particular at high magnetic fields, and finite wavefunction size of the atoms on the lattice sites [134].

NLCE dynamics

The numerical linked cluster expansion (NLCE) algorithm used to calculate the dynamics in this work is an extension of the NLCE technique for thermodynamic quantities, reviewed in refs. [121, 133]. Our NLCE calculations take into account next-nearest neighbor (diagonal) interactions, lattice anisotropy, and the finite time for turning on and off the Rabi frequencies during "sudden" quenches. We discuss some of the major modifications that are made to the algorithm, assuming the reader's familiarity with the standard algorithm.

For systems with the symmetry of the square lattice and only nearest neighbor interactions, each embedding of a graph on the lattice is dependent only on the topology of the graph, which allows for a significant reduction in the number of clusters that need to be diagonalized. Taking into account next-nearest neighbor interactions and lattice anisotropy means that this is no longer true, as two topologically identical graphs may have different graph Hamiltonians. Thus, we break down topologically identical graphs further into classes of graphs with the same Hamiltonian up to graph symmetries, each of which we only need to solve once.

For each of these, we then perform a time evolution starting from the initial state using sparse representations of the Hamiltonian. The initial and final ramp is simulated by breaking down the overall ramp time into five time steps, and applying the time evolution between these steps with the appropriate time-averaged Hamiltonian. Then, the appropriate correlation functions can be extracted from the final state. The subgraph subtraction then proceeds as usual, except that each embedding should be treated independently, as the contribution of a graph to a particular correlator depends on its embedding in the lattice. Finally, we perform an Euler

resummation starting from the 3rd order to reduce odd-even order fluctuation. Note that the graphical expansion done here is site-based, rather than link-based.

Finally, we have checked the effect of including beyond-next-nearest neighbor interactions, and the number of time steps, and found that our results are well converged with respect to them.

Fitting sudden quench dynamics to NLCE results

The correlator dynamics are computed using NLCE for a grid of Δ and C_6 values at 9th order in the expansion, taking into account the independently calibrated Rabi frequency $\Omega = 2\pi \times 4.05\,\text{MHz}$. The correlators C(0,0), C(1,0), and C(0,1) are simultaneously fit to the results using two fit parameters: C_6 and a scaling factor α corresponding to a Rydberg atom detection efficiency. The scaling factor reduces the nearest neighbor correlators C(1,0) and C(0,1) as α^2 . Since $C(0,0) = \langle n^2 \rangle - \langle n \rangle^2$ and $n^2 = n$ since n is either 0 or 1, we obtain $C(0,0) = \langle n \rangle - \langle n \rangle^2$. This leads to a corrected correlator $C^*(0,0) = \alpha \langle n \rangle - \alpha^2 \langle n \rangle^2$.

Convergence of NLCE dynamics calculations

To go beyond the regime where the dynamics can be calculated with NLCE, we perform a longer quench with $\Omega T = 2.97(7)\pi$. The extracted correlators are shown in Fig. 4.4e-h. In this case, even the next-nearest neighbor correlations exhibit a zero crossing as a function of detuning, showing that the system is building up longer range correlations. The different NLCE orders already stop converging at much earlier times.

To back up the claim that the quench shown in Fig. 4.4e-h is outside of the regime which exact state-of-the-art numerical methods can study, we show the results of an NLCE simulation up to $\Omega T = 3\pi$. Fig. 4.5 shows the time evolution of the C(0,0) and C(0,1) correlators. The fitted C_6 values and parameters of Fig. 4.4a-d were

used. The difference between the solid and dotted lines is the order at which the Euler resummation is started. The series is converged up to times where both of these curves coincide. For the time corresponding to the quench studied in Fig. 4.4a-d ($\Omega T = 0.5\pi$) it is clear that the series is converged and as such we can use it for fitting. However, for the quench studied in Fig. 4.4e-h ($\Omega T = 3\pi$) the series is far from converged. This points to the strength of platforms such as ours as benchmark results for numerical methods.

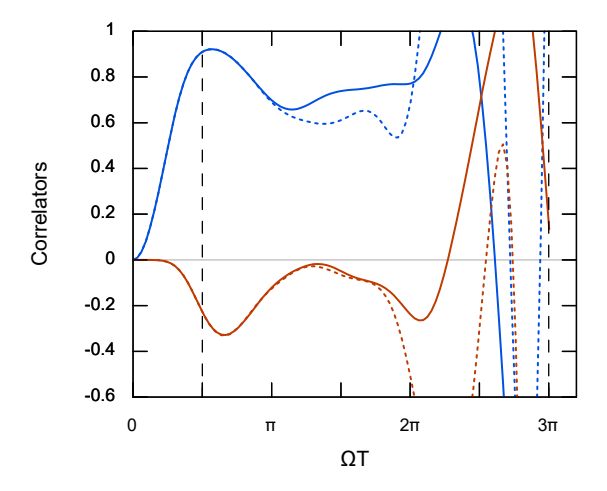


Figure 4.5: **NLCE** convergence. 11th-order numerical linked clusted expansion calculations for a sudden quench with parameters $J = h \times 6 \,\text{MHz}$, $\Omega = 2\pi \times 4.05 \,\text{MHz}$, and $\Delta = 0$. C(0,0) (blue) and C(0,1) (red) correlators are shown vs. time. The solid line is an Euler resummation starting at the 3rd order while the dotted line is one starting at the 5th order. The black dashed lines correspond to the pulse lengths shown in Fig. 4.4.

4.4 Near-"adiabatic" quenches

To prepare many-body states with longer antiferromagnetic correlations, we investigate a more adiabatic quench scheme [128, 135, 136], illustrated in the inset of Fig. 4.6. In the following, we use $J = h \times 6$ MHz for all presented units. We start from the same initial state but use a soft switch on and off of the Rabi frequency and a linear ramp of the detuning from $\Delta_i = 3.3J$ to a varying Δ_f . During the detuning ramp, the Rabi frequency is fixed at $\Omega_0 = 0.9(1)J/\hbar$. We explore a variety of detuning ramp rates $\dot{\Delta}$ ranging from $8.9J^2/h$ to $1.6J^2/h$. For each $\dot{\Delta}$ we measure correlations at different times in the ramp. Fig. 4.6 shows the buildup of nearest neighbor and next-nearest neighbor antiferromagnetic correlations as the longitudinal field is ramped at

different rates. The buildup of antiferromagnetic correlations starts approximately at the time the detuning ramp crosses $\Delta=0$. For the fastest quench rates we see a correlation buildup before crossing of the resonance which we attribute to strong non-adiabaticities. For all quench rates studied, we observe that the correlations reach a maximum at $\Delta/J \sim -2$, as would be expected in the adiabatic limit from the phase diagram in Fig. 4.1a. The peak value of the correlations initially increases as the quench rate is reduced as one might expect for approaching the adiabatic limit, but then decreases for slower ramps. This is likely due to decoherence starting to play a role in the slower quenches. Therefore, we have to take decoherence effects into account for a numerical modeling of the time-dependence of the correlations.

We performed a phenomenological study of the influence of decoherence on the near-adiabatic ramps by solving the master equation using the Monte Carlo Wave Function method (MCWF) on a 4×4 lattice [137, 138] (Sec. 4.4.2). Single particle decoherence comes in the form of decay from the Rydberg state (T_1) and dephasing that can be characterized in our system using a Ramsey sequence in a sparse cloud (T_2) . In Fig. 4.6, we show MCWF simulations with values of $T_1 = 20 \,\mu s$ and $T_2 =$ 0.5 µs. We found that the impact of single particle decoherence on the correlations is too small to reproduce our experimental results. However, motional effects can lead to many-body decoherence. Mechanisms leading to atomic motion include strong attractive forces between atoms in the Rydberg state, laser recoil and changes of the lattice potential experienced by the atoms due to a difference in the polarizability between the ground and Rydberg states. These motional effects are stronger in our system compared to previous optical tweezer experiments [43, 114] due to the light mass of lithium and the relatively small lattice spacing. This motion of the atoms, estimated in Sec. 4.2.4, leads to decoherence in the spin system by changing the coupling J. To model this two-particle decoherence, we approximated the movement of the atoms as "interaction noise" between nearest neighbor pairs. Although the

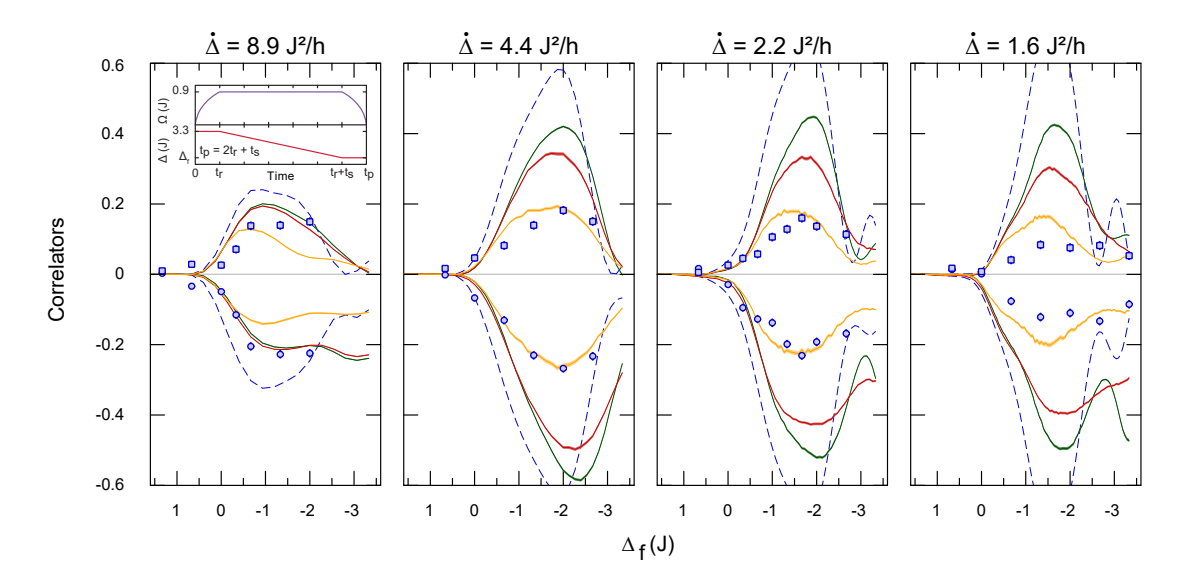


Figure 4.6: Time evolution of spin correlations after near-adiabatic quenches and comparison with phenomenological decoherence models. Experimental correlations after near-adiabatic quenches (blue circles for C(0,1) and blue squares for C(1,1) for different quench rates (left to right panel) and varying final detuning Δ_f . These are compared with MCWF simulations taking into account different types of decoherence (lines). We studied T_1 type decoherence with $T_1 = 20 \,\mu s$ (green) and T_2 type decoherence with $T_2 = 0.5 \,\mu s$ (red). The T_1 value is chosen as the lifetime of the Rydberg state and the T_2 value is an aggressive lower bound given by our Ramsey calibration Additionally, we show the combination of T_1 decoherence with two-particle "interaction noise" for nearest neighbor pairs (yellow). For the latter, the decoherence rate $(\Gamma_J = 1 \,\mu\text{s}^{-1})$ was a free parameter chosen to obtain reasonable agreement with experimental correlations for all four quenches simultaneously. The shaded regions are s.e.m. of the simulations. For reference, the calculations without decoherence are also shown (dashed blue lines). Inset, time dependence of the Rabi frequency Ω and detuning Δ used for the near-adiabatic quenches. The time for switching on and off the laser coupling was fixed to $t_r = 0.6h/J$ for all quenches. The maximum total length of the quench t_p varies from 0.3 μ s to 0.9 μ s depending on the quench rate.

motion is expected to be coherent at short times, we make the assumption that the motion is sufficiently chaotic at long times to allow us to use this decoherence approximation. We implement the "interaction noise" by adding a time-independent conditional nearest-neighbor dephasing term with rate $\Gamma_J = 1 \,\mu\text{s}^{-1}$ to the Lindblad master equation. As the "interaction noise" is not constrained by our single-particle calibrations we use its strength as a single free parameter to fit our data. This phenomenological simulation allows us to achieve better agreement with our data for the longer quench rates, suggesting that our main source of decoherence is two- or many-body in nature.

At the end of the ramps, where significant antiferromagnetic correlations have built up, we find that we can fit the decay of the correlations with distance to an exponential (Fig. 4.7a). The fitted correlation lengths range from $\xi = 0.74(6)a_{latt}$ to $\xi = 1.9(2)a_{latt}$ depending on $\dot{\Delta}$. We compared this data to the results of equilibrium Monte Carlo calculations at $\Delta_f = -2J$ and $\Omega = 0$ to check if we can describe the system in terms of an effective temperature (Sec. 4.4.1). While these calculations also give correlations that decay exponentially, there is no temperature that reproduces both the strength and range of the correlations. We find a temperature of $k_B T_{\xi} \approx 0.51(1)J$ for matching the correlation length and $k_B T_{nn} \approx 0.82(4)J$ when matching the nearest-neighbor correlator for the data shown in Fig. 4.7a. The fact that these two temperatures are not within error bars leads us to the conclusion that the system is not equilibrated at the end of the quench.

Another way to characterize the states created by these slow quenches is by extracting the probabilities for observing a particular spin configuration in a sub-system. In Fig. 4.7b, we show the probability of observing different spin configurations in 3×3 sub-systems, not correcting for detection fidelities. The two antiferromagnetic states are the most probable states near the end of the ramp, with an enhancement of a factor of 16(2) over a uniform distribution in the Hilbert space.

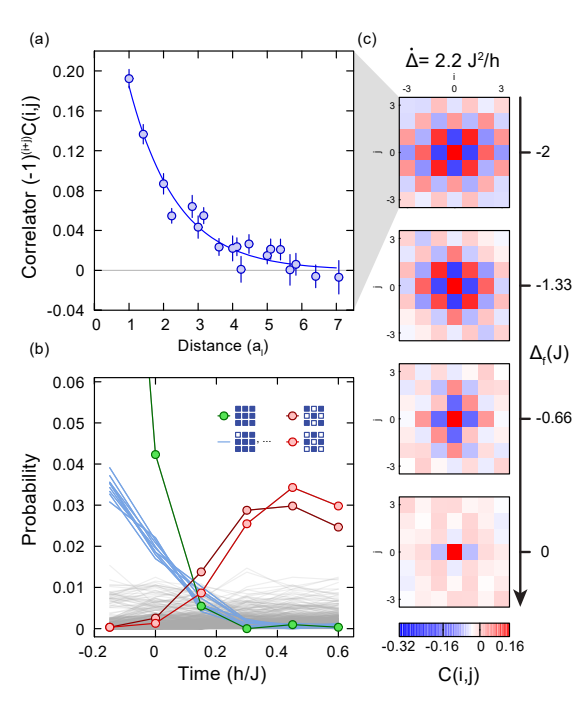


Figure 4.7: Characterizing many-body states during and after a slow quench. (a) Spatial decay of the correlations after a sweep with $\dot{\Delta} = 2.2J^2/h$, with an exponential fit that yields a correlation length $\xi = 1.4(1)a_{latt}$ sites. (b) Time evolution of the probabilities of observing different configurations in 3×3 sub-systems, not corrected for detection efficiencies. The probabilities are shown for the two antiferromagnetic states (red), the all-grounds state (green), one Rydberg atom states (blue), and all other states (grey). The evolution is shown during a ramp with $\Delta =$ $4.4J^2/h$. The antiferromagnetic configurations become most probable at the end of the quench. (c) Full correlation matrices C(i,j) at different final detunings during a slow quench with $\dot{\Delta} = 2.2J^2/h$, showing the growing range of the antiferromagnetic correlations.

4.4.1 Effective temperature by comparison with classical Monte Carlo

We compared our data from the near-adiabatic ramps ending at $\Delta_f = -2J$ with classical Monte Carlo simulations. At this detuning, the fields approximately vanish and the Hamiltonian has the form of a classical Ising model, $H = \sum_{i \neq j} \frac{V_{ij}}{2} \hat{S}_i^z \hat{S}_j^z$. We study the equilibrium behavior of the classical model using the Metropolis algorithm on a 64×64 system [139, 140]. In the case of only nearest neighbor interactions, we extracted the critical temperature $k_B T \approx 0.57J$ which agrees with the known exact result [141]. Since we have long-range interactions in our system, we added a next-nearest neighbor interaction term and compared the resulting correlations and correlation length to our measurements (see Fig. 4.8). Our calculations suggest that this extended Ising model has a critical temperature of $k_B T \approx 0.38J$. We cannot simultaneously match the correlation length and the correlation amplitude

for any given temperature, leading to the conclusion that our near-adiabatic ramps do not leave the system in a thermalized state. However, our measured correlation lengths for different quench rates would correspond to temperatures in the range $k_BT \approx 0.46 - 0.72J$.

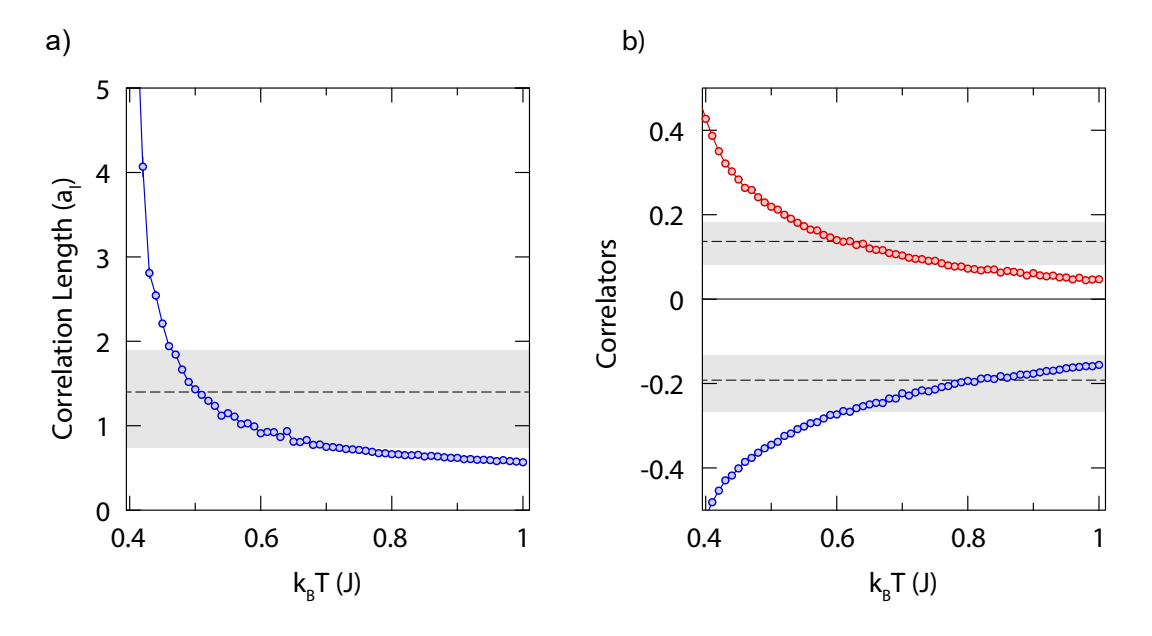


Figure 4.8: Effective temperature characteristics of an Ising system calculated with the Metropolis algorithm in a 64×64 periodic system. (a) Correlation length versus temperature (blue circles with lines to guide the eye). (b) C(0,1) (blue circles) and C(1,1) (red circles) versus temperature. The shaded regions are bounded by the minimum and maximum values attained in the near-adiabatic ramps. The dotted lines correspond to the data shown in Fig. 4.6a.

4.4.2 Investigation of phenomenological decoherence models

To investigate if the reduction of the measured correlators after the near-adiabatic quenches can be explained by single-particle decoherence, we look at phenomenological models with varying assumptions. All these models are based on exact diagonalization (ED) of 4×4 systems with periodic boundary conditions. The full time-dependence of the pulse shape of the near-adiabatic ramps shown in the inset of Fig. 4.6 is taken into account as well as the measured values of $\Omega = 0.9(1)J/\hbar$

and $\Delta_i = 3.3J$ for J/h = 6.0(3) MHz. It is important to note that a 4 × 4 system still shows finite-size effects which can lead to deviations of the simulation from our experimental results. However, it is expected that decoherence reduces the finite-size effects. All simulations shown include the measured scaling factor α .

Shot-to-shot Rabi frequency fluctuations

Here, we assume that the decay of the single-particle Rabi oscillation is purely caused by Rabi frequency fluctuations from shot to shot, i.e. the Rabi frequency within a single run of the experiment is assumed to be constant. We simulate this by ED on a 4×4 periodic system at varying Rabi frequency values and average them according to a Gaussian intensity fluctuation model. We find that the decay of the single particle Rabi oscillation can be explained by Rabi frequency fluctuations of $\approx 3\%$ (standard deviation) around the mean ($\sigma \approx 0.02J$ in the case of the ramps with $\Omega = 0.9(1)J/\hbar$). This amount of Rabi frequency fluctuation is consistent with our measurement of pulse intensity fluctuations. When using this same fluctuation model for the near-adiabatic quenches we see weak influence on the strength of the correlations (see Fig. 4.9). We conclude that a model based on shot-to-shot Rabi frequency fluctuations cannot explain our decay in the many-particle case.

Modeling the decoherence in the time evolution of the near-adiabatic quenches

In the presence of decoherence, we model our many-body system using a Master equation formalism. In this approach the equation of motion for the density matrix is,

$$\frac{\mathrm{d}}{\mathrm{d}t}\rho = -i[\hat{H}(t), \rho] + \sum_{i} \mathcal{L}(\hat{c}_{i}), \tag{4.2}$$

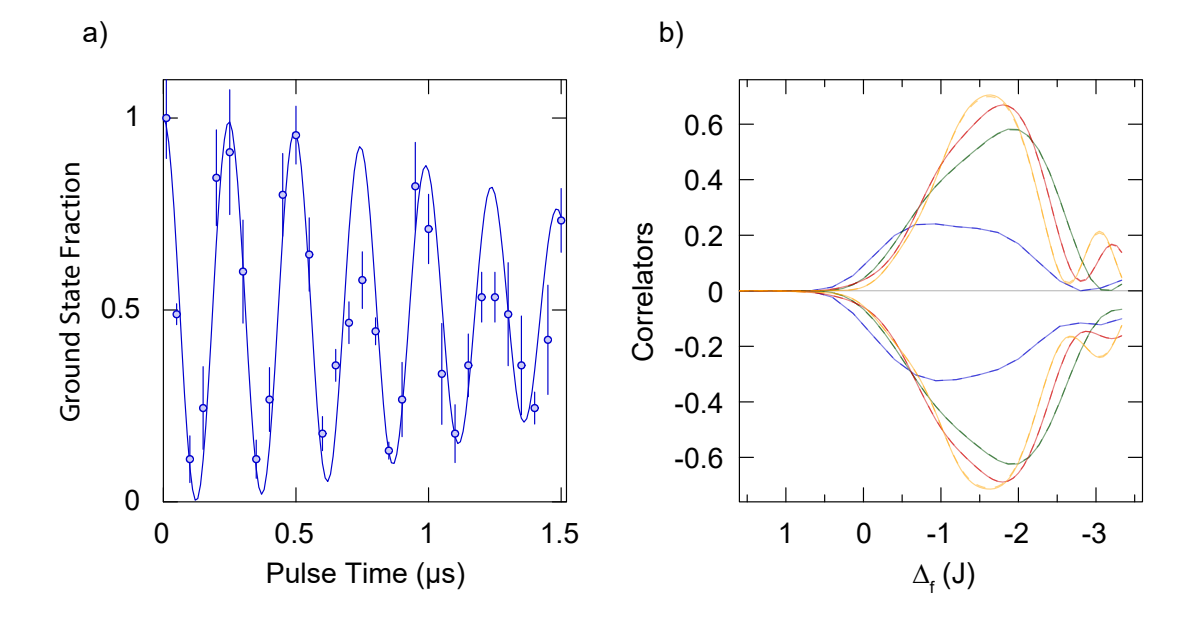


Figure 4.9: Effect of shot-to-shot Rabi Frequency fluctuations. (a) Comparison of a classical model with Rabi frequency fluctuations following a normal distribution of $\Omega_0 = 2\pi \times 4.05\,\mathrm{MHz}$ and $\sigma_\Omega = 2\pi \times 0.12\,\mathrm{MHz}$ with the normalized data of Fig. 4.3. (b) Comparison of ED simulations of the near-adiabatic ramps on a 4×4 periodic system without Rabi frequency fluctuations (solid lines) and including them (dashed lines) for different quench rates $\dot{\Delta} = 8.9J^2/h$ (blue), $4.4J^2/h$ (green), $2.2J^2/h$ (red), and $1.6J^2/h$ (yellow). The effect of the fluctuations on the quenches is negligible.

where ρ is the density matrix of the full system which evolves coherently with our Hamiltonian H and the dissipative part \mathcal{L} which can be written as

$$\mathcal{L}(\hat{c}_i) = \frac{\Gamma}{2} (2\hat{c}_i \rho \hat{c}_i^{\dagger} - \hat{c}_i^{\dagger} \hat{c}_i \rho - \rho \hat{c}_i^{\dagger} \hat{c}_i). \tag{4.3}$$

Here, \hat{c}_i is the single particle quantum jump operator at site i describing the decoherence type and Γ is the decay rate determining the strength of the decoherence in the system.

In order to study the effects of decoherence on the evolution of the system throughout a quench, it is important to properly choose both the quantum jump operator \hat{c}_i and its weight Γ [137, 138]. Since solving for the full density matrix becomes intractable even for relatively small systems, we employ the Monte Carlo Wave Function (MCWF) method [137, 142, 143]. In this method, it is only required to keep track of a single wavefunction $|\phi(t)\rangle$ where the quantum jump operator \hat{c}_i acts at random times with Poisson distribution. The probability per time step of length dt of the quantum jump occurring is therefore $dp = \Gamma dt |\langle e_i | \phi(t) \rangle|^2$. By averaging over many trajectories with different random jumps, it is possible to reconstruct the full density matrix results. For all of our simulations we used dt = 5 ns which is very short compared to all energy scales of the system $(hdt^{-1} \gg J, \hbar\Omega, \Delta)$. We also checked for convergence with respect to variations in dt.

Single-particle decoherence For T_1 decoherence (spontaneous emission), one has to take into account a quantum jump operator $\hat{c}_i = \hat{\sigma}_i^-$ that decays the single particle wavefunction $|\phi_i\rangle$ into the ground state $|g_i\rangle$. Since the lifetime of the Rydberg state is $\tau \sim 20 \,\mathrm{ps}$, we did a simulation with $\Gamma_{T_1} = 1/\tau = 0.05 \,\mathrm{ps}^{-1}$. For T_2 decoherence (phase noise), the quantum jump operator $\hat{c}_i = \hat{\sigma}_i^z$ mixes the phase of the $|\phi_i\rangle$ state. In a previous section, we showed that $T_2 > 0.5 \,\mathrm{ps}$ and as such we chose an upper bound $\Gamma_{T_2} = 1/2T_2 = 1 \,\mathrm{ps}^{-1}$. Fig. 4.6 shows the ED simulations taking into account these two decoherence sources. For the fastest quench, it agrees very well with our measured correlations. However, the agreement is much worse for the slower quenches. We conclude that single-particle decoherence effects are not the main limitation in our experiment.

Nearest-neighbor pair decoherence Since we cannot explain our results by single-particle decoherence effects, we look into the simulation of beyond single particle effects in the following. We estimated in a previous section that within times of the order of 100 ns two adjacent Rydberg atoms can attract each other and move considerable distances thereby changing the effective interaction between them. The effect of the movement of the atoms can be approximately simulated as "interaction noise". Since we found that T_1 type decoherence had a significant effect on the simu-

lations, we kept its dissipative term and implement the "interaction noise" by adding a second dissipative term to our master equation

$$\sum_{\langle ij\rangle} \mathcal{L}_2(\hat{c}_{ij}) = \sum_{\langle ij\rangle} \frac{\Gamma_J}{2} (2\hat{c}_{ij}\rho\hat{c}_{ij}^{\dagger} - \hat{c}_{ij}^{\dagger}\hat{c}_{ij}\rho - \rho\hat{c}_{ij}^{\dagger}\hat{c}_{ij}). \tag{4.4}$$

Where \hat{c}_{ij} is a quantum jump operator acting on nearest neighbor pair spins. We choose the quantum jump operator to be $\hat{c}_{ij} = (\hat{\sigma}_i^z - \hat{\mathbb{I}}) \otimes (\hat{\sigma}_j^z - \hat{\mathbb{I}}) = |e_i\rangle\langle e_i| \otimes |e_j\rangle\langle e_j| = \hat{n}_i^e \otimes \hat{n}_j^e$ and the probability with which it is applied in each simulation step as $dp = \Gamma_J dt \, |\langle e_i e_j | \phi(t) \rangle|^2$. This is analogous to the MCWF method for single particle decoherence but expanded to a two-body dissipative process. This quantum jump operator has the same structure as the interaction term in our Hamiltonian \hat{H} . It describes random dephasing between two atoms if both are in the Rydberg state, which is the effect of "interaction noise". The full master equation thus looks like

$$\frac{\mathrm{d}}{\mathrm{d}t}\rho = -i[\hat{H}(t), \rho] + \sum_{i} \mathcal{L}(\hat{\sigma}_{i}^{-}) + \sum_{\langle ij \rangle} \mathcal{L}_{2}(\hat{n}_{i}^{e} \otimes \hat{n}_{j}^{e}). \tag{4.5}$$

For the T_1 dissipative term we used $\Gamma_{T_1} = 0.05 \,\mathrm{µs^{-1}}$ as before. Since we do not have prior knowledge of the value for Γ_J , we vary it to minimize deviations for all quench rates simultaneously. We find reasonable simultaneous agreement for $\Gamma_J = 1 \,\mathrm{µs^{-1}}$. Fig. 4.6 shows the ED simulations using this two-body decoherence approach. We achieve reasonable quantitative agreement for the longer quenches. The worse agreement for the shortest quench might be caused by the fact that the movement is not randomized enough to allow for our simple interaction noise approximation. We conclude that this two-body decoherence is a good approximation to our experimental system's dissipation process.

Effect on short "sudden" quenches We also implemented the full decoherence models using MCWF on ED simulations of the sudden quenches shown in Fig. 4.4. Their effect was negligible as expected given their much shorter pulse times.

4.5 Conclusion

In conclusion, we studied quench dynamics in a 2D Ising model realized with ultracold atoms coupled to a Rydberg state in an optical lattice. The use of a light fermionic atom, ⁶Li, allows us to use Pauli blocking in a relatively large spacing lattice to create 2D atomic arrays with high-filling ($\sim 96\%$), comparable to what is achieved in atomby-atom assembler experiments [144, 145]. Combining the large spacing with the use of a low-lying Rydberg state, we reached the strong correlation regime with $R_b \sim a_l$ and prepared states exhibiting strong short-range antiferromagnetic correlations. We found good agreement of our data with state-of-the-art numerics for short-time quench dynamics without taking into account decoherence. In our study of near-adiabatic quenches we obtained evidence for beyond single-particle decoherence in our system and observed non-equilibrated final states with longer-range antiferromagnetic correlations. Our new ultracold ⁶Li Rydberg platform opens many interesting directions for future work. Rydberg excitation in a Fermi gas may allow the exploration of impurity dynamics in the presence of Pauli blocking effects [146, 147]. Finally, another direction is the use of Rydberg dressing techniques to realize a dipolar Fermi gas [36, 37, 75, 88]. Recently, we have implemented this technique to for the first time realize an itinerant strongly interacting system with long-range correlations [14].

4.5.1 Current State-of-the-art

The use of direct excitation of Rydberg atoms in tweezer arrays has ballooned since our work was first published [43, 50–53]. As a platform, the "interaction noise"

decoherence we found limited us from studying the physics of phase transitions [148, 149] and Kibble-Zurek dynamics [150–154]. In fact, very recent work has been able to explore these physics in 2D tweezer array [115]. Nevertheless, the measurements we were able to do here speak to the flexibility that Rydberg atoms offer as a platform for quantum simulation.

Furthermore, the motional "interaction noise" we observed in our experiment has recently been exactly modeled [155]. While it is stronger in our optical lattice experiments than in optical tweezer arrays. Being able to fully take it into account will be necessary in order to achieve high quantum-gate fidelities.

Chapter 5

Subdiffusive charge transport in a tilted Hubbard system

This chapter presents the work published as

E. Guardado-Sanchez, A. Morningstar, B. M. Spar, P. T. Brown, D. A. Huse, and W. S. Bakr. Subdiffusion and heat transport in a tilted two-dimensional Fermi-Hubbard system. *Phys. Rev. X* **10**, 011042 (2020) [13]

After the previous publication, our group went back to focusing on studying the Fermi-Hubbard model. In this time, we managed to uncover a previously unknown bad-metallic phase in the repulsive Fermi-Hubbard model [9] and developed an ARPES analogue protocol for atoms in optical lattices [11]. After these two projects, we focused on developing the Rydberg dressing platform described in Ch. 3. However, we were forced to wait while parts for the intensity stabilization (Sec. 3.4.3) arrived. It is during this time that we became aware of two theoretical publications claiming the existence of many-body localization (MBL) in tilted one-dimensional interacting lattice models due to kinetic constraints [156, 157]. We realized that with the addition of one laser beam we could study this physics and decided to change directions for the time being. In fact, we took data that we misinterpreted as a transition to MBL

in a 2D system. However, with the help of our theory collaborators we realized that what we were actually observing was very slow dynamics due to subdiffusion. In this way, this project which is equal parts experimental and theoretical came to be.

5.1 Introduction

While non-interacting particles in a tilted lattice potential have been studied for almost a century [158–161], the dynamics of strongly tilted and isolated many-body systems with strong interactions have been relatively unexplored. Characterizing the late-time behavior of such closed quantum many-body systems away from equilibrium is a topic of fundamental interest. In a series of recent papers [162–168] it was shown how irreversible dissipative dynamics can emerge from the unitary evolution of closed quantum systems. Thus generically we expect the transport of conserved quantities in such systems to behave hydrodynamically at late times as long as the system does thermalize. On the experimental front, advances in quantum simulation with cold atoms and other platforms have allowed for unprecedented control of quantum many-body systems, and for the controlled study of their dynamics [9, 43, 169–173]. For example, in a recent study diffusive charge transport was observed in an isolated strongly-interacting 2D Fermi-Hubbard system [9]. Here we follow that work by observing the dynamics of the same cold-atom Fermi-Hubbard system subject to a strong external linear potential, or "tilt", and find a crossover to qualitatively different subdiffusive behavior at strong tilts.

The dynamics of a weakly tilted 2D Fermi-Hubbard model were studied in Ref. [174] using semiclassical methods. That work formulated an understanding of the long-time dynamics in which regions with positive local temperature (lower energy and lower entropy than infinite temperature) heat up and transport charge "up" the tilt, and regions with negative local temperature [175, 176] (higher energy

and lower entropy than infinite temperature) transport charge "down" the tilt as the system approaches an infinite-temperature equilibrium. This infinite-temperature equilibrium of many fermions hopping in a single band has a spatially uniform density and zero expectation value of the hopping energy. In contrast, recent theoretical works [156, 157] explored the prospect of a transition to a localized phase in strongly tilted interacting 1D systems. While some evidence for this was found, it was suggested that this was the result of energetically-imposed local kinetic constraints that conserve the center of mass (COM)—a phenomenon later referred to as "Hilbert space fragmentation" [39, 40]. This mechanism for nonergodicity at strong tilts depends on factors such as the range of interactions, the dimensionality of the system, and the direction of the tilt. In what follows, we explore a system which does not exhibit such nonergodicity. Thus this work is most directly related to Refs. [9, 174] which deal with conductivity, although initial motivation for this study was derived from Refs. [156, 157] which deal with fragmentation, and investigating any nonergodic aspects of tilted systems is an interesting avenue for future work.

In this work we study the effect of an external tilt on the late-time high-temperature emergent hydrodynamics of a 2D cold-atom system. This is done by varying the tilt strength and observing the relaxation of prepared initial density waves of various wavelengths λ . We observe a crossover from a diffusive regime at weak tilts, where the relaxation time τ scales like $\tau \propto \lambda^2$, to a subdiffusive regime at stronger tilts, where $\tau \propto \lambda^4$. We then construct a hydrodynamic model that exhibits the same universal crossover, and discuss the underlying physics that leads to the subdiffusive transport. Using the hydrodynamic model we extract the infinite-temperature tilt-dependent thermal diffusivity of this system. We further verify our understanding of the underlying physics by measuring the local inverse temperature profile of the system, thus confirming a prediction of our theoretical

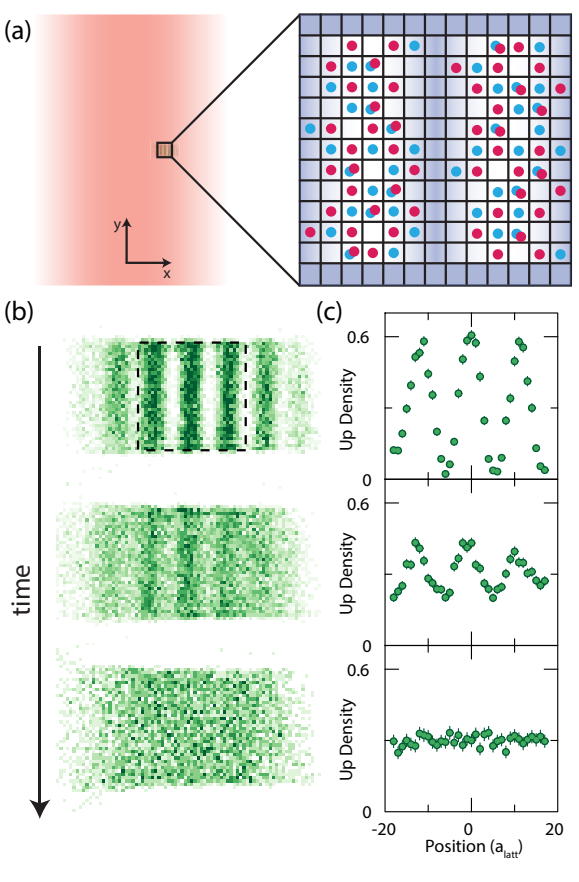


Figure 5.1: Experimental setup and measurements. (a) An off-centered beam generates a potential at the atoms that is approximately linear in x and independent of y. Blue-detuned light projected through a spatial light modulator is used to prepare the initial density waves of our experiments, with tunable wavelength in the direction of the tilt and hard walls a distance of 35 a_{latt} apart in the perpendicular direction. The figure is a schematic intended to portray the experimental setup and is not to scale. (b) Spin up (\uparrow) component of density vs. time, averaged over ~ 10 images. The dotted square denotes the region of interest (ROI) in which our measurements were taken. (c) Evolution of the y-averaged density in the ROI of (b) as a function of x. The data corresponds to a system with interaction energy $U/t_h =$ 3.9(1), tilt strength $Fa_{latt}/t_h = 0.99(3)$, and an initial density modulation of wavelength $\lambda/a_{latt} = 11.46(3)$. The density profile is shown at times $0 \,\mathrm{ms} \, (0 \, \hbar/t_h), \, 0.5 \,\mathrm{ms}$ $(2.6 \ \hbar/t_h)$, and $15 \,\mathrm{ms} \ (77 \ \hbar/t_h)$ from top to bottom.

model that this profile should correspond to local equilibrium and be displaced by a quarter wavelength relative to the density profile.

5.2 Experimental Setup

Our system is well-described by the tilted Fermi-Hubbard hamiltonian $\hat{H} = \hat{H}_{\rm FH} - F\hat{N}_f\hat{x}_{\rm COM}$ where $\hat{H}_{\rm FH}$ is the conventional Fermi-Hubbard Hamiltonian on a square lattice, F is the tilt strength, \hat{N}_f is the total number of fermions, and $\hat{x}_{\rm COM}$ is the x component of the COM. The repulsive on-site interaction energy is denoted by U, and the single-particle hopping energy by t_h . We emphasize that the system is tilted in only one of the lattice directions, which we denote with x. Because of this alignment,

transport along the y direction does not couple to the tilt potential. Thus each row of sites at each x position forms a thermal bath along an equipotential of the tilt. These local baths allow this closed system to thermalize. This is in contrast to the 1D case for which recent works [156, 157] have suggested the possibility of ergodicity breaking in strongly tilted systems.

5.2.1 Tilt Potential

We realize our tilted 2D Fermi-Hubbard model by loading a balanced mixture of two hyperfine ground states of 6 Li into an optical lattice [7]. The tilt is generated by an ALS MOPA laser which outputs $\sim 40 \,\mathrm{W}$ at a wavelength of $1064 \,\mathrm{nm}^1$. This laser is aligned to be off-centered from the atoms and focused to a waist of $\sim 180 \,\mathrm{\mu m}$, as depicted in Figs. 5.1a and 5.2a. The gradient of the resulting potential is uniform to within 10% across a region of length $40 \, a_{latt}$ (30 $\,\mathrm{\mu m}$), where a_{latt} is the spacing of the optical lattice, and the strength of the potential gradient can be tuned from 0 to $\sim h \times 5.5 \,\mathrm{kHz}/a_{latt}$. The beam is oriented such that the gradient is aligned with one of the two principal axes of the square lattice.

Tilt potential calibration

To calibrate the gradient and characterize its homogeneity across the region of interest, we used the SLM to prepare an initial state consisting of three thin stripes of width $\sim 1 a_{latt}$ and a separation of $\sim 20 a_{latt}$, with their long direction oriented orthogonal to the tilt direction. Each stripe consists of a spin-polarized gas of the lowest hyperfine ground state of ⁶Li.

For weak tilts, we are able to directly measure Bloch oscillations of these noninteracting particles. We do so by fitting a Gaussian profile to the density profile

¹This laser has since been appropriated by the Molecule Lab. However, an alternative laser system was built to generate tilt potentials at arbitrary angles using the existing IPG Photonics laser (Fig. 5.2b).

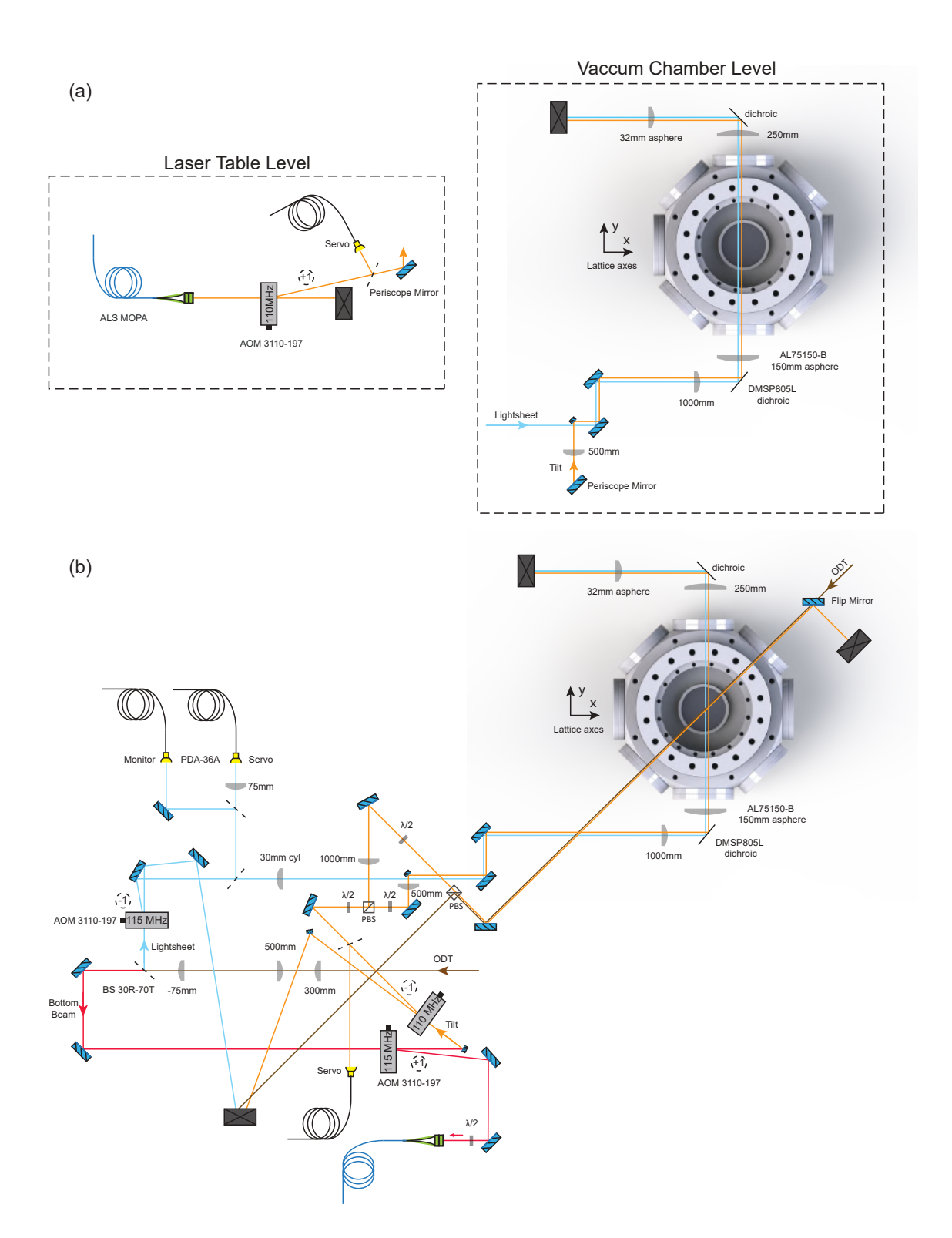


Figure 5.2: **Tilt potential laser system.** This figure was adapted from [92]. (a) Laser system setup used for this project. (b) Laser system used for tilt potentials at arbitrary angles in unpublished work.

integrated along the direction perpendicular to the tilt which is used to quantify the "breathing" oscillation of the width of the stripes. This is similar to what was done in [177]. From the theory of Bloch oscillations, we expect the width of each stripe to oscillate with a maximal half-width of $A = 4t_h/F$ and a period of $T = h/Fa_{latt}$. Thus, by fitting a sinusoid to the evolution of the width of each stripe, we can extract the tilt strength at their respective positions. Fig. 5.3a shows an example of such oscillations.

For stronger tilts, directly measuring the Bloch oscillations becomes challenging due to their small amplitude. Instead we use a modulation technique analogous to what was done in [178]. We modulate the lattice potential at frequencies on the order of the tilt strength. This brings lattice sites that were decoupled due to the tilt into resonance which results in photon-assisted tunneling. We again measure the width of the thin stripes versus modulation frequency and observe a broadening of the stripes at resonance. Fig. 5.3b shows an example of such a measurement.

We corroborated that for the same potential strength at intermediate tilts, the gradient extracted using the two techniques agrees. In the case of tilt potentials at arbitrary potentials, analogue protocols were developed where the main difference was that instead of initializing a profile of three thin stripes, we divide each stripe into 3 squares resulting in a spatial profile of 9 squares in a 3×3 distribution aligned with the lattice axes. With the laser system shown in Fig. 5.2b, we are able to generate tilt strengths of up to $F = h \times 8.3(1) \,\mathrm{kHz}/a_{latt}$ at an irrational angle of $32.8(4)^\circ$ from the lattice axes although these tilt strength seem to still be too small for our system size in order to observe true Hilbert space fragmentation physics. Instead, we might have observed some slow down of the heating up to infinite temperatures explored in this chapter. Rather than continue exploring these two dimensional tilt potentials, we decided to resume the Rydberg dressing project described in Ch. 6.

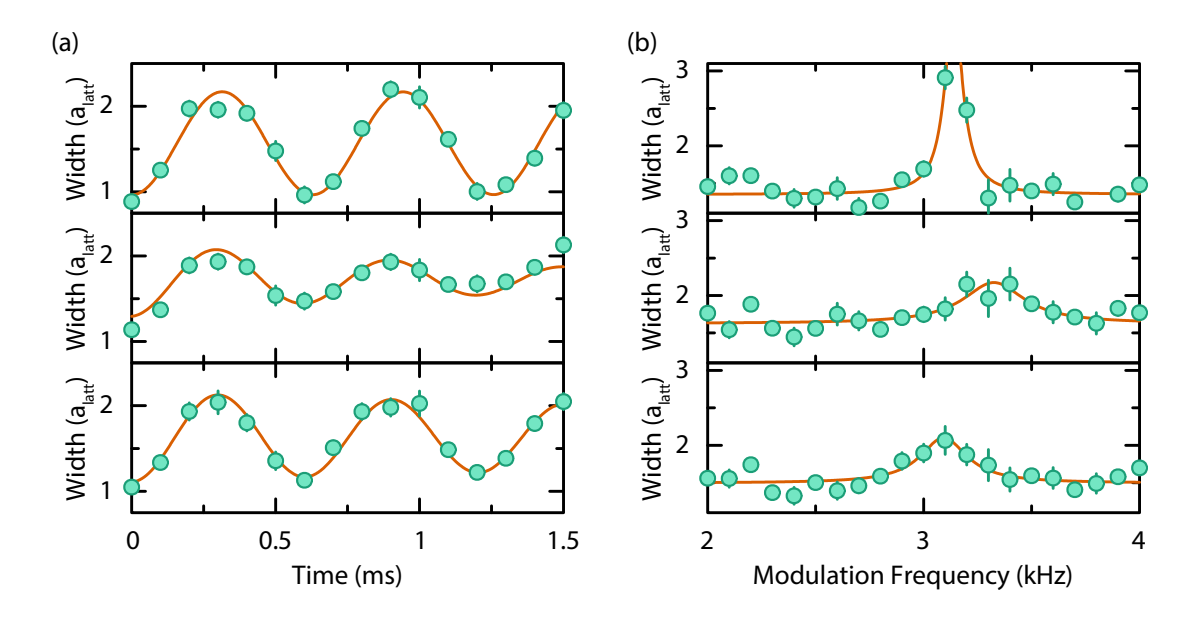


Figure 5.3: **Tilt potential calibration.** (a) Bloch oscillation method for characterization of tilt strengths. Each graph corresponds to a measurement of the local gradient at the position of one of the three stripes. The measured tilt strength is $F = h \times 1.64(3) \, \text{kHz}/a_{latt}$ with a maximal difference of 4.6% between stripes. (b) Lattice modulation method for characterization of tilt strengths. The measured tilt strength is $F = h \times 3.19(7) \, \text{kHz}/a_{latt}$ with a maximal difference of 7.5% between stripes.

5.2.2 Spatial Light Modulator

A spatial light modulator (SLM) is used to project sinusoidal potentials of tunable wavelength along the direction of the gradient, and also remove any harmonic confinement from trapping potentials in the region of interest, similar to what was done in [9]. This allows us to prepare initial density modulations of tunable wavelength. We also add "hard walls" in the direction perpendicular to the gradient in order to contain the atoms in that direction and keep the average density constant over the experimental runtime (see Fig. 5.1a).

5.2.3 Experimental parameters

The atoms are adiabatically loaded into the lattice plus SLM potential at zero gradient (no tilt). The sinusoidal component of the SLM potential is chosen such that the

resulting atom-density wave varies spatially with $0.0 \lesssim \langle \hat{n}_i \rangle \lesssim 1.2$ (see Fig. 5.1b-c), where $\hat{n}_i = \hat{n}_{i,\uparrow} + \hat{n}_{i,\downarrow}$. We also performed experiments with smaller-amplitude density waves and found no qualitative difference in our results as shown in Sec. 5.2.4. Once the initial density wave is prepared we suddenly turn off the sinusoidal component of the potential created by the SLM, and turn on the tilt potential, thus initiating the dynamics. We focus on a square region of interest with a size of 35×35 lattice sites and measure only the single spin component $\langle \hat{n}_{i,\uparrow} \rangle$ using fluorescence imaging [7] since in a spin-balanced system $\langle \hat{n}_i \rangle = 2 \langle \hat{n}_{i,\uparrow} \rangle$.

We performed all experiments at an optical lattice depth of $7.4(1) E_R$, where $E_R/h = 14.66 \,\mathrm{kHz}$ is the recoil energy and h is Planck's constant. This leads to a hopping rate of $t_h/h = 820(10) \,\mathrm{Hz}$. We work at a magnetic field of 595.29(4) G nearby a Feshbach resonance centered on 690 G. This leads to a scattering length of $472.0(9) \, a_0$, where a_0 is a Bohr radius, which translates to an interaction energy of $U/t_h = 3.9(1)$ in the Fermi-Hubbard Hamiltonian. We tune the tilt strength F to values of up to $Fa_{latt}/t_h \approx 6$ which allows us to explore tilts well above the crossover from diffusive to subdiffusive dynamics.

It is of note that we do not reach tilt strengths so strong that it would be accurate to describe our system over the experimental runtime using an effective Hamiltonian which exactly conserves the COM. Therefore we emphasize that this work does not focus on the physics of fracton-like systems with a strictly conserved dipole moment, nor does it explore the possible nonergodic dynamics in such systems, although these topics are an interesting direction for future research [39, 40, 46, 156, 157, 179, 180]. However, our tilted system does show an emergent conservation of the COM in the long wavelength limit where the potential energy of the tilt dominates the conserved total energy, and we believe this feature to be universal for tilted interacting lattice systems with energy and charge conservation as long as the particles are restricted to a limited set of bands.

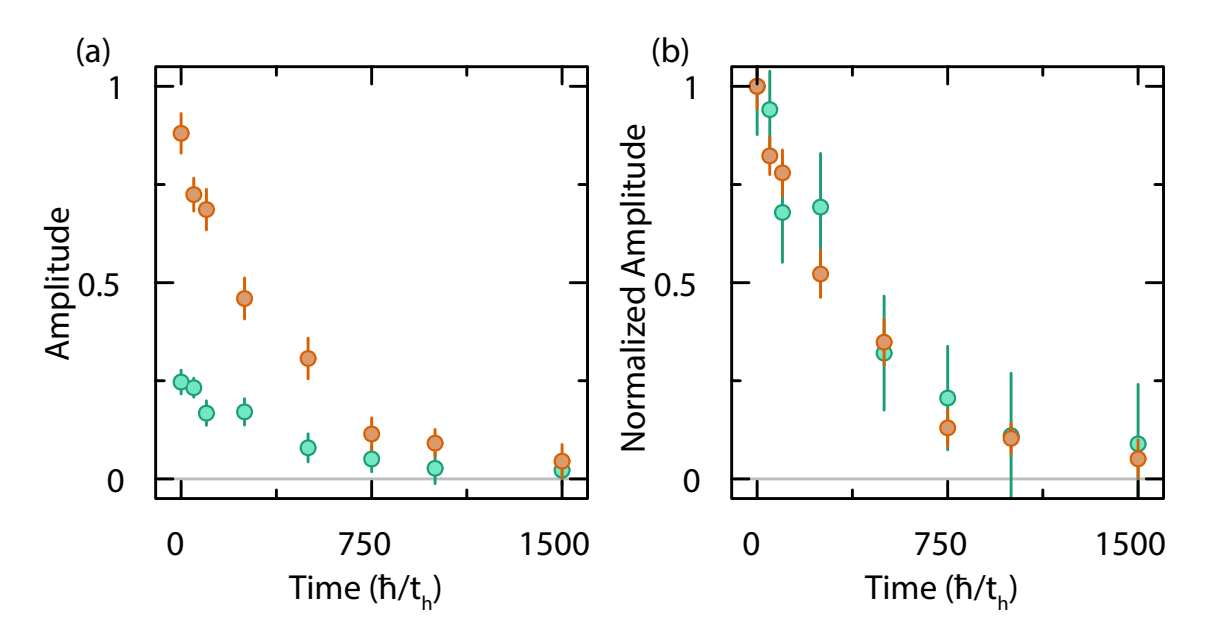


Figure 5.4: **Test of linear response.** Decay of the amplitude of the density modulation vs. time for two different initial amplitudes of the modulation. Here $\lambda = 11.46(3)a_{latt}$, $Fa_{latt}/t_h = 6.1(2)$ and $U/t_h = 3.9(1)$. (a) Shows the amplitudes. (b) Shows the amplitudes normalized to the baseline at t = 0.

5.2.4 Linear response

Our hydrodynamic model assumes linearity in the amplitude of the initial inhomogeneities. In this experiment, we worked with relatively large amplitude density modulations. In a previous study ([9]), we worked with very small amplitude modulations and fit to a linear hydrodynamic model we developed. In the "tilted" system studied in this work, we are no longer working close to a ground state, and as such, the strength of the modulation is not expected to be as important.

Fig. 5.4 shows a comparison between the decay of strong and weak density modulations in a tilted potential. We observe that when we normalize the sinusoid amplitude and look at its decay, there is no measurable difference between the decays within the errorbars. This justifies working with strong modulations in this work to reduce the statistical error in the measurements for a fixed number of repetitions.

5.3 Results

Our experimental protocol consists of preparing initial density waves of various wavelengths in a potential with tilt F and imaging the system's density profile after it has evolved under its own unitary dynamics for some time t. We analyze our data by averaging all measurements from a certain wavelength, tilt, and time, and we also average the density in the direction perpendicular to the tilt. This yields the averaged density profile along the tilted direction as a function of time, as shown in Fig. 5.1c. For each wavelength, tilt, and time we fit the density profile to a sinusoid, $n(x,t) = \bar{n} + A(t)\cos(\phi(t) + 2\pi x/\lambda)$, after adjusting for any small amount of atom loss, with the wavelength being fixed by the fit to the initial profile. We extract both the phase ϕ and amplitude A of the sinusoidal fit as a function of time, normalizing the amplitude by its initial value A(0). The main results of this paper are derived from tracking the decay of the amplitude A(t) with time.

5.3.1 Early-time dynamics

Any change in the phase with time is a result of the distance the center of mass "falls down" the tilt as the system heats up in the lowest band of the lattice potential. More precisely, an initial state with energy density corresponding to a finite temperature in the non-tilted Fermi-Hubbard system will slide down the gradient of the tilted potential. As this happens the tilt does work $\sim F\Delta x_{\rm COM}$ per particle for a bulk shift of $\Delta x_{\rm COM}$, and this work gets converted locally to kinetic and interaction energy in the system (the t_h and U terms) [174]. Since the t_h and U terms can only accommodate up to an energy of order $\sim t_h + U$ per particle before reaching infinite temperature, the shift of the COM of the system cannot be more than $\sim (t_h + U)/F$. We observe phase changes during the early-time dynamics that are consistent with this approximate

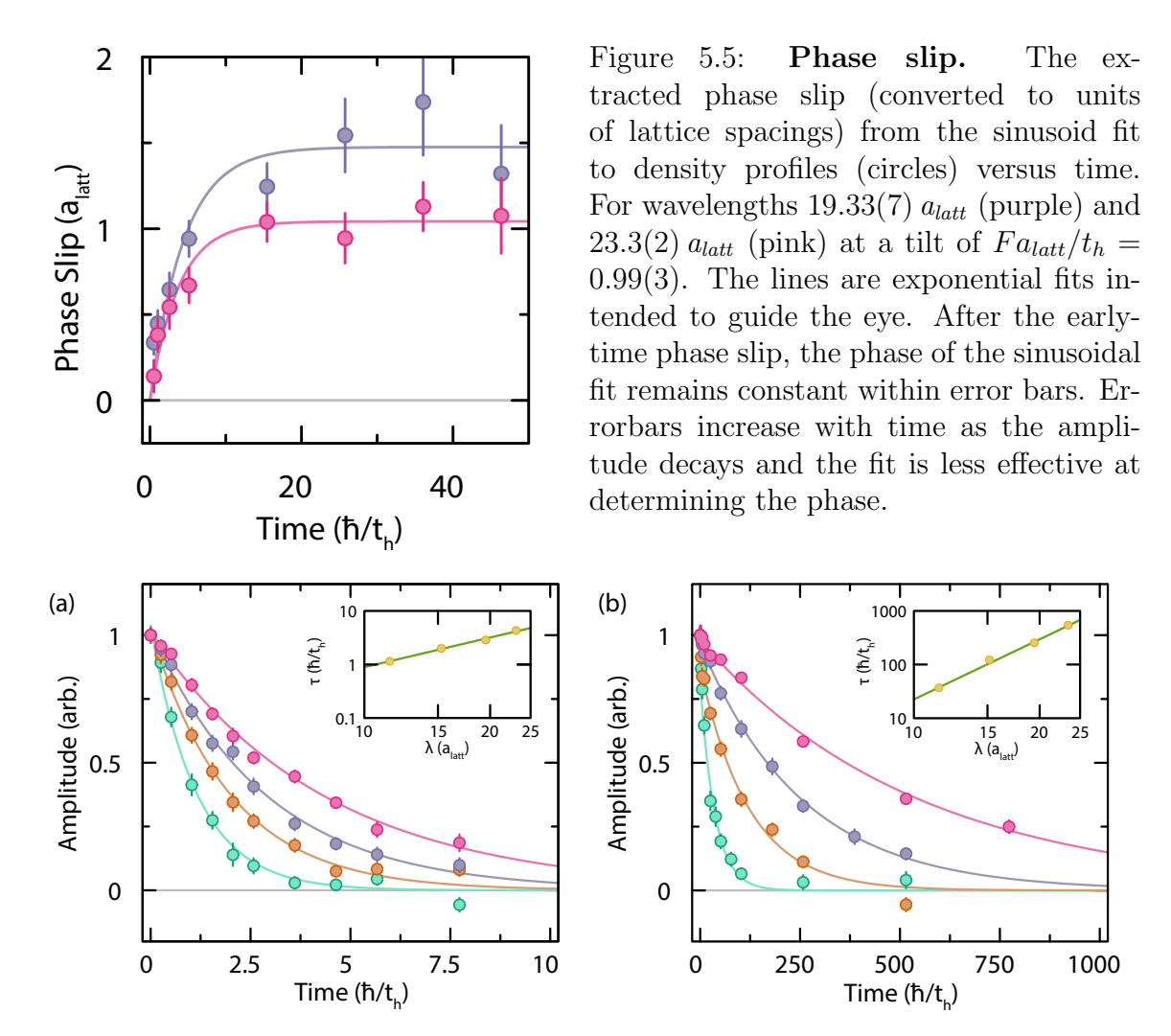


Figure 5.6: **Time decay of density waves.** Fitted normalized relative amplitudes of the periodic density modulation (circles) vs. time for wavelengths 11.46(3) (green), 15.16(5) (orange), 19.33(7) (purple), and 23.3(2) (pink) in units of a_{latt} . The lines are exponential fits to the decay at late times after any initial average heating (phase change). (Insets) Log-log plot of the fitted decay times vs. wavelength (yellow circles) and a power law fit of the form $\tau \propto \lambda^{\alpha}$ (green line). (a) Dataset for tilt strength $Fa_{latt}/t_h = 0$. (b) Dataset for tilt strength $Fa_{latt}/t_h = 2.00(3)$.

bound as shown in Fig. 5.5. We corroborate that the atoms are not excited to higher bands using a technique described in [11].

5.3.2 Late-time dynamics

At late times we observe an approximately exponential decay of the density modulation (see Fig. 5.6). We fit an exponential to these curves to extract decay times τ as a function of λ and F. This is done at tilts $Fa_{latt}/t_h \in$ $\{0, 0.39(1), 0.99(3), 2.00(3), 3.88(9), 6.1(2)\}$ and for initial density waves with wavelengths $\lambda/a_{latt} \in \{11.46(3), 15.16(5), 19.33(7), 23.3(2)\}$. We also use $\lambda/a_{latt} = 7.69(3)$ for $Fa_{latt}/t_h \approx 6$ as the decay time of the longest-wavelength modulation becomes very large for this tilt. Decay times that we observe vary increasingly with the tilt strength F, from 1-5 \hbar/t_h at zero gradient up to 10^3-10^4 \hbar/t_h for $Fa_{latt}/t_h \approx 6$. At each value of the tilt strength we fit a power law of the form $\tau \propto \lambda^{\alpha}$ to our measured decay times. Diffusive relaxation has a characteristic $\tau \propto \lambda^2$ dependence ($\alpha = 2$), while values of $\alpha > 2$ indicate slower subdiffusive dynamics. Fig. 5.6 shows the full analysis for two of the values of F. From the extracted exponents α we observe a crossover from diffusive relaxation at weak tilts, where $\alpha \approx 2$, to subdiffusive behavior with an exponent of $\alpha \approx 4$ at stronger tilts. This crossover is shown in Fig. 5.7 along with the theoretical prediction of our hydrodynamic model.

Our observation of diffusive dynamics at weak tilts is consistent with the analysis of Ref. [174], and with the diffusive transport observed in previous experiments on the same system at F = 0 [9], albeit at lower temperatures. The crossover to subdiffusion with $\alpha \approx 4$ at strong tilts was, until now, previously unobserved, and its observation and explanation is the main result of this work. Below, we construct a hydrodynamic model of our system to help explain these observations. We also further test our understanding of the mechanism behind the subdiffusive transport by experimentally verifying our model's predictions for the local temperature profile.

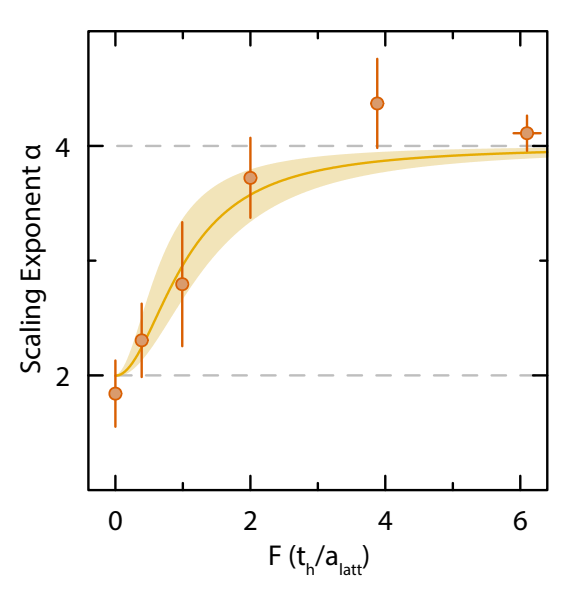


Figure 5.7: **Diffusive to subdiffusive** crossover. Extracted scaling exponent α for $\tau \propto \lambda^{\alpha}$ from datasets at different tilts (orange circles). As the tilt is increased from $Fa_{latt}/t_h = 0$ to $Fa_{latt}/t_h \approx 6$ the relaxation of initial density waves crosses over from characteristically diffusive ($\alpha = 2$) to subdiffusive with $\alpha \approx 4$. The shaded curve is a prediction of our hydrodynamic model which is derived in detail in the supplemental material of Ref. [13].

5.4 Hydrodynamic Model

We denote the non-tilt energy density due to t_h and U terms by e(x,t), and the number density of fermions by n(x,t). Our system is, on average, uniform along the y direction, so e and n are assumed to only depend on x and t. n is a conserved density and so is $\epsilon = e - Fxn$, the total energy density including the tilt potential.

For nonzero tilt, our system heats up to near infinite temperature within the lowest band, where the thermodynamic properties are readily calculated using the high-temperature expansion. There are then three unknown transport coefficients in the most general formulation of our model: diffusivities for each of the two conserved densities and a thermopower coefficient which might be significant for this system since the energy and atom transport are strongly coupled by the tilt. Our data does not have enough detail to allow us to estimate all three of these transport parameters. However, in the stronger-tilt regime where $\tau \sim \lambda^4$, a tilt-dependent thermal diffusivity is the only transport coefficient that enters in the relaxation, and thus this one parameter can be determined from our measurements. We therefore present our hydrodynamic model in this strong-tilt regime in Sec. 5.4.1, and encourage

interested readers to see the supplemental material of Ref. [13] for a more detailed presentation of the theory that includes the weaker-tilt diffusive regime.

5.4.1 Simplified Model

Let us first consider the infinite temperature equilibrium that our system thermalizes to at late times. This is a limit of zero inverse temperature $(\beta \to 0)$ and infinite chemical potential $(\mu \to \infty)$, with a finite spatially uniform $\beta \mu$; we call this equilibrium value $\bar{\beta}\mu$. This uniform equilibrium has atom number density $\bar{n} = 2e^{\bar{\beta}\mu}/(1 + e^{\bar{\beta}\mu})$ per site and zero expectation value of the hopping kinetic energy (the t_h term in the Hamiltonian). It is convenient when separating the energy into tilt and nontilt terms to choose the interaction term at each site to be $U(n_{\uparrow} - (\bar{n}/2))(n_{\downarrow} - (\bar{n}/2))$. This choice amounts to changing the total energy and potential V(x) by constants, so it does not change the physics. With this choice, the equilibrium nontilt energy density vanishes: $\bar{e} = 0$.

The density profile at finite long times has an additional sinusoidal component: $n(x,t) = \bar{n} + A_0 e^{-t/\tau} \cos kx$ with $k = 2\pi/\lambda$ (choosing the origin so there is no added phase in the argument of the cosine). In the strong tilt, long time, small k regime we are considering now, this density profile is at *local* equilibrium with a time-dependent and spatially nonuniform inverse temperature $\beta(x,t)$. We assume the system is also near global equilibrium, so we work to lowest order in A_0 and β . Near position x, if we have local equilibrium in the tilted potential V(x) = -Fx in this high temperature limit, the density is given by $n(x) = 2e^{\beta(\mu+Fx)}/(1+e^{\beta(\mu+Fx)})$. So, in the long wavelength limit we are considering here, the density gradient is

$$\frac{dn}{dx} = Fn\left(1 - \frac{n}{2}\right)\beta(x) \ . \tag{5.1}$$

For positive β the sign of this density gradient is familiar: at equilibrium, the density increases as one goes to lower potential energy, since the atoms are favored to sit at lower-energy positions. At negative temperature for fermions in a band, higher-energy positions are instead favored, so the density gradient is of the opposite sign. Quantitatively, the product $F\beta$ captures how much a system at inverse temperature β "notices" the tilt F. Thus indeed we expect that when the system maintains local equilibrium, $dn/dx \propto F\beta$ holds to leading order near $\beta = 0$. It follows that to leading order the temperature profile is given by $-A_0ke^{-t/\tau}\sin kx = F\bar{n}(1-(\bar{n}/2))\beta(x,t)$. Using this result, along with a high temperature expansion to write e as a function of β to leading order, we obtain the nontilt energy profile

$$e(x,t) = \frac{A_0}{F} \left(4t_h^2 + U^2 \frac{\bar{n}}{4} \left(1 - \frac{\bar{n}}{2} \right) \right) k e^{-t/\tau} \sin kx$$
 (5.2)

at local equilibrium to lowest order in A_0 and k. Now that we have determined the profiles of n and e assuming local equilibrium, next we consider the dynamics and use energy and number conservation to determine the relaxation time τ . In the regime we are now considering, the rate-limiting bottleneck is the transport of nontilt energy (heat) through the system. This limits the rate at which tilt energy can be converted to heat and dissipated to the rest of the system, and thus the rate at which the whole system relaxes.

The relaxation of the number density implies, via the continuity equation for atom number, an atom number current density of

$$j_n(x,t) = \frac{A_0}{k\tau} e^{-t/\tau} \sin kx$$
 (5.3)

This current density flows locally along the tilt direction, locally converting tilt energy to nontilt energy. In addition, there is a heat current $j_h(x,t) = -D_{\text{th}}\nabla e(x,t)$ flowing due to the temperature gradients, where $D_{\text{th}}(F)$ is a tilt-dependent thermal diffusivity.

Conservation of energy is then

$$\dot{e} = D_{th} \nabla^2 e + F j_n , \qquad (5.4)$$

showing the contribution of heat diffusion and the conversion of energy from tilt to nontilt due to the atom current j_n . In the strong tilt regime we are considering, the two terms on the RHS of Eqn. (5.4) are each much larger in magnitude than the LHS: the motion of the atoms converts tilt energy to nontilt energy and this is dissipated by thermal transport, while the amplitude of the inhomogeneities decays slowly $(D_{\text{th}}k^2\tau \gg 1)$. In this strong tilt regime, the decay rate is

$$\frac{1}{\tau} = \frac{D_{\rm th}k^4}{F^2} \left(4t_h^2 + U^2 \frac{\bar{n}}{4} \left(1 - \frac{\bar{n}}{2} \right) \right) \ll D_{\rm th}k^2 , \qquad (5.5)$$

and the condition for the validity of this regime is

$$k^2 \left(4t_h^2 + U^2 \frac{\bar{n}}{4} \left(1 - \frac{\bar{n}}{2}\right)\right) \ll F^2$$
 (5.6)

We use Eqn. (5.5) to extract the infinite-temperature thermal diffusivity $D_{\rm th}(F)$ as a function of tilt strength F in the regime consistent with $\tau \propto \lambda^4$ and plot the result in Fig. 5.8.

From the validity condition of Eqn. (5.6) we can also estimate the location of the crossover shown in Fig. 5.7. Plugging in the experimental values of $U/t_h = 4$ and $\bar{n} = 0.6$, and any value of k from the experimental range $ka_{latt} \in [2\pi/24, 2\pi/12]$, we get the condition that $\alpha \approx 4$ when $Fa_{latt}/t_h \gg 1$, which is consistent with the data shown in Fig. 5.7. A more complete model is detailed in the supplemental material of Ref. [13], and this model is used to derive the superimposed curve of Fig. 5.7 which agrees quantitatively with our experimental results. This more detailed model also gives the thermal diffusivity D_{th} in terms of all of the transport coefficients, including

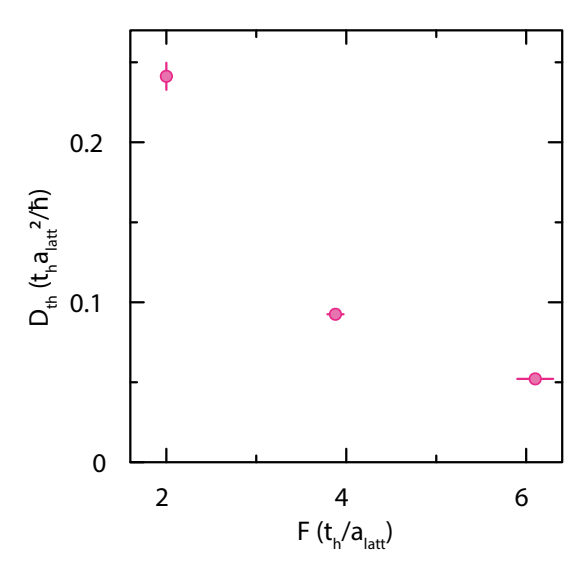


Figure 5.8: **Thermal diffusivity.** Extracted thermal diffusivity (circles) vs. gradient. The values were extracted by doing a fit of our hydrodynamic model to all wavelengths of each gradient simultaneously as shown in Fig. 5.10.

the thermopower. We therefore conclude that our hydrodynamic model captures the essential physics leading to the main observation of this paper: the crossover from diffusive to subdiffusive relaxation with $\tau \propto \lambda^4$ as the tilt becomes strong.

The infinite-temperature thermal diffusivity $D_{\rm th}(F)$ that we are able to measure in this long-wavelength limit is the thermal diffusivity in the presence of a tilt potential and the absence of a mass current. In this long-wavelength limit $(k \to 0)$ the heat current becomes much larger than the mass current: $j_h \sim A_0 k^2 / F \gg j_n \sim A_0 k^3 / F^2$. In the limit of small tilt, this thermal diffusivity must be of order $t_h a_{latt}^2 / \hbar$, with an order one prefactor that depends on \bar{n} and U/t_h . In the large tilt regime where $Fa_{latt} \gg 4t_h$ this heat must be conducted by processes that are second-order in the hopping, with one uphill hop and one downhill hop and the intermediate virtual state off-shell in energy by Fa_{latt} . This produces an effective matrix element $\sim t_h^2/F$ for these processes, which should result in $D_{\rm th} \sim 1/F^2$ at large F. But our results are actually in an intermediate regime of F, where we are able to access this subdiffusive regime, but we are not fully in the large F regime where one step in the tilt energy is large compared to the interaction U and the bandwidth $4t_h$ for motion along equipotential rows. The results in Fig. 5.8 seem consistent with matching on

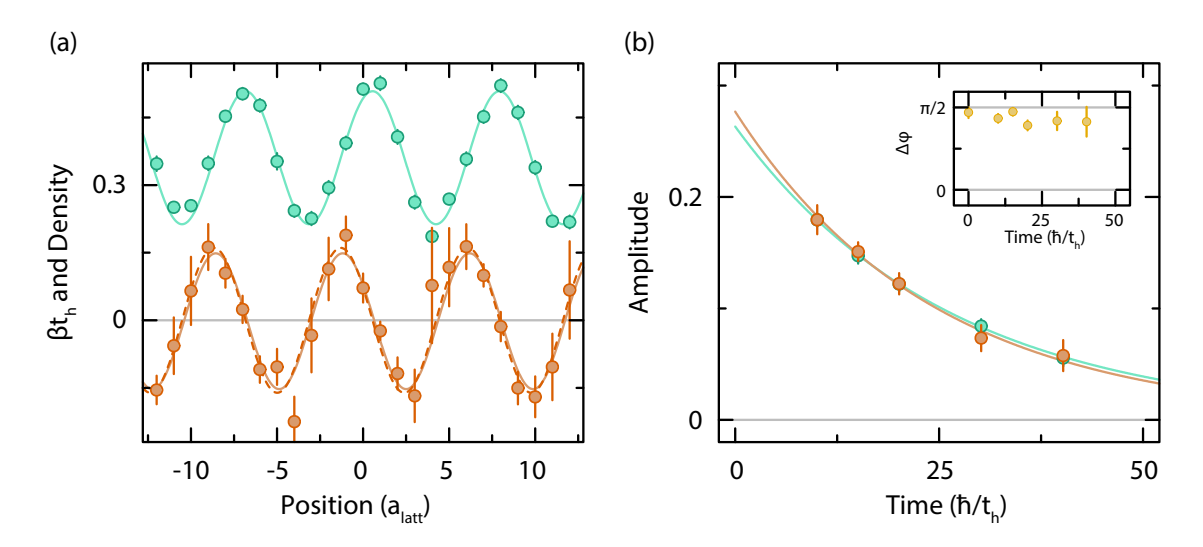


Figure 5.9: Local inverse temperature. Near infinite temperature, the density of singles can be used for thermometry. For a tilt strength of $Fa_{latt}/t_h=3.4(1)$ (potential is V(x)=-Fx) and periodic modulation of wavelength 7.69(3) a_{latt} , we measure the average single component density (green) and the density of singles (not shown) in order to extract the local inverse temperature of the cloud (orange). (a) The measured average single component density (green circles) and extracted inverse temperature βt_h (orange circles) with sinusoid fits (solid lines) after a decay time of $15.1\hbar/t_h$. In the case of the inverse temperature, the dashed line is the predicted inverse temperature profile from the density fit and local equilibrium (Eqn. 5.1). The fitted offset of the inverse temperature is $\bar{\beta}t_h=-0.002(8)$ in agreement with an infinite average local temperature. (b) The amplitude of the density (green) and inverse temperature (orange) modulations vs. time (circles) with exponential decay fits (solid lines). (inset) Shows the phase difference of the sinusoid fits between the single component density and the extracted local inverse temperature vs. time (yellow circles).

to these expected small- and large-F limiting behaviors, but we leave quantitative theoretical estimation of $D_{th}(F)$ for future work.

The picture we have laid out in this section is one where, at strong tilts and long wavelengths, the system quickly achieves local equilibrium, locking the local inverse temperature to the density profile (Eqn. (5.1)). As the density profile decays, local number density currents flow, and by conservation of energy this necessitates the flow of nontilt energy in the system. It is this flow of nontilt energy that we show bottlenecks the relaxation in the large F regime, and thus $D_{\rm th}$ sets the relaxation rate of the system. This mechanism only relies on the fact that the system does thermalize,

has a finite maximum kinetic and interaction energy per particle, and obeys energy and charge conservation. Thus our qualitative conclusions are not specific to the Fermi-Hubbard system we study but can be considered universal. A prediction of this understanding is local equilibrium between $\beta(x,t)$ and n(x,t) summarized in Eqn. (5.1). We verify this prediction by measuring the single component density and singlen occupancy profiles in our system and solving for the inverse temperature in the atomic limit, which is an effective method of thermometry at such high temperatures. In Fig. 5.9a-b we show both the density and local inverse temperature profiles, the decay of both of their amplitudes, and the phase difference between them in time (inset). From this we see that the $\beta(x,t)$ profile is at local equilibrium near infinite temperature ($\beta = 0$), locked at a quarter wavelength phase shift from the density profile, and both profiles decay together in time, as predicted by our understanding of the subdiffusive regime of this system.

5.4.2 Complete hydrodynamic model

A full derivation of the complete hydrodynamic model taking into account the charge and energy conservation laws of the system is presented in the supplemental material of Ref. [13]. The derivation works by writing down the currents in term of entropic "forces" and their Onsager's reciprocal relations including a crossterm. We can calculate these relations using a high-temperature expansion of the entropy. The resulting system of equations can be used to find regimes of charge dynamics characteristically diffusive $(\propto k^2)$ and subdiffusive $(\propto k^4)$ as a factor of the tilt strength. In the limit of large F (and/or small k) we find that the slowest decay rate can be written as

$$\Gamma_{-} \approx \frac{D_{\text{th}}}{F^2} \left(\frac{s_{nn}}{s_{ee}} - \frac{s_{ne}^2}{s_{ee}^2} \right) k^4, \tag{5.7}$$

where D_{th} is the thermal diffusivity and $s_i j$ are the high-temperature expansion terms of the entropy.

5.4.3 Simultaneous fitting of the model

As explained in the previous sections, there is a fast and a slow exponential decay solution to our hydrodynamic model. In the strong tilt regime, Eqn. 5.7 shows that the slow decay depends only on the thermal diffusivity $D_{\rm th}$.

We perform a simultaneous fit to all wavelengths at a given tilt strength as explained in the supplement of [9]. The fitting function is

$$A(t) = A_0 e^{-\Gamma_{-}(D_{\text{th}}, F, k)t},$$
 (5.8)

and it is fitted only to the late-time decay. Here, A_0 is a fitting parameter that can vary for each wavelength while $D_{\rm th}$ is fitted globally to all wavelengths. The parameters F and k are fixed according to our experimentally measured values. The fitting to this model is shown in Fig. 5.10 and the extracted diffusivities are shown in Fig. 5.8.

5.5 Conclusion

We studied a new regime of thermalization in a square-lattice cold-atom Fermi-Hubbard system subject to an external linear potential. Our system was effectively closed and evolved under its own unitary dynamics starting from prepared initial density waves of various wavelengths λ . By observing how the amplitude of these initial density modulations evolved in time we found two qualitatively different hydrodynamic regimes and a crossover between them: At weak tilts the system relaxes diffusively, in accordance with previous theory [174] and experiments [9]. At strong tilts, we found a new regime where the system relaxes subdiffusively with a decay

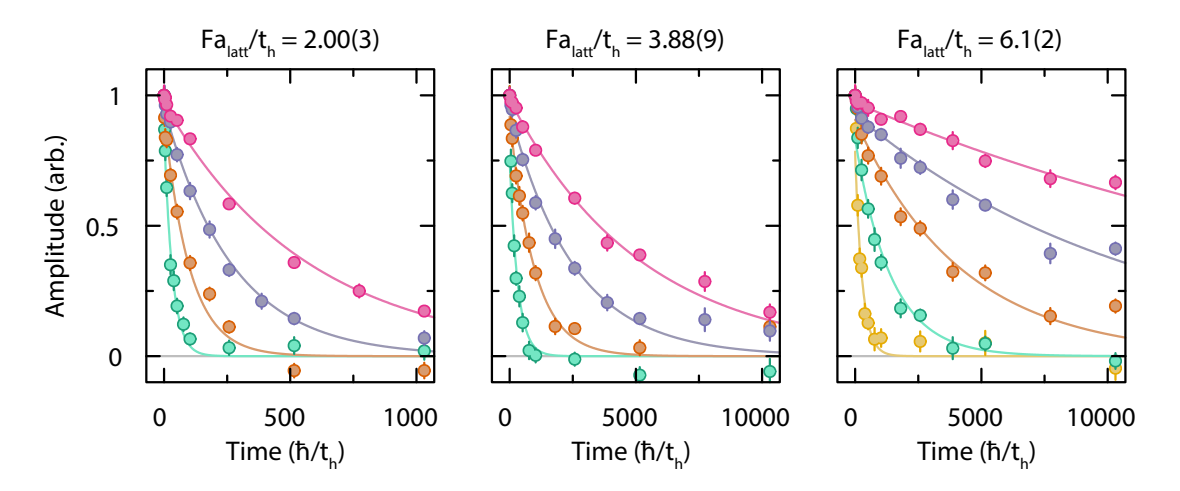


Figure 5.10: **Simultaneous fitting of hydrodynamic model.** Fitted normalized relative amplitudes of the periodic density modulation (circles) vs. time for wavelengths 7.69(3) a_{latt} (yellow), 11.46(3) a_{latt} (green), 15.16(5) a_{latt} (orange), 19.33(7) a_{latt} (purple), and 23.3(2) a_{latt} (pink) at different tilts. The lines are simultaneous fits of the hydrodynamic model to the long-time decay after the initial average heating (phase change). We are able to extract the thermal diffusivity through this fitting method.

time τ that scales as $\tau \propto \lambda^4$. We argued that this subdiffusive behavior is a result of having to "drain" the large reservoir of tilt energy via the bottleneck of heat transport en route to global equilibrium, and is captured effectively by a hydrodynamic description with the system remaining near local equilibrium. To test this understanding we measured the local temperature profile and do indeed find that the system remains near local equilibrium as it relaxes in this subdiffusive regime. In the supplemental material of Ref. [13], we also develop and present a more complete and detailed hydrodynamic model that quantitatively captures the universal crossover between the diffusive and subdiffusive regimes (Fig. 5.7). In the strongly tilted regime we used our model to extract the tilt-strength-dependent thermal diffusivity that bottlenecks the relaxation of the system. One perspective on why this novel subdiffusive regime appears is that in the strong-tilt and long-wavelength limit the center-of-mass potential energy is the dominant part of the total energy, so energy conservation becomes an emergent almost-conservation of the center of mass.

In contrast to recent theoretical studies of potential ergodicity breaking in tilted 1D systems [156, 157], in this work we focused on the novel effects of a tilt on the approach to equilibrium in an isolated system that does indeed thermalize. This thermalization was robust because our system had a tilt potential along only one of the two principal axes of the lattice, and the resulting unconstrained motion of atoms in the perpendicular direction produced good thermal baths in each such row of the lattice. To arrest this thermalization more microscopically, one avenue of future exploration will be to apply tilt potentials along both axes of the lattice to suppress such local thermalization.

5.5.1 Outlook

After this project, we focused back on Rydberg dressing but had to wait yet again due to technical difficulties. In this second interim, we re-built the laser system to generate tilt potentials as shown in Fig. 5.2b. With this update we were able to generate much stronger tilt potentials. However, we very quickly realized that even these stronger tilt strength were not enough to reach the regime of Hilbert space fragmentation due to our large system sizes. We did however study a second transition to subdiffusive dynamics for the system in all directions. In this regime we found that the system did not quickly reach local equilibrium in the same way that we found in Fig. 5.9. Potentially showing that we were starting to peek into the pre-thermal regime of fractonic physics. It is my hope that in the future, this 2D tilted system will be studied again and our theory collaborators have some ideas of how to proceed.

It is also important to note that recently, non-ergodic dynamics have been observed in tilted 1D Fermi-Hubbard chains [181].

Chapter 6

Quench Dynamics of a Fermi Gas with Strong Long-Range Interactions

This chapter presents the work published as

E. Guardado-Sanchez, B. M. Spar, P. Schauss, R. Belyansky, J. T. Young,
P. Bienias, A. V. Gorshkov, T. Iadecola, and W. S. Bakr. Quench dynamics
of a Fermi gas with strong nonlocal interactions. *Phys. Rev. X* 11, 021036
(2021) [14]

In this chapter, we present experiments were we induce long-range interactions in a 2D Fermi gas in an optical lattice using Rydberg dressing. The system is approximately described by a t-V model on a square lattice where the fermions experience isotropic nearest-neighbor interactions and are free to hop only along one direction. This is the first quantum simulation using a degenerate quantum gas with strong non-local interactions. Much effort has been dedicated to this goal, including explorations of quantum gases of magnetic atoms [20–23] and polar molecules [24, 25] by many groups.

6.1 Introduction

Ultracold gases are a versatile platform for studying quantum many-body physics [3]. The ability to engineer and control the interactions in these systems has played an important role in observing novel phases of matter including crossover fermionic superfluids [182] and dipolar supersolids [20, 183, 184] and in studying out-of-equilibrium dynamical processes such as thermalization [21]. Recent efforts have focused on degenerate quantum gases with long-range interactions including those of magnetic atoms [20–23] and polar molecules [24, 25]. These systems may be distinguished from other quantum platforms with long-range interactions including ions [26, 27], Rydberg atoms [15], polar molecules in optical tweezers [28, 29] and atoms in optical cavities [30], in that the particles are itinerant. This can lead to an interesting interplay between interactions, kinetic energy and quantum statistics. Rydberg dressing has been proposed as an alternative route to realize quantum gases with tunable long-range interactions [17–19]. Experimental demonstrations of Rydberg dressing [55, 71–75, 88–91] have been performed with localized atoms or quantum gases of heavy atoms where observation of motional effects has been elusive.

Here we investigate Rydberg dressing of lithium-6, a light fermionic atom. Its fast tunneling in an optical lattice allows us to study the quench dynamics of itinerant fermions with strong, purely off-site interactions.

Atoms in a quantum gas resonantly coupled to a Rydberg state experience strong van der Waals interactions many orders of magnitude larger than their kinetic energy for typical interatomic spacings, hindering access to the interesting regime where the two energy scales compete. At the same time, the population of atoms in the Rydberg state decays on a timescale of tens of microseconds, short compared to millisecond motional timescales. Rydberg dressing addresses both of these issues. Using an off-resonant coupling, the atoms are prepared in a laser-dressed eigenstate $|g_{\rm dr}\rangle \approx |g\rangle + \beta |r\rangle$ of predominant ground state $(|g\rangle)$ character and a small Rydberg

 $(|r\rangle)$ admixture, where $\beta = \frac{\Omega}{2\Delta} \ll 1$, Ω is the coupling strength, and Δ is the laser detuning from the transition frequency. This enhances the lifetime of the dressed atom by a factor of $1/\beta^2$ relative to the bare Rydberg state lifetime. On the other hand, the interaction between two atoms a distance r apart is reduced in strength and can be approximately described by a tunable softcore potential $V(r) = V_{\text{max}}/(r^6 + r_c^6)$ with strength $V_{\text{max}} \sim \beta^3 \Omega$ and range $r_c \sim (|C_6/2\Delta|)^{1/6}$, where C_6 is the van der Waals coefficient for the Rydberg-Rydberg interaction. Early experiments with 3D quantum gases were limited by rapid collective atom loss attributed to a blackbody-induced avalanche dephasing effect [71–74]. Nevertheless, Rydberg dressing has been successfully used to entangle atoms in optical tweezers [88], perform electrometry in bulk gases [91], and study spin dynamics [55, 75, 90].

In this work, we report on the single-photon Rydberg dressing of a 2D 6 Li Fermi gas in an optical lattice in the presence of tunneling. This results in a lattice gas of fermions with strong, non-local interactions. We characterize the interaction potential using many-body Ramsey interferometry [75]. A careful study of the lifetime of spin-polarized gases shows different behavior compared to previous Rydberg dressing realizations, with the lifetime depending strongly on the density but not on the atom number at fixed density. We also observe that the presence of tunneling in the system has no effect on the lifetime. Finally, we use this platform to realize a 2D coupled-chain t-V model consisting of interaction-coupled chains and study the short-time quench dynamics of charge-density wave states, finding that the strong attractive interactions inhibit the motion of the atoms.

Theoretical studies of the 1D t-V model [47, 48] have shown that it can exhibit Hilbert-space fragmentation (HSF) [39, 40], in which dynamical constraints "shatter" the Hilbert space into exponentially many disconnected subspaces. Like many-body localization (MBL) [41, 42] and quantum many-body scars [43, 44], HSF is a mechanism whereby isolated quantum systems can fail to reach thermal equilibrium after a quantum quench [45]. In the t-V model, HSF arises in the limit of strong interactions, where the number of "bond" excitations, i.e., nearest-neighbor pairs of fermions, joins the total fermion number as a conserved quantity. Our mixed-dimensional t-V model inherits properties of the 1D version, including the HSF in the limit $t/V \to 0$.

6.2 Experimental setup

Our system consists of a degenerate Fermi gas of ⁶Li atoms in a square optical lattice of spacing $a_{\text{latt}} = 752 \,\text{nm}$ (Fig. 6.1a) [12]. We apply a 591.8(3) G magnetic field perpendicular to the 2D system. We load spin-polarized gases prepared in a state that may be labeled at high fields as $|nl, m_l, m_s, m_I\rangle = |2S, 0, -1/2, 1\rangle = |1\rangle$, or alternatively $|2S, 0, -1/2, -1\rangle = |3\rangle$ depending on the measurement. We have control over the initial density profile by employing a spatial light modulator. Using a 231 nm laser beam with linear polarization parallel to the magnetic field and propagating along the lattice x-direction, we couple the ground state atoms to the $|28P, 0, -1/2\rangle$ Rydberg state. By tuning the intensity and the detuning of the dressing light, we have real-time control over the isotropic soft-core interaction potential between the atoms in the gas (Fig. 6.1b).

6.2.1 Simulation of a t - V model

The lattice system is described by a single-band spinless fermion Hamiltonian

$$\hat{H} = -t \sum_{\langle i,j \rangle} (\hat{c}_i^{\dagger} \hat{c}_j + \text{h.c.}) + \sum_{i \neq j} \frac{V_{ij}}{2} \hat{n}_i \hat{n}_j + \sum_i \delta_i \hat{n}_i, \tag{6.1}$$

where t is a tunneling matrix element, V_{ij} is the off-site interaction [Eq. 3.6 and Fig. 6.1b(inset)] and δ_i is the potential due to single-particle light shifts contributed by the lattice and Rydberg dressing beams. Since our dressing beam is tightly fo-

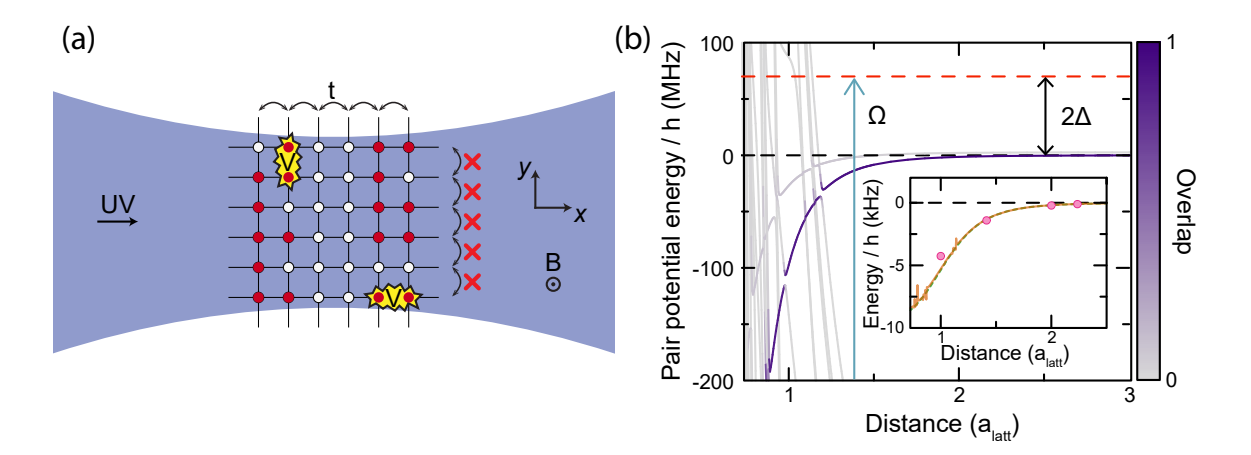


Figure 6.1: Realization of a t-V model with Rydberg dressing. (a) The Rydberg dressing beam propagates along the x-direction of the lattice, effectively decoupling 1D chains in the y-direction due to a differential light shift. Hopping of fermions (red dots) along the x-direction is unaffected. Interactions are isotropic. (b) ⁶Li pair potentials for dressing to the state $|28P, m_l = 0, m_s = -1/2\rangle$ calculated using [87]. The color of the lines represents the overlap with the target pair-state $(|28P, 0, -1/2\rangle \otimes |28P, 0, -1/2\rangle)$ coupled via the laser with Rabi coupling Ω and detuning Δ from the target state. Inset: Calculated dressed potential for $\Omega = 2\pi \times 7.66$ MHz and $\Delta = 2\pi \times 35$ MHz taking into account the overlaps to all pair potentials (orange solid line). The dashed green line represents the expected dressed potential for a simple van der Waals potential with $C_6 = h \times 90.19$ MHz $a_{\rm latt}^6$. Pink points are the interaction at each lattice distance taking into account the wavefunction spread of the atoms.

cused with a waist of $16.1(4) \mu m$, the change in δ between rows in the y-direction, which is orthogonal to the beam propagation axis, is much larger than t (for typical experiments presented in Sec. 6.5, the minimum change in δ between rows is > 3t near the intensity maximum of the Rydberg dressing beam). On the other hand, because of the large Rayleigh range of the beam ($\sim 3.5 \,\mathrm{mm}$), the variation of δ along the beam propagation direction (x-direction) is negligible. To first approximation, we drop the light shift term and the hopping along the y-direction. Thus, we can rewrite our Hamiltonian as a coupled-chain t-V model of the form

$$\hat{H} = -t \sum_{\langle i,j \rangle_x} (\hat{c}_i^{\dagger} \hat{c}_j + \text{h.c.}) + \sum_{i \neq j} \frac{V_{ij}}{2} \hat{n}_i \hat{n}_j.$$

$$(6.2)$$

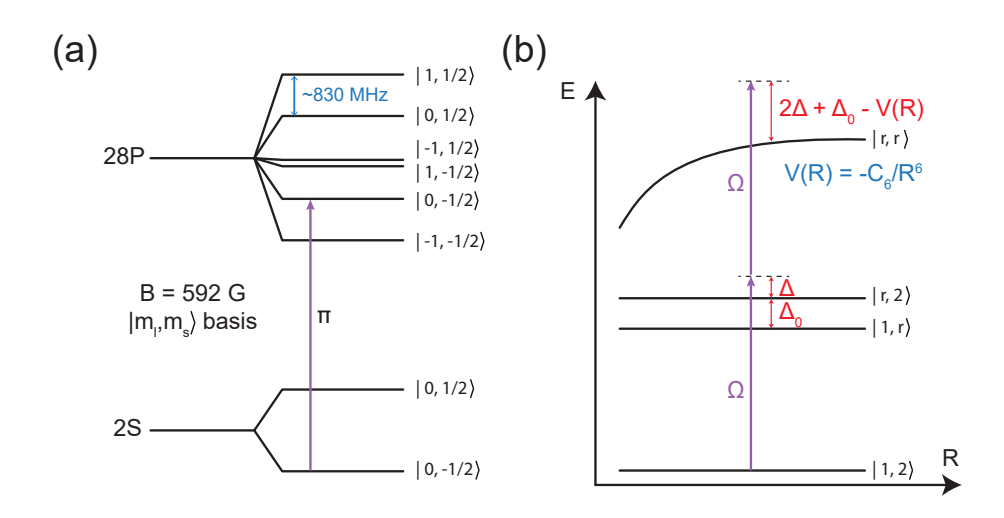


Figure 6.2: **Rydberg dressing of** ⁶**Li.** (a) Level diagram showing the hyperfine ground states of ⁶Li directly coupled to the 28P Rydberg state using linearly (π) polarized light at a field of 592 G. The basis used is $|m_l, m_s\rangle$. (b) Rydberg dressing scheme for two atoms in different hyperfine ground states $|1\rangle$ and $|2\rangle$ coupled to the Rydberg state $|r\rangle$. Ω is the Rabi coupling of the laser, Δ is the detuning from the resonant transition between $|1\rangle$ and $|r\rangle$, Δ_0 is the hyperfine splitting between $|1\rangle$ and $|2\rangle$ and $V(R) = -C_6/R^6$ is the van der Waals interaction potential between two Rydberg states $|r\rangle$.

6.2.2 Ground and Rydberg states used in the experiments

We work at a magnetic field of 592 G pointing in the direction perpendicular to the 2D lattice plane. At this field, both the ground and Rydberg states are in the Paschen-Back regime such that we can approximately label them using the $|nl, m_l, m_s, m_I\rangle$ basis (Fig. 6.2a). The hyperfine ground states we use are $|1\rangle$, $|2\rangle$ and $|3\rangle$ numbered from lowest to highest in energy and having $m_I = 1, 0, -1$ respectively. For the Rydberg states, the nuclear spin splitting is negligible so states with different m_I can be considered degenerate. This approximation means that two atoms in different hyperfine ground states will couple to Rydberg states at the same energy (both labeled as $|r\rangle$) and interact with each other via a van der Waals potential (Fig. 6.2b).

In our quenches and lifetime measurements, we always start with a spin-polarized gas of either state $|1\rangle$ or $|3\rangle$ atoms (both states are essentially equivalent and we happen to have take some of our data in this paper using one or the other). However,

for the interferometry measurements, we need to take into account the dressed interaction potential between two atoms in different hyperfine ground states which couple to $|r\rangle$.

6.3 Rydberg-dressed interaction potentials

In order to characterize the Rydberg dressing interaction potentials, we perform many-body Ramsey interferometry between states $|1\rangle$ and $|2\rangle = |2S, 0, -1/2, 0\rangle$ following the procedure introduced in Ref. [75]. Starting from a spin-polarized band insulator of atoms prepared in state $|1\rangle$ in a deep lattice that suppresses tunneling, a $\pi/2$ radiofrequency pulse prepares a superposition of state $|1\rangle$ and $|2\rangle$, which acquire a differential phase during a subsequent evolution for time T in the presence of the dressing light. Unlike Ref. [75], the splitting between the hyperfine ground-states of ⁶Li is comparable to the detuning Δ of the dressing laser (Fig. 6.3a), and both states are significantly dressed by the light (Sec. 3.3.3). First, we obtain the spatial profile of the Rabi coupling strength $\Omega(i,j)$ by measuring the population of $|2\rangle$ after a $\pi/2 - T - \pi/2$ pulse sequence using a detuning $\Delta = 2\pi \times 100\,\mathrm{MHz}$. The large detuning is chosen so that the interactions, whose strength scales as $1/\Delta^3$, are negligible, while the single-particle light shifts that scale as $1/\Delta$ lead to a large differential phase during the evolution. From these measurements, we extract the waist of the beam $(16.1(4) \,\mu\text{m})$ and measure Rabi couplings up to $\Omega = 2\pi \times 9.48(8)\,\text{MHz}$ (Fig. 6.3b). The measured spatial profile of the Ramsey fringe frequency confirms the rapid variation of δ_i along the y-direction, while no variation of δ_i is observed along the x-direction within the statistical uncertainty of the measurement ($\sim 1 \text{ kHz}$).

To probe interactions in the system, we switch to a smaller detuning $\Delta = 2\pi \times 35 \,\text{MHz}$. We measure density correlations of state $|1\rangle$ $(C(\mathbf{r}) = \langle n_1(\mathbf{r})n_1(0)\rangle - \langle n_1(\mathbf{r})\rangle \langle n_1(0)\rangle)$ after a spin-echo pulse sequence $(\pi/2 - T - \pi - T - \pi/2)$ which

eliminates differential phases due to the light shift. Fig. 6.3c shows the measured correlations after different evolution times T compared to the theoretical expectation (Sec. 3.8.1). Fig. 6.3d depicts the evolution of the nearest-neighbor and next-nearest-neighbor correlations with the correlation offset $C(\infty)$ subtracted. This offset is attributed to correlated atom number fluctuations in the images [75]. We find good agreement with the theoretical model, which predicts a nearest-neighbor (next-nearest-neighbor) attractive interaction $|V_{10}| = h \times 4.2(2)$ kHz ($|V_{11}| = h \times 1.37(6)$ kHz) (Fig. 6.1b)

6.4 Lifetime Characterization

To probe coherent many-body physics in our system, the lifetime τ of the sample has to be larger than the interaction and tunneling times. Atoms resonantly excited to a Rydberg state are lost from our system on a timescale of tens of microseconds for several reasons: photon recoils due to spontaneous emission and large forces due to anti-trapping optical potentials and due to interactions with other Rydberg atoms. Due to its Rydberg admixture, an isolated dressed atom decays with a lifetime $\tau_{\rm eff} =$ τ_0/β^2 , where τ_0 is the lifetime of the Rydberg state determined by radiative and blackbody-driven transitions to other states. Previous experiments with frozen 2D and 3D systems have observed much shorter lifetimes than τ_{eff} [71–75]. A simplified model used to explain these experiments considers a blackbody-driven decay of the dressed state to a pure Rydberg state of opposite parity. The first such contaminant appears in the system on a timescale $\tau_c = \tau_{\rm BB}/(N\beta^2)$ where $\tau_{\rm BB}$ is the blackbody lifetime of the Rydberg state and N is the number of atoms in the system. This atom interacts with other dressed atoms through resonant state-exchange characterized by a C_3 coefficient, broadening the Rydberg line. In particular, other atoms at a certain facilitation radius $(|C_3/\Delta|)^{1/3}$ will be resonantly excited, leading to avalanche loss of

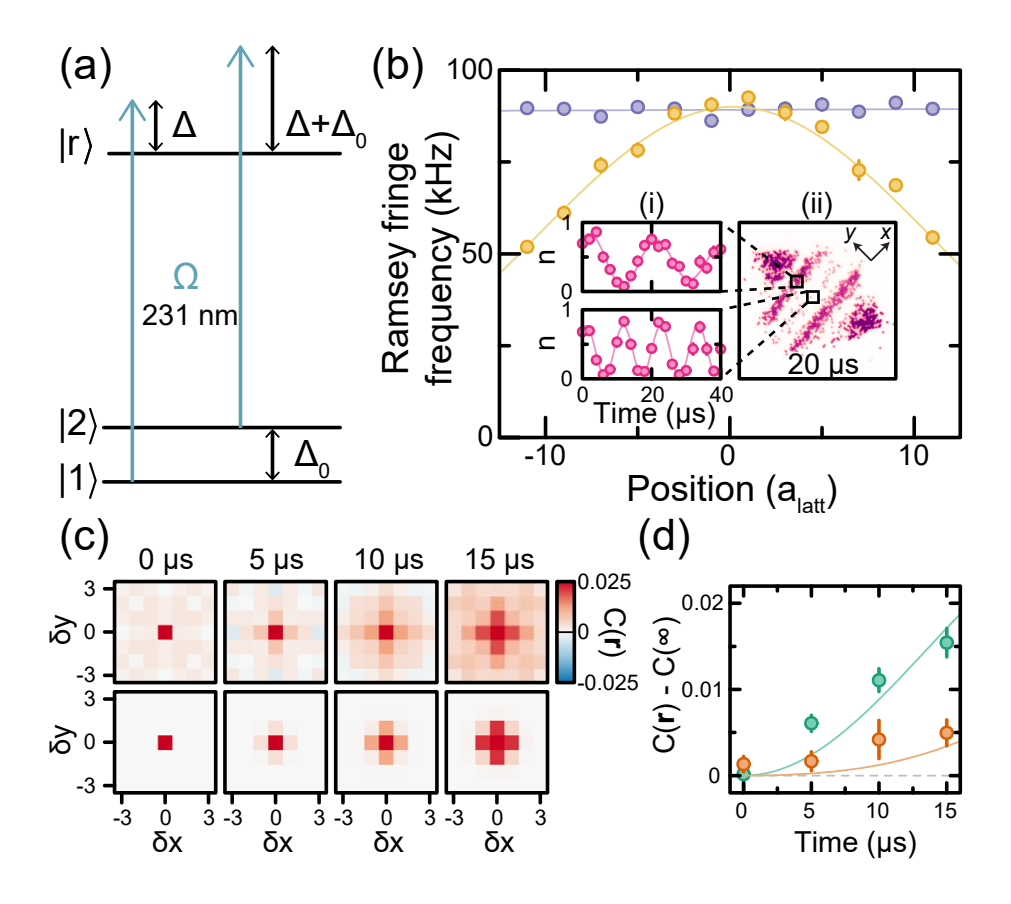


Figure 6.3: Measuring Rydberg dressed interactions with many-body Ramsey interferometry. (a) Energy level diagram for ^6Li showing that the dressing of the other hyperfine ground state cannot be ignored. Here $\Delta/2\pi$ is varied between 30 MHz and 100 MHz while $\Delta_0/2\pi = 75.806(1)$ MHz. (b) Ramsey fringe frequency measured at a detuning of $\Delta = 2\pi \times 100$ MHz at different positions in the cloud. The frequency is almost constant along the propagation direction of the beam (purple). In the transverse direction (yellow), it varies rapidly as expected for a tightly focused Gaussian beam. Insets: (i) Ramsey oscillations at two representative positions in the cloud. (ii) Sample image of one spin state in the cloud at $T = 20\,\mu\text{s}$. (c) Spin correlations for different spin-echo pulse times at $\Omega = 2\pi \times 7.66(7)$ MHz and $\Delta = 2\pi \times 35$ MHz. Measurement (top) and theoretical expectation (bottom). (d) Nearest (green) and next-nearest (orange) neighbor correlations after subtracting $C(\infty)$. Lines correspond to the expected correlations. Experimental error bars correspond to standard error of the mean.

all the atoms from the trap. Experiments in 2D have indeed observed a collective lifetime close to τ_c and a bimodal atom number distribution in lifetime measurements [75]. We have not observed such bimodality in our 2D systems, and the lifetime does not depend strongly on N at fixed density (App. 6.4.1). In this regard, our 2D ⁶Li experiments are closer to ⁸⁷Rb experiments with 1D chains where the avalanche mechanism is suppressed to some extent [90].

The atom number decay in a frozen system of 7 by 7 sites is shown in Fig. 6.4a. The decay is not exponential, indicating a density-dependent lifetime which we extract by fitting different sections of the decay curve. For dressing to $|28P\rangle$, $\tau_0=30.5\,\mu\text{s}$ [66]. We measured the density-dependent lifetime for $\Omega=2\pi\times9.25(8)$ MHz at three different detunings, $\Delta=2\pi\times(30,40,60)$ MHz (Fig. 6.4b). Around half-filling, the collective lifetime is $\sim0.3\tau_{\text{eff}}$ for $\Delta=2\pi\times30$ MHz and approaches τ_{eff} for the smallest densities ($n\sim0.1$). For comparison, perfect avalanche loss would predict $\tau_c=0.08\tau_{\text{eff}}$.

Next, we measure the lifetime of the dressed gas in the presence of tunneling, which has been a topic of theoretical debate [108, 109]. We measure the density-dependent lifetime for different lattice depths, spanning the frozen gas regime to a tunneling of 1.7 kHz (Fig. 6.4c). We do not observe any change of the lifetime with tunneling. A potential concern in this measurement is that the tunneling along the x-direction may be suppressed by uncontrolled disorder in δ_i . We rule this out by preparing a sparse strip of atoms and observing its tunneling dynamics. As expected for a clean dressed system, the tunneling dynamics along the x-direction is almost identical to the case without the dressing light, while the dynamics is frozen along the y-direction (Fig. 6.4c(inset)). Combining the results of our interferometry and lifetime measurements, we achieve a lifetime of several interaction times measured by the figure of merit $V_{10}\tau/\hbar \sim 20$ [90] for a mobile system with n = 0.5.

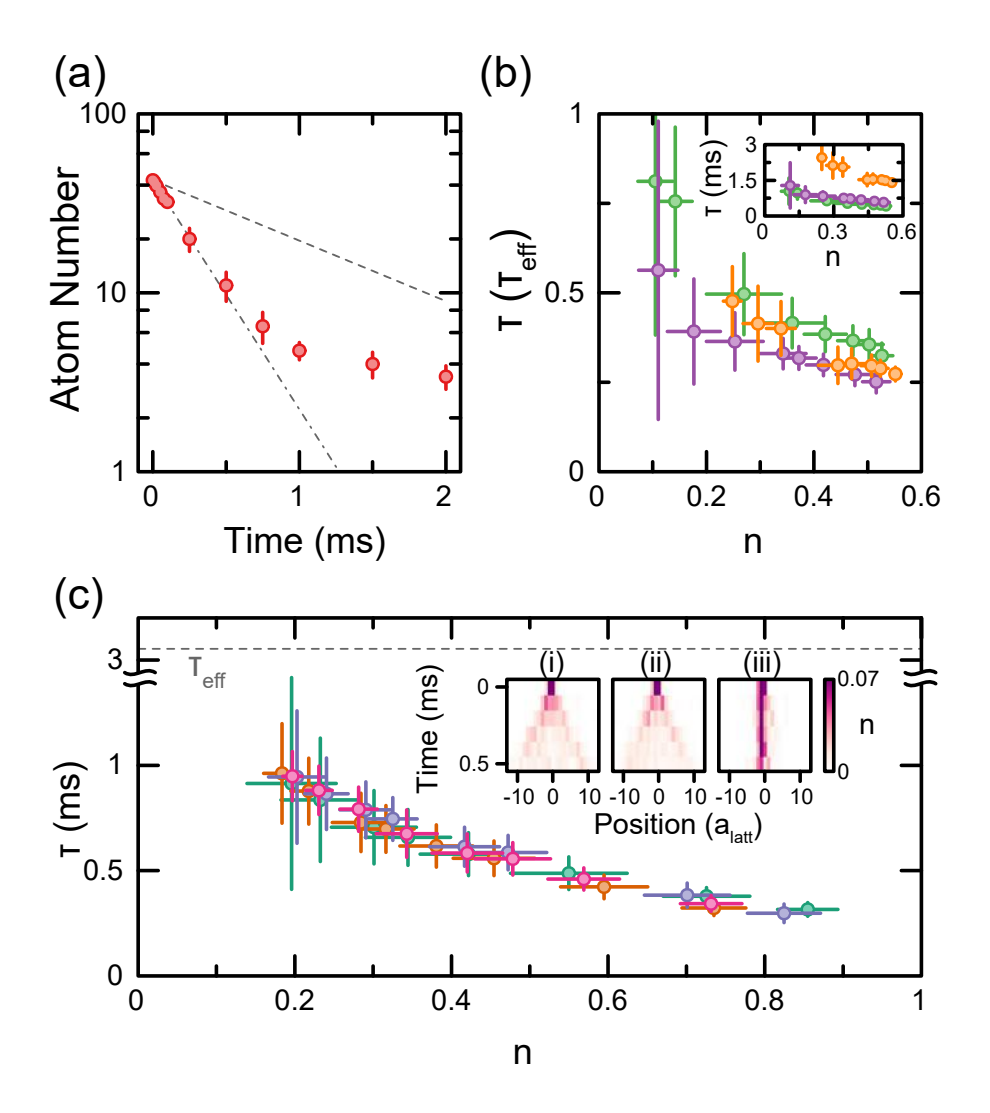


Figure 6.4: Lifetime of itinerant Rydberg dressed fermions. (a) Atom number vs. dressing time for a frozen gas. The red circles correspond to measurements on a system of 7 by 7 sites. Dashed-dotted line corresponds to an exponential fit to the first 5 data points and dashed line corresponds to the expected single-particle dressed lifetime $\tau_{\rm eff}$. (b) Measured lifetime in a frozen gas in units of $\tau_{\rm eff}$ vs. the initial density for $\Omega = 2\pi \times 9.25(8)$ MHz and $\Delta = 2\pi \times (30 \text{ (green)}, 40 \text{ (purple)}, 60 \text{ (orange)})$ MHz. Inset: Same measurements in units of ms. (c) Lifetime vs. initial density for different tunnelings: 0.01 kHz (green), 0.25 kHz (purple), 1.0 kHz (orange), and 1.7 kHz (pink). The data is taken with $\Omega = 2\pi \times 6.04(8)$ MHz, $\Delta = 2\pi \times 30$ MHz. Insets: (i) Tunneling dynamics of atoms sparsely initialized on a strip along the y-direction with no dressing light. From this data, we extract a tunneling rate $t = h \times 1.7 \text{ kHz}$. (ii) Same measurement in the presence of the dressing light. (iii) Same measurement in the presence of the dressing light but with the strip along the x-direction. Experimental error bars correspond to standard error of the mean.

6.4.1 Dependence of lifetime on atom number at fixed density

In our search for a suitable Rydberg state to use for our dressing experiments, we explored many different principal quantum numbers. We eventually chose 28P because it gave us a good ratio between the measured collective lifetime and the theoretical single-particle lifetime, while also having a large enough C_6 to achieve strong nearest-neighbor interactions in the lattice. We explored larger principal quantum numbers but found much shorter lifetimes than the expected values. One possible reason is the coupling to neighboring pair-potentials that have non-zero overlaps with the target state at close distances (Fig. 6.1). However, the general behavior of the many-body lifetimes with atom number and geometry of the cloud remained the same over significantly different principal quantum numbers. In particular, the lifetime showed no strong dependence on the atom number at fixed density over the range we could explore in the experiment. Fig. 6.5 shows the initial lifetime vs. the initial atom number for 2D systems $4 \, a_{latt}$ wide and of variable length along the direction parallel to the dressing beam for the 31P and 40P Rydberg states.

6.5 Quench Dynamics

To probe the interplay of interactions and tunneling in our system, we use light patterned with a spatial light modulator to initialize the system in a charge density wave state of atoms in state $|3\rangle$. The initial density pattern approximates a square wave with period $\lambda = 4\,\mathrm{a_{latt}}$ and width $w = 7\,\mathrm{a_{latt}}$, with the average density oscillating between $n \sim 0$ and $n \sim 0.7$. (see Figs. 6.6a-b). Dynamics in a lattice with $t = h \times 1.7\,\mathrm{kHz}$ is initiated by suddenly turning off the patterning potential while keeping walls in the y-direction as in [13]. We average the density profiles over the non-hopping direction and observe a qualitative change in the dynamics as we increase V/t (here

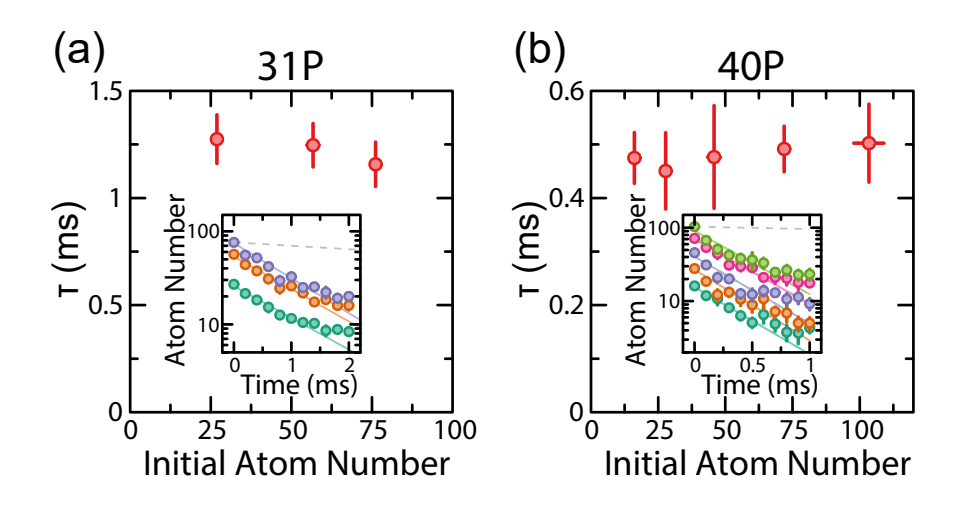


Figure 6.5: Dependence of lifetime on atom number at fixed density. (a) Initial lifetime for 2D systems with different initial atom number dressed to 31P. Measurements are made in a 2D rectangular system of small width $\sim 4\,\mathrm{a_{latt}}$ and variable length along the dressing beam direction. We observe no strong dependence on the atom number. The Rabi frequency is approximately constant over the entire system. For this data, $\Omega = 2\pi \times 7.02(5)\,\mathrm{MHz}$, $\Delta = 2\pi \times 60\,\mathrm{MHz}$ and n = 0.8. (b) Same as in (a) but for systems dressed to 40P. For this data, $\Omega = 2\pi \times 5.6(2)\,\mathrm{MHz}$, $\Delta = 2\pi \times 40\,\mathrm{MHz}$ and n = 0.55. (insets) Raw data with exponential fits to extract the initial decay rate. Experimental error bars correspond to standard error of the mean.

 $V \equiv |V_{10}|$) from 0 to 2.9(2) (Fig. 6.6c). To emphasize the evolution of the pattern, we scale the data to account for atom loss during the evolution (SecS. 6.5.1). In the non-interacting quench, we observe that the phase of the charge density wave inverts at a time $\sim \hbar/t$ as is expected for a coherent evolution [9]. For strong interactions, the decay of the charge density wave slows down and the system retains a memory of its initial state for longer times.

This can be understood as an interplay between two conservation laws: the intrinsic U(1) particle number ($\hat{N} = \sum_x \hat{n}_x$) conservation as well as an emergent conservation of the number of bonds $\hat{N}_b = \sum_x \hat{n}_x \hat{n}_{x+1}$. The latter becomes a conserved quantity when the longer range interactions are ignored, and in the limit of infinite V/t. States of the form $|...0011001100...\rangle$ along the hopping direction, which the imprinted density pattern attempts to approximate, would be completely frozen in the

limit of infinite V/t [47]. For a large but finite V, moving a single atom (and hence breaking a bond) costs an energy of up to 3V, which is energetically unfavorable, and hence leads to reduced relaxation dynamics.

To quantify the difference in the dynamics of the different quenches, we employ two different methods. The first is to fit a sinusoid of the form $n(x,t) = A \sin(2\pi x/\lambda + \phi) + B$ to determine the amplitude of the wave relative to its mean, A/B (Fig. 6.6d). The fit is restricted to $|x| \le 6 a_{\text{latt}}$, and ϕ is fixed by the initial pattern. The second method is to calculate the autocorrelation function

$$\rho(t) = \frac{\operatorname{cov}_x(n(x,0), n(x,t))}{\sigma_x(n(x,0))\sigma_x(n(x,t))},\tag{6.3}$$

where cov_x and σ_x are the covariance and the standard deviation respectively (Fig. 6.6e).

Further confirmation that the slower decay of the charge density waves is an interaction effect is obtained by varying the average density in the initial state. Fig. 6.7a shows these initial states and their time evolution for V/t = 2.9(2). As the average density of the initial state is decreased, it approaches a "sparse" limit where the probability of having two neighboring atoms is negligible. In this regime, the system is effectively non-interacting and we recover the phase inversion during the evolution. Since these measurements are done at fixed power of the dressing light, they rule out disorder-induced localization as a mechanism for arresting the dynamics.

6.5.1 Atom loss during charge density wave dynamics

We observe an atom loss of $\sim 30\%$ for the longest evolution times for the dataset with the maximum initial density and interaction strength. For the dataset where interaction was varied by changing the dressing laser intensity, the lifetime gets longer for smaller interactions due to the reduction of the Rydberg dressing parameter $\beta =$

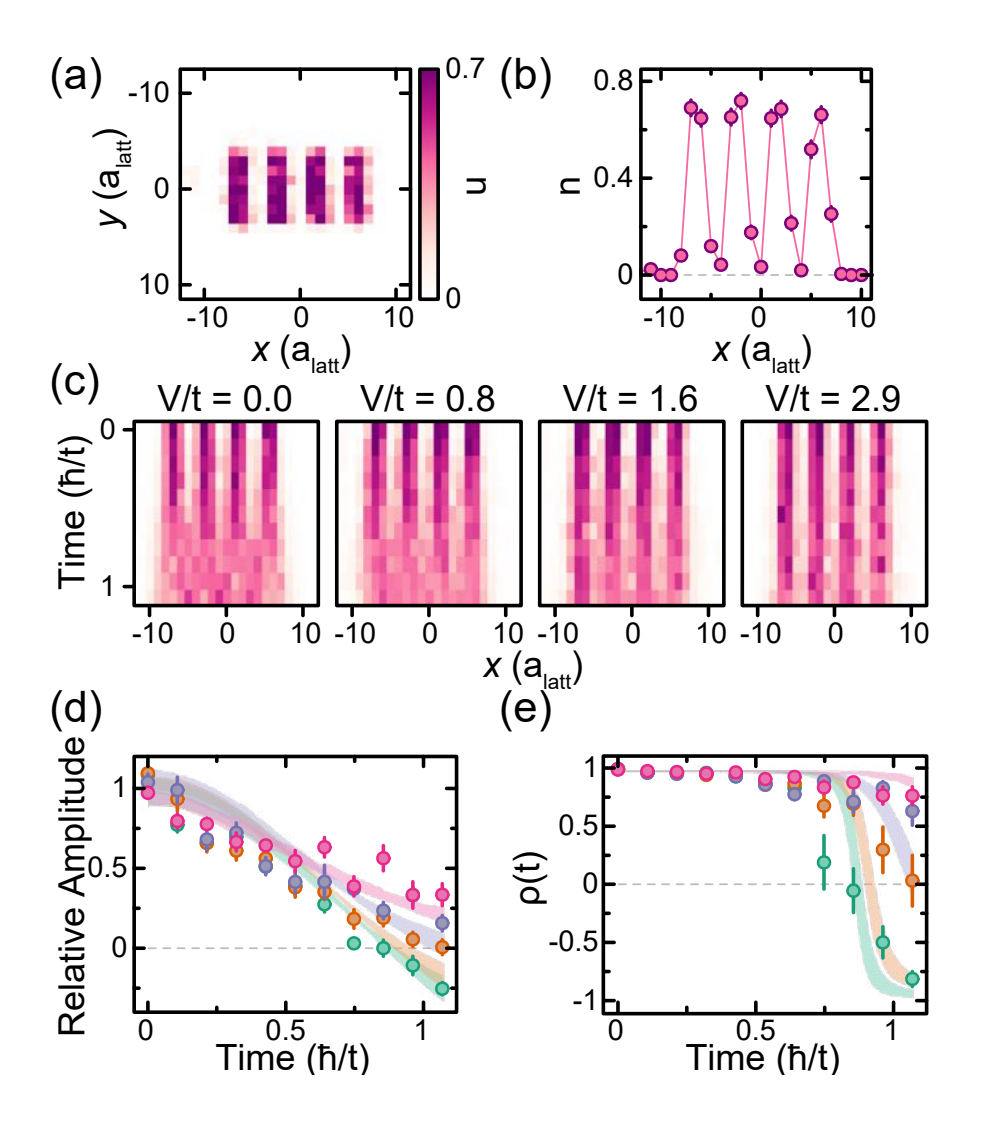


Figure 6.6: Interaction dependence of quench dynamics of a charge density wave. (a) Average initial state density profile for the quench measurements. (b) Density profile averaged along the y-direction of the initial state shown in (a). (c) Density profile time evolution for interactions V/t = [0, 0.78(7), 1.61(8), 2.9(2)]. Color scale is the same as in (a). (d) Fitted relative amplitude of density profile vs. time. Colors (green, orange, purple, and pink) correspond to the interactions in (c) from lowest to highest. (e) Autocorrelation function of the density pattern. Colors are same as in (d). Shaded curves correspond to numerical simulations. Experimental error bars correspond to standard error of the mean.

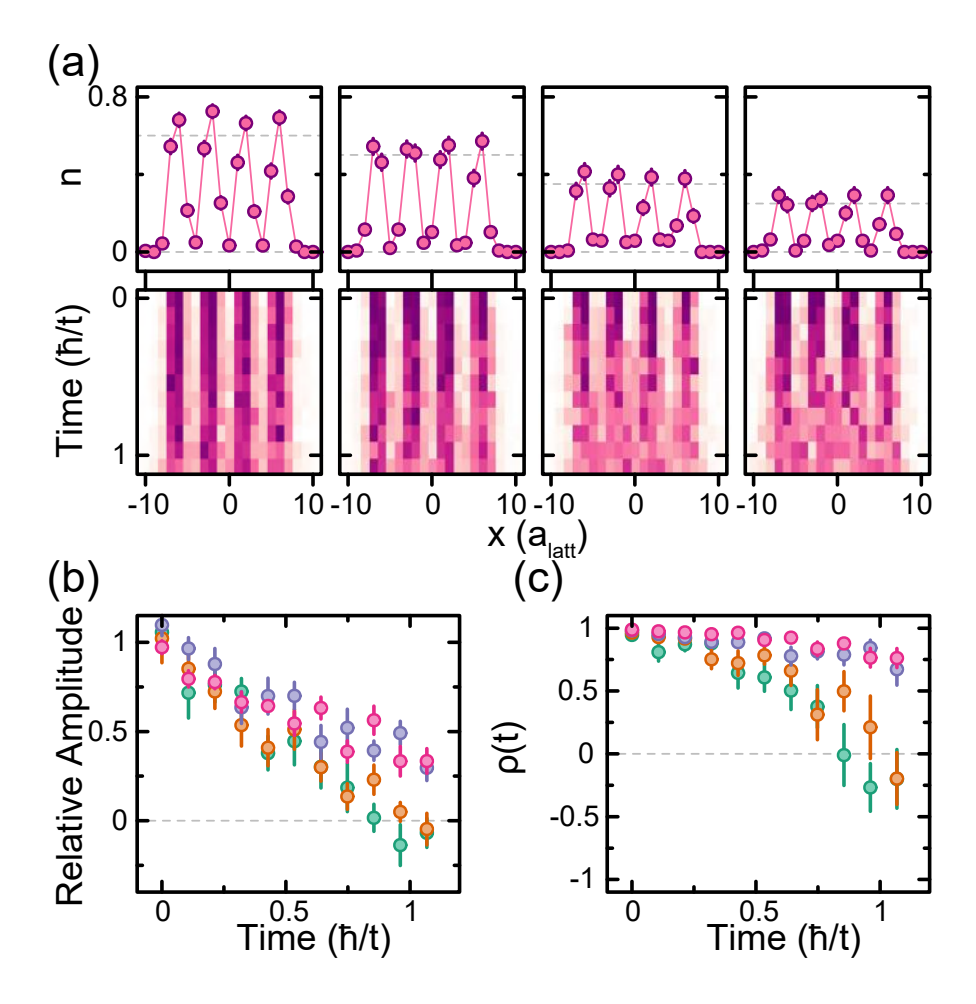


Figure 6.7: **Density dependence of quench dynamics.** (a) (top) Initial state density profiles. (bottom) Corresponding time evolution of each initial state for V/t = 2.9(2). Colorbar is same as Fig. 6.6a with limits set by dotted lines on top panel. (b) Fitted relative amplitude of density profiles vs. time. Colors (green, orange, purple, and pink) correspond to the initial states in (a) from low to high density. (c) Autocorrelation function of the density pattern. Colors are same as in (b). Experimental error bars correspond to standard error of the mean.

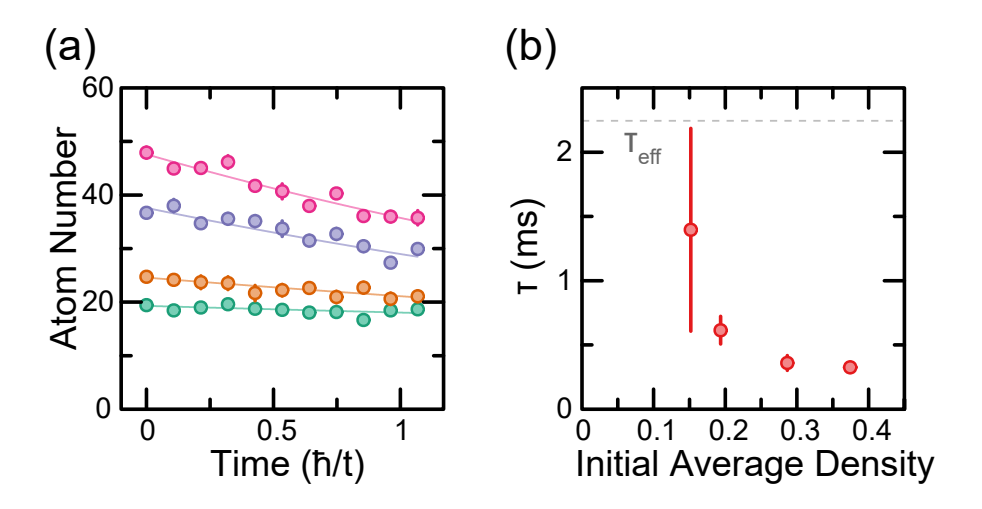


Figure 6.8: Atom loss during charge density wave dynamics. (a) Atom number decay over the quenches shown in Fig. 6.7. Each color represents a set with a different initial density. Circles are measured data with error bars and lines are simple exponential decay fits. The dressing parameters were $\Omega = 2\pi \times 6.99(8)\,\mathrm{MHz}$ and $\Delta = 2\pi \times 30\,\mathrm{MHz}$. (b) Lifetime vs. the initial average density of the charge density wave as extracted from the data in (a). This behavior is in agreement with our observations shown in Fig. 6.4. Experimental error bars correspond to standard error of the mean.

 $\frac{\Omega}{2\Delta}$. For the dataset where the initial density was varied at fixed interaction strength, the lifetime increased for lower initial densities (Fig. 6.8). These measurements are in accordance with our observed density dependent lifetime measurements shown in Fig. 6.4.

6.6 Numerical simulations

We use exact diagonalization to simulate the quench dynamics of our experiment. As the simulation for the full experimental 2D system ($\sim 7 \times 21$) is computationally intractable, we compare instead to numerics on a $2 \times 11 \ t-V$ model with only nearest-neighbor interactions and no tunneling along the y-direction and find qualitative agreement with the measurements.

We account for atom loss during the experiment via a Lindblad master equation $\partial_t \hat{\rho} = -i(\hat{H}_{\text{eff}}\hat{\rho} - \hat{\rho}\hat{H}_{\text{eff}}^{\dagger}) + \Gamma \sum_i \hat{a}_i \hat{\rho} \hat{a}_i^{\dagger}. \text{ Here, } \hat{H}_{\text{eff}} = \hat{H} - i\frac{\Gamma}{2}\hat{N} \text{ is the effective non-}$

Hermitian Hamiltonian $[\hat{H}]$ is the t-V Hamiltonian from Eq. (6.2)] and the second term describes quantum jumps corresponding to atom loss with rate Γ . We solve the master equation using the quantum trajectory approach [185]. Note that the anti-Hermitian term in \hat{H}_{eff} is a constant due to the particle number conservation, and hence it can be neglected since \hat{H}_{eff} and \hat{H} generate the same dynamics (up to the normalization, which only serves to determine the timings of the quantum jumps).

The initial state for each trajectory is sampled directly from the experimental data taken at t=0. We pick a 2×9 region centered on 2 of the 4 density peaks from the experimental images (Fig. 6.6a). In order to reduce boundary effects, we add empty sites on each end of the chain. We average the resulting dynamics over the different trajectories, whose number is comparable to the number of experimental snapshots. Next, we analyze the averaged simulated dynamics using the same methods we use for the experimental data. Fig. 6.6 shows the comparison of the experiments with these numerical simulations. We find good qualitative agreement with this small 2D coupled-chain numerical model.

The 2D nature of the system is important for fully understanding the relaxation time-scales in our system. In particular, in a one-dimensional system, moving a single atom from the initial "...00110011..." pattern (and hence breaking a bond) costs an energy V. However, in the coupled-chain t-V model with isotropic interaction, breaking a bond now costs up to 3V for the idealized initial charge density wave state. We thus expect the 2D system to have slower relaxation rate compared to a 1D system with the same interaction strength.

To verify this, we perform additional numerical simulations on a single chain of 21 atoms. Similarly to our 2D simulation, we sample 1×19 arrays from the experimental snapshots at t = 0 and add empty sites at the ends. We find that the atoms spread quicker than they do in the ladder geometry and have worse agreement with the experimental results. Fig. 6.9 shows a comparison between the 1D and 2D coupled-

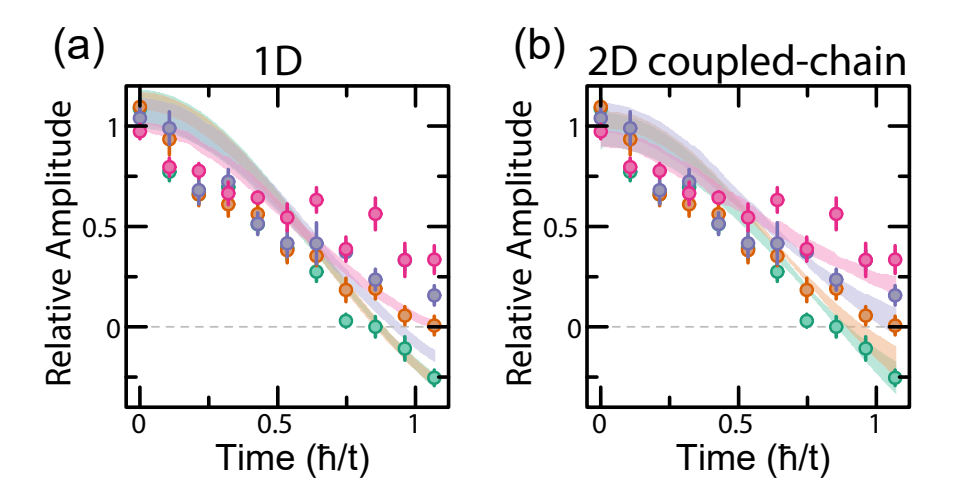


Figure 6.9: Role of interchain couplings in slowing down charge density wave relaxation. Numerical simulations of a t-V model with tunneling t along only one direction and isotropic nearest-neighbor interactions V. (a) Fitted relative sinusoid amplitude to observed (circles) and calculated quench dynamics of 1×21 systems (shaded regions). The colors represent the different interaction strengths V/t = [0 (green), 0.78(7) (orange), 1.61(8) (purple), 2.9(2) (pink)] explored in the experiment. (b) Same comparison as in (a) but for calculations done on 2×11 systems. This is Fig. 4d. Experimental error bars correspond to standard error of the mean.

chain numerical simulations on the one hand and the experimental data on the other.

This comparison highlights the importance of the interchain interactions in order to fully understand our system.

The remaining discrepancy between some of the numerical and experimental results could be attributed to several factors. First, we are only able to simulate a smaller system than in the experiment. We expect that adding additional chains could further slow down the relaxation dynamics. Second, our modelling of the atom loss via a Lindblad master equation assumes that the decay rate is exponential. However, as we showed in Sec. 6.4, the decay rate is actually non-uniform in space and time, and depends on the density.

6.7 Conclusions

Our results present a new frontier in quantum simulations of itinerant lattice models with strong off-site interactions. By working with larger r_c/a , spinless fermion models may be used to explore equilibrium phases such as topological Mott states [186] or cluster Luttinger liquid phases [31]. Moreover, the system considered in this work provides a platform for the experimental realization of models prevalent in theoretical studies of non-equilibrium dynamics. For example, the 1D t-V model can be mapped to the XXZ spin chain, which has long been studied in the context of many-body localization [187–189]. This model and variants thereof have also been proposed to harbor dynamical phases intermediate between full MBL and thermalization [190–192]. Our work lays the foundation for future studies of such phenomena, as well as other non-equilibrium dynamical regimes including prethermalization [193]. Furthermore, the close spacing between the hyperfine ground states of ⁶Li also opens the door for the simultaneous dressing of two spin states and the exploration of extended Fermi-Hubbard models.

The present experiment has allowed us to start probing coherent dynamics in t - V models, which we plan to continue to explore especially upon improving the interaction-lifetime figure of merit. For example, for small but finite t/|V|, it is possible to access a complex hierarchy of timescales for quench dynamics that depends crucially on the initial state [48].

Our work motivates further theoretical and experimental exploration of the mixeddimensional models in the context of both the non-equilibrium dynamics and groundstate physics [194] such as meson formation. Another promising direction based on the interplay of Rydberg-dressing and atomic motion is vibrational dressing [195, 196], non-destructive cooling [197], an exploration of multi-band physics, as well as the use of microwave-dressed Rydberg states, allowing for both attractive and repulsive dressed $1/r^3$ dipole-dipole interactions [80].

There are several possible approaches to improve the interaction-lifetime figure of merit. Enhancement of the Rabi coupling by over an order of magnitude may be achieved using a build-up cavity [198]. For a single-particle system, the figure of merit scales with Ω at fixed β , while further enhancement of the collective lifetime is expected in this regime due to shrinking facilitation radii for increasing Δ . Increasing Ω by a factor of 10 at fixed β leads to facilitation radii that are a factor of $10^{1/3}$ smaller. For almost all states coupled to by blackbody radiation, the facilitation radii become less than one site. If collective loss is completely inhibited, the combined effect is to enhance the figure of merit by a factor of ~ 30 . The principal quantum number used in this experiment was chosen to keep the range of the interaction on the order of one site. Relaxing this constraint or alternatively using a larger lattice spacing would allow using longer-lived Rydberg states at higher principal quantum number. Using electric fields to tune close to a Förster resonance results in deep potential wells that may be exploited to enhance the figure of merit by a factor of $|\Delta|/\Omega$ [199] and potentially allow us to achieve repulsive interactions. Finally, the single particle lifetime can be improved and the collective black-body induced atom loss may be completely eliminated by operating at cryogenic temperatures (improving the figure of merit by a factor of ~ 6 for fixed dressing laser parameters).

Chapter 7

Conclusion and Outlook

In this thesis we have reported on a variety of experiments where we have expanded on the capabilities of our existing Fermion Quantum Gas Microscope [92, 93]. We emphasized the physics of Rydberg atoms and particularly the development of Rydberg dressing for ⁶Li atomic systems. Our experiments show that quantum simulation experiments based on single-photon excitation of lithium-6 atoms to Rydberg states can serve as a highly-flexible platform to study different types of many-body systems.

We were able to study the quench dynamics of a many-body 2D quantum Ising model well beyond the capabilities of state-of-the-art numerical simulations. While our realization using an optical lattice is not ideal, our experiments point to the importance of taking into account motional decoherence effects [155]. This decoherence is stronger in our optical lattice, but is also present in tweezer arrays and should be taken into account to achieve high fidelities of quantum-gates.

Outside of Rydberg physics, we studied the 2D tilted Fermi-Hubbard model observing the onset of subdiffusive charge dynamics with tilt strength. To understand the slow relaxation dynamics we built an universal hydrodynamic theory for the equilibration of systems at infinite temperatures. From this model, we uncovered that the observed subdiffusive charge dynamics were a product of slow heat diffusion in

the system which bottlenecks the density relaxation to maintain local equilibrium. At much stronger tilt strengths we would expect the system to reach a nonergodic phase where the system is dynamically constrained.

Finally, we successfully implemented the technique of Rydberg dressing in our system of 6 Li atoms. Using this novel platform, we were successful in realizing an itinerant lattice model in the presence of long-range interactions. We realized a spinless t-V model and observed a clear effect of interactions on the relaxation dynamics of charge density waves. This experiment opens the door to studying many more strongly-interacting quantum gas systems which are detailed in Ch. 6.

7.1 Outlook

With the advent of other platforms working towards degenerate quantum gases with long-range interactions such as polar molecules [24, 25] and magnetic atoms [20–23], it will be important to fix the non-trivial decay mechanisms currently limiting Rydberg dressing experiments. In Sec. 3.7 we detailed the lifetime characterization of our system and present evidence that the limiting decay mechanism in our system is not satisfactorily explained by complete black-body avalanche loss observed in experiments with Rb and Cs systems. Instead, we observe a density-dependent lifetime which is invariant on the atom number. It is possible that our observed decay is could be explained by direct excitation to pair-states which have non-zero overlap with the target Rydberg state at short distances. An issue like this one could be fixed by changing the geometry of the system. Recently in our lab, we have developed a technique to build Fermi-Hubbard models using optical tweezers which should allow us to vary the spacing between the lattice sites. This opens the door to studying the dependence of the lifetime on the spacing when coupling to a fixed Rydberg state, or alternatively, coupling to states with larger principal quantum numbers.

Another option is to modify the Rydberg dressing scheme away from the simple picture described in Sec. 2.8. One such way, is to further explore the Förster resonances that can be tuned using magnetic or electric fields (App. C) and dress on a strong avoided-crossing of the target pair-state with a different state. For lower principal quantum numbers, the resonant lines should move much closer in distance and allow us to explore very strong repulsive interacting models.

Without truly fixing the limiting decay mechanism, we can still increase the coherence by enhancing the Rabi coupling of our UV laser. In Table 2.5 we show that the interaction-to-lifetime ratio increases with power. At 230 nm it is not really feasible to get a laser with a much larger power output than our current laser. However, we could employ the use of a build-up cavity [198] to greatly enhance the Rabi coupling and thus the coherence.

For Rydberg systems in general, the black-body radiation does not only lead to global loss through the avalanche mechanism. It also limits the bare Rydberg lifetimes of single atoms for large principal quantum numbers (Eq. 2.13). The only way to avoid these decay channels is to build cryogenic experiments where the black-body spectrum no longer couples nearby Rydberg states so strongly. There are currently multiple groups building or designing Rydberg cryogenic experiments.

Appendix A

Numerov's Algorithm

Numerov's algorithm was developed in 1924 [68] to numerically solve second order differential equations of the form

$$\left(\frac{\partial^2}{\partial x^2} + a(x)\right)y(x) = 0\tag{A.1}$$

$$y''(x) + a(x)y(x) = 0$$
 (A.2)

taking into account corrections up to 5th order of a discrete stepsize h. Eq. 2.8 is an example of an equation solvable with this method. In this appendix, we will describe how to derive the algorithm and how to use it to solve for the radial wavefunctions of Rydberg atoms.

A.1 Derivation

The method essentially works by discretizing the space and using Taylor expansions to build the function y(x) one step at a time starting on one end. To derivate it, first you can do a Taylor expansion of $y(x_n \pm h) = y_{n\pm 1}$ up to 5th order where x_n denotes

a particular step n in the function:

$$y_{n\pm 1} = y_n \pm hy'_n + \frac{h^2}{2!}y''_n \pm \frac{h^3}{3!}y'''_n + \frac{h^4}{4!}y''''_n \pm \frac{h^5}{5!}y'''''_n + O[h^6]$$
 (A.3)

Next, we add both of these functions together to get:

$$y_{n+1} + y_{n-1} = 2y_n + h^2 y_n'' + \frac{h^4}{12} y_n'''$$
(A.4)

Substituting in Eq. A.2 and using the second-order finite difference¹:

$$y_{n+1} + y_{n-1} = 2y_n - h^2 y_n a_n - \frac{h^4}{12} \frac{\partial^2}{\partial x_n^2} (a(x_n)y(x_n))$$
(A.5)

$$y_{n+1} + y_{n-1} = 2y_n - h^2 y_n a_n - \frac{h^2}{12} \left(a_{n+1} y_{n+1} - 2a_n y_n + a_{n-1} y_{n-1} \right)$$
(A.6)

Finally, one can solve for either y_{n+1} or y_{n-1} . In this case, we choose to solve the function backwards as we know that in the case of Rydberg atoms, the function a(x) has a much slower rate of change and as such is a nicer place to start the algorithm. With this consideration, we end up with the following equation which will be useful to find solutions for wavefunctions in arbitrary potentials:

$$y_{n-1} = \frac{(24 - 10h^2 a_n) y_n - (12 + h^2 a_{n+1}) y_{n+1}}{12 + h^2 a_{n-1}}$$
(A.7)

A.2 Implementation for Rydberg atoms

This algorithm is relatively simple to implement using modern computers. For the particular case of solving for the wavefunction of Rydberg atoms (Eq. 2.8), we took a few considerations. First, it is useful to choose a sufficiently small stepsize where the algorithm is well defined. In our case we used $h = 0.005 a_0$ as the equation is

This follows from $f'(x) \approx \frac{f(x+h)-f(x)}{h} \approx \frac{f(x)-f(x)}{h} = \frac{f(x)-f(x)-f(x)}{h^2} = \frac{f(x)-f(x)-f(x)-f(x)}{h^2}$ so that $f''(x) \approx \frac{f'(x+h)-f'(x)}{h} = \frac{f(x)-f(x)-f(x)-f(x)}{h^2}$

written in atomic units. Next, we need to make a good choice of initial parameters to "seed" Eq. A.7 with. For this purpose, we choose to discretize the space from 0 to a maximum radius $r_{max} = 2n (n + 15)^2$ where the wavefunction is certainly zero. We set our initial parameters to:

$$y(r_{max}) = y_{end} = 0 (A.8)$$

$$y(r_{max} - h) = y_{end-1} = (-1)^{n+l+1} \times 10^{-10}$$
(A.9)

Where $(-1)^{n+l+1}$ is an important consideration for the proper integration of dipole matrix elements with different quantum numbers. We use this values to point-by-point build the wavefunction using Eq. A.7. An interesting consideration, is that the algorithm prefers to work with very small numbers so we make sure to divide by 10 if the calculated value of $|y_{n-1}|$ is ever above 10^{-9} .

Finally, the last important step is to decide when to stop the algorithm. At close distances, the potential changes much more rapidly so our choice of h might no longer be correct. A work around we found was to flag the position at which a(x) changes sign (same as when the bound energy and the potential are equal) and after that the first time that $|y_{n-1}| > |y_n|$ we set it to 0 and stop the algorithm. Using this we are able to calculate the radial wavefunctions of Rydberg atoms as shown in Fig. 2.1.

While not in the scope of this thesis, during this PhD, the same algorithm was used to successfully find the bound states of NaRb molecular potentials. These bound states were used to calculate Franck-Condon factors in order to design the STIRAP sequence of a new molecular microscope currently being built in our group.

²From Table. 2.1 we know that the orbital radius increases quadratically with n so this ensures that we choose a suitably large r_{max} for any principal quantum number n.

Appendix B

Calculated C_6 values of 6 Li pair-states.

This Appendix presents a summary of calculated C_6 values of ⁶Li pair-states with full angular dependence. The calculations were made as described in Sec. 2.5.1 and span principal quantum numbers $n = \{20, 50\}$. It is important to note that we found no difference in the C_6 values for pair states with the same absolute value of |m|.

From the tables, one can note that only the nP pair-states have a Förster resonance at zero field. Moreover, only nS pair states have repulsive interactions ($C_6 < 0$) while the rest are attractive. These calculations helped decide on a single-photon Rydberg dressing design to directly connect our ground-state atoms with nP Rydberg states.

n	c_1/n^{*11}	c_2/n^{*11}	c_3/n^{*11}	$C_6(0)/n^{*11}$	$C_6(\pi/4)/n^{*11}$	$C_6(\pi/2)/n^{*11}$
20	-0.490621	-1.30832	-0.654161	-1.962485	-1.9624857	-1.9624857
21	-0.509414	-1.35843	-0.679219	-2.037658	-2.0376586	-2.0376586
22	-0.526561	-1.40416	-0.702081	-2.106245	-2.1062455	-2.1062455
23	-0.542266	-1.44604	-0.723022	-2.169067	-2.1690672	-2.1690672
24	-0.556706	-1.48454	-0.742274	-2.226824	-2.2268248	-2.2268248
25	-0.570026	-1.52007	-0.760035	-2.280107	-2.2801079	-2.2801079
26	-0.582354	-1.55294	-0.776472	-2.329417	-2.3294176	-2.3294177
27	-0.593795	-1.58345	-0.791727	-2.375183	-2.3751829	-2.3751830
28	-0.604443	-1.61184	-0.805924	-2.417773	-2.4177730	-2.4177730
29	-0.614376	-1.63833	-0.819169	-2.457507	-2.4575076	-2.4575076
30	-0.623666	-1.66310	-0.831554	-2.494664	-2.4946646	-2.4946646
31	-0.632371	-1.68632	-0.843162	-2.529487	-2.5294873	-2.5294873
32	-0.640547	-1.70812	-0.854063	-2.562189	-2.5621891	-2.5621891
33	-0.648239	-1.72863	-0.864319	-2.592958	-2.5929583	-2.5929583
34	-0.655490	-1.74797	-0.873987	-2.621961	-2.6219617	-2.6219617
35	-0.662336	-1.76622	-0.883114	-2.649344	-2.6493443	-2.6493443
36	-0.668811	-1.78349	-0.891749	-2.675247	-2.6752473	-2.6752473
37	-0.674946	-1.79985	-0.899928	-2.699785	-2.6997854	-2.6997854
38	-0.680786	-1.81543	-0.907715	-2.723146	-2.7231469	-2.7231469
39	-0.686273	-1.83006	-0.915031	-2.745094	-2.7450945	-2.7450945
40	-0.691532	-1.84408	-0.922043	-2.766129	-2.7661291	-2.7661291
41	-0.696536	-1.85743	-0.928715	-2.786145	-2.7861459	-2.7861459
42	-0.701306	-1.87015	-0.935075	-2.805225	-2.8052259	-2.8052259
43	-0.705858	-1.88228	-0.941144	-2.823434	-2.8234348	-2.8234348
44	-0.710207	-1.89388	-0.946943	-2.840831	-2.8408312	-2.8408313
45	-0.714367	-1.90497	-0.952489	-2.857468	-2.8574687	-2.8574687
46	-0.718348	-1.91559	-0.957798	-2.873395	-2.8733959	-2.8733959
47	-0.722164	-1.92577	-0.962885	-2.888657	-2.8886574	-2.8886574
48	-0.725823	-1.93552	-0.967764	-2.903294	-2.9032939	-2.9032940
49	-0.729335	-1.94489	-0.972447	-2.917343	-2.9173434	-2.9173434
50	-0.732710	-1.95389	-0.976946	-2.930840	-2.9308404	-2.9308404

Table B.1: Calculated C_6 values for $^6\mathrm{Li}\ |nS,1/2,\pm1/2\rangle\otimes|nS,1/2,\pm1/2\rangle$ pairstates. Calculated parameters to calculate C_6 values of $^6\mathrm{Li}$ pair-states with full angular dependence according to Eq. 2.19 and some angles θ . The values are in natural units of $\mathrm{E}_{\mathrm{h}} a_{\theta}{}^6$.

n	c_1/n^{*11}	c_2/n^{*11}	c_3/n^{*11}	$C_6(0)/n^{*11}$	$C_6(\pi/4)/n^{*11}$	$C_6(\pi/2)/n^{*11}$
20	3.0797687	9.5403891	6.7617034	12.3190748	15.30633808	18.29360135
21	3.0707908	9.5159692	6.748775	12.2831632	15.26934899	18.25553455
22	3.0611628	9.4895449	6.7344387	12.2446512	15.22915048	18.21364988
23	3.0532504	9.4683839	6.723766	12.2130016	15.19736286	18.1817239
24	3.0419273	9.4363715	6.7050339	12.1677092	15.14798133	18.12825358
25	3.0301324	9.4031952	6.685861	12.1205296	15.09692451	18.07331965
26	3.0166094	9.3649297	6.663422	12.0664376	15.03787314	18.0093089
27	3.0003553	9.3186366	6.6358519	12.0014212	14.96622169	17.93102208
28	2.9796283	9.2592573	6.6000013	11.9185132	14.87407227	17.82963123
29	2.9510654	9.1770163	6.5497709	11.8042616	14.74615582	17.68804993
30	2.9071215	9.0499715	6.4714573	11.628486	14.54819304	17.46790043
31	2.8265265	8.8162691	6.3264321	11.306106	14.18355242	17.06099873
32	2.6172654	8.2081752	5.9472888	10.4690616	13.2338634	15.9986652
33	0.3348758	1.5691428	1.798782	1.33950356	2.860819498	4.38213539
34	3.7419911	11.481356	7.994748	14.9679644	18.34906903	21.7301741
35	3.3631619	10.379877	7.3071056	13.4526476	16.628399	19.8041495
36	3.2529224	10.059716	7.1077416	13.0116896	16.12851575	19.245341
37	3.1994038	9.9045309	7.0114467	12.7976152	15.88638698	18.97515888
38	3.1672309	9.8114148	6.9539063	12.6689236	15.74122167	18.81352008
39	3.1454148	9.7484024	6.9151455	12.5816592	15.64307574	18.70449218
40	3.1294258	9.702318	6.8869326	12.5177032	15.57136379	18.62502415
41	3.117054	9.6667346	6.8652532	12.468216	15.51604485	18.5638737
42	3.1070915	9.6381403	6.8479148	12.428366	15.47163279	18.5148998
43	3.0988213	9.6144512	6.8336171	12.3952852	15.43487254	18.47445978
44	3.0917899	9.5943495	6.8215395	12.3671596	15.40370663	18.44025378
45	3.0856935	9.576955	6.8111362	12.342774	15.37676186	18.41074995
46	3.0803035	9.5616169	6.80202	12.321214	15.35303114	18.3848485
47	3.0757957	9.5486458	6.7941087	12.3031828	15.33286159	18.36254028
48	3.0713433	9.5360844	6.7867956	12.2853732	15.3135033	18.3416334
49	3.0674262	9.5249796	6.7802545	12.2697048	15.29635176	18.32299883
50	3.0638503	9.5148495	6.7742977	12.2554012	15.28071072	18.30602013

Table B.2: Calculated C_6 values for $^6\mathrm{Li}\ |nP,1/2,\pm1/2\rangle\otimes|nP,1/2,\pm1/2\rangle$ pairstates. Calculated parameters to calculate C_6 values of $^6\mathrm{Li}$ pair-states with full angular dependence according to Eq. 2.19 and some angles θ . The values are in natural units of $\mathrm{E}_{\mathrm{h}} a_{\theta}{}^6$.

n	c_1/n^{*11}	c_2/n^{*11}	c_3/n^{*11}	$C_6(0)/n^{*11}$	$C_6(\pi/4)/n^{*11}$	$C_6(\pi/2)/n^{*11}$
20	3.70375	9.6359359	5.0744761	14.815	14.62075819	15.12132123
21	3.689001	9.6087281	5.0669051	14.756004	14.58220348	15.08953748
22	3.6735845	9.579522	5.058212	14.694338	14.54060263	15.0545615
23	3.6638456	9.5562746	5.0498794	14.6553824	14.50732749	15.02607425
24	3.6460229	9.5215441	5.0381729	14.5840916	14.45721509	14.98191193
25	3.6292211	9.4857599	5.0250543	14.5168844	14.40537821	14.93559328
26	3.6107069	9.4447655	5.0092139	14.4428276	14.34572073	14.88143818
27	3.5891943	9.3954968	4.9892886	14.3567772	14.27370731	14.81509365
28	3.5625848	9.3326795	4.9628852	14.2503392	14.18153356	14.7290765
29	3.526888	9.2461466	4.9253376	14.107552	14.05413933	14.6088976
30	3.4732031	9.1131234	4.8661533	13.8928124	13.85777583	14.42204803
31	3.3765344	8.8695727	4.7558063	13.5061376	13.49754393	14.07709858
32	3.1294358	8.2399117	4.4669866	12.5177432	12.56493958	13.18015565
33	0.5505337	1.6303068	1.4170023	2.20213476	2.768792366	3.738788865
34	4.4654343	11.673285	6.0557757	17.8617372	17.65517803	18.09092963
35	4.0079553	10.503443	5.5172354	16.0318212	15.92180711	16.42173495
36	3.8750095	10.165646	5.3627752	15.500038	15.42166518	15.9412537
37	3.8100801	10.002091	5.2886807	15.2403204	15.17975529	15.70961168
38	3.7707077	9.9039136	5.244694	15.0828308	15.0347201	15.5712692
39	3.7437433	9.8374054	5.2152579	14.9749732	14.93659947	15.47807358
40	3.7237738	9.788697	5.193974	14.8950952	14.86483795	15.4102153
41	3.7081593	9.7510294	5.1777269	14.8326372	14.80941928	15.35804483
42	3.6954567	9.7207117	5.1648171	14.7818268	14.76487446	15.31629518
43	3.6848088	9.6955544	5.1542382	14.7392352	14.72795989	15.28184475
44	3.6756723	9.6741732	5.1453556	14.7026892	14.69662545	15.2527224
45	3.6676823	9.6556421	5.1377482	14.6707292	14.6695013	15.22761575
46	3.6605594	9.6392694	5.1311185	14.6422376	14.64557208	15.20557603
47	3.6545895	9.625513	5.1253904	14.618358	14.6253816	15.1867179
48	3.6486103	9.6120211	5.1201248	14.5944412	14.60574651	15.1688911
49	3.6433304	9.6001272	5.1154348	14.5733216	14.58840778	15.1530587
50	3.6384845	9.5892692	5.1111811	14.553938	14.57258834	15.13864198

Table B.3: Calculated C_6 values for $^6\text{Li}\ |nP,3/2,\pm 1/2\rangle \otimes |nP,3/2,\pm 1/2\rangle$ pair-states. Calculated parameters to calculate C_6 values of ^6Li pair-states with full angular dependence according to Eq. 2.19 and some angles θ . The values are in natural units of $E_h a_\theta^{\ 6}$.

n	c_1/n^{*11}	c_2/n^{*11}	c_3/n^{*11}	$C_6(0)/n^{*11}$	$C_6(\pi/4)/n^{*11}$	$C_6(\pi/2)/n^{*11}$
20	2.3634474	9.1767562	9.5173272	9.4537896	16.26820913	23.7774336
21	2.3572976	9.160533	9.4973288	9.4291904	16.23717148	23.7262874
22	2.3506236	9.1422357	9.4754828	9.4024944	16.20263014	23.6704599
23	2.34437	9.1235802	9.4623932	9.37748	16.1727164	23.6347547
24	2.3365105	9.1003132	9.4337608	9.346042	16.12847043	23.5624723
25	2.3278776	9.0737002	9.4063087	9.3115104	16.08093077	23.49207218
26	2.3178138	9.0417724	9.3748002	9.2712552	16.02477251	23.41111425
27	2.3055609	9.001907	9.3366425	9.2222436	15.95539701	23.31300653
28	2.2897672	8.9494135	9.2876237	9.1590688	15.86482032	23.18692053
29	2.267812	8.8751483	9.219645	9.071248	15.73754515	23.01201325
30	2.2338153	8.7585556	9.1145688	8.9352612	15.53877383	22.7415951
31	2.1712338	8.541783	8.9214291	8.6849352	15.17061819	22.24444928
32	2.0088716	7.9755539	8.4205282	8.0354864	14.21126315	20.95506005
33	0.3014292	2.0014559	3.1557185	1.20571664	4.102086834	7.401795785
34	2.8965491	11.086203	11.157154	11.5861964	19.47201478	28.0001456
35	2.5945597	10.030958	10.225848	10.3782388	17.68550718	25.6027177
36	2.5075329	9.7279813	9.957352	10.0301316	17.17187269	24.9115749
37	2.4655108	9.5824297	9.8276345	9.8620432	16.92465552	24.57768843
38	2.4403676	9.4958699	9.749967	9.7614704	16.77730198	24.37779335
39	2.4233949	9.4378299	9.6975005	9.6935796	16.67825139	24.24277103
40	2.4110101	9.3957765	9.6591879	9.6440404	16.60629428	24.14418288
41	2.4014677	9.3636062	9.6296469	9.6058708	16.55110028	24.06817323
42	2.3938148	9.3379889	9.6059392	9.5752592	16.50703201	24.007178
43	2.3874865	9.3169521	9.5863229	9.549946	16.47074937	23.95671303
44	2.3821255	9.299251	9.5696984	9.528502	16.4401441	23.9139469
45	2.3774931	9.2840573	9.5553353	9.5099724	16.41381384	23.87699753
46	2.3734101	9.2707712	9.5427195	9.4936404	16.39074984	23.84452898
47	2.3700108	9.2594901	9.5316593	9.4800432	16.37098742	23.81624423
48	2.3666533	9.2488049	9.5215202	9.4666132	16.35242395	23.79007375
49	2.3637099	9.2393662	9.512395	9.4548396	16.33593664	23.76659865
50	2.3610292	9.2308	9.5040636	9.4441168	16.32094308	23.7451723

Table B.4: Calculated C_6 values for $^6\mathrm{Li}\ |nP,3/2,\pm 3/2\rangle\otimes |nP,3/2,\pm 3/2\rangle$ pairstates. Calculated parameters to calculate C_6 values of $^6\mathrm{Li}$ pair-states with full angular dependence according to Eq. 2.19 and some angles θ . The values are in natural units of $\mathrm{E}_{\mathrm{h}} a_{\theta}{}^6$.

n	c_1/n^{*11}	c_2/n^{*11}	c_3/n^{*11}	$C_6(0)/n^{*11}$	$C_6(\pi/4)/n^{*11}$	$C_6(\pi/2)/n^{*11}$
20	72.871573	178.76251	73.384203	291.486292	260.6043312	237.9860298
21	73.194583	179.54211	73.697346	292.778332	261.7382766	239.0136115
22	73.479386	180.22416	73.970151	293.917544	262.7302364	239.9122258
23	73.727866	180.81923	74.208197	294.911464	263.5957111	240.6963093
24	73.94583	181.34125	74.417055	295.78332	264.3549572	241.3842038
25	74.137954	181.80148	74.601255	296.551816	265.0243594	241.9907778
26	74.30818	182.2093	74.764511	297.23272	265.6175449	242.5283298
27	74.459656	182.57226	74.909844	297.838624	266.1454938	243.006805
28	74.594999	182.8966	75.039756	298.379996	266.6172875	243.43445
29	74.716387	183.18756	75.156329	298.865548	267.0405368	243.8181273
30	74.825648	183.44949	75.261305	299.302592	267.4215723	244.1635843
31	74.924316	183.68607	75.356155	299.697264	267.7657449	244.4756648
32	75.013696	183.90043	75.442121	300.054784	268.0776008	244.7584683
33	75.094895	184.09521	75.520263	300.37958	268.3609829	245.0154868
34	75.168861	184.27267	75.591487	300.675444	268.6191804	245.2497068
35	75.2364	184.43475	75.656563	300.9456	268.8550104	245.4636668
36	75.298554	184.58393	75.716465	301.194216	269.0720713	245.6606003
37	75.354959	184.71942	75.770952	301.419836	269.2692478	245.839601
38	75.407145	184.84474	75.821325	301.62858	269.4516141	246.0051263
39	75.455362	184.9605	75.867825	301.821448	269.6200546	246.1579683
40	75.499864	185.06729	75.910762	301.999456	269.7754709	246.2990785
41	75.540819	185.16583	75.950449	302.163276	269.9188911	246.4293293
42	75.578838	185.25724	75.987266	302.315352	270.0519416	246.5501865
43	75.614125	185.34211	76.021459	302.4565	270.1754757	246.6624078
44	75.646922	185.42101	76.053263	302.587688	270.2903272	246.7667638
45	75.677449	185.49446	76.08289	302.709796	270.3972554	246.8639515
46	75.705902	185.56296	76.110527	302.823608	270.4969769	246.9545878
47	75.732457	185.6269	76.136343	302.929828	270.5900697	247.0392288
48	75.757272	185.68667	76.160489	303.029088	270.6770968	247.1183723
49	75.78049	185.74262	76.183101	303.12196	270.7585643	247.1924673
50	75.802237	185.79504	76.204302	303.208948	270.8348991	247.2619165

Table B.5: Calculated C_6 values for $^6\text{Li}\ |nD,5/2,\pm 1/2\rangle\otimes |nD,5/2,\pm 1/2\rangle$ pairstates. Calculated parameters to calculate C_6 values of ^6Li pair-states with full angular dependence according to Eq. 2.19 and some angles θ . The values are in natural units of $E_h a_\theta{}^6$.

n	c_1/n^{*11}	c_2/n^{*11}	c_3/n^{*11}	$C_6(0)/n^{*11}$	$C_6(\pi/4)/n^{*11}$	$C_6(\pi/2)/n^{*11}$
20	55.043003	169.46958	119.22624	220.172012	271.4787883	323.302043
21	55.28656	170.20766	119.73105	221.14624	272.6539731	324.6814225
22	55.499762	170.85372	120.17335	221.999048	273.6828849	325.8897995
23	55.685755	171.4174	120.55935	222.74302	274.5806481	326.9442925
24	55.848888	171.91188	120.89808	223.395552	275.368257	327.869568
25	55.992686	172.34786	121.19686	223.970744	276.0627478	328.685621
26	56.120083	172.73419	121.46171	224.480332	276.6781964	329.4089305
27	56.233443	173.07803	121.69753	224.933772	277.2260051	330.0528855
28	56.334723	173.3853	121.90836	225.338892	277.7155958	330.628533
29	56.425558	173.66094	122.09757	225.702232	278.1548301	331.1450905
30	56.507313	173.90909	122.26799	226.029252	278.5502989	331.6102905
31	56.581139	174.13324	122.42201	226.324556	278.9075604	332.0306615
32	56.648011	174.33633	122.56162	226.592044	279.2312853	332.411656
33	56.70876	174.52088	122.68856	226.83504	279.525495	332.75802
34	56.764095	174.68903	122.80428	227.05638	279.79359	333.073725
35	56.81462	174.84261	122.91003	227.25848	280.0384831	333.3621875
36	56.861114	174.98396	123.00739	227.444456	280.2638904	333.6277415
37	56.903302	175.11236	123.09601	227.613208	280.4687361	333.8693245
38	56.942338	175.23112	123.17792	227.769352	280.6581745	334.092658
39	56.978413	175.34081	123.25349	227.913652	280.8331026	334.2987655
40	57.011648	175.44202	123.32343	228.046592	280.9946139	334.4893655
41	57.042305	175.53541	123.38797	228.16922	281.1436456	334.6652375
42	57.070739	175.62205	123.4479	228.282956	281.2819348	334.828514
43	57.097126	175.70248	123.50357	228.388504	281.4103296	334.9801585
44	57.12165	175.77727	123.55537	228.4866	281.5297369	335.1212325
45	57.144475	175.8469	123.60363	228.5779	281.6409231	335.2526425
46	57.165748	175.91182	123.64867	228.662992	281.7446114	335.3752555
47	57.185601	175.97244	123.69075	228.742404	281.8414421	335.4897885
48	57.204152	176.0291	123.73012	228.816608	281.931968	335.596922
49	57.221508	176.08214	123.76699	228.886032	282.0167164	335.6972355
50	57.237764	176.13184	123.80158	228.951056	282.0961498	335.791319

Table B.6: Calculated C_6 values for $^6\text{Li}\ |nD,5/2,\pm 3/2\rangle \otimes |nD,5/2,\pm 3/2\rangle$ pairstates. Calculated parameters to calculate C_6 values of ^6Li pair-states with full angular dependence according to Eq. 2.19 and some angles θ . The values are in natural units of $E_h a_\theta{}^6$.

n	c_1/n^{*11}	c_2/n^{*11}	c_3/n^{*11}	$C_6(0)/n^{*11}$	$C_6(\pi/4)/n^{*11}$	$C_6(\pi/2)/n^{*11}$
20	22.484735	145.37462	212.2876	89.93894	288.5794063	500.131835
21	22.588789	145.99518	213.18437	90.355156	289.8079829	502.2536215
22	22.679002	146.53331	213.97464	90.716008	290.8804593	504.121942
23	22.757664	147.00283	214.66438	91.030656	291.8163135	505.752519
24	22.826611	147.41475	215.26975	91.306444	292.6374809	507.1835485
25	22.887348	147.77804	215.80372	91.549392	293.3617245	508.445718
26	22.941121	148.1	216.27711	91.764484	294.0036546	509.5646185
27	22.988935	148.3866	216.69864	91.95574	294.5751438	510.560875
28	23.031622	148.64277	217.07553	92.126488	295.0860074	511.4515645
29	23.069877	148.87263	217.41382	92.279508	295.5444518	512.250972
30	23.104279	149.07961	217.71854	92.417116	295.9573098	512.970994
31	23.13532	149.26662	217.99395	92.54128	296.3303744	513.6217075
32	23.163412	149.4361	218.24363	92.653648	296.6685074	514.2115795
33	23.188908	149.59015	218.47066	92.755632	296.975892	514.747893
34	23.21211	149.73055	218.67765	92.84844	297.2560744	515.2368225
35	23.233274	149.85883	218.86684	92.933096	297.5120998	515.683664
36	23.25274	149.9769	219.04102	93.01096	297.7477713	516.095035
37	23.270342	150.08429	219.19962	93.081368	297.962198	516.469487
38	23.28665	150.18357	219.34618	93.1466	298.160405	516.815555
39	23.30175	150.27523	219.48137	93.207	298.3433419	517.1348325
40	23.315565	150.35976	219.60671	93.26226	298.5123956	517.4306625
41	23.328338	150.43801	219.72216	93.313352	298.6685608	517.703198
42	23.340159	150.51056	219.82944	93.360636	298.8134798	517.956399
43	23.351115	150.57793	219.92912	93.40446	298.94808	518.191635
44	23.361284	150.64059	220.02188	93.445136	299.0732923	518.410514
45	23.370737	150.69895	220.10832	93.482948	299.189933	518.614457
46	23.379535	150.75339	220.18898	93.51814	299.2987488	518.80474
47	23.387734	150.80424	220.26437	93.550936	299.4004116	518.9825665
48	23.395385	150.85179	220.33491	93.58154	299.4954969	519.1489325
49	23.402533	150.89633	220.401	93.610132	299.584567	519.304783
50	23.409217	150.93808	220.46299	93.636868	299.6680761	519.4509445

Table B.7: Calculated C_6 values for ${}^6\mathrm{Li}\ |nD,5/2,\pm5/2\rangle\otimes|nD,5/2,\pm5/2\rangle$ pairstates. Calculated parameters to calculate C_6 values of ${}^6\mathrm{Li}$ pair-states with full angular dependence according to Eq. 2.19 and some angles θ . The values are in natural units of $\mathrm{E}_{\mathrm{h}} a_{\theta}{}^6$.

Appendix C

Forster Resonances of ⁶Li.

We calculated the Förster defects $\delta_{\alpha\beta}^{-1}$ for ⁶Li $|nP\rangle$ Rydberg states using Pair-Interaction [87]. Fig. C.1 shows these calculated defects for all relevant channels that can be used to tune a Förster resonance. The main channel that can be used to tune such resonances is the $|(n\pm 1)D\rangle\otimes|(n\mp 1)D\rangle$ pair state. This is because it has strongest dipole matrix element couplings with target states $|nP\rangle\otimes|nP\rangle$ and also is least "sharp" which would lead to broader resonances.

¹See Eq. 2.14.

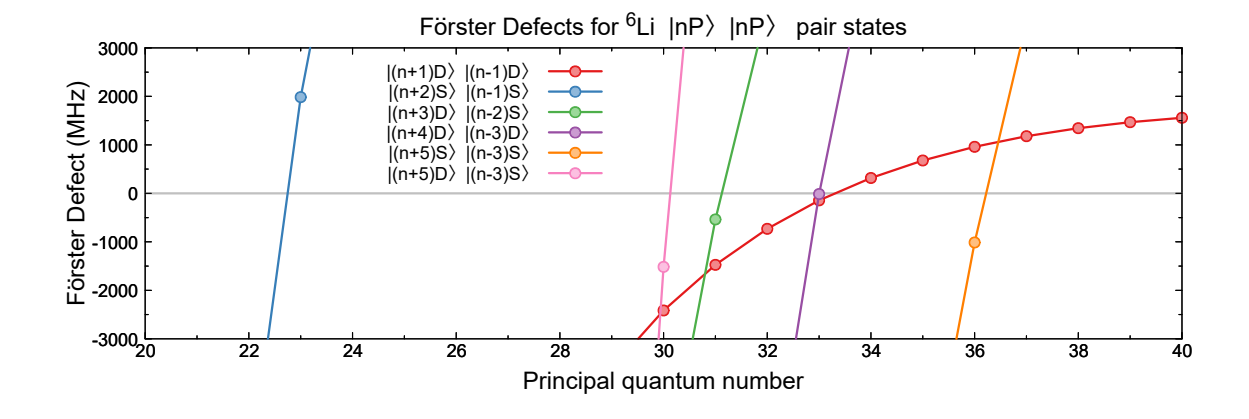


Figure C.1: Förster defects of ${}^6\mathrm{Li} |nP\rangle \otimes |nP\rangle$ Rydberg states. Relevant channels that could be used to tune a Förster resonance with a field. The specific $|j,m\rangle$ channels can be easily derived from the selection rules.

Table C.1 shows all the magnetic fields less than 1000 G that would lead to a Förster resonance for each possible principal quantum number. We can calculate these values by matching the Förster defect $\delta_{\alpha\beta}$ and the magnetic field dispersion from Eq. 3.1. With these results, it seems we could be able to tune reasonable resonances using magnetic fields for states as low as $|30P\rangle \otimes |30P\rangle$.

nP state	B field (G)		
23P	708.5		
30P	542.0 863.0		
31P	191.9 526.6		
32P	261.0		
33P	4.9 51.6		
34P	113.2		
35P	242.4		
36P	343.0 361.9		
37P	420.7		
38P	479.9		
39P	524.3		
40P	556.7		

Table C.1: Magnetic fields to tune Förster resonances in $|nP, nP\rangle$ states. Predicted Förster resonances with magnetic field according to the known magnetic dispersion of Eq. 3.1 and Förster defects shown in Fig. C.1. These predictions do not have any information as to the width of these resonances.

C.1 C_6 coefficients with Pair-Interaction

To test the predicted Förster resonances, we developed two different methods to calculate C_6 coefficients using Pair-Interaction. The first method involves comparing the energy of the bare pair-state $E_{|k^*,k^*\rangle}(\infty) = 2E_{|k^*\rangle}$ to the calculated energy of the pair state at a large distance (e.g. 5 a_{latt} is sufficient). By matching the energy difference between these two and applying it to a simple van der Waals potential $V(R) = -C_6/R^6$ we extract coefficients that we find agree very well to the full pair potential at closer distances when accounting for overlap. While this method is very

good at finding a good C_6 coefficient, pair-state calculations are very computationally expensive. This makes the method too costly to do a full exploratory calculation.

Instead, we decided to calculate the C_6 perturbatively as explained in Sec. 2.5.1. This requires only single-particle calculations and is much faster due to its implementation in the Pair-Interaction package which very efficiently calculates dipole matrix elements between Rydberg states. Similarly to the 0 field calculation of Sec. 2.5.1 for the $|j,m\rangle$ basis. We can calculate full angular dependence of the C_6 coefficients by keeping track of $|\Delta m_a + \Delta m_b| = 0, 1, 2^2$. We perform calculations at many different magnetic and electric fields. We find the exact same results shown in Fig. 2.4 for 0 field. Fig. C.2 shows these calculated C_6 coefficients for an angle $\theta = \pi/2$ for various principal quantum numbers and fields. We find very good agreement with the predicted resonances from Table. C.1. It is important to note that in the case of $|31P\rangle$ Rydberg states, we were dressing relatively close to a Förster resonance which could also have impacted our ability to dress the atoms within the simple Rydberg dressing scheme.

We should also note that tuning the Förster resonances with electric field is much more complicated and asymmetric for different $|k^*\rangle \otimes |k^*\rangle$ pair-states. This implies that Rydberg dressing schemes at high magnetic fields can be much more straightforward to implement and tune. Furthermore, it is important to mention that implementing the same calculations for different species is very easy within the Pair-Interaction package.

²Even though m is not a "good" quantum number at high magnetic fields. The symmetry considerations that allowed for these separations carry forward.

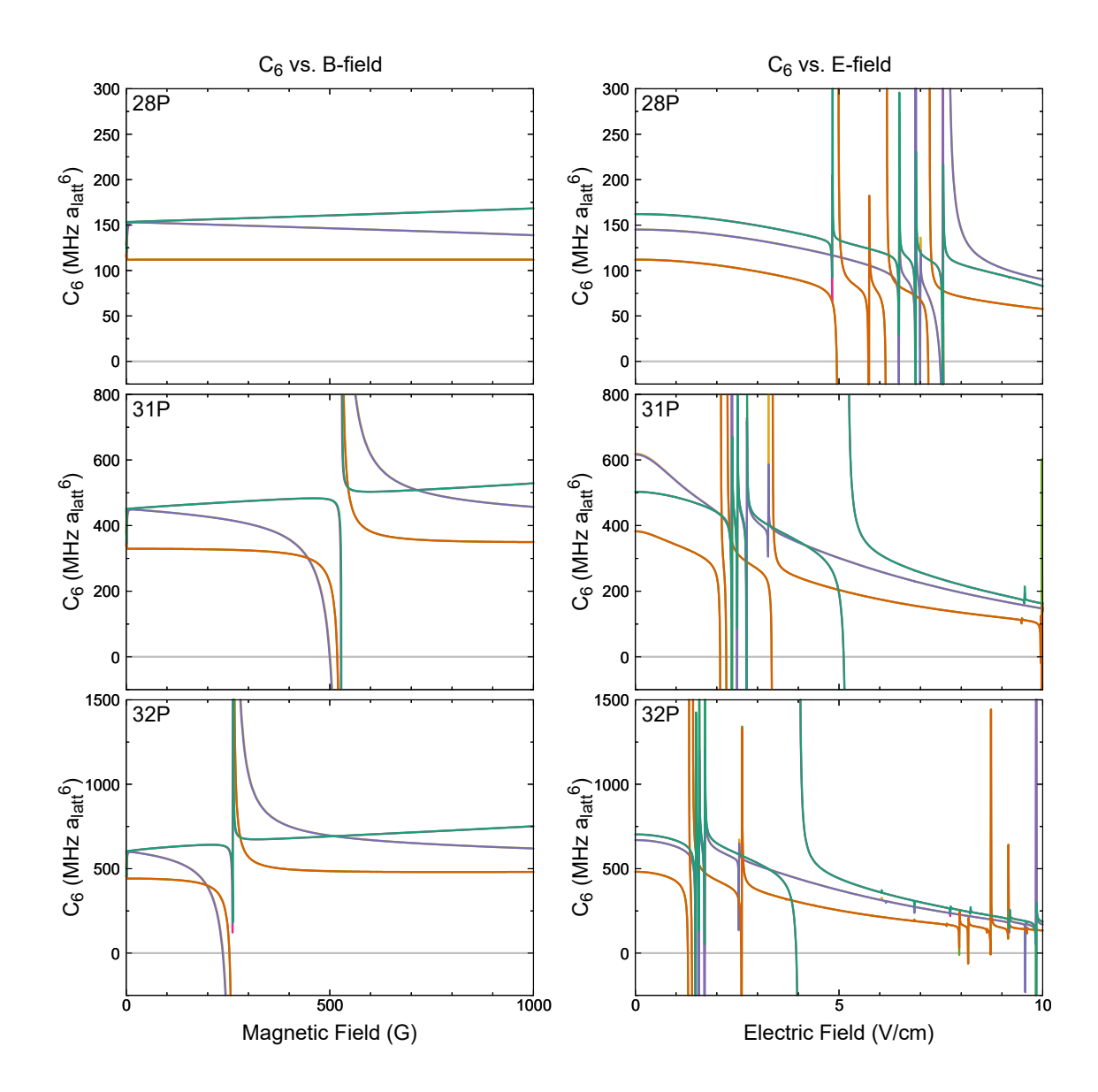


Figure C.2: ⁶Li $C_6(\pi/2)$ coefficients vs. electromagnetic fields and principal quantum number. Plots for the C_6 coefficients of $|k^*\rangle \otimes |k^*\rangle$ pair-states as a function of magnetic (left column $E=0\,\mathrm{V/cm}$) and electric (right column $B=600\,\mathrm{G}$) fields and for $|28P\rangle$, $|31P\rangle$, and $|41P\rangle$ Rydberg states. This are for dipoles parallel to eachother aligned perpendicularly to their distance vector ($\theta=\pi/2$). The colors correspond to the different possible pair-states as numbered in Fig. 3.1b and shown in Fig. 3.2. Note how the Förster resonances with magnetic field agree with the predicted values from Table. C.1.

Appendix D

Measured $|2S\rangle \rightarrow |nP\rangle$ Rydberg Lines of ⁶Li.

For the purpose of this thesis, we found a lot of the Rydberg lines of Lithium-6 for the purpose of using these states for experiments. The methods used to find these lines are explained in Sec. 3.5. Developing these techniques was necessary as these lines were not exactly known before, The NIST Atomic Spectra Database in Ref. [105] only lists approximate wavelengths up to the transition to $|32P\rangle$. However, it is simple to calculate the expected wavelength transitions in terms of the ionization energy $(E_{ion}^{Li} = 5.391714996(22) \,\text{eV} \, [105])$ and the binding energy with quantum defects of Eq. 2.1. We can calculate the energy difference between these convert to wavelength $(\lambda = hc/\Delta E)$ and multiply by 4 to extract the pre-quadrupoled wavelength of our laser system λ_{exp} .

We reference the wavelength to the modes of the ULE cavity (Sec. 3.4.2) using a wavemeter (Burleigh WA-20VIS) and find the necessary sideband frequency $\Delta\nu$ to drive the EOM and lock the laser from that line. We can extract $\lambda_{meas} = \lambda_{mode} - \lambda_{mode}^2 \Delta\nu/c$, although these value does not have much real meaning since the wavemeter we use is not that precise. However, the fact that measured and expected

n	$\lambda_{exp} \; (\mathrm{nm})$	Closest mode (nm)	Sideband (MHz)	$\lambda_{meas} (nm)$	$\lambda_{UV} \text{ (nm)}$
23	924.2510	924.2510	211	924.25040	231.06260
25	923.5671	923.5660	-651	923.56785	230.89196
26	923.2832	923.2870	349	923.28601	230.82150
28	923.8044	922.8040	-379	922.80508	230.70127
30	922.4186	922.4220	728	922.41994	230.60498
31	922.2533	922.2560	605	922.25428	230.56357
32	922.1033	922.1020	-425	922.10320	230.52580
33	921.9667	921.9670	-217	921.96761	230.49190
34	921.8421	921.8440	350	921.84301	230.46075
35	921.7281	921.7290	160	921.72855	230.43214
36	921.6235	921.6240	-345	921.62498	230.40624
37	921.5272	951.5300	680	951.52795	237.88199
38	921.4385	921.4410	555	921.43943	230.35986
39	921.3566	921.3550	-452	921.35628	230.33907
40	921.2807	921.2790	-611	921.28073	230.32018
44	921.0274	921.0300	603.5	921.02829	230.25707

Table D.1: Measured wavelengths of ${}^{6}\text{Li} |2S\rangle \rightarrow |nP\rangle$ transitions. Summary of measured values for various Rydberg transitions. The method of finding these lines is described in Sec. 3.5.

values are so close means that we can trust the calculated values to find any state as long as we have access to a "ruler" such as the ULE cavity. Table. D.1 shows these calculations along with $\lambda_{UV} = \lambda_{meas}/4$.

Using the "V-scheme" spectroscopy method we found lines up to $|40P\rangle$, at which point the spectroscopy signal as shown in Fig. 3.9c was too small to observe due to the inverse scaling of dipole matrix element with principal quantum number (Table. 2.1). As a proof of principle, we found the $|44P\rangle$ Rydberg line using only "MOT spectroscopy" where we look at depletion of our magneto-optical trap as explained in Sec. 3.5. It is important to mention that the values listed in Table. D.1 were taken over the course of 4 years and we never observed a drift in their values larger than $\sim 1\,\mathrm{MHz}$ in sideband frequency, even when referencing to the same Rydberg line years apart.

Bibliography

- [1] I. Bloch. Ultracold quantum gases in optical lattices. Nature Physics 1, 23–30 (2005). Review Article. (Cited on page 1.)
- [2] M. Lewenstein, A. Sanpera, V. Ahufinger, B. Damski, A. Sen(De), and U. Sen. Ultracold atomic gases in optical lattices: mimicking condensed matter physics and beyond. *Advances in Physics* **56**, 2, 243–379 (2007). (Cited on page 1.)
- [3] I. Bloch, J. Dalibard, and W. Zwerger. Many-body physics with ultracold gases. *Rev. Mod. Phys.* **80**, 885–964 (2008). (Cited on pages 1 and 133.)
- [4] C. Gross and W. S. Bakr. Quantum gas microscopy for single atom and spin detection. arXiv:2010.15407 (2020). (Cited on page 1.)
- [5] T. Esslinger. Fermi-Hubbard physics with atoms in an optical lattice. Annual Review of Condensed Matter Physics 1, 1, 129–152 (2010). (Cited on page 2.)
- [6] P. W. Anderson. The resonating valence bond state in La2CuO4 and superconductivity. *Science* **235**, 4793, 1196–1198 (1987). (Cited on page **2**.)
- [7] P. T. Brown, D. Mitra, E. Guardado-Sanchez, P. Schauß, S. S. Kondov, E. Khatami, T. Paiva, N. Trivedi, D. A. Huse, and W. S. Bakr. Spin-imbalance in a 2D Fermi-Hubbard system. *Science* 357, 6358, 1385–1388 (2017). (Cited on pages 2, 90, 94, 113, and 117.)
- [8] D. Mitra, P. T. Brown, E. Guardado-Sanchez, S. S. Kondov, T. Devakul, D. A. Huse, P. Schauß, and W. S. Bakr. Quantum gas microscopy of an attractive Fermi-Hubbard system. *Nat. Phys.* (2017). (Cited on page 2.)
- [9] P. T. Brown, D. Mitra, E. Guardado-Sanchez, R. Nourafkan, A. Reymbaut, C.-D. Hébert, S. Bergeron, A.-M. S. Tremblay, J. Kokalj, D. A. Huse, P. Schauß, and W. S. Bakr. Bad metallic transport in a cold atom Fermi-Hubbard system. Science 363, 6425, 379–382 (2019). (Cited on pages 2, 109, 110, 111, 116, 118, 121, 129, and 144.)
- [10] E. Khatami, E. Guardado-Sanchez, B. M. Spar, J. F. Carrasquilla, W. S. Bakr, and R. T. Scalettar. Visualizing strange metallic correlations in the two-dimensional Fermi-Hubbard model with artificial intelligence. *Phys. Rev.* A 102, 033326 (2020). (Cited on page 2.)

- [11] P. T. Brown, E. Guardado-Sanchez, B. M. Spar, E. W. Huang, T. P. Devereaux, and W. S. Bakr. Angle-resolved photoemission spectroscopy of a Fermi-Hubbard system. *Nature Physics* 16, 1, 26–31 (2020). (Cited on pages 2, 109, and 120.)
- [12] E. Guardado-Sanchez, P. T. Brown, D. Mitra, T. Devakul, D. A. Huse, P. Schauß, and W. S. Bakr. Probing the quench dynamics of antiferromagnetic correlations in a 2D quantum Ising spin system. *Phys. Rev. X* 8 (2018). (Cited on pages 2, 7, 85, and 135.)
- [13] E. Guardado-Sanchez, A. Morningstar, B. M. Spar, P. T. Brown, D. A. Huse, and W. S. Bakr. Subdiffusion and heat transport in a tilted two-dimensional Fermi-Hubbard system. *Phys. Rev. X* 10, 011042 (2020). (Cited on pages 2, 3, 109, 122, 123, 125, 128, 130, and 143.)
- [14] E. Guardado-Sanchez, B. M. Spar, P. Schauss, R. Belyansky, J. T. Young, P. Bienias, A. V. Gorshkov, T. Iadecola, and W. S. Bakr. Quench dynamics of a Fermi gas with strong nonlocal interactions. *Phys. Rev. X* 11, 021036 (2021). (Cited on pages 2, 78, 107, and 132.)
- [15] M. Saffman, T. G. Walker, and K. Mølmer. Quantum information with Rydberg atoms. Rev. Mod. Phys. 82, 3, 2313–2363 (2010). (Cited on pages 2, 3, 7, and 133.)
- [16] P. Schauss. Quantum simulation of transverse Ising models with Rydberg atoms. Quantum Sci. Technol. 3, 023001 (2018). (Cited on pages 2 and 3.)
- [17] G. Pupillo, A. Micheli, M. Boninsegni, I. Lesanovsky, and P. Zoller. Strongly correlated gases of Rydberg-dressed atoms: Quantum and classical dynamics. *Phys. Rev. Lett.* **104**, 223002 (2010). (Cited on pages 2, 23, and 133.)
- [18] N. Henkel, R. Nath, and T. Pohl. Three-dimensional roton excitations and supersolid formation in Rydberg-excited Bose-Einstein condensates. *Phys. Rev.* Lett. 104, 195302 (2010). (Cited on pages 2, 23, and 133.)
- [19] J. E. Johnson and S. L. Rolston. Interactions between Rydberg-dressed atoms. *Phys. Rev. A* 82, 033412 (2010). (Cited on pages 2 and 133.)
- [20] F. Böttcher, J.-N. Schmidt, M. Wenzel, J. Hertkorn, M. Guo, T. Langen, and T. Pfau. Transient supersolid properties in an array of dipolar quantum droplets. Phys. Rev. X 9, 011051 (2019). (Cited on pages 3, 132, 133, and 154.)
- [21] Y. Tang, W. Kao, K.-Y. Li, S. Seo, K. Mallayya, M. Rigol, S. Gopalakrishnan, and B. L. Lev. Thermalization near integrability in a dipolar quantum Newton's cradle. *Phys. Rev. X* 8, 021030 (2018). (Cited on pages 3, 132, 133, and 154.)
- [22] A. Patscheider, B. Zhu, L. Chomaz, D. Petter, S. Baier, A.-M. Rey, F. Ferlaino, and M. J. Mark. Controlling dipolar exchange interactions in a dense three-dimensional array of large-spin fermions. *Phys. Rev. Research* 2, 023050 (2020). (Cited on pages 3, 132, 133, and 154.)

- [23] L. Gabardos, B. Zhu, S. Lepoutre, A. M. Rey, B. Laburthe-Tolra, and L. Vernac. Relaxation of the collective magnetization of a dense 3D array of interacting dipolar s=3 atoms. *Phys. Rev. Lett.* **125**, 143401 (2020). (Cited on pages 3, 132, 133, and 154.)
- [24] L. De Marco, G. Valtolina, K. Matsuda, W. G. Tobias, J. P. Covey, and J. Ye. A degenerate Fermi gas of polar molecules. *Science* 363, 6429, 853–856 (2019). (Cited on pages 3, 132, 133, and 154.)
- [25] J. L. Bohn, A. M. Rey, and J. Ye. Cold molecules: Progress in quantum engineering of chemistry and quantum matter. Science 357, 6355, 1002–1010 (2017). (Cited on pages 3, 132, 133, and 154.)
- [26] R. Blatt and C. F. Roos. Quantum simulations with trapped ions. Nat. Phys. 8, 4, 277–284 (2012). (Cited on pages 3 and 133.)
- [27] C. D. Bruzewicz, J. Chiaverini, R. McConnell, and J. M. Sage. Trapped-ion quantum computing: Progress and challenges. *Appl. Phys. Rev.* **6**, 2, 021314 (2019). (Cited on pages **3** and **133**.)
- [28] L. Anderegg, L. W. Cheuk, Y. Bao, S. Burchesky, W. Ketterle, K.-K. Ni, and J. M. Doyle. An optical tweezer array of ultracold molecules. *Science* 365, 6458, 1156–1158 (2019). (Cited on pages 3 and 133.)
- [29] L. R. Liu, J. D. Hood, Y. Yu, J. T. Zhang, K. Wang, Y.-W. Lin, T. Rosenband, and K.-K. Ni. Molecular assembly of ground-state cooled single atoms. *Phys. Rev. X* 9, 021039 (2019). (Cited on pages 3 and 133.)
- [30] H. Ritsch, P. Domokos, F. Brennecke, and T. Esslinger. Cold atoms in cavity-generated dynamical optical potentials. *Rev. Mod. Phys.* **85**, 553–601 (2013). (Cited on pages 3 and 133.)
- [31] M. Mattioli, M. Dalmonte, W. Lechner, and G. Pupillo. Cluster Luttinger liquids of Rydberg-dressed atoms in optical lattices. *Phys. Rev. Lett.* **111**, 165302 (2013). (Cited on pages **3** and **151**.)
- [32] A. Dauphin, M. Müller, and M. A. Martin-Delgado. Quantum simulation of a topological Mott insulator with Rydberg atoms in a Lieb lattice. *Phys. Rev. A* **93**, 043611 (2016). (Cited on page 3.)
- [33] T. Grass, P. Bienias, M. J. Gullans, R. Lundgren, J. Maciejko, and A. V. Gorshkov. Fractional quantum Hall phases of bosons with tunable interactions: From the Laughlin liquid to a fractional Wigner crystal. *Phys. Rev. Lett.* **121**, 25, 253403 (2018). (Cited on page **3**.)
- [34] M. Burrello, I. Lesanovsky, and A. Trombettoni. Reaching the quantum Hall regime with rotating Rydberg-dressed atoms. *Phys. Rev. Research* 2, 023290 (2020). (Cited on page 3.)

- [35] F. Grusdt, M. Kánasz-Nagy, A. Bohrdt, C. S. Chiu, G. Ji, M. Greiner, D. Greif, and E. Demler. Parton theory of magnetic polarons: Mesonic resonances and signatures in dynamics. *Phys. Rev. X* 8, 1, 011046 (2018). (Cited on page 3.)
- [36] X. Li and S. D. Sarma. Exotic topological density waves in cold atomic Rydberg-dressed fermions. Nat. Commun. 6, May, 7137 (2015). (Cited on pages 3 and 107.)
- [37] B. Xiong, H. H. Jen, and D.-W. Wang. Topological superfluid by blockade effects in a Rydberg-dressed Fermi gas. *Phys. Rev. A* **90** (2014). (Cited on pages 3 and 107.)
- [38] W.-h. Li, T.-c. Hsieh, C.-y. Mou, and D.-w. Wang. Emergence of a metallic quantum solid phase in a Rydberg-dressed Fermi gas. *Phys. Rev. Lett.* **035301**, July, 1–5 (2016). (Cited on page 3.)
- [39] P. Sala, T. Rakovszky, R. Verresen, M. Knap, and F. Pollmann. Ergodicity breaking arising from Hilbert space fragmentation in dipole-conserving Hamiltonians. *Phys. Rev. X* **10**, 011047 (2020). (Cited on pages 4, 111, 117, and 134.)
- [40] V. Khemani, M. Hermele, and R. Nandkishore. Localization from Hilbert space shattering: From theory to physical realizations. *Phys. Rev. B* 101, 174204 (2020). (Cited on pages 4, 111, 117, and 134.)
- [41] R. Nandkishore and D. A. Huse. Many-body localization and thermalization in quantum statistical mechanics. *Annu. Rev. Condens. Matter Phys* **6**, 1, 15–38 (2015). (Cited on pages **4** and **134**.)
- [42] D. A. Abanin, E. Altman, I. Bloch, and M. Serbyn. Colloquium: Many-body localization, thermalization, and entanglement. Rev. Mod. Phys. 91, 021001 (2019). (Cited on pages 4 and 134.)
- [43] H. Bernien, S. Schwartz, A. Keesling, H. Levine, A. Omran, H. Pichler, S. Choi, A. S. Zibrov, M. Endres, M. Greiner, V. Vuletić, and M. D. Lukin. Probing many-body dynamics on a 51-atom quantum simulator. Nature 551, 579 584 (2017). (Cited on pages 4, 7, 86, 87, 98, 107, 110, and 134.)
- [44] C. J. Turner, A. A. Michailidis, D. A. Abanin, M. Serbyn, and Z. Papić. Quantum scarred eigenstates in a Rydberg atom chain: Entanglement, breakdown of thermalization, and stability to perturbations. *Phys. Rev. B* 98, 155134 (2018). (Cited on pages 4 and 134.)
- [45] L. D'Alessio, Y. Kafri, A. Polkovnikov, and M. Rigol. From quantum chaos and eigenstate thermalization to statistical mechanics and thermodynamics. *Adv. Phys* **65**, 3, 239–362 (2016). (Cited on pages 4 and 135.)
- [46] R. M. Nandkishore and M. Hermele. Fractons. Annu. Rev. Condens. Matter Phys. 10, 1, 295–313 (2019). (Cited on pages 4 and 117.)

- [47] G. De Tomasi, D. Hetterich, P. Sala, and F. Pollmann. Dynamics of strongly interacting systems: From Fock-space fragmentation to many-body localization. *Phys. Rev. B* **100**, 214313 (2019). (Cited on pages 4, 134, and 145.)
- [48] Z.-C. Yang, F. Liu, A. V. Gorshkov, and T. Iadecola. Hilbert-space fragmentation from strict confinement. *Phys. Rev. Lett.* 124, 207602 (2020). (Cited on pages 4, 134, and 151.)
- [49] T. F. Gallagher. *Rydberg Atoms*. Cambridge University Press, Cambridge, (1994). ISBN 9780511524530. (Cited on pages 6, 8, and 86.)
- [50] V. Lienhard, S. de Léséleuc, D. Barredo, T. Lahaye, A. Browaeys, M. Schuler, L.-P. Henry, and A. M. Läuchli. Observing the space- and time-dependent growth of correlations in dynamically tuned synthetic Ising models with antiferromagnetic interactions. *Phys. Rev. X* 8, 021070 (2018). (Cited on pages 7, 86, and 107.)
- [51] I. S. Madjarov, A. Cooper, A. L. Shaw, J. P. Covey, V. Schkolnik, T. H. Yoon, J. R. Williams, and M. Endres. An atomic-array optical clock with single-atom readout. *Phys. Rev. X* 9, 041052 (2019). (Cited on pages 7 and 107.)
- [52] M. A. Norcia, A. W. Young, W. J. Eckner, E. Oelker, J. Ye, and A. M. Kaufman. Seconds-scale coherence on an optical clock transition in a tweezer array. Science 366, 6461, 93–97 (2019). (Cited on pages 7 and 107.)
- [53] A. Browaeys and T. Lahaye. Many-body physics with individually controlled Rydberg atoms. *Nat. Phys* **16**, 2, 132–142 (2020). (Cited on pages **7**, **17**, and **107**.)
- [54] L. W. Clark, N. Schine, C. Baum, N. Jia, and J. Simon. Observation of Laughlin states made of light. *Nature* **582**, 7810, 41–45 (2020). (Cited on page **7**.)
- [55] V. Borish, O. Marković, J. A. Hines, S. V. Rajagopal, and M. Schleier-Smith. Transverse-field Ising dynamics in a Rydberg-dressed atomic gas. *Phys. Rev. Lett.* **124**, 063601 (2020). (Cited on pages **7**, **34**, **35**, **133**, and **134**.)
- [56] S. H. Cantu, A. V. Venkatramani, W. Xu, L. Zhou, M. D. Jelenković, Brana nd Lukin, and V. Vuletić. Repulsive photons in a quantum nonlinear medium. Nature Physics 16, 9, 921–925 (2020). (Cited on page 7.)
- [57] P. Schauß, J. Zeiher, T. Fukuhara, S. Hild, M. Cheneau, T. Macrì, T. Pohl, I. Bloch, and C. Gross. Crystallization in Ising quantum magnets. Science 347, 6229, 1455–1458 (2015). (Cited on page 7.)
- [58] X. Wu, X. Liang, Y. Tian, F. Yang, C. Chen, Y.-C. Liu, M. K. Tey, and L. You. A concise review of Rydberg atom based quantum computation and quantum simulation. *Chinese Physics B* **30**, 2, 020305 (2021). (Cited on page **7**.)

- [59] J. D. Pritchard. Cooperative Optical Non-linearity in a blockaded Rydberg Ensemble. PhD thesis, Department of Physics, Durham University, (2011). (Cited on pages 7 and 17.)
- [60] N. Henkel. Rydberg-dressed Bose-Einstein condensates. PhD thesis, der Fakultät Mathematik und Naturwissenschaften der Technoschen Universität Dresden, (2013). (Cited on pages 7, 17, and 20.)
- [61] P. Schauß. *High-resolution imaging of ordering in Rydberg many-body systems*. PhD thesis, Fakultät für Physik, Ludwig–Maximilians–Universität München, (2014). (Cited on page 7.)
- [62] J. Zeiher. Realization of Rydberg-dressed quantum magnets. PhD thesis, Fakultät für Physik, Ludwig-Maximilians-Universität München, (2017). (Cited on pages 7, 17, 72, 74, and 80.)
- [63] R. M. Langer. A generalization of the Rydberg formula. Phys. Rev. 35, 649–650 (1930). (Cited on page 7.)
- [64] P. Goy, J. Liang, M. Gross, and S. Haroche. Quantum defects and specific-isotopic-shift measurements in nS and nP highly excited states of lithium: Exchange effects between Rydberg and core electrons. *Phys. Rev. A* 34, 2889–2896 (1986). (Cited on pages 7, 8, and 12.)
- [65] NIST. 2018 CODATA Value: Rydberg constant times c in Hz, (The NIST Reference on Constants, Units, and Uncertainty). Accessed: 2021-04-20. (Cited on page 7.)
- [66] I. I. Beterov, I. I. Ryabtsev, D. B. Tretyakov, and V. M. Entin. Quasiclassical calculations of blackbody-radiation-induced depopulation rates and effective lifetimes of Rydberg nS, nP, and nD alkali-metal atoms with $n \leq 80$. Phys. Rev. A 79 (2009). (Cited on pages 9, 15, 92, and 141.)
- [67] M. Marinescu, H. R. Sadeghpour, and A. Dalgarno. Dispersion coefficients for alkali-metal dimers. Phys. Rev. A 49, 982–988 (1994). (Cited on pages 10, 11, and 12.)
- [68] B. V. Noumerov. A method of extrapolation of perturbations. *Mon. Not. R. Astron. Soc* 84, 8, 592–602 (1924). (Cited on pages 10, 12, and 156.)
- [69] E. P. Wigner. On the Matrices Which Reduce the Kronecker Products of Representations of S. R. Groups, pages 608–654. Springer Berlin Heidelberg, Berlin, Heidelberg, (1993). ISBN 978-3-662-02781-3. (Cited on page 13.)
- [70] B. E. King. Angular momentum coupling and Rabi frequencies for simple atomic transitions. *arXiv:0804.4528* (2008). (Cited on page 13.)

- [71] J. B. Balewski, A. T. Krupp, A. Gaj, S. Hofferberth, R. Löw, and T. Pfau. Rydberg dressing: understanding of collective many-body effects and implications for experiments. New J. Phys 16, 6, 063012 (2014). (Cited on pages 14, 34, 71, 133, 134, and 139.)
- [72] E. A. Goldschmidt, T. Boulier, R. C. Brown, S. B. Koller, J. T. Young, A. V. Gorshkov, S. L. Rolston, and J. V. Porto. Anomalous broadening in driven dissipative Rydberg systems. *Phys. Rev. Lett.* 116, 113001 (2016). (Cited on pages 14, 34, 71, 133, 134, and 139.)
- [73] J. A. Aman, B. J. DeSalvo, F. B. Dunning, T. C. Killian, S. Yoshida, and J. Burgdörfer. Trap losses induced by near-resonant Rydberg dressing of cold atomic gases. *Phys. Rev. A* 93, 043425 (2016). (Cited on pages 14, 34, 71, 133, 134, and 139.)
- [74] T. Boulier, E. Magnan, C. Bracamontes, J. Maslek, E. A. Goldschmidt, J. T. Young, A. V. Gorshkov, S. L. Rolston, and J. V. Porto. Spontaneous avalanche dephasing in large Rydberg ensembles. *Phys. Rev. A* 96, 053409 (2017). (Cited on pages 14, 34, 71, 133, 134, and 139.)
- [75] J. Zeiher, R. van Bijnen, P. Schauß, S. Hild, J.-Y. Choi, T. Pohl, I. Bloch, and C. Gross. Many-body interferometry of a Rydberg-dressed spin lattice. *Nat. Phys.* 12, 12, 1095–1099 (2016). (Cited on pages 14, 34, 35, 50, 71, 79, 80, 82, 84, 107, 133, 134, 138, 139, and 141.)
- [76] N. Šibalić, J. Pritchard, C. Adams, and K. Weatherill. ARC: An open-source library for calculating properties of alkali Rydberg atoms. *Comput. Phys. Commun* 220, 319–331 (2017). (Cited on pages 14 and 30.)
- [77] A. Browaeys, D. Barredo, and T. Lahaye. Experimental investigations of dipole-dipole interactions between a few Rydberg atoms. J. Phys. B: At. Mol. Opt. Phys. 49, 15, 152001 (2016). (Cited on page 16.)
- [78] M. Tanasittikosol, J. D. Pritchard, D. Maxwell, A. Gauguet, K. J. Weatherill, R. M. Potvliege, and C. S. Adams. Microwave dressing of Rydberg dark states. J. Phys. B: At. Mol. Opt. Phys. 44, 18, 184020 (2011). (Cited on page 17.)
- [79] S. Sevinçli and T. Pohl. Microwave control of Rydberg atom interactions. New J. Phys 16, 12, 123036 (2014). (Cited on page 17.)
- [80] J. T. Young, P. Bienias, R. Belyansky, A. M. Kaufman, and A. V. Gorshkov. Asymmetric blockade and multi-qubit gates via dipole-dipole interactions. arXiv:2006.02486 (2020). (Cited on pages 17 and 151.)
- [81] K.-Y. Liao, H.-T. Tu, S.-Z. Yang, C.-J. Chen, X.-H. Liu, J. Liang, X.-D. Zhang, H. Yan, and S.-L. Zhu. Microwave electrometry via electromagnetically induced absorption in cold Rydberg atoms. *Phys. Rev. A* **101**, 053432 (2020). (Cited on page **17**.)

- [82] K. Singer, M. Reetz-Lamour, T. Amthor, L. G. Marcassa, and M. Weidemüller. Suppression of excitation and spectral broadening induced by interactions in a cold gas of Rydberg atoms. *Phys. Rev. Lett.* **93**, 16 (2004). (Cited on pages 23 and 86.)
- [83] D. Tong, S. M. Farooqi, J. Stanojevic, S. Krishnan, Y. P. Zhang, R. Côté, E. E. Eyler, and P. L. Gould. Local blockade of Rydberg excitation in an ultracold gas. *Phys. Rev. Lett.* **93**, 6 (2004). (Cited on pages **23** and **86**.)
- [84] R. Heidemann, U. Raitzsch, V. Bendkowsky, B. Butscher, R. Löw, and T. Pfau. Rydberg excitation of Bose-Einstein condensates. *Phys. Rev. Lett.* **100**, 3 (2008). (Cited on pages **23** and **86**.)
- [85] E. Urban, T. A. Johnson, T. Henage, L. Isenhower, D. D. Yavuz, T. G. Walker, and M. Saffman. Observation of Rydberg blockade between two atoms. *Nat. Phys.* 5, 2, 110–114 (2009). (Cited on pages 23 and 86.)
- [86] A. Gaëtan, Y. Miroshnychenko, T. Wilk, A. Chotia, M. Viteau, D. Comparat, P. Pillet, A. Browaeys, and P. Grangier. Observation of collective excitation of two individual atoms in the Rydberg blockade regime. *Nat. Phys.* 5, 2, 115–118 (2009). (Cited on pages 23 and 86.)
- [87] S. Weber, C. Tresp, H. Menke, A. Urvoy, O. Firstenberg, H. P. Büchler, and S. Hofferberth. Calculation of Rydberg interaction potentials. J. Phys. B: At. Mol. Opt. Phys. 50, 13 (2017). (Cited on pages 30, 31, 32, 38, 41, 84, 93, 136, and 167.)
- [88] Y.-Y. Jau, A. M. Hankin, T. Keating, I. H. Deutsch, and G. W. Biedermann. Entangling atomic spins with a Rydberg-dressed spin-flip blockade. *Nat. Phys.* 12, 1, 71–74 (2016). (Cited on pages 34, 85, 107, 133, and 134.)
- [89] C. Gaul, B. J. DeSalvo, J. A. Aman, F. B. Dunning, T. C. Killian, and T. Pohl. Resonant Rydberg dressing of alkaline-earth atoms via electromagnetically induced transparency. *Phys. Rev. Lett.* 116, 243001 (2016). (Cited on pages 34 and 133.)
- [90] J. Zeiher, J.-Y. Choi, A. Rubio-Abadal, T. Pohl, R. van Bijnen, I. Bloch, and C. Gross. Coherent many-body spin dynamics in a long-range interacting Ising chain. *Phys. Rev. X* 7, 041063 (2017). (Cited on pages 34, 35, 73, 133, 134, and 141.)
- [91] A. Arias, G. Lochead, T. M. Wintermantel, S. Helmrich, and S. Whitlock. Realization of a Rydberg-dressed Ramsey interferometer and electrometer. *Phys. Rev. Lett.* **122**, 053601 (2019). (Cited on pages 34, 133, and 134.)
- [92] D. Mitra. Exploring attractively interacting fermions in 2D using a quantum gas microscope. PhD thesis, Department of Physics, Princeton University, (2018). (Cited on pages 35, 60, 62, 77, 89, 114, and 153.)

- [93] P. T. Brown. Probing dynamical quantities in the 2D Fermi-Hubbard model with quantum gas microscopy. PhD thesis, Department of Physics, Princeton University, (2019). (Cited on pages 35, 77, 89, and 153.)
- [94] G. Zürn, T. Lompe, A. N. Wenz, S. Jochim, P. S. Julienne, and J. M. Hutson. Precise characterization of ⁶Li Feshbach resonances using trap-sideband-resolved rf spectroscopy of weakly bound molecules. *Phys. Rev. Lett.* **110**, 135301 (2013). (Cited on page 35.)
- [95] E. Arimondo, M. Inguscio, and P. Violino. Experimental determinations of the hyperfine structure in the alkali atoms. Rev. Mod. Phys. 49, 31–75 (1977). (Cited on page 36.)
- [96] M. Houbiers, H. T. C. Stoof, W. I. McAlexander, and R. G. Hulet. Elastic and inelastic collisions of ⁶Li atoms in magnetic and optical traps. *Phys. Rev. A* 57, R1497–R1500 (1998). (Cited on pages 36 and 77.)
- [97] W. Li, P. J. Tanner, and T. F. Gallagher. Dipole-dipole excitation and ionization in an ultracold gas of Rydberg atoms. *Phys. Rev. Lett.* 94, 173001 (2005). (Cited on page 44.)
- [98] T. Vogt, M. Viteau, J. Zhao, A. Chotia, D. Comparat, and P. Pillet. Dipole blockade at Förster resonances in high resolution laser excitation of Rydberg states of cesium atoms. *Phys. Rev. Lett.* 97, 083003 (2006). (Cited on page 44.)
- [99] A. Reinhard, T. Cubel Liebisch, K. C. Younge, P. R. Berman, and G. Raithel. Rydberg-Rydberg collisions: Resonant enhancement of state mixing and Penning ionization. *Phys. Rev. Lett.* 100, 123007 (2008). (Cited on page 44.)
- [100] J. Nipper, J. B. Balewski, A. T. Krupp, B. Butscher, R. Löw, and T. Pfau. Highly resolved measurements of Stark-tuned Förster resonances between Rydberg atoms. *Phys. Rev. Lett.* 108, 113001 (2012). (Cited on page 44.)
- [101] S. Ravets, H. Labuhn, D. Barredo, L. Béguin, T. Lahaye, and A. Browaeys. Coherent dipole–dipole coupling between two single Rydberg atoms at an electrically-tuned förster resonance. *Nature Physics* 10, 12, 914–917 (2014). (Cited on page 44.)
- [102] R. M. W. van Bijnen and T. Pohl. Quantum magnetism and topological ordering via Rydberg dressing near Förster resonances. *Phys. Rev. Lett.* **114** (2015). (Cited on pages 44, 45, and 47.)
- [103] S. Hollerith, J. Zeiher, J. Rui, A. Rubio-Abadal, V. Walther, T. Pohl, D. M. Stamper-Kurn, I. Bloch, and C. Gross. Quantum gas microscopy of Rydberg macrodimers. Science 364, 6441, 664–667 (2019). (Cited on pages 44, 47, and 48.)
- [104] J. I. Thorpe, K. Numata, and J. Livas. (Cited on page 54.)

- [105] A. Kramida, Yu. Ralchenko, J. Reader, and and NIST ASD Team. NIST Atomic Spectra Database (ver. 5.8), [Online]. Available: https://physics.nist.gov/asd [2021, May 17]. National Institute of Standards and Technology, Gaithersburg, MD., (2020). (Cited on pages 58 and 171.)
- [106] P. Thoumany, T. Hänsch, G. Stania, L. Urbonas, and T. Becker. Optical spectroscopy of rubidium Rydberg atoms with a 297 nm frequency-doubled dye laser. Opt. Lett. 34, 11, 1621 (2009). (Cited on page 58.)
- [107] L. Festa, N. Lorenz, L.-M. Steinert, Z. Chen, P. Osterholz, R. Eberhard, and C. Gross. Motion assisted facilitated excitation of Rydberg atoms in optical tweezers. arXiv:2103.14383 (2021). (Cited on pages 72 and 74.)
- [108] W. Li, C. Ates, and I. Lesanovsky. Nonadiabatic motional effects and dissipative blockade for Rydberg atoms excited from optical lattices or microtraps. *Phys. Rev. Lett.* **110**, 213005 (2013). (Cited on pages 77 and 141.)
- [109] T. Macrì and T. Pohl. Rydberg dressing of atoms in optical lattices. Phys. Rev. A 89, 011402(R) (2014). (Cited on pages 77 and 141.)
- [110] R. Mukherjee, T. C. Killian, and K. R. A. Hazzard. Accessing Rydberg-dressed interactions using many-body Ramsey dynamics. *Phys. Rev. A* **94**, 053422 (2016). (Cited on page **79**.)
- [111] P. Schauß, M. Cheneau, M. Endres, T. Fukuhara, S. Hild, A. Omran, T. Pohl, C. Gross, S. Kuhr, and I. Bloch. Observation of spatially ordered structures in a two-dimensional Rydberg gas. *Nature* 491, 7422, 87–91 (2012). (Cited on page 85.)
- [112] P. Schauß, J. Zeiher, T. Fukuhara, S. Hild, M. Cheneau, T. Macrì, T. Pohl, I. Bloch, and C. Gross. Crystallization in Ising quantum magnets. Science 347, 6229, 1455–1458 (2015). (Cited on page 85.)
- [113] K. M. Maller, M. T. Lichtman, T. Xia, Y. Sun, M. J. Piotrowicz, A. W. Carr, L. Isenhower, and M. Saffman. Rydberg-blockade controlled-not gate and entanglement in a two-dimensional array of neutral-atom qubits. *Phys. Rev. A* 92 (2015). (Cited on page 85.)
- [114] H. Labuhn, D. Barredo, S. Ravets, S. de Léséleuc, T. Macrí, T. Lahaye, and A. Browaeys. Tunable two-dimensional arrays of single Rydberg atoms for realizing quantum Ising models. *Nature* **534**, 7609, 667–670 (2016). (Cited on pages 85, 86, and 98.)
- [115] A. Keesling, A. Omran, H. Levine, H. Bernien, H. Pichler, S. Choi, R. Samajdar, S. Schwartz, P. Silvi, S. Sachdev, P. Zoller, M. Endres, M. Greiner, V. Vuletić, and M. D. Lukin. Quantum Kibble–Zurek mechanism and critical dynamics on a programmable Rydberg simulator. *Nature* **568**, 7751, 207–211 (2019). (Cited on pages **86** and **108**.)

- [116] A. Avella and F. Mancini, editors. Strongly Correlated Systems. Springer Series in Solid-State Sciences. Springer-Verlag, Berlin, Heidelberg, (2013). (Cited on page 86.)
- [117] W. von der Linden. A quantum Monte Carlo approach to many-body physics. *Phys. Rep.* **220**, 2, 53–162 (1992). (Cited on page 86.)
- [118] S. R. White. Density matrix formulation for quantum renormalization groups. *Phys. Rev. Lett.* **69**, 2863–2866 (1992). (Cited on page 86.)
- [119] U. Schollwöck. The density-matrix renormalization group. Rev. Mod. Phys. 77, 259–315 (2005). (Cited on page 86.)
- [120] K. A. Hallberg. New trends in density matrix renormalization. Adv. Phys. 55, 5-6, 477–526 (2006). (Cited on page 86.)
- [121] B. Tang, E. Khatami, and M. Rigol. A short introduction to numerical linkedcluster expansions. Comput. Phys. Commun. 184, 3, 557–564 (2013). (Cited on pages 86, 93, and 95.)
- [122] R. Orús. A practical introduction to tensor networks: Matrix product states and projected entangled pair states. *Ann. Phys.* **349**, Supplement C, 117–158 (2014). (Cited on page 86.)
- [123] G. Vidal. Efficient simulation of one-dimensional quantum many-body systems. *Phys. Rev. Lett.* **93** (2004). (Cited on page 86.)
- [124] S. R. White and A. E. Feiguin. Real-time evolution using the density matrix renormalization group. *Phys. Rev. Lett.* **93** (2004). (Cited on page 86.)
- [125] K. R. A. Hazzard, M. van den Worm, M. Foss-Feig, S. R. Manmana, E. G. Dalla Torre, T. Pfau, M. Kastner, and A. M. Rey. Quantum correlations and entanglement in far-from-equilibrium spin systems. *Phys. Rev. A* 90 (2014). (Cited on page 86.)
- [126] P. Fendley, K. Sengupta, and S. Sachdev. Competing density-wave orders in a one-dimensional hard-boson model. *Phys. Rev. B* **69** (2004). (Cited on page 87.)
- [127] H. Weimer, R. Löw, T. Pfau, and H. P. Büchler. Quantum critical behavior in strongly interacting Rydberg gases. Phys. Rev. Lett. 101 (2008). (Cited on page 87.)
- [128] T. Pohl, E. Demler, and M. D. Lukin. Dynamical crystallization in the dipole blockade of ultracold atoms. Phys. Rev. Lett. 104, 4 (2010). (Cited on pages 87 and 97.)
- [129] E. Sela, M. Punk, and M. Garst. Dislocation-mediated melting of one-dimensional Rydberg crystals. *Phys. Rev. B* **84** (2011). (Cited on page **87**.)

- [130] A. Yanase, Y. Takeshige, and M. Suzuki. Critical behaviour of the susceptibility of the Ising model with a transverse field. J. Phys. Soc. Jpn. 41, 4, 1108–1115 (1976). (Cited on page 87.)
- [131] C. J. Hamer and A. C. Irving. Cluster expansions in the (2+1)D Ising model. J. Phys. A: Math. Gen. 17, 8, 1649 (1984). (Cited on page 87.)
- [132] I. G. White, B. Sundar, and K. R. A. Hazzard. Quantum dynamics from a numerical linked cluster expansion. arXiv:1710.07696 (2017). (Cited on page 93.)
- [133] M. Rigol, T. Bryant, and R. R. P. Singh. Numerical linked-cluster algorithms. i. spin systems on square, triangular, and kagomé lattices. *Phys. Rev. E* **75** (2007). (Cited on pages **93** and **95**.)
- [134] M. L. Wall and L. D. Carr. Dipole-dipole interactions in optical lattices do not follow an inverse cube power law. New J. Phys. 15, 12, 123005 (2013). (Cited on page 95.)
- [135] J. Schachenmayer, I. Lesanovsky, A. Micheli, and A. J. Daley. Dynamical crystal creation with polar molecules or Rydberg atoms in optical lattices. *New J. Phys.* 12, 10 (2010). (Cited on page 97.)
- [136] R. M. W. van Bijnen, S. Smit, K. a. H. van Leeuwen, E. J. D. Vredenbregt, and S. J. J. M. F. Kokkelmans. Adiabatic formation of Rydberg crystals with chirped laser pulses. J. Phys. B: At. Mol. Opt. Phys. 44, 18 (2011). (Cited on page 97.)
- [137] K. Mølmer, Y. Castin, and J. Dalibard. Monte Carlo wave-function method in quantum optics. J. Opt. Soc. Am. B 10, 3, 524–538 (1993). (Cited on pages 98, 104, and 105.)
- [138] H. Weimer. Tailored jump operators for purely dissipative quantum magnetism. J. Phys. B: At. Mol. Opt. Phys. 50, 2 (2017). (Cited on pages 98 and 104.)
- [139] N. Metropolis, A. W. Rosenbluth, M. N. Rosenbluth, A. H. Teller, and E. Teller. Equation of state calculations by fast computing machines. J. Chem. Phys. 21, 6, 1087–1092 (1953). (Cited on page 101.)
- [140] D. V. Schroeder. An Introduction to Thermal Physics. Addison Wesley Longman, Boston, (2000). ISBN 0321277791. (Cited on page 101.)
- [141] S. M. Bhattacharjee and A. Khare. Fifty years of the exact solution of the two-dimensional Ising model by Onsager. Current Science 69, 10, 816–821 (1995). (Cited on page 101.)
- [142] J. Dalibard, Y. Castin, and K. Mølmer. Wave-function approach to dissipative processes in quantum optics. *Phys. Rev. Lett.* **68**, 580–583 (1992). (Cited on page 105.)

- [143] R. Dum, P. Zoller, and H. Ritsch. Monte Carlo simulation of the atomic master equation for spontaneous emission. *Phys. Rev. A* 45, 4879–4887 (1992). (Cited on page 105.)
- [144] D. Barredo, S. de Léséleuc, V. Lienhard, T. Lahaye, and A. Browaeys. An atom-by-atom assembler of defect-free arbitrary two-dimensional atomic arrays. *Science* 354, 6315, 1021–1023 (2016). (Cited on page 107.)
- [145] M. Endres, H. Bernien, A. Keesling, H. Levine, E. R. Anschuetz, A. Krajen-brink, C. Senko, V. Vuletic, M. Greiner, and M. D. Lukin. Atom-by-atom assembly of defect-free one-dimensional cold atom arrays. Science 354, 6315, 1024–1027 (2016). (Cited on page 107.)
- [146] A. Gaj, A. T. Krupp, J. B. Balewski, R. Löw, S. Hofferberth, and T. Pfau. From molecular spectra to a density shift in dense Rydberg gases. *Nat. Comm.* 5 (2014). (Cited on page 107.)
- [147] R. Schmidt, H. R. Sadeghpour, and E. Demler. Mesoscopic Rydberg impurity in an atomic quantum gas. *Phys. Rev. Lett.* **116** (2016). (Cited on page 107.)
- [148] S. Sachdev. *Quantum Phase Transitions*. Cambridge University Press, Cambridge, England, (1999). (Cited on page 108.)
- [149] S. Tanaka, R. Tamura, and B. K. Chakrabarti. *Quantum Spin Glasses, Annealing and Computation*. ISBN 978-1-107-11319-0. (Cited on page 108.)
- [150] A. Polkovnikov. Universal adiabatic dynamics in the vicinity of a quantum critical point. Phys. Rev. B 72 (2005). (Cited on page 108.)
- [151] J. Dziarmaga. Dynamics of a quantum phase transition: Exact solution of the quantum Ising model. *Phys. Rev. Lett.* **95** (2005). (Cited on page 108.)
- [152] W. H. Zurek, U. Dorner, and P. Zoller. Dynamics of a quantum phase transition. *Phys. Rev. Lett.* **95** (2005). (Cited on page 108.)
- [153] B. Damski. The simplest quantum model supporting the Kibble-Zurek mechanism of topological defect production: Landau-Zener transitions from a new perspective. *Phys. Rev. Lett.* **95** (2005). (Cited on page **108**.)
- [154] D. Jaschke, K. Maeda, J. D. Whalen, M. L. Wall, and L. D. Carr. Critical phenomena and Kibble-Zurek scaling in the long-range quantum Ising chain. New J. Phys. 19, 3 (2017). (Cited on page 108.)
- [155] Z. Zhang, M. Yuan, B. Sundar, and K. R. Hazzard. Effect of atom motion in Rydberg-atom arrays. DAMOP, (2021). https://meetings.aps.org/Meeting/DAMOP21/Session/S07.4. (Cited on pages 108 and 153.)
- [156] E. van Nieuwenburg, Y. Baum, and G. Refael. From Bloch oscillations to many-body localization in clean interacting systems. *Proc. Natl. Acad. Sci. U.S.A.* 116, 19, 9269–9274 (2019). (Cited on pages 109, 111, 113, 117, and 131.)

- [157] M. Schulz, C. A. Hooley, R. Moessner, and F. Pollmann. Stark many-body localization. *Phys. Rev. Lett.* **122**, 040606 (2019). (Cited on pages 109, 111, 113, 117, and 131.)
- [158] F. Bloch. Über die quantenmechanik der elektronen in kristallgittern. Z. Phys. **52**, 7, 555–600 (1929). (Cited on page 110.)
- [159] G. H. Wannier. Dynamics of band electrons in electric and magnetic fields. *Rev. Mod. Phys.* **34**, 645–655 (1962). (Cited on page **110**.)
- [160] E. E. Mendez, F. Agulló-Rueda, and J. M. Hong. Stark localization in GaAs-GaAlAs superlattices under an electric field. Phys. Rev. Lett. 60, 2426–2429 (1988). (Cited on page 110.)
- [161] P. Voisin, J. Bleuse, C. Bouche, S. Gaillard, C. Alibert, and A. Regreny. Observation of the Wannier-Stark quantization in a semiconductor superlattice. Phys. Rev. Lett. 61, 1639–1642 (1988). (Cited on page 110.)
- [162] A. Nahum, J. Ruhman, S. Vijay, and J. Haah. Quantum entanglement growth under random unitary dynamics. *Phys. Rev. X* 7, 031016 (2017). (Cited on page 110.)
- [163] A. Nahum, S. Vijay, and J. Haah. Operator spreading in random unitary circuits. *Phys. Rev. X* 8, 021014 (2018). (Cited on page 110.)
- [164] C. W. von Keyserlingk, T. Rakovszky, F. Pollmann, and S. L. Sondhi. Operator hydrodynamics, OTOCs, and entanglement growth in systems without conservation laws. *Phys. Rev. X* 8, 021013 (2018). (Cited on page 110.)
- [165] V. Khemani, A. Vishwanath, and D. A. Huse. Operator spreading and the emergence of dissipative hydrodynamics under unitary evolution with conservation laws. *Phys. Rev. X* 8, 031057 (2018). (Cited on page 110.)
- [166] T. Rakovszky, F. Pollmann, and C. W. von Keyserlingk. Diffusive hydrodynamics of out-of-time-ordered correlators with charge conservation. *Phys. Rev.* X 8, 031058 (2018). (Cited on page 110.)
- [167] S. Gopalakrishnan, D. A. Huse, V. Khemani, and R. Vasseur. Hydrodynamics of operator spreading and quasiparticle diffusion in interacting integrable systems. *Phys. Rev. B* **98**, 220303 (2018). (Cited on page 110.)
- [168] T. Banks and A. Lucas. Emergent entropy production and hydrodynamics in quantum many-body systems. *Phys. Rev. E* **99**, 022105 (2019). (Cited on page 110.)
- [169] F. Meinert, M. J. Mark, E. Kirilov, K. Lauber, P. Weinmann, M. Gröbner, and H.-C. Nägerl. Interaction-induced quantum phase revivals and evidence for the transition to the quantum chaotic regime in 1D atomic Bloch oscillations. *Phys. Rev. Lett.* 112, 193003 (2014). (Cited on page 110.)

- [170] J.-y. Choi, S. Hild, J. Zeiher, P. Schauß, A. Rubio-Abadal, T. Yefsah, V. Khemani, D. A. Huse, I. Bloch, and C. Gross. Exploring the many-body localization transition in two dimensions. Science 352, 6293, 1547–1552 (2016). (Cited on page 110.)
- [171] S. Scherg, T. Kohlert, J. Herbrych, J. Stolpp, P. Bordia, U. Schneider, F. Heidrich-Meisner, I. Bloch, and M. Aidelsburger. Nonequilibrium mass transport in the 1D Fermi-Hubbard model. Phys. Rev. Lett. 121, 130402 (2018). (Cited on page 110.)
- [172] M. Rispoli, A. Lukin, R. Schittko, S. Kim, M. E. Tai, J. Léonard, and M. Greiner. Quantum critical behaviour at the many-body localization transition. *Nature* **573**, 7774, 385–389 (2019). (Cited on page 110.)
- [173] E. Guardado-Sanchez, P. T. Brown, D. Mitra, T. Devakul, D. A. Huse, P. Schauß, and W. S. Bakr. Probing the quench dynamics of antiferromagnetic correlations in a 2D quantum Ising spin system. *Phys. Rev. X* 8, 021069 (2018). (Cited on page 110.)
- [174] S. Mandt, A. Rapp, and A. Rosch. Interacting fermionic atoms in optical lattices diffuse symmetrically upwards and downwards in a gravitational potential. *Phys. Rev. Lett.* **106**, 250602 (2011). (Cited on pages 110, 111, 119, 121, and 129.)
- [175] A. Rapp, S. Mandt, and A. Rosch. Equilibration rates and negative absolute temperatures for ultracold atoms in optical lattices. *Phys. Rev. Lett.* **105**, 220405 (2010). (Cited on page 110.)
- [176] S. Braun, J. P. Ronzheimer, M. Schreiber, S. S. Hodgman, T. Rom, I. Bloch, and U. Schneider. Negative absolute temperature for motional degrees of freedom. Science 339, 6115, 52–55 (2013). (Cited on page 110.)
- [177] P. M. Preiss, R. Ma, M. E. Tai, A. Lukin, M. Rispoli, P. Zupancic, Y. Lahini, R. Islam, and M. Greiner. Strongly correlated quantum walks in optical lattices. Science 347, 6227, 1229–1233 (2015). (Cited on page 115.)
- [178] R. Ma, M. E. Tai, P. M. Preiss, W. S. Bakr, J. Simon, and M. Greiner. Photon-assisted tunneling in a biased strongly correlated Bose gas. Phys. Rev. Lett. 107, 095301 (2011). (Cited on page 115.)
- [179] S. Pai, M. Pretko, and R. M. Nandkishore. Localization in fractonic random circuits. *Phys. Rev. X* **9**, 021003 (2019). (Cited on page **117**.)
- [180] S. Pai and M. Pretko. Dynamical scar states in driven fracton systems. *Phys. Rev. Lett.* **123**, 136401 (2019). (Cited on page 117.)
- [181] S. Scherg, T. Kohlert, P. Sala, F. Pollmann, B. H. M., I. Bloch, and M. Aidelsburger. Observing non-ergodicity due to kinetic constraints in tilted Fermi-Hubbard chains. arXiv:2010.12965 (2020). (Cited on page 131.)

- [182] M. Inguscio, W. Ketterle, and C. Salomon, editors. *Ultracold Fermi Gases, Proceedings of the International School of Physics Enrico Fermi, Course CLXIV, Varenna 2006*, Amsterdam, (2008). IOS Press. (Cited on page 133.)
- [183] L. Tanzi, E. Lucioni, F. Famà, J. Catani, A. Fioretti, C. Gabbanini, R. N. Bisset, L. Santos, and G. Modugno. Observation of a dipolar quantum gas with metastable supersolid properties. *Phys. Rev. Lett.* **122**, 130405 (2019). (Cited on page 133.)
- [184] L. Chomaz, D. Petter, P. Ilzhöfer, G. Natale, A. Trautmann, C. Politi, G. Durastante, R. M. W. van Bijnen, A. Patscheider, M. Sohmen, M. J. Mark, and F. Ferlaino. Long-lived and transient supersolid behaviors in dipolar quantum gases. *Phys. Rev. X* **9**, 021012 (2019). (Cited on page 133.)
- [185] A. J. Daley. Quantum trajectories and open many-body quantum systems. Adv. Phys. 63, 2, 77–149 (2014). (Cited on page 149.)
- [186] A. Dauphin, M. Müller, and M. A. Martin-Delgado. Rydberg-atom quantum simulation and Chern-number characterization of a topological Mott insulator. *Phys. Rev. A* 86, 053618 (2012). (Cited on page 151.)
- [187] M. Žnidarič, T. Prosen, and P. Prelovšek. Many-body localization in the Heisenberg XXZ magnet in a random field. Phys. Rev. B 77, 064426 (2008). (Cited on page 151.)
- [188] J. H. Bardarson, F. Pollmann, and J. E. Moore. Unbounded growth of entanglement in models of many-body localization. *Phys. Rev. Lett.* **109**, 017202 (2012). (Cited on page 151.)
- [189] M. Serbyn, Z. Papić, and D. A. Abanin. Local conservation laws and the structure of the many-body localized states. *Phys. Rev. Lett.* **111**, 127201 (2013). (Cited on page 151.)
- [190] D. J. Luitz, N. Laflorencie, and F. Alet. Many-body localization edge in the random-field Heisenberg chain. *Phys. Rev. B* **91**, 081103 (2015). (Cited on page 151.)
- [191] M. Schecter, T. Iadecola, and S. Das Sarma. Configuration-controlled many-body localization and the mobility emulsion. *Phys. Rev. B* **98**, 174201 (2018). (Cited on page **151**.)
- [192] T. Rakovszky, P. Sala, R. Verresen, M. Knap, and F. Pollmann. Statistical localization: From strong fragmentation to strong edge modes. *Phys. Rev. B* **101**, 125126 (2020). (Cited on page 151.)
- [193] N. Nessi, A. Iucci, and M. A. Cazalilla. Quantum quench and prethermalization dynamics in a two-dimensional Fermi gas with long-range interactions. *Phys. Rev. Lett.* **113**, 210402 (2014). (Cited on page 151.)

- [194] F. Grusdt, Z. Zhu, T. Shi, and E. Demler. Meson formation in mixed-dimensional t-J models. SciPost Phys. 5, 57 (2018). (Cited on page 151.)
- [195] P. P. Mazza, R. Schmidt, and I. Lesanovsky. Vibrational dressing in kinetically constrained Rydberg spin systems. Phys. Rev. Lett. 125, 3, 033602 (2020). (Cited on page 151.)
- [196] F. M. Gambetta, W. Li, F. Schmidt-Kaler, and I. Lesanovsky. Engineering nonbinary Rydberg interactions via phonons in an optical lattice. *Phys. Rev. Lett.* 124, 043402 (2020). (Cited on page 151.)
- [197] R. Belyansky, J. T. Young, P. Bienias, Z. Eldredge, A. M. Kaufman, P. Zoller, and A. V. Gorshkov. Nondestructive cooling of an atomic quantum register via state-insensitive Rydberg interactions. *Phys. Rev. Lett.* 123, 21, 213603 (2019). (Cited on page 151.)
- [198] S. F. Cooper, Z. Burkley, A. D. Brandt, C. Rasor, and D. C. Yost. Cavity-enhanced deep ultraviolet laser for two-photon cooling of atomic hydrogen. Opt. Lett. 43, 6, 1375–1378 (2018). (Cited on pages 152 and 155.)
- [199] R. M. W. van Bijnen and T. Pohl. Quantum magnetism and topological ordering via Rydberg dressing near Förster resonances. *Phys. Rev. Lett.* **114**, 243002 (2015). (Cited on page 152.)